SMALL-CRACK TEST METHODS

LARSEN/ALLISON
EDITORS

STP 1149

STP 1149

Small-Crack Test Methods

James M. Larsen and John E. Allison, editors

ASTM Publication Code Number (PCN)
04-011490-30

ASTM
1916 Race Street
Philadelphia, PA 19103

Library of Congress Cataloging-in-Publication Data

Small-crack test methods/James M. Larsen and John E. Allison, editors
(STP ; 1149)
Includes bibliographical references and index.
"ASTM publication code number (PCN) 04-011490-30."
ISBN 0-8031-1469-9
1. Fracture mechanics—Congresses. 2. Materials—Fatigue
—Testing—Congresses. I. Larsen, James M. II. Allison, John E.
(John Edmond), 1950- . III. Series: ASTM special technical
publication: 1149.
TA409.S6 1992
620 . 1 126—dc20 92-10509
CIP

Peer Review Policy

Each paper published in this volume was evaluated by three peer reviewers. The authors addressed all of the reviewers' comments to the satisfaction of both the technical editor(s) and the ASTM Committee on Publications.

The quality of the papers in this publication reflects not only the obvious efforts of the authors and the technical editor(s), but also the work of these peer reviewers. The ASTM Committee on Publications acknowledges with appreciation their dedication and contribution to time and effort on behalf of ASTM.

Printed in Chelsea, MI
June 1992

Foreword

This book represents the proceedings of the Symposium on Small-Crack Test Methods sponsored by the joint ASTM E-9 on Fatigue and E-24 on Fracture Testing and Task Group on Small Fatigue Cracks. The symposium was held in the Hilton Palacio del Rio Hotel in San Antonio, TX, on 14 Nov. 1990. The symposium was organized by J. M. Larsen, U.S. Air Force, Wright Laboratory, Wright-Patterson Air Force Base, OH, and J. E. Allison, Research Staff, Ford Motor Company, Dearborn, MI, who also served as coeditors of this Special Technical Publication (STP).

This publication presents state-of-the-art reviews from leading experts on methods for characterizing small-crack behavior. It should be of use to students and practicing researchers in the fields of materials science and engineering and mechanical engineering.

The editors would foremost like to express their appreciation to the authors for their high quality manuscripts and responsiveness to reviewer comments. Special appreciation is due to the many reviewers who have sacrificed their time and effort in ensuring the accuracy and high quality of the papers included in this publication. We would also like to commend the ASTM staff, who provided for the smooth administration of the symposium (Dorothy Savini and Patrick Barr) and the editorial review of this publication (Monica Siperko, Rita Hippensteel, and Kathy Dernoga). Finally, we gratefully acknowledge the support of our own organizations: the U.S. Air Force and Ford Motor Company.

Contents

Introduction 1

Fracture Mechanics Parameters for Small Fatigue Cracks—J. C. NEWMAN, JR. 6

Monitoring Small-Crack Growth by the Replication Method—M. H. SWAIN 34

Measurement of Small Cracks by Photomicroscopy: Experiments and Analysis—J. M. LARSEN, J. R. JIRA, AND K. S. RAVICHANDRAN 57

The Experimental Mechanics of Microcracks—D. L. DAVIDSON 81

Real-Time Measurement of Small-Crack Opening Behavior Using an Interferometric Strain/Displacement Gage—W. N. SHARPE, JR., J. R. JIRA, AND J. M. LARSEN 92

Direct Current Electrical Potential Measurement of the Growth of Small Cracks—R. P. GANGLOFF, D. C. SLAVIK, R. S. PIASCIK, AND R. H. VAN STONE 116

An Ultrasonic Method for Measurement of Size and Opening Behavior of Small Fatigue Cracks—M. T. RESCH AND D. V. NELSON 169

Simulation of Short Crack and Other Low Closure Loading Conditions Utilizing Constant K_{max} ΔK-Decreasing Fatigue Crack Growth Procedures—R. HERTZBERG, W. A. HERMAN, T. CLARK, AND R. JACCARD 197

Summary 221

Introduction

It is widely understood that small, three-dimensional fatigue cracks can propagate at rates that are considerably faster than those of large cracks subjected to a nomimally equivalent stress intensity factor range ΔK. Because many design life predictions are based on data from large-crack specimens, this crack-size effect potentially can lead to nonconservative designs. Thus, the topic of small-crack propagation has become important to the engineering community. There have been a number of recent conferences on this topic [*1–3*] that provide good reviews of the nature and extent of the "small-crack effect."

This Special Technical Publication (STP) is the result of a Symposium sponsored by the Joint ASTM E-9 on Fatigue and E-24 on Fracture Testing Task Group on Small Fatigue Cracks, which was held in San Antonio, TX, in Nov. 1990. The purpose of this STP is to review the state-of-the-art in small-crack test methods and provide the testing community with a single, authoritative reference describing recommended experimental and analytical procedures. Recognizing the unique role of ASTM in developing test standards, each of the authors was invited to provide detailed, quantitative guidance on necessary procedures for testing and data acquisition, including descriptions of the advantages and limitations of the specific technique with sufficient detail to allow use by the inexperienced user. The emphasis in this STP is on characterizing small, three-dimensional fatigue cracks, either naturally or artificially initiated. The potential user is encouraged to consider the specific attributes of the various experimental methods when selecting one or more of the test methods to satisfy his particular research needs. To aid in this process, the following discussion presents an overview of the contents of this monograph.

Fracture Mechanics Parameters for Small Fatigue Cracks—J. C. Newman, Jr.

This paper provides a good introduction to the unique behavior of small fatigue cracks and the primary factors responsible for this uniqueness. A central focus of the author is fracture-mechanics parameters that have been used to correlate or predict the growth of small cracks, with an emphasis on continuum mechanics concepts, crack closure, and nonlinear behavior of small cracks. A review of common small-crack test specimens and stress intensity solutions is provided. A major portion of this paper is spent discussing elastic-plastic analysis. The literature in this area is reviewed and simple elastic-plastic and cyclic J-integral estimators are considered for small-crack geometries. The author formulates and applies a simple plastic-zone corrected stress-intensity factor that approximates the J integral surprisingly well. The conclusion is presented that plasticity effects are small for the majority of small-crack data in the literature, and only for situations in which the applied stress was appreciably higher than the flow stress are cyclic plasticity effects significant. The author concludes that crack closure transients are the major factor causing the small-crack effect. These closure transients are attributed to the build up of plasticity-induced crack closure as the crack length increases, and a model is presented for predicting this transient. Finally, using methods described in this paper, accurate predictions of crack shape and sample life are demonstrated for aluminum alloys.

Monitoring Small-Crack Growth by the Replication Method—M. H. Swain

This paper provides a detailed overview of one of the most important, widely used, and least expensive small-crack test methods. The author gives details on preparation of the specimen surface and the replica and discusses replica characterization methods, including many practical tips on use of the technique. The procedure involves creating a series of acetate replicas of the surface of a fatigue specimen throughout its life to produce a permanent record of the state of cracking. The method has been applied to a wide variety of specimen geometries and materials and is applicable to naturally initiated corner and surface cracks. A key attribute of the technique is the ability to track backward in a series of replicas to identify the earliest stages of damage. Replicas may be viewed using either optical microscopy or scanning electron microscopy (SEM). The latter method provides a resolution of approximately 0.1 μm, although the labor and time involved are considerably greater than for optical microscopy. The author discusses stress intensity factor calibrations and presents example small-crack data acquired by replication. A series of practical advantages and limitations of these experimental methods are presented, including effects of hold times and environmental effects. In addition, an appendix is presented, which outlines criteria for selecting cracks that are sufficiently separated as to be considered to have noninteracting stress fields.

Measurement of Small Cracks by Photomicroscopy: Experiments and Analysis—J. M. Larsen, J. R. Jira, and K. S. Ravichandran

The authors discuss a second optically based technique that uses a relatively inexpensive photomicroscope for recording the growth of small fatigue cracks. The experimental apparatus includes a microscope mounted with a 35-mm camera that is triggered by a standard microcomputer, which also controls the testing machine. The paper addresses small-crack issues associated with specimen preparation, effects of surface residual stresses, and characterization of crack shape. The capabilities of the method are documented by data characterizing practical optical resolution, and data are presented to quantify the typical precision of crack length measurements ($\approx$ 1 μm). While this method offers a lower resolution than acetate replication, the semi-automated nature of the approach facilitates the acquisition of a large number of data, which can be analyzed statistically.

The second half of the paper discusses possible pitfalls in the calculation of crack growth rates. A series of analyses is presented of a single, analytically generated, data set to illustrate the influence of the precision of crack length measurement and measurement interval on calculated crack growth rates. It is shown that the ratio of measurement error to measurement interval that typifies many small-crack experiments may have dramatic effects on the calculated crack growth rates over the life of the test. The analysis illustrates the importance of differentiating such effects from any physically inherent variability in small-crack growth rates. To address this problem, a modified incremental polynomial method for calculation of crack growth rates is presented.

The Experimental Mechanics of Microcracks—D. L. Davidson

This paper reviews the extensive accomplishments of the author and his colleagues in applying the scanning electron microscope to the study of small fatigue cracks. The author's pioneering efforts in the development of a high-temperature fatigue loading stage in the SEM are highlighted, and numerous applications of this specialized capability are discussed. The SEM affords high resolution imaging of detailed features of behavior of small cracks,

and through the use of stereoimaging, it has been possible to make measurements of a wide range of crack field parameters useful in characterizing the driving force of both small and large cracks. The instrument has provided measurements of displacements and strains in the vicinity of a crack, facilitating documentation of both crack-tip deformation fields and crack closure in the wake of the crack. Probably no other experimental approach has provided such a detailed view of the physical phenomena associated with the propagation of small and large fatigue cracks.

Much of the paper is devoted to highlighting achievements made possible by the SEM observations, including assessments of the factors that appear to be responsible for the differences between the behavior of large and small fatigue cracks. It is concluded from extensive characterization of both small and large cracks using the SEM that the most important factors that differentiate small from large cracks are the crack-size dependence of crack closure and the poor similitude between the crack-tip deformation fields of small versus large cracks. Microstructural effects are also deemed to have a significant influence on small-crack behavior, but changes in crack growth mechanism as a function of crack size have not been observed.

Real-Time Measurement of Small-Crack Opening Behavior Using an Interferometric Strain/Displacement Gage—W. N. Sharpe, Jr., J. R. Jira, and J. M. Larsen

This paper discusses the application of a laser interferometric strain/displacement gage (ISDG) to the study of small fatigue cracks. The technique, which is applicable to both naturally and artificially initiated cracks, is essentially a noncontacting, short-gage-length extensometer having a displacement resolution of approximately 5 nm. From data of applied load versus crack-mouth-opening displacement, measurements of crack-opening compliance and observations of crack closure are obtained. Computerization makes real-time analysis of the data possible and efficiently handles the large quantity of data that is acquired. The general principles of operation of the ISDG are discussed, and four variations of the instrument currently in use are reviewed. The authors offer a number of practical considerations for application of this approach to small-crack testing and present example data illustrating the capabilities of the method for measurement of crack closure and crack length. When combined with independent measurements of surface crack length, the compliance measurements provided by the ISDG may be used to calculate instantaneous crack shape. Because the data are available in real time, the ISDG may be used for feedback control of fatigue tests following procedures similar to those used for automated testing of conventional large-crack specimen (for example, $\Delta K_{\text{decreasing}}$, ΔK_{th} tests).

Direct Current Electrical Potential Measurement of the Growth of Small Fatigue Cracks—R. P. Gangloff, D. C. Slavik, R. S. Piascik, and R. H. Van Stone

This paper provides an extensive and detailed review of direct current electric potential techniques for characterizing small fatigue cracks. Using the descriptions provided of the required apparatus and experimental arrangements, any good experimentalist should be able to duplicate and apply this technique. In particular, there is an excellent description of experimental issues such as probe location, the effect of changes in probe location, thermal electromotive force effects, and methods for dealing with crack shorting effects. Materials covered include ferrous, aluminum, titantium, and nickel alloys. The authors conclude that, in these metallic materials, electric potential techniques can be used to monitor cracks greater than 75 μm and resolve crack length changes of 1 to 5 μm. A review of models for predicting the dimensions of three-dimensional cracks from changes in measured electric potential is

provided. For accurately predicting crack length, assumptions regarding crack shape must be made, however, the authors provide evidence that, in general, crack shape is well-controlled and can be predicted. For materials in which crack shape has not been previously characterized, methods are suggested for verifying the required assumptions. The paper contains many examples of applications of the electric potential technique to small-crack characterization, with special emphasis on novel applications in investigations involving environmental and elevated temperature effects. The authors include examples demonstrating how this technique can be used in sophisticated ways to develop an understanding of the mechanisms controlling small-crack propagation.

An Ultrasonic Method for Measurement of Size and Opening Behavior of Small Fatigue Cracks—M. T. Resch and D. V. Nelson

In the past 25 years ultrasonic techniques have only occasionally been used to monitor fatigue cracks. In this paper, the authors provide a case for more wide spread use of the surface acoustic wave (SAW) technique and give tips on how to effectively apply it. A detailed and thorough review is given of SAW techniques for use in detecting and measuring small fatigue cracks. Models are described for predicting a normalized crack depth from amplitude of the reflected signal, however, similar to electric potential techniques, relating this value to the actual crack depth and length dimensions requires either a knowledge of the crack surface length or assumptions about the crack aspect ratio. Fortunately, for many materials and specimen designs, such assumptions can be readily made and have been verified. Experimental details such as optimizing operating frequency and coupling wedge design are described. Cracks as small as 50 μm can be measured and, using special signal processing techniques (split spectrum processing), cracks as small 20 μm have been detected. The authors point out that a maximum measureable crack size limitation of 150 to 250 μm exists. This limit can, however, be altered by appropriate changes in transducer design and operating frequency. The use of the SAW method for measuring crack opening behavior of small cracks is also reviewed along with recent findings. The SAW technique is shown to be quite sensitive to crack opening and can detect both the initial opening of a crack and the point at which the crack is fully opened. These results are compared to those obtained using SEM (compliance) techniques, and the authors conclude that the SAW method gives information that complements compliance techniques and thus provides a more complete picture of closure. They show that crack-opening behavior as determined by both techniques is sensitive to surface residual stresses.

Simulation of Short Crack and Other Low Closure Loading Conditions Utilizing Constant-K_{max} ΔK-Decreasing Fatigue Crack Growth Procedures—R. W. Hertzberg, W. A. Herman, T. Clark, and R. Jaccard

As an alternative to small-crack testing, the authors present an argument for a large-crack approach that obviates many of the difficulties associated with small-crack testing. This approach employs conventional large-crack specimens tested under constant-K_{max}, ΔK-decreasing conditions. The key presumption of this approach is that the rapid growth of small cracks is the result of differences in crack closure for small versus large cracks. Thus, conventional large-crack data, which typically exhibit fully developed levels of crack closure, particularly in the near-ΔK_{th} regime, are assumed to be nonconservative relative to the data of small cracks which, due to their size, may not have fully developed crack closure. During a constant-K_{max} test, as ΔK decreases, K_{min} eventually exceeds the stress intensity factor for crack closure, resulting in closure-free crack growth rates. The resulting data are useful for

estimating maximum crack growth rates that may result under a variety of "low-closure" conditions. Potential applications include effects of high tensile residual stresses produced by welding and effects of compressive loads under negative R or variable amplitude fatigue. The paper provides guidelines for conducting constant-K_{max}, ΔK-decreasing tests, and data from a number of materials are presented to demonstrate the capabilities of this approach for estimating an upper bound for small-crack growth rates. This approach cannot be expected to address small-crack effects associated with factors other than crack closure, such as test conditions that violate the applicability of the linear elastic parameter ΔK or effects of microstructural variables.

References

[1] *Small Fatigue Cracks*, R. O. Ritchie and J. Lankford, Eds., The Metallurgical Society, Inc., Warrendale, PA, 1986.

[2] *The Behaviour of Short Fatigue Cracks*, EGF Publication 1, K. J. Miller and E. R. de los Rios, Eds., Mechanical Engineering Publications Ltd., London, 1986.

[3] *Short-Crack Growth Behaviour in Various Aircraft Materials*, AGARD Report 767, P. R. Edwards and J. C. Newman, Jr., Eds., NATO Advisory Group for Aerospace Research and Development, 1990.

James M. Larsen
Wright Laboratory, Materials Directorate,
Wright-Patterson Air Force Base, OH 45433;
symposium cochairman and coeditor.

John E. Allison
Ford Scientific Laboratory,
P.O. Box 2053
Dearborn, MI 48121;
symposium cochairman and coeditor.

J. C. Newman, Jr.[1]

Fracture Mechanics Parameters for Small Fatigue Cracks

REFERENCE: Newman, J. C., Jr., **"Fracture Mechanics Parameters for Small Fatigue Cracks,"** *Small-Crack Test Methods, ASTM STP 1149*, J. Larsen and J. E. Allison, Eds., American Society for Testing and Materials, Philadelphia, 1992, pp. 6–33.

ABSTRACT: The small-crack anomaly, where small cracks tend to grow either faster or slower than large cracks when compared on the basis of linear-elastic stress-intensity factors, has been shown to be significant for some materials and loading conditions. Conventional linear-elastic analyses of small cracks in homogeneous bodies are considered inadequate because of microstructural influences not accounted for in the stress-intensity factor and because of the nonlinear stress-strain behavior at notches and in the crack-front region. In this paper, plasticity effects and crack-closure transients are reviewed and investigated.

This paper presents a review of some common small-crack test specimens, the underlying causes of the small-crack effect, and the fracture-mechanics parameters that have been used to correlate or predict their growth behavior. Although microstructural features are important in the initiation and growth of small cracks, this review concentrates on continuum mechanics concepts and on the nonlinear behavior of small cracks. The paper reviews some stress-intensity factor solutions for small-crack test specimens and develops some simple elastic-plastic J integral and cyclic J integral expressions that include the influence of crack closure. These parameters were applied to small-crack growth data on two aluminum alloys, and a fatigue life prediction methodology is demonstrated. For these materials, the crack-closure transient from the plastic wake was found to be the major factor in causing the small-crack effect. Plasticity effects on small-crack growth rates were found to be small in the near threshold region, in that the elastic stress-intensity factor range and the equivalent value from the cyclic J integral gave nearly the same value.

KEY WORDS: cracks, elasticity, plasticity, stress-intensity factor, J integral, crack opening displacement, surface crack, crack closure, crack propagation, fatigue (material), microstructure

Linear-elastic fracture mechanics methods are widely accepted for damage-tolerance analyses [*1*]. There has also been a trend towards the use of the same methodology for fatigue durability analyses [*2*]. To obtain acceptably long lives without a significant weight penalty, these analyses must assume a small initial crack. However, since the mid-1970s, numerous investigators [*3–11*] have observed that the growth characteristics of small fatigue cracks in plates and at notches can differ considerably from those of large cracks in the same material. These studies have concentrated on the growth of small cracks ranging in length from 10 μm to 1 mm. On the basis of linear-elastic fracture mechanics (LEFM), small cracks generally grew much faster, but in some cases grew slower, than would be predicted from large crack data. This behavior is illustrated in Fig. 1, where crack-growth rate is plotted against the linear-elastic stress-intensity factor range ΔK. The solid (sigmoidal) curve shows typical large-crack results for a given material and environment under constant-amplitude loading. The solid curve is usually obtained from tests with cracks greater than about 2mm in length.

[1]Senior scientist, NASA Langley Research Center, Hampton, VA 23665.

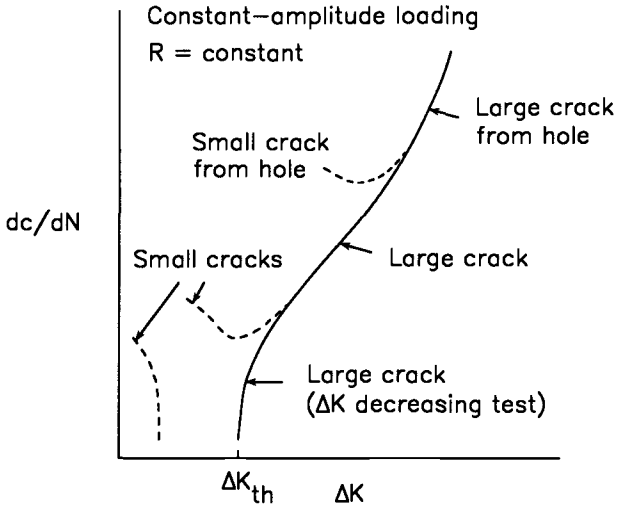

FIG. 1—*Typical fatigue-crack growth rate data for small and large cracks.*

At low growth rates, the large-crack threshold stress-intensity factor range ΔK_{th} is usually obtained from load-reduction (ΔK-decreasing) tests. Some typical experimental results for small cracks in plates and at notches are shown by the dashed curves. These results show that small cracks grow at ΔK levels below the large-crack threshold and that they also can grow faster than large cracks at the same ΔK level above threshold.

Many views have been expressed on the small-crack effect. In the mid-1980s, several books [*12–14*] reviewed the behavior of small fatigue cracks in tests and analyses. Based on LEFM, some materials and loading conditions show the existence of a strong small-crack effect, such as aluminum and titanium alloys under cyclic tension-compression loading [*15,16*], whereas other materials, such as high-strength steel [*17*], show good agreement between small and large crack behavior over a wide range in loading conditions. In all these studies, the applicability of LEFM concepts to small-crack growth behavior has been questioned. Some of the "classical" small or short crack experiments [*3–5*] were conducted at high stress levels, which may invalidate LEFM procedures because plastic-yield zones would be large compared to the crack size. Nonlinear or elastic-plastic fracture mechanics concepts, such as the *J*-integral [*5,8*] and crack closure [*9,18*], have also been used to explain the observed small-crack effects.

In addition, the metallurgical similitude [*7,19*] breaks down for small cracks (which means that the growth rate is no longer an average taken over many grains). Thus, the local growth behavior is controlled by metallurgical features [*11,20*]. If the material is markedly inhomogeneous and anisotropic (differences in modulus and yield stress in different crystallographic directions), the local grain orientation will influence the rate of crack growth, and crack-growth rate relations will differ in different directions. Crack front irregularities and small particles or inclusions affect the local stresses and, therefore, the crack growth response. In the case of large cracks (which have long crack fronts), all of these metallurgical effects are averaged over many grains, except in very coarse-grained materials. The influence of metallurgical features on stress-intensity factors, strain-energy densities, *J* integrals, and other crack-driving parameters are currently being explored (see Ref *21*).

As the crack size approaches zero, a crack size must exist below which continuum mechanics assumptions are violated, but the transition from valid to invalid conditions does

not occur abruptly. For many applications, a continuum mechanics approach that extends into the "gray area" of validity may still prove to be very useful. Certainly from a structural designer's viewpoint, a continuum mechanics approach that is applicable to all crack sizes is very desirable.

This paper presents a review of some of the small-crack test specimens, the underlying causes of the small-crack effect, and the fracture-mechanics parameters that have been used to correlate or predict the growth behavior of small cracks. Although microstructural features are important in the initiation and growth of small cracks, this review concentrates on continuum mechanics concepts and on the nonlinear behavior of small cracks. The paper reviews the stress-intensity factor solutions for some of the most commonly used small-crack test specimens and the nonlinear crack-tip parameters. The paper also develops some simple elastic-plastic J integral and cyclic J integral expressions that include the influence of crack closure. These parameters are applied to small-crack growth data on two aluminum alloys. A fatigue life prediction methodology is demonstrated on notched aluminum specimens using small-crack data and microstructural information on crack initiation sites.

Small-Crack Test Specimens

Since the mid-1970s, several small or short crack test specimens have been developed to obtain fatigue crack growth rate data. Some of the early specimens were prepared by growing large cracks and machining away the material to obtain a physically small through crack [*5*]. However, the most widely used specimen contained a surface crack that initiated from either a small hole, an electrical-discharged machined notch, or from natural initiation sites, such as inclusion particles, voids or scratches (see for example, papers in Refs *12* through *14*). The surface crack specimens were subjected to either remote tension or bendings loads, see Fig. 2*a*. In the surface crack specimen, the crack length ($2c$) on the surface was monitored by either visual, photographic or plastic-replica [*22*] techniques. Crack depths a were determined by either experimental calibration (breaking specimens to record depths), heat-tinting, or compliance methods [*23*].

Recently, two AGARD studies [*15*,*24*] introduced two small-crack specimens. The corner-crack specimen (Fig. 2*b*), was developed to simulate three-dimensional stress fields such as those encountered in critical locations in engine discs [*25*]. In Ref *24*, the small corner crack was introduced into the specimen by electrical-discharge machining a 200 to 250 μm deep notch into one edge. The crack size was monitored by using an electrical potential method. This specimen has the advantage that both crack length c and crack depth a can be monitored by either visual or photographic means. The surface and corner crack at a semi-circular edge notch specimen [*26*], referred to as the single-edge-notch-tension (SENT) specimen, was developed to produce naturally occurring cracks at material defects and to propagate cracks through a three-dimensional stress field similar to that encountered at bolt holes in aircraft structures. Crack sizes, as small as 10 to 20 μm in length along the bore of the notch, were monitored by the plastic-replica method, and crack shapes were determined by experimental calibration. Note that the crack depth (a or $2a$) is always measured in the plate or sheet thickness B direction, and crack length (c or $2c$) is measured in the width (w or $2w$) direction. For a surface crack at a notch, thickness is denoted as $2t$ because of convenience in expressing stress-intensity factors as a function of a/t ratios, that is, a/t varies from 0 to 1. For a surface crack, corner crack and corner crack at a notch configuration, thickness is denoted as t. This nonmenclature was selected so that all surface and corner cracks will become a through crack of length c when a/t approaches unity.

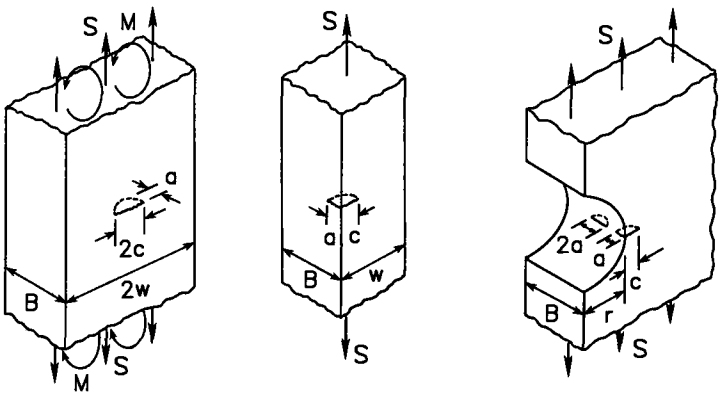

(a) Surface crack (b) Corner crack (c) Surface or corner crack at notch

FIG. 2—*Commonly used small crack test specimens.*

Stress-Intensity Factors

The stress-intensity factor solutions for the small crack specimens shown in Fig. 2 can be expressed as

$$K = S_i\sqrt{\pi a/Q}\, F_j \tag{1}$$

where S_i is the remote uniform tensile stress ($i = t$) or outer fiber bending stress ($i = b$), Q is the elliptical crack shape factor, and F_j is the boundary-correction factor that accounts for the influence of various free-boundary conditions (see Appendix A). The subscript j is used to denote different crack configurations.

The most widely used stress-intensity factor solution and equation for a surface crack in a plate is that of Raju and Newman [*27,28*], which was developed from three-dimensional (3D) finite-element analyses. Pickard [*25,29*] developed a stress-intensity factor solution and equation for the corner-crack specimen, again, using 3D finite-element analyses. Both the surface- and corner-crack equations have been used to analyze crack-growth rate data for a wide variety of materials. The original stress-intensity factor solution for the SENT specimen [*26*] was estimated from the results for surface and corner cracks at open holes [*28*], and a two-dimensional (2D) analysis of a through crack at an edge notch [*30*]. Recently, the stress-intensity factor equation for a surface crack in the SENT specimen was found to be 5 to 10% low in the region where the crack front intersects the notch boundary [*31*] for notch-radii-to-thickness (a/t) ratios ranging from 1 to 3, respectively. Tan et al. [*31*], and Shivakumar and Newman [*32*], using 3D finite-element methods (FEM) with improved finite-element models, and Zhao and Wu [*33,34*], using a 3D weight-function method (WFM), analyzed the SENT specimen for a wide range in crack shapes and crack sizes. Some typical comparisons between the stress-intensity factors from these two methods are shown in Figs. 3 and 4 for a semi-circular surface crack located at the center of the notch root and a quarter-circular corner crack, respectively. These figures show the boundary-correction factors (F_{sn}, F_{cn}) plotted against the parametric angle ϕ for various crack-depth-to-thickness ratios a/t for a particular r/t ratio. The parametric angle ϕ is measured along the crack front with

$\phi = \pi/2$ at the location where the crack front intersects the notch root. The WFM gave results that were generally within ±3% of the FEM results. In the WFM, only the two-dimensional stress distribution [*30*] was used in the analysis. Some of the differences between the WFM and FEM can be traced to the three-dimensional stress distribution through the thickness, which is accounted for in the FEM method (for $r/B = 1.5$ the stress concentration is about 2% higher in the interior and about 3% lower at the edge of the notch than the 2D solution, see Ref *35*). Thus, the results from the WFM should be slightly low for small surface cracks in the interior and slightly high for small corner cracks. The curves show the results from an equation that was fit to these results. These equations are given in Appendix A and they will be used later to compare small and large crack growth data on two aluminum alloys.

Elastic-Plastic Analyses

Elastic-plastic analyses of small cracks have been the subject of many articles. Dowling [*6*], El Haddad et al. [*5*], Hudak [*8*], Hudak and Chan [*36*], and Chan [*37*] have made ΔJ estimates for small cracks. The early estimates were based on the work of Dowling [*6*] where J was approximated by adding the elastic and fully plastic solutions. For a small surface crack, the J expression [*5,6*] was

$$J = J_e + J_p = 2\pi F^2 a[W_e + f(n)W_p] \tag{2}$$

where W_e and W_p are the elastic and plastic components of the remote strain energy density, respectively, F is the elastic boundary-correction factor, and $f(n)$ is a function of the strain-hardening coefficient n. The elastic strain energy density was given by $S/(2E)$ where S is the remote stress, and E is Young's modulus. The plastic strain energy was given by $S\varepsilon_p/(n+1)$ where ε_p is the plastic strain, and n is the strain-hardening coefficient based on the Ramberg-Osgood stress-strain relation. For cyclic loading, the stress and strain values in Eq 2 were

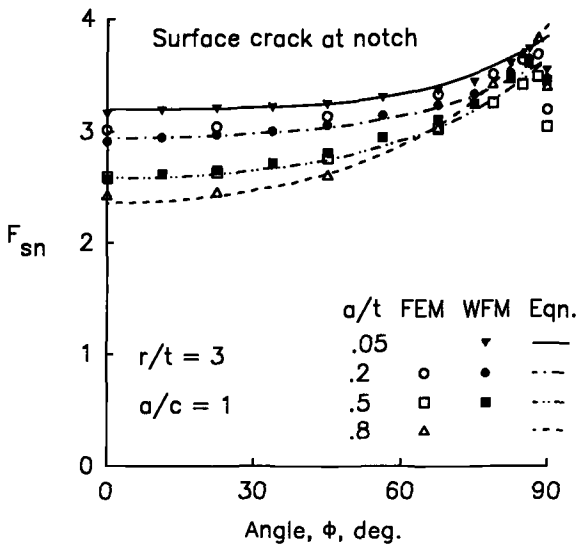

FIG. 3—*Comparison of stress-intensity factors from finite-element and weight-function for surface crack at an edge notch.*

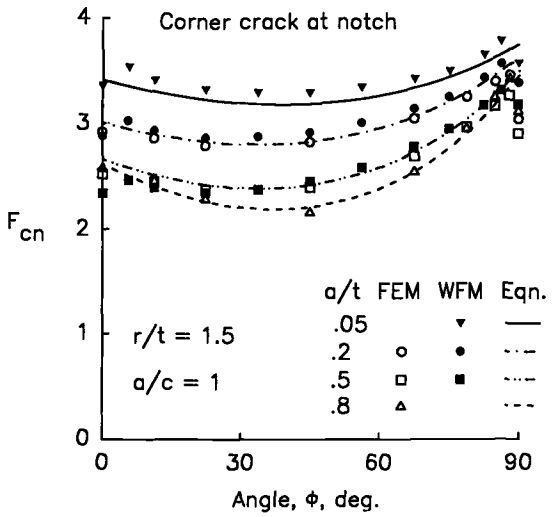

FIG. 4—*Comparison of stress-intensity factors from finite-element and weight-function methods for corner crack at an edge notch.*

replaced by their cyclic values, ΔS and $\Delta\varepsilon_p$, to give an estimate for ΔJ. Dowling noted that ΔJ should be computed using only that portion of the load cycle during which the crack is fully open, that is, ΔJ_{eff}. The cyclic plastic strain $\Delta\varepsilon_p$ was obtained from a remotely measured cyclic stress-strain curve. However, to correlate small crack data with large crack data on A533B steel, El Haddad et al. [*5*] needed to add a length parameter ℓ_o to the crack length a. This length parameter was assumed to be constant for a given material and was related to the threshold stress-intensity factor ΔK_{th} and the fatigue limit.

In combination with Eq 2, small and large crack data correlated with each other when plotted against ΔJ, even down to the large crack threshold. The correlation of the small and large crack data, with the use of the length parameter and ΔJ, may have been fortuitous because many experiments (see Ref *38*) and analyses [*18*] have shown that a rise in the crack-closure level may be partly responsible for threshold development. Conversely, experiments [*39*] and analyses [*18*] have also shown that a lack of closure in the early stages of small crack growth may be partly responsible for the rapid growth of small cracks. Therefore, crack-closure effects may be one of the key elements in small crack growth behavior. Crack-closure effects on crack-tip parameters and on small crack growth behavior will be discussed later.

Dugdale Model

Many researchers have used the Dugdale model [*40*] to estimate ΔJ (see, for example, Ref *37*). But before these results are discussed, some background information on the Dugdale model will be reviewed. Drucker and Rice [*41*] presented some very interesting observations concerning the model. In a detailed study of the stress field in the elastic region of the model under small-scale yielding conditions, they reported that the model violates neither the Tresca nor von Mises yield criteria. They also found that for two-dimensional plane-stress perfect plasticity theory, the model satisfies the plastic flow rules for a Tresca material. Thus, the Dugdale model represents an exact two-dimensional plane-stress solution for a Tresca material even up to the plastic-collapse load. Therefore, the J-integral calculations

[*42*] and ΔJ estimates may be reasonable and accurate under certain conditions. Of course, the application of the Dugdale model to strain-hardening materials and to plane-strain conditions, as was done in Ref *18*, may raise serious questions because plane-strain yielding behavior is vastly different than that depicted by the strip-yield model. The influence of strain-hardening and 3D constraint of crack-tip yielding using a modified Dugdale model will be discussed later.

Rice [*42*] evaluated the J integral from the Dugdale model and found that

$$J = \sigma_0\delta = 8\sigma_0^2 c/(\pi E)\ \ell n[\sec(\pi S/2\sigma_0)] \tag{3}$$

where σ_0 is the flow stress, and δ is the crack-tip-opening displacement. To develop a J-integral expression for small cracks, it is convenient to define an equivalent plastic stress-intensity factor K_J as

$$K_J^2 = JE/(1 - \eta^2) \tag{4}$$

where $\eta = 0$ for plane stress, and $\eta = \upsilon$ (Poisson's ratio) for plane strain. Dugdale model solutions for plastic-zone size ρ and crack-tip opening displacement δ are available for a large number of crack configurations (see Ref *43*). Thus, J and K_J can be calculated for these configurations. However, for complex crack configurations, such as a through crack or surface crack at a hole, closed-form solutions are more difficult to obtain. A simple method is needed to estimate J for complex crack configurations. A common practice in elastic-plastic fracture mechanics has been to add a portion of the plastic zone ρ to the crack length, like Irwin's plastic-zone correction [*44*], to approximate the influence of crack-tip yielding on the crack-driving parameter. Herein, this same concept will be applied to obtain some estimates for J and ΔJ using some exact and approximate solutions. Defining a plastic-zone corrected stress-intensity factor as

$$K_p = S\sqrt{\pi d}\ F_j(d/w,\ d/r,\ \ldots) \tag{5}$$

where $d = c + \gamma\rho$, and F_j is the boundary-correction factor. In general, the boundary-correction factor may be a function of any number of variables. F_j is evaluated at an effective crack length d. The term γ was assumed to be a constant, and it was evaluated by equating K_p to K_J for several crack configurations. The crack configurations that were considered in the evaluation are shown in Fig. 5. The particular crack configurations were (1) a crack in an infinite plate ($r = 0$), (2) cracks emanating from a circular hole, and (3) an embedded circular crack in an infinite solid. These configurations were chosen because exact solutions are available for a crack and an embedded circular crack in an infinite solid [*43*]. The yielding behavior of a surface or corner crack should lie between these two configurations. Equations for ρ and δ for Cases 1 and 3 are given in Ref *43*. A crack emanating from a hole configuration was chosen because it represents an important configuration for structures and for studying small crack behavior. The equations for ρ and δ for this configuration are given in Ref *18*. Trial-and-error calculations were used to obtain a value for γ. From this evaluation, a value of ¼ was found to give good agreement between K_p and K_J up to large values of applied stress to flow stress ratios. To put the value of one-quarter in perspective, Irwin's plastic-zone corrected stress-intensity factor [*44*] is given by γ equal to about 0.4 and Barenblatt's cohesive modulus [*45*] is given by $\gamma = 1$. The author had used $\gamma = 1$ in Ref *18*.

In this section, comparisons between K_e (elastic stress-intensity factor), K_p, and K_J for

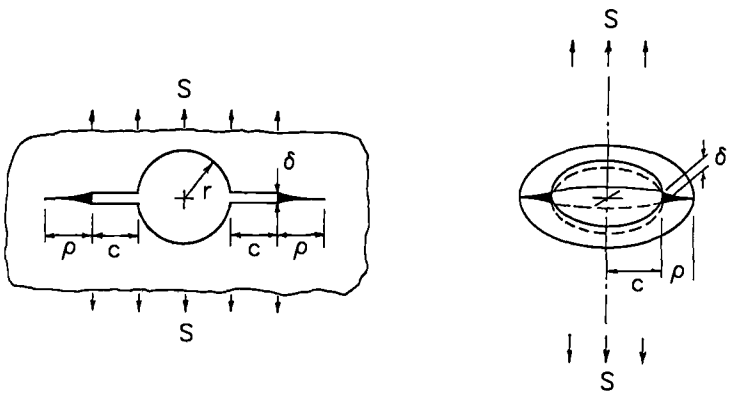

(a) Through crack at hole (b) Embedded circular crack

FIG. 5—*Dugdale model configurations evaluated for J integrals and plasticity-corrected stress-intensity factors.*

the three crack configurations are made. The comparison of K_e/K_J and K_p/K_J plotted against S/σ_o for a through crack and an embedded circular crack in an infinite solid, and for symmetrical through cracks emanating from a circular hole, are shown in Figs. 6 and 7, respectively. The solid curves show K_p/K_J for $\gamma = 0.25$, and the dashed curves show K_e/K_J. The results from the K_p equation for a through crack (Fig. 6) are within about 3% of K_J up to an applied stress level of about 80% of the flow stress of the material. But the equation for an embedded crack can be applied up to 95% of the flow stress. Note that the elastic solutions show about 20% difference at these high stress levels. The behavior of a surface crack in a plate or at a notch would be expected to lie between the behavior of these two crack configurations. Similarly, the results from the K_p equation for through cracks at a hole (Fig. 7) are also within about 5% of K_J for applied stress levels up to 80% of the flow stress. The elastic solutions for small cracks (low c/r ratios) differ by a factor of two from K_J at these high stress levels. (For typical aircraft fastener hole radii and sheet thicknesses, a c/r value of 0.05 gives a crack size of about 100 to 300 μm.)

The K_e/K_J and K_p/K_J results for through cracks at a hole are plotted in Fig. 8 as a function of ρ/c. These results show that the K_p is nearly equivalent to K_J for plastic-zone sizes an order-of-magnitude larger than the crack size. For small cracks (small c/r ratios), the results show that the K_p equation is within 5% of K_J for plastic-zone sizes nearly 50 times larger than the crack size. These conditions are ideal for studying the influence of yielding on small crack growth rate behavior. An important point concerning Eq 5 is that no physical meaning is attached to K_p, but only that it gives an accurate expression for $\sqrt{J}$. Furthermore, throughout this analysis the material is assumed to be elastic-perfectly-plastic. Strain-hardening effects are approximated only by averaging the yield and ultimate tensile strength of the material to estimate a flow stress. Strain-hardening modifications to the Dugdale model are beyond the scope of this paper.

To convert K_p to ΔK_p in Eqs 3 to 5, the applied stress and flow stress are replaced by ΔS and $2\sigma_o$, respectively, and ρ is replaced by the cyclic plastic zone ω (see Ref *36*). Thus, Figs. 6 and 7 would be identical if K_i/K_J is replaced by $\Delta K_i/\Delta K_J$ and S/σ_o is replaced by $\Delta S/(2\sigma_o)$, again, with $\gamma = 0.25$. Thus, ΔK_p is evaluated at a crack length plus one-quarter of the cyclic plastic zone. The influence of crack closure on these calculations will be discussed later.

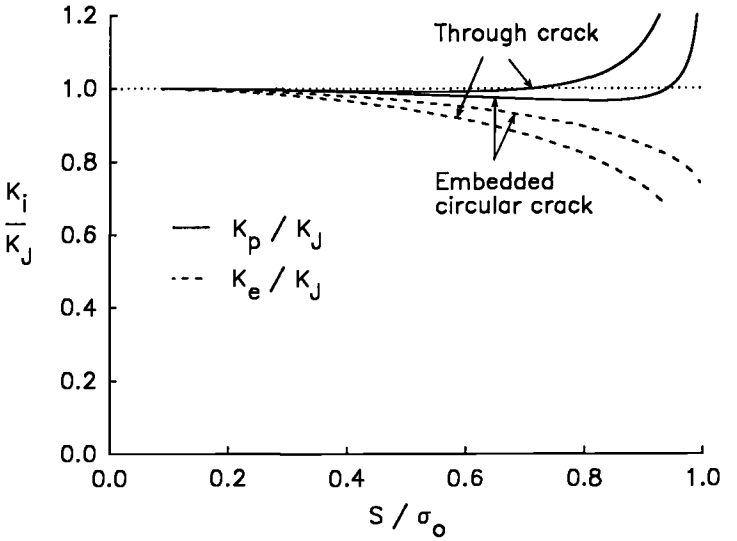

FIG. 6—*Ratio of elastic and elastic-plastic* K *values to* K *from exact* J *integral for through crack and embedded circular crack in an infinite body against normalized applied stress.*

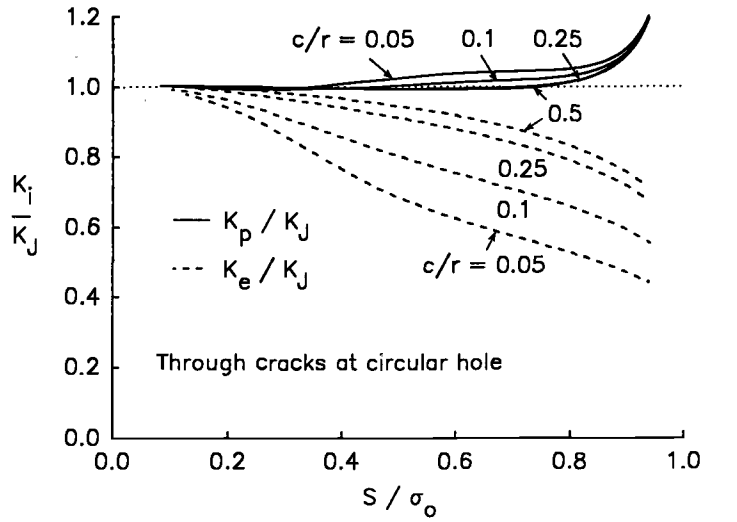

FIG. 7—*Ratio of elastic and elastic-plastic* K *values from* J *integral for through cracks at a circular hole in an infinite body against normalized applied stress.*

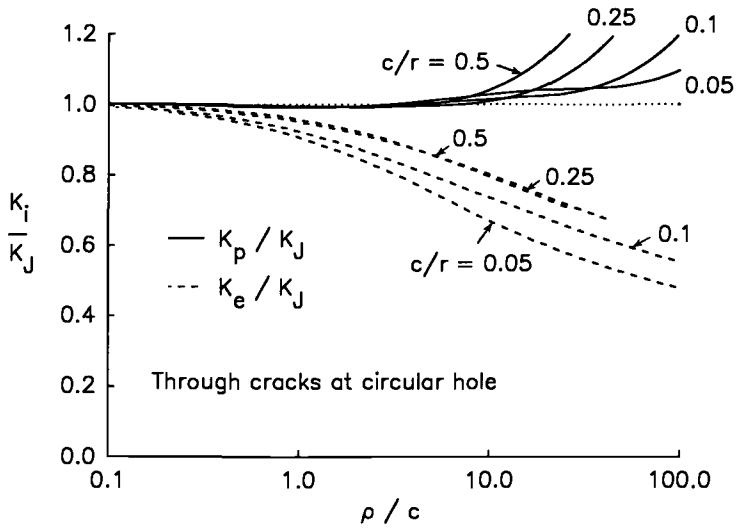

FIG. 8—*Ratio of elastic and elastic-plastic* K *values to* K *from* J *integral for through cracks at a circular hole in an infinite body against normalized plastic-zone size.*

Small-Crack Test Data

At this point it may be useful to review some of the conditions under which small-crack data were generated in some of the earlier references. El Haddad et al. [5] tested middle-crack tension specimens made of G40.11 steel under $R = -1$ loading at a $\Delta S/(2\sigma_o)$ of 0.47. For this specimen and loading, the difference between ΔK_e and ΔK_p is only about 5% (Fig. 6). For cracks at a hole, the minimum c/r ratio was 0.06 and $\Delta S/(2\sigma_o)$ was 0.26. The difference between elastic and elastic-plastic values was less than 10%.

Taylor and Knott [*11*] tested surface cracks in a cast nickel-aluminum-bronze material under bending loads. The maximum applied stress range to twice the flow stress, $\Delta S/(2\sigma_o)$, at $R = 0.1$, was 0.27. From Fig. 6, the plasticity effects are again quite small. However, the material in question here exhibited a large strain-hardening effect (the maximum applied stress exceeded the yield stress of the material in the outer fiber). Thus, the evaluation may not be appropriate because accurate strain-hardening effects were not considered.

In the AGARD Cooperative Test Program [*15*], surface cracks at an edge notch were monitored under a wide range in loading conditions. The maximum value of $\Delta S/(2\sigma_o)$ was 0.27 under $R = -2$ loading. Assuming that the surface cracks can be treated as a through crack at a hole, the ΔK_e value was within 10% of ΔK_p.

Ravichandran and Larsen [*23*] tested surface cracks in titanium alloy (Ti-24Al-11Nb) plates under tension. Again, the maximum value of $\Delta S/(2\sigma_o)$ was about 0.27, and there were, again, small differences between elastic and elastic-plastic values. With the exception of the Taylor and Knott results, the nonlinear effects on some of the "classical" and recent small-crack data appear to be small, if ΔK_p (or ΔJ from the Dugdale model) is the appropriate crack-driving parameter for small cracks.

Cyclic Plasticity and Closure Effects

As previously mentioned, fatigue crack-closure effects on the crack-drive parameters must be addressed. A review of some of the applications of plasticity-induced closure on small crack growth behavior will be covered in the next sections.

Numerous investigators [*5–11,18*] have suggested that fatigue crack closure [*46*] may be a major factor in causing some of the differences between the growth of small and large cracks. Reference *47* has shown, on the basis of crack closure, that a large part of the small-crack effect in an aluminum alloy was caused by a small crack emanating from a defect "void" of incoherent inclusion particles and a breakdown of LEFM concepts.

A crack-closure model was developed in Ref *48* and applied to small cracks in Refs *18* and *47*. The results from the model are reviewed herein to illustrate how crack-closure transients lead to the unusual behavior of small cracks. For completeness, a brief description of the model and of the assumptions made in the application of the model to the growth of small and large cracks are given in Appendix B.

Reference *47* showed how an initial defect "void" influenced the crack-closure transient as a small crack grew from the void under constant-amplitude loading. Some typical results of calculated crack-opening stresses normalized by the maximum applied stress as a function of half-crack length a are shown in Fig. 9. The crack-growth stimulation was performed under $R = -1$ loading ($S_{max}/\sigma_o = 0.15$) with an initial defect (void or crack) size a_i of 3 μm, c_i of 12 μm, and for various values of h, void half-height (see insert on Fig. 9). This defect void size is typical of those that occur at inclusion particle sites in 2024-T3 and 7075-T6 aluminum alloys [*15,16*]. Results shown in the figure demonstrate that the defect height ($2h$) had a large influence on the closure behavior of small cracks. For h greater than about 0.4 μm, the initial defect surfaces did not close, even under compressive loading. The newly created crack surfaces, however, did close and the crack-opening stresses are shown by the lower solid curve. The crack-opening stress was initially at the minimum applied stress, but rapidly rose and tended to level off as the crack grew. For $h = 0$, however, the defect surfaces made contact under the compressive loading, and the contacting surfaces greatly influenced the amount of residual plastic deformation left behind as the crack grew. The calculated crack-opening stresses stabilized very quickly at the steady-state value, as shown by the upper solid curve. These results suggest that part of the small crack effect may be due to an initial defect height that is sufficient to prevent closure over the initial defect surfaces.

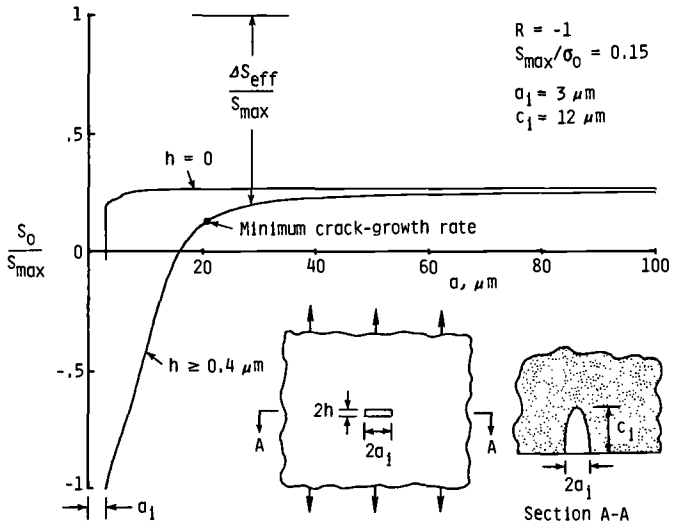

FIG. 9—*Influence of defect "void" height on calculated crack-opening stresses for small cracks.*

Initially, the low crack-opening stresses give rise to high effective stress ranges and, consequently, high growth rates. However, as the crack grows the crack-opening stresses rise much more rapidly than the stress-intensity factor causing a reduction in the effective stress-intensity factor range. This behavior causes a "minimum" in crack-growth rate to occur at a half-crack length of about 20 μm for $h \geq 0.4$ μm (solid symbol in Fig. 9). This minimum in crack-growth rate behavior for small cracks is illustrated in Fig. 1. Several researchers [*12–14,20*] have observed multiple minima and attributed this behavior to crack-grain boundary interaction. The minimum in the analysis, however, was caused by a decrease in the effective stress range (ΔS_{eff}) with an increase in crack length, such that the ΔK_{eff} reaches a minimum. Thus, a minimum in growth rates for small cracks may be caused by at least two different phenomena. One is the crack-grain boundary interaction, and the other is a transient behavior of crack-opening stresses.

The calculated crack-opening stresses for small cracks under four constant-amplitude loading conditions are shown in Fig. 10. The values of S_{max}/σ_o used are as shown. The initial defect size (a_i, c_i) was the same as shown previously and the defect height was 0.4 μm. The high stress ratio ($R = 0.5$) results show that the crack is always fully open, that is, $S_o = S_{min}$. Results at $R = 0$ stabilized very quickly after about 20 μm of crack growth. Negative stress ratio results showed the largest transient behavior on crack-opening stresses. Results at $R = -2$ had not stabilized after about 100 μm of crack growth. The results at the negative stress ratios are also strongly influenced by the maximum applied stress level [*47,48*].

Crack Growth Rate Relations

Elber [*46*] proposed to modify the crack-growth relation of Paris et al. [*49*] to account for the influence of crack closure. He attributed crack-closure effects to residual plastic deformations that were left along the crack surfaces as the crack grew. The crack-growth relation was

$$dc/dN = C\Delta K_{eff}^m = C[(1 - S_o/S_{max})/(1 - R)]^m \Delta K^m \quad (6)$$

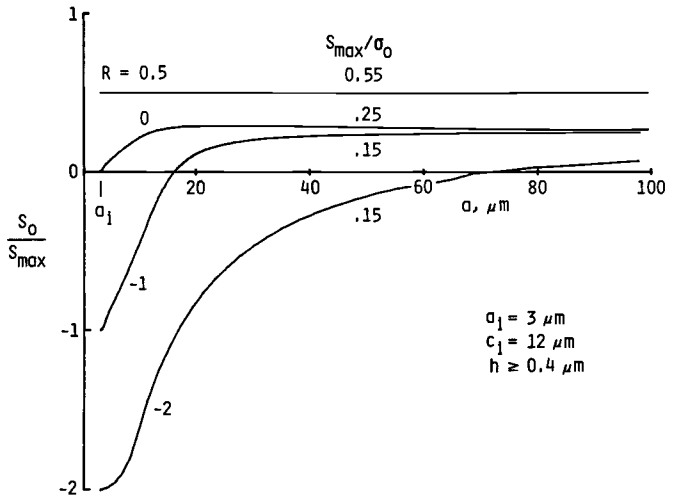

FIG. 10—*Calculated crack-opening stresses for various constant-amplitude loading for small cracks.*

The material constants C, m, and S_o (crack-opening stress) were determined from tests. The effective stress-intensity factor relation has been successfully used to correlate and predict large-crack growth rate behavior under a wide variety of loading conditions. Equation 6 is a good first-order approximation to account for plasticity-induced closure effects but does not include the effects of plastic-dissipation energy. Other investigators (see Refs *36* and *37*) have proposed that the crack-tip-opening displacement or ΔJ may be more appropriate parameters for correlating crack-growth rate data for small cracks. However, the influence of crack closure on these parameters should also be addressed.

The analytical crack-closure model provides a method to study the local crack-tip deformations for small cracks under cyclic loading [*18*]. Figure 11 shows calculations from the model for a small crack. This figure shows the applied stress plotted against the crack-tip displacement of the first intact element in the plastic zone (see Appendix B). (Note that the crack was not allowed to grow during the loading portion of the cycle.) During loading, the crack-tip displacement δ does not change until the element yields in tension (model had rigid plastic elements). The solid symbol shows the stress level at which the crack-tip region became fully open (crack-opening stress, S_o). The effective stress range ΔS_{eff} is used in Eq 6 to compute the rate of growth. During unloading, some intact elements in the crack-tip region yield in compression before any broken elements contact. Further unloading causes part of the crack surfaces to come into contact. Contacting surfaces are also allowed to yield in compression.

A natural output from the model is the effective cyclic crack-tip displacement $\Delta\delta_{eff}$ and the effective cyclic plastic strain energy W^p_{eff}. Thus, one may propose to use these parameters because they automatically account for both plasticity and closure effects. Crack-growth rate relations could be developed as

$$dc/dN = g(\Delta\delta_{eff}) \tag{7}$$

or

$$dc/dN = h(W^p_{eff}) \tag{8}$$

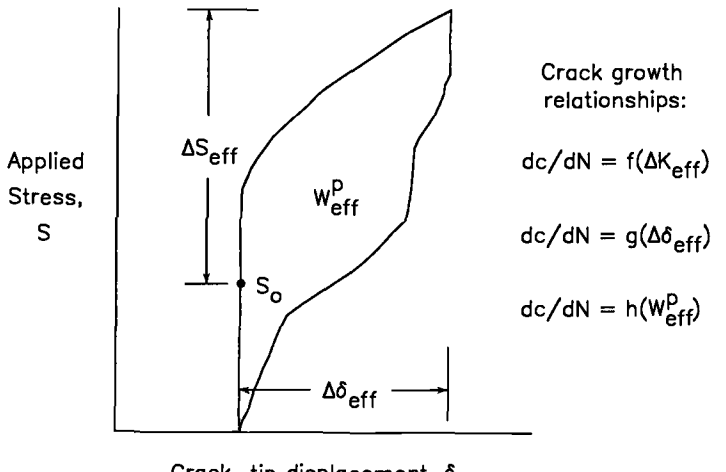

FIG. 11—*Calculated cyclic crack-tip displacement history for small crack.*

Of course, using the $J - \delta$ analogy, both Eqs 7 and 8 could also be expressed in terms of ΔJ_{eff}. Although the cyclic crack-tip displacement or plastic strain energy may be more fundamental crack-tip parameters, their use would be restricted because these parameters are not readily available for complex crack configurations. However, further study is warranted to investigate the usefulness of these parameters.

Returning our attention to the plasticity-corrected stress-intensity factor, a crack-growth relation could also be expressed as

$$dc/dN = C(\Delta K_p)^n_{eff} \tag{9}$$

where $(\Delta K_p)_{eff}$ is the effective ΔK_p. This parameter is a combination of Elber's approach and the cyclic version of Eq 5 by replacing S by ΔS_{eff}. This parameter may be an approximation of $\sqrt{\Delta J_{eff}}$ and is given by

$$(\Delta K_p)_{eff} = \Delta S_{eff}\sqrt{\pi d}\, F_j(d/w, d/r, \ldots) \tag{10}$$

where $d = c + \omega/4$, and ω is the closure-corrected cyclic plastic zone. The cyclic plastic-zone size is greatly influenced by closure because contact forces tend to support the crack surfaces and reduce the amount of reverse yielding. An estimate for the closure-corrected cyclic plastic zone is

$$\omega = (1 - S_o/S_{max})^2\rho/4 \tag{11}$$

where ρ is calculated using the maximum applied stress and $\alpha\sigma_o$. The term α is a constraint factor used to approximate the elevation of flow stresses in the crack-front region caused by state-of-stress variations (see Appendix B). As an example, consider the behavior of a small crack under $R = 0$ conditions. Initially, when the small crack is fully open, $S_o/S_{max} = 0$ and $\omega = \rho/4$, the exact value from the cyclic strip-yield model [*50*]. However, as the small crack grows and builds a plastic wake, the stabilized crack-closure conditions gives S_o/S_{max} of about 0.5 under plane-stress conditions ($\alpha = 1$) and $\omega = \rho/16$. Thus, the cyclic plastic zone for a large crack is greatly reduced from the nonclosure value.

Small Surface-Crack Growth Shapes

One of the most difficult tasks in monitoring the growth of small surface cracks is determining the crack shape. Many of the early reports on small-crack growth used the experimental calibration method where specimens were broken at various stages, and microscopic examinations of the fatigue surfaces revealed the crack shape. Many of these investigators

found that the small cracks tended to stay nearly semi-circular (a/c = 0.9 to 1.1). For surface cracks in some of the commercial alloys, the preferred propagation pattern is nearly semi-circular [*51*]. But for highly anisotopic or textured materials, the propagation patterns are not semi-circular [*23*].

In the following sections, comparisons are made between experimental and predicted crack shape changes for small surface cracks at an edge notch for two aluminum alloys. Figures 12 and 13 show the results for the 2024-T3 [*15,26*] and 7075-T6 aluminum alloys, respectively. These figures show crack-depth-to-crack-length (a/c) ratios plotted against the crack-depth-to-sheet-half-thickness (a/t) ratios. The solid symbols show the sizes and shapes of the inclusion-particle clusters or voids that initiated the small cracks.

For both materials, the experimental calibration method was used to determine the crack depth and crack length (open symbols). In the analysis of the 2024-T3 material, three different initial crack shapes and sizes were used. In one case, the initial crack was an average of the inclusion particle sizes, whereas the other two crack sizes and shapes were arbitrarily selected. The curves show the calculations using the stress-intensity factor equations (Appendix A) and a ΔK_{eff}-rate (dc/dN) relation established from large crack data [*47*]. (Note that the plasticity corrections on the large crack data were insignificant (much less than 1%), such that $(\Delta K_p)_{eff}$ was equal to ΔK_{eff}). Because crack-closure differences are expected to occur along the surface-crack front [*52*], the stress-intensity factor range at the location where the crack front intersects a free surface has been multiplied by a factor β_R [*51*] to account for local closure differences (β_R ranges from 0.9 to 1 for R = 0 to 1; β_R = 0.9 for negative stress ratios). For the 2024-T3 material, the crack-growth rate relation for da/dN was assumed to be the same as dc/dN. Although a large amount of scatter was evident, all curves tended to predict the trend in the experimental data reasonably well for a/t greater than 0.05. No information on the crack shape development between the particle sizes and a/t less than 0.05 was available.

These analyses show that small cracks tend to approach very rapidly a preferred crack shape of about an a/c = 1.1 for a large part of their growth through the thickness. For deep cracks (large a/t), the cracks begin to grow more rapidly along the bore of the notch than in the length direction causing a/c to increase rapidly.

In the analysis of the 7075-T6 material (Fig. 13), two different crack-growth rate relations were used for da/dN. One relation assumed that da/dN was the same as dc/dN as a function of ΔK_{eff}. For this material, however, the crack-growth rate relation for da/dN was found experimentally to be different than dc/dN in the mid-range on rates. These two rate relations were used in the crack shape predictions shown by the solid curve. In both analyses, the initial crack was an average of the inclusion particle sizes. Although a large amount of scatter was, again, evident, the solid curve predicted nearly the same trend as the experimental data for a/t greater than 0.1. The analyses, again, show that small cracks tend to approach an a/c ratio of about 1.1 for a large part of its growth through the thickness. Deep cracks in the 7075-T6 showed a much different behavior than those in the 2024-T3 material, because of the differences in crack-growth rate relations in the a- and c-direction.

Comparison of Experimental and Calculated Small Crack Growth Rates

At this point all of the elements are in place to assess the influence of the various fracture-mechanics parameters on the growth of small cracks from continuum-mechanics principles. The small-crack data generated in the AGARD Cooperative Test Program [*15*] on 2024-T3 aluminum alloy will be analyzed using the plasticity and closure analyses previously presented. The results from these analyses will be presented in terms of ΔK plotted against crack-growth rate.

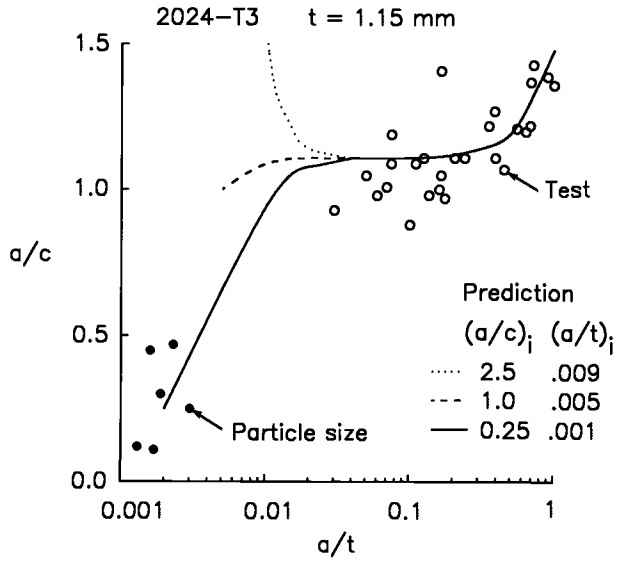

FIG. 12—*Comparison of experimental and predicted surface-crack shapes for single-edge-notched 2024-T3 aluminum alloy sheet.*

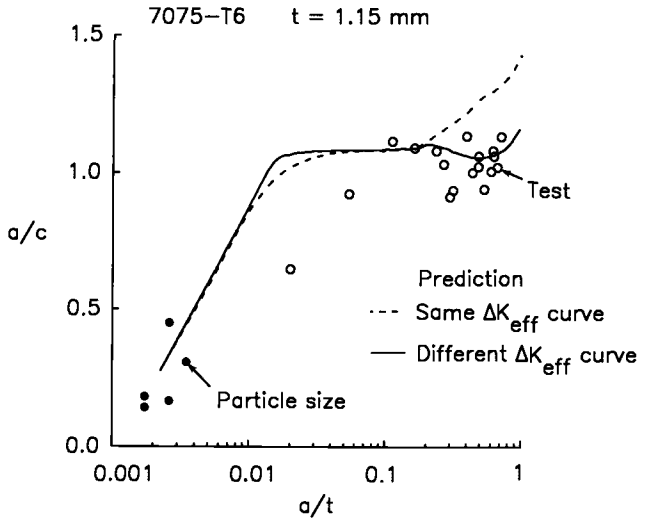

FIG. 13—*Comparison of experimental and predicted surface-crack shapes for single-edge-notched 7075-T6 aluminum alloy sheet.*

The influence of plasticity effects and closure transients on the predicted growth of small surface cracks at an edge notch for a wide range of stress levels under $R = -1$ conditions are shown in Fig. 14. The dashed curve shows the ΔK-rate data generated on large cracks, and the dotted curve is the effective stress-intensity factor curve. The effective curve was based on elastic stress-intensity factors and crack-closure effects under $\alpha = 1.73$ constraint conditions for rates less than 10^{-4} mm/cycle, $\alpha = 1.1$ for rates greater than 10^{-3} mm/cycle, and a linear α-relationship on log rate between these two α values and rates (see Ref *47*). A brief discussion on the constraint factor α is given in Appendix B.

Note that the large-crack threshold data for rates lower than about 10^{-6} mm/cycle has been ignored in estimating the effective curve. The effective threshold was established by fitting to fatigue-limit data under $R = -1$ loading and using the average defect particle size and shape ($a_i = 3$ μm, $c_i = 12$ μm, and $h \geq 0.4$ μm). As previously mentioned, the plasticity effects on the ΔK_{eff} curve were extremely small, therefore, $(\Delta K_p)_{eff}$ was assumed to be equal to ΔK_{eff}. Because small cracks were assumed to have no plastic wake on the first cycle, the elastic analyses (dash-dot curves) start on the ΔK_{eff} curve and approach the large crack curve as the plastic wake develops. The low stress level (S_{max}/σ_o) results show a minimum in rates after some amount of crack growth and plastic-wake development. At low stress levels there is a small difference between the elastic and elastic-plastic results. But at high stress levels, a strong plasticity effect is evident, as shown by the solid curves. For a given ΔK, the rates are higher than the effective curve because the crack is fully open and the plasticity correction gives a higher $(\Delta K_p)_{eff}$. Recall that the "classical" and recent small-crack data from the literature for cracks emanating from holes were generated under S_{max}/σ_o levels less than 0.3. Thus, the results shown in Fig. 14 suggest that the closure transient is one of the major small-crack effects and that the plasticity correction may be small.

Comparisons between experimental and predicted small-crack growth rates for 2024-T3 aluminum alloy SENT specimens are shown in Figs. 15 through 17 for various stress ratios. Each figure shows results for only one stress level. The experimental data (crack length

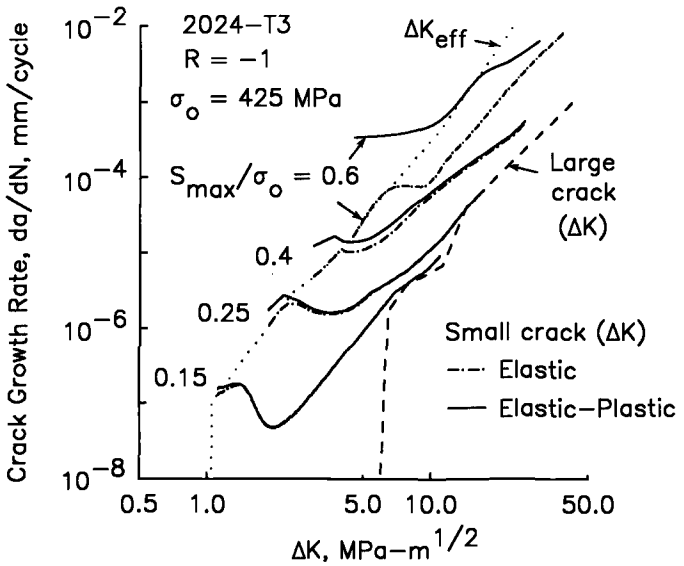

FIG. 14—*Calculated influence of plasticity and closure on growth behavior of small cracks in 2024-T3 aluminum alloy.*

against cycles) were obtained by using the plastic-replica method [*22*,*26*]. The smallest cracks consistently recorded by this method had a half-length of about 5 μm, slightly larger than the inclusion-particle cluster (or void left by the cluster during machining) that initiated the crack. The dashed curve shows the ΔK-rate data generated on large cracks under the respective stress ratio; and the dotted curve is the effective stress-intensity factor curve ($\alpha = 1.73$ for rates less than 10^{-4} mm/cycle and $\alpha = 1.1$ for rates greater than 10^{-3} mm/cycle). Although the small-crack experimental results show a large amount of scatter, probably caused by microstructural effects, the analyses with elastic or elastic-plastic conditions agree reasonably well with the mean of the data for $R = -1$ and 0. However, the results for the high stress ratio ($R = 0.5$) condition tend to agree well in the early stages but tend to generally over predict the rates. Whereas, the low stress ratio tests had elastic conditions at the notch root, the high stress ratio tests had peak stresses above the yield stress.

Several explanations for the over prediction of rates under the $R = 0.5$ condition are proposed. First, notch-root yielding may cause a loss of constraint and a small crack may develop more closure, causing a lower effective stress range and, consequently, lower rate for a given ΔK. Second, notch-root yielding reduces the peak stresses and the local stress ratio at the notch (stress-intensity factor range is still the same). This would give a lower rate for a given applied ΔK calculated without yielding. Lastly, the *da*/*dN* relation may be different than the *dc*/*dN* relation. However, based on cyclic *J*, these results again show that the plasticity correction is small under these conditions.

Prediction of Fatigue Life Using Small Crack Analyses

The small crack analysis using elastic and elastic-plastic stress-intensity factors was used to predict the fatigue (*S*-*N*) behavior for specimens other than those used to obtain the

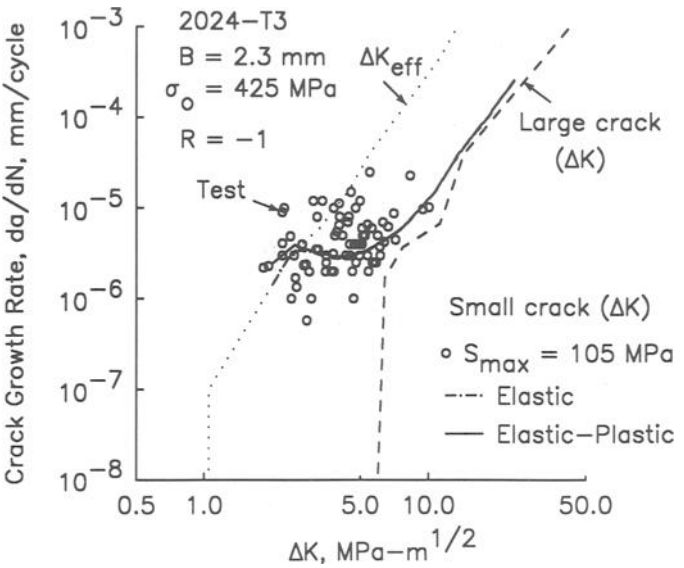

FIG. 15—*Comparison of experimental and predicted small-crack growth rates in 2024-T3 aluminum alloy under* R = −*1 loading.*

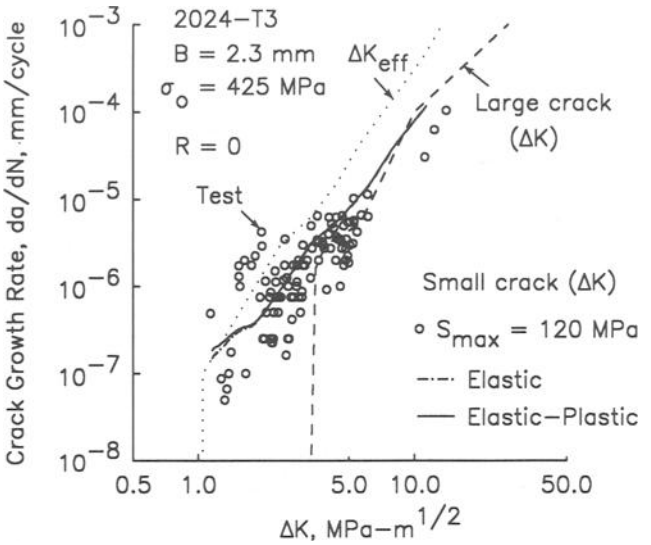

FIG. 16—*Comparison of experimental and predicted small crack growth rates in 2024-T3 aluminum alloy under* R = *0 loading.*

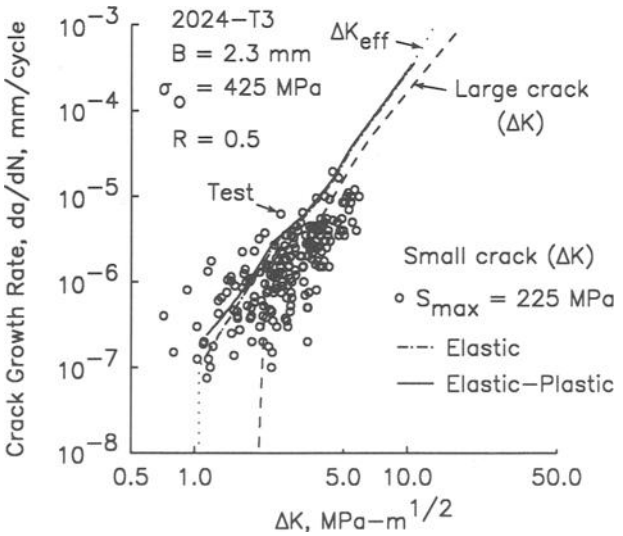

FIG. 17—*Comparison of experimental and predicted small crack growth rates in 2024-T3 aluminum alloy under* R = *0.5 loading.*

small-crack data shown in Figs. 15 through 17. Landers and Hardrath [*53*] conducted fatigue tests on 2024-T3 aluminum alloy sheet material with specimens containing a central hole with a hole-diameter-to-width ration of 1/16. The large crack growth rate properties for the 2024-T3 material are given in Ref *47* for elastic stress-intensity factor analysis. The life-prediction code, FASTRAN [*54*], was modified to include the elastic-plastic stress-intensity factor analysis, and the crack-growth properties were obtained from a reanalysis of the large crack data. As previously mentioned, the plasticity effects on the large crack effective stress-intensity factor curve were insignificant near the large crack threshold but not at effective stress-intensity factors greater than 10 MPa · $m^{1/2}$. The initial crack size was, again, based on the average inclusion-particle size [*15*].

A comparison of tests and predictions under $R = 0$ loading are shown in Fig. 18. The predictions were made using either an elastic or elastic-plastic analysis. Both predictions agreed near the fatigue limit but differed substantially as the applied stress approached the flow stress (σ_o = 425 MPa). In these predictions, a ΔK-effective threshold for small cracks was 1.05 MPa · $m^{1/2}$ (see Ref *47*). The predicted fatigue limit agreed well with experimental data for tests up to 10^7 cycles. However, Landers and Hardrath, generally, ran their tests out to greater than 10^8 cycles and found that failures were still occurring. This may indicate that fatigue damage or small-crack growth is continuing below the lower test levels. This would indicate that the lower portion of the effective stress-intensity factor curve should have a steep slope instead of being vertical as shown in Fig. 14. Above a stress level of about 250 MPa ($S_{max}/\sigma_o = 0.6$), the results from the elastic and elastic-plastic analyses differ substantially. These results are consistent with Fig. 14 in that the plasticity effects are only important for extremely high stress levels (S_{max}/σ_o greater than 0.6) for the aluminum alloys. Unfortunately, only one test was conducted above this level, but the fatigue life agreed well with the elastic-plastic analysis. Static tests (pull to failure) on this configuration gave an average of 400 MPa for three tests. The highest predicted stress for one cycle from the elastic-plastic analysis was 422 MPa (plastic-zone extended across the net section).

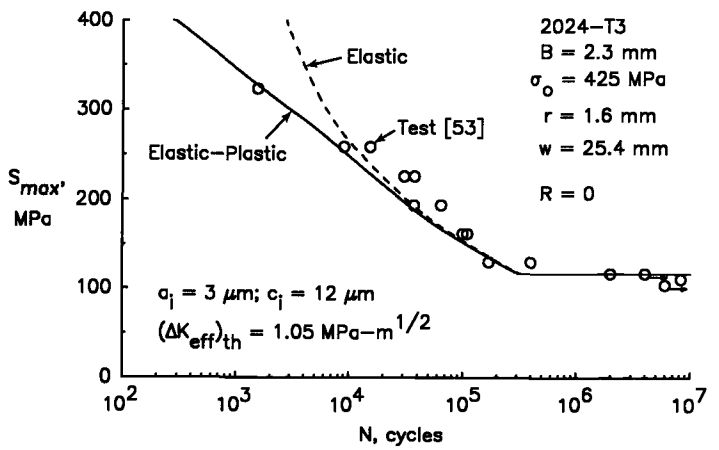

FIG. 18—*Comparison of experimental and predicted fatigue lives for 2024-T3 aluminum alloy sheet specimens with a circular hole.*

Conclusions

A review and development of the fracture-mechanics parameters for small fatigue cracks reveal the following:

1. Accurate stress-intensity factor solutions and equations are available for a wide range of surface and corner crack shapes and sizes in plates, bars, and at holes and notches. These solutions can be used in the development of standard test methods for small-crack effects.
2. A plastic-zone corrected stress-intensity factor was formulated that was found to be equivalent to the J integral from the Dugdale model (within 5%) for large-scale yielding around small cracks in two- and three-dimensional bodies (applied stress levels less than 80% of the flow stress and plastic-zone sizes an order-of-magnitude larger than the crack size).
3. For a large portion of the small-crack data in the literature, the elastic stress-intensity factor ranges were within about 10% of ΔK_p (cyclic plastic-zone corrected stress-intensity factor).
4. Surface crack shape changes in plates and at notches can be reasonably predicted if crack-growth rate data are obtained in both the depth and length directions.
5. From an analysis of small-crack data, the crack-closure transients were found to be the major cause of the small crack effect and cyclic plasticity effects on the crack-drive parameter were found to be small for most of the "classical" and recent small crack test data. Cyclic plasticity effects were found to be significant for extremely high applied-stress-range-to-twice-flow-stress levels (greater than 0.6).
6. Fatigue-life predictions using an initial defect size from microstructural examination of initiation sites and closure-based crack growth prediction methodology agreed well with experimental data for a notched aluminum alloy.

APPENDIX A

Stress-Intensity Factor Equations for a Surface-, Corner-, or Through-Crack at a Semi-Circular Notch

Approximate stress-intensity factor equations for a semi-elliptical surface crack located at the center of a semi-circular edge notch, a quarter-elliptical corner crack located at the edge of the notch, and a through crack at the notch subjected to remote uniform stress or uniform displacement (specimen-length-to-width ratio, $L/w = 1.5$) are given herein. The surface and corner crack configurations are shown in Fig. 19. These equations have been developed from stress-intensity factors calculated from finite-element [*31,32*] and weight-function [*33,34*] methods for surface and corner cracks, from boundary-force analyses of through cracks at a semi-circular notch [*30*], and from previously developed equations for similar crack configurations at an open hole [*29*]. The stress-intensity factors are expressed as

$$K = S\sqrt{\pi a/Q}\, F_{jn}\left(\frac{a}{c}, \frac{a}{t}, \frac{c}{r}, \frac{c}{w}, \frac{r}{t}, \frac{r}{w}, \phi\right) \tag{12}$$

where F_{jn} is the boundary-correction factor. The equations have been developed for a wide range of configuration parameters with $r/w = 1/16$. Note that here t is defined as one-half

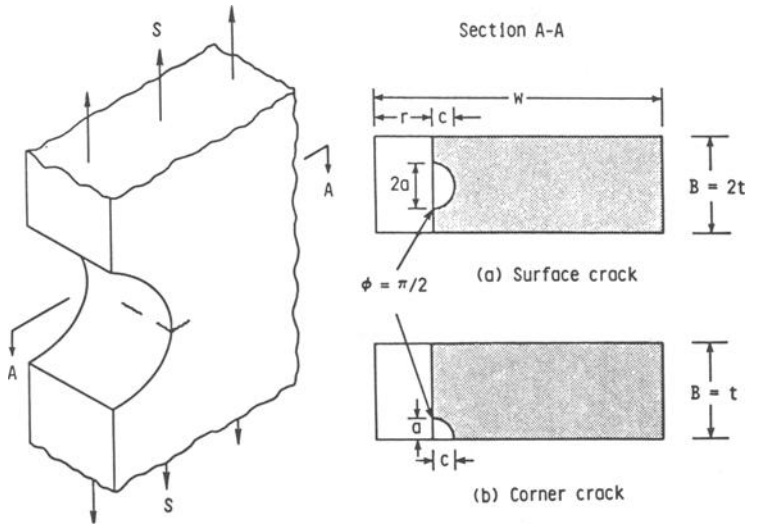

FIG. 19—*Definition of dimensions for specimen, surface-crack, and corner crack configurations.*

of the full sheet thickness for surface cracks ($j = s$), and t is full sheet thickness for corner cracks ($j = c$). The shape factor Q is given by

$$Q = 1 + 1.464(a/c)^{1.65} \quad \text{for } a/c \leq 1 \tag{13a}$$

$$Q = 1 + 1.464(c/a)^{1.65} \quad \text{for } a/c > 1 \tag{13b}$$

Surface Crack at a Semi-Circular Notch

The boundary-correction factor equation for a semi-elliptical surface crack located at the center of a semi-circular edge notch (Fig. 19*a*) subjected to remote uniform stress or uniform displacement is

$$F_{sn} = [M_1 + M_2(a/t)^2 + M_3(a/t)^4]g_1g_2g_3g_4g_5f_\phi f_w \tag{14}$$

for $0.2 < a/c < 2$, $a/t < 1$, $1 < r/t < 3.5$, $(r + c)/w < 0.5$, $r/w = 1/16$, and $-\pi/2 < \phi < \pi/2$. (Note that here t is defined as one-half of the full sheet thickness.) For $a/c \leq 1$

$$M_1 = 1 \tag{15}$$

$$M_2 = 0.05/[0.11 + (a/c)^{3/2}] \tag{16}$$

$$M_3 = 0.29/[0.23 + (a/c)^{3/2}] \tag{17}$$

$$g_1 = 1 - [(a/t)^4(2.6 - 2a/t)^{1/2}/(1 + 4a/c)]\cos\phi \tag{18}$$

$$g_2 = [1 + 0.358\lambda + 1.425\lambda^2 - 1.578\lambda^3 + 2.156\lambda^4]/(1 + 0.08\lambda^2) \quad (19)$$

$$\lambda = 1/[1 + (c/r)\cos(0.9\phi)] \quad (20)$$

$$g_3 = 1 + 0.1(1 - \cos\phi)^2(1 - a/t)^{10} \quad (21)$$

$$g_4 = K_T[0.36 - 0.032/(1 + c/r)^{1/2}] \quad (22)$$

where K_T is the elastic stress-concentration factor ($K_T = 3.17$ for uniform stress, $K_T = 3.15$ for uniform displacement) at the semi-circular notch, and

$$g_5 = 1 + (a/c)^{1/2}[0.003(r/t)^2 + 0.035(r/t)(1 - \cos\phi)^3] - 0.35(a/t)^2(1 - 0.5a/c)^3\cos\phi \quad (23)$$

The finite-width correction f_w was

$$f_w = 1 - 0.2\gamma + 9.4\gamma^2 - 19.4\gamma^3 + 27.1\gamma^4 \quad (24a)$$

for uniform stress and

$$f_w = 1 + 2.17\gamma^2 - 3.4\gamma^4 + 3.7\gamma^6 \quad (24b)$$

for uniform displacement with a specimen-length-to-width (L/w) ratio of 1.5 (L is measured from the crack plane to the grip line on the specimen) where

$$\gamma = (a/t)^{1/2}(c + r)/w$$

The function f_ϕ is given by

$$f_\phi = [(a/c)^2\cos^2\phi + \sin^2\phi]^{1/4} \quad (25)$$

For $a/c > 1$

$$M_1 = (c/a)^{1/2}(1.04 - 0.04c/a) \quad (26)$$

The functions M_2, M_3, g_1, g_2, λ, g_3, g_4, g_5, and f_w are given by Eqs 16 through 24, respectively, and f_ϕ is given by

$$f_\phi = [(c/a)^2\sin^2\phi + \cos^2\phi]^{1/4} \quad (27)$$

Corner Crack at a Semi-Circular Notch

The boundary-correction factor equation for a quarter-elliptical corner crack located at the edge of a semi-circular edge notch (Fig. 19*b*) subjected to remote uniform stress or uniform displacement is

$$F_{cn} = [M_1 + M_2(a/t)^2 + M_3(a/t)^4]g_1g_2g_3g_4g_5f_\phi f_w \quad (28)$$

for $0.2 < a/c < 2$, $a/t < 1$, $1 < r/t < 2$, $(r + c)/w < 0.5$, $r/w = 1/16$, and $0 < \phi < \pi/2$. (Note that here t is defined as the full sheet thickness.) For $a/c \leq 1$

$$M_1 = 1.13 - 0.09a/c \tag{29}$$

$$M_2 = -0.54 + 0.89/(0.2 + a/c) \tag{30}$$

$$M_3 = 0.5 - 1/(0.65 + a/c) \tag{31}$$

$$g_1 = 1 + [0.1 + 0.2(a/t)^2](1 - \sin\phi)^2 - 0.16(a/t)\sin\phi\cos\phi \tag{32}$$

$$g_2 = [1 + 0.358\lambda + 1.425\lambda^2 - 1.578\lambda^3 + 2.156\lambda^4]/(1 + 0.13\lambda^2) \tag{33}$$

$$\lambda = 1/[1 + (c/r)\cos(0.8\phi)] \tag{34}$$

$$g_3 = (1 + 0.04a/c)[1 + 0.1(1 - \cos\phi)^2][0.97 + 0.03(a/t)^{1/4}] \tag{35}$$

The functions g_4, g_5, and f_w are given by Eqs 22 through 24, respectively, and f_ϕ is given by Eq 25. For $a/c > 1$

$$M_1 = (c/a)^{1/2}(1 + 0.04c/a) \tag{36}$$

$$M_2 = 0.2(c/a)^4 \tag{37}$$

$$M_3 = -0.11(c/a)^4 \tag{38}$$

$$g_1 = 1 + (c/a)[0.1 + 0.2(a/t)^2](1 - \sin\phi)^2 - 0.16(a/t)(c/a)\sin\phi\cos\phi + 0.07(1 - a/c)(1 - a/t)\cos^2\phi \tag{39}$$

$$g_3 = (1.13 - 0.09c/a)[1 + 0.1(1 - \cos\phi)^2](0.97 + 0.03(a/t)^{1/4}] \tag{40}$$

The functions g_2 and λ are given by Eqs 33 and 34; g_4 is given by Eq 22; g_5 is given by Eq 23; f_w is given by Eq 24; and f_ϕ is given by Eq 27.

Through Crack at a Semi-Circular Notch

When the surface-crack length, $2a$, reaches sheet thickness, $2t$, or when the corner-crack length a reaches the sheet thickness t the crack is assumed to be a through crack of length c. The stress-intensity factors for a through crack emanating from a semi-circular notch subjected to remote uniform stress or uniform displacement is

$$K = S\sqrt{\pi c}\, F_n\left(\frac{c}{w}, \frac{c}{r}, \frac{r}{w}\right) \tag{41}$$

for $r/w = 1/16$, and $(c + r)/w < 0.8$. The boundary correction factor F_n is

$$F_n = f_1 g_4 f_w \tag{42}$$

where g_4 and f_w are given by Eqs 22 and 24, respectively. The function f_1 is given by

$$f_1 = 1 + 0.358\lambda + 1.425\lambda^2 - 1.578\lambda^3 + 2.156\lambda^4 \tag{43}$$

where

$$\lambda = 1/(1 + c/r)$$

APPENDIX B

Analytical Crack-Closure Model

The analytical crack-closure model was developed for a central crack in a finite-width specimen subjected to uniform applied stress. The model was later extended to through cracks emanating from a circular hole in a finite-width specimen also subjected to uniform applied stress [*18*]. The model was based on the Dugdale model [*40*], but modified to leave plastically deformed material in the wake of the crack. The primary advantage in using this model is that the plastic-zone size and crack-surface displacements are obtained by superposition of two elastic problems—a crack in a plate subjected to a remote uniform stress and to a uniform stress applied over a segment of the crack surface.

Figure 20 shows a schematic of the model at maximum and minimum applied stress. The model is composed of three regions: (1) a linear-elastic region containing a circular hole with a fictitious crack of half-length $c' + \rho$, (2) a plastic region of length ρ, and (3) a residual plastic deformation region along the crack surface. The physical crack is of length $c' - r$, where r is the radius of the hole. The compressive plastic zone is ω. Region 1 is treated as an elastic continuum. Regions 2 and 3 are composed of rigid-perfectly plastic (constant stress) bar elements with a flow stress σ_o. The flow stress σ_o is the average between the yield stress and the ultimate strength of the material. This is a first-order approximation for strain hardening.

The shaded regions in Figs. 20*a* and 9*b* indicate material that is in a plastic state. At any applied stress level, the bar elements are either intact (in the plastic zone) or broken (residual plastic deformation). The broken elements carry compressive loads only, and then only if they are in contact. At the maximum applied stress and when the crack is fully open, the effects of state of stress on plastic-zone size and displacements are approximately accounted for by using a constraint factor α. The constraint factor was used to elevate the tensile flow stress for the intact elements in the plastic zone.

The effective flow stress $\alpha\sigma_o$ under simulated plane-stress conditions is σ_o (usual Dugdale model) and under simulated plane-strain conditions is $3\sigma_o$. The value of $3\sigma_o$ was established from elastic-plastic finite-element analyses under plane-strain conditions using an elastic-perfectly-plastic material (normal stress elevation in the crack-tip region was about 2.7 from the analysis). For sheet and plate material, fully plane-strain conditions may not be possible.

Irwin [*44*] suggested a modification to account for through-the-thickness variation in stress state by introducing a constraint factor ($\alpha = 1.73$) to represent nominal plane-strain conditions. At the minimum applied stress, some elements in the plastic zone and elements

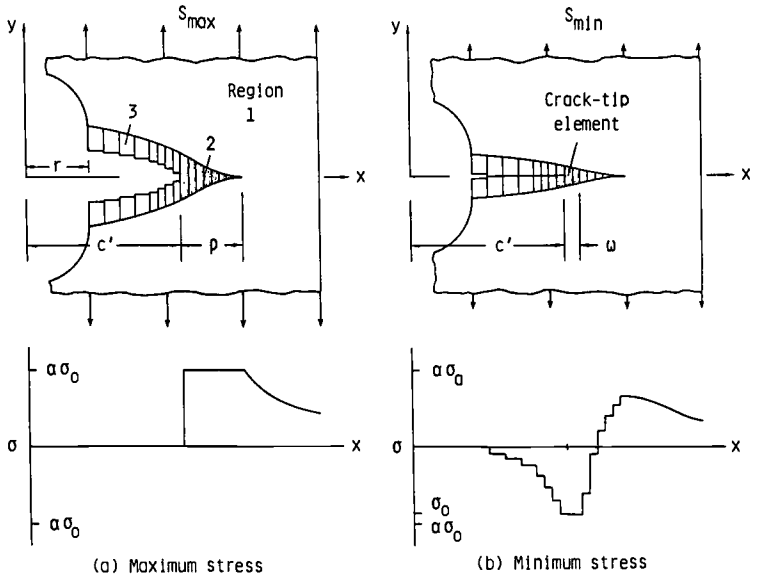

FIG. 20—*Schematic of analytical crack-closure model under cyclic loading.*

along the crack surface that are in contact may yield in compression when the contact or compressive stress reaches $-\sigma_o$. This assumption was justified on the grounds that when a crack closes the large stress gradient at the crack tip is greatly reduced and a more uniform stress field is produced.

References

[1] Gallagher, J. P., Giessler, F. J., Berens, A. P., and Engle, R. M., Jr., *USAF Damage Tolerant Design Handbook: Guidelines for the Analysis and Design of Damage Tolerant Aircraft Structures*, AFWAL-TR-82-3073, May 1984.

[2] Manning, S. D. and Yang, J. N., *USAF Durability Design Handbook: Guidelines for the Analysis and Design Aircraft Structures*, AFWAL TR-83-3027, Jan. 1984.

[3] Pearson, S., "Initiation of Fatigue Cracks in Commercial Aluminum Alloys and the Subsequent Propagation of Very Short Crack," *Engineering Fracture Mechanics*, Vol. 7, 1975, pp. 235–247.

[4] Kitagawa, H. and Takahashi, S., "Applicability of Fracture Mechanics to Very Small Cracks or the Cracks in the Early Stage," *Proceedings of the 2nd International Conference on Mechanical Behaviour of Materials*, Boston, MA, 1976, pp. 627–631.

[5] El Haddad, M. H., Dowling, N. E., Topper, T. H., and Smith, K. N., "*J*-Integral Application for Short Fatigue Cracks at Notches," *International Journal of Fracture*, Vol. 16, No. 1, 1980, pp. 15–30.

[6] Dowling, N. E., "Crack Growth During Low-Cycle Fatigue of Smooth Axial Specimens," *Cyclic Stress-Strain and Plastic Deformation Aspects of Fatigue Crack Growth, ASTM STP 637*, American Society for Testing and Materials, Philadelphia, 1977, pp. 97–121.

[7] Morris, W. L., James, M. R., and Buck, O., "Growth Rate Models for Short Surface Cracks in Al 2219-T851," *Metallurgical Transactions A*, Vol. 12A, Jan. 1981, pp. 57–64.

[8] Hudak, S. J., Jr., "Small Crack Behavior and the Prediction of Fatigue Life," *Journal of Engineering Materials and Technology*, Vol. 103, 1981, pp. 26–35.

[9] Nisitani, H. and Takao, K. I., "Significance of Initiation, Propagation, and Closure of Microcracks in High Cycle Fatigue of Ductile Materials," *Engineering Fracture Mechanics*, Vol. 15, No. 3–4, 1981, pp. 445–456.

[10] Schijve, J., "Difference Between the Growth of Small and Large Fatigue Cracks—The Relation to Threshold K-Values," *Fatigue Thresholds*, Vol. II, 1982, pp. 881–908; also: Delft University of Technology Report LR-327, 1981.

[11] Taylor, D. and Knott, J. F., "Fatigue Crack Propagation Behavior of Short Cracks—The Effects of Microstructure," *Fatigue of Engineering Materials and Structures*, Vol. 4, No. 2, 1981, pp. 147–155.

[12] Tanaka, T., Jono, M. and Komai, K., Eds., *Current Research on Fatigue Cracks*, The Society of Materials Science, Kyoto, Japan, 1985.

[13] Ritchie, R. O. and Lankford, J., Eds., *Small Fatigue Cracks*, The Metallurgical Society, Inc., Warrendale, PA, 1986.

[14] Miller, K. J. and de los Rios, E. R., Eds., *The Behaviour of Short Fatigue Cracks*, European Group on Fracture, Publication No. 1, 1986.

[15] Newman, J. C., Jr. and Edwards, P. R., "Short-Crack Growth Behaviour in an Aluminum Alloy—an AGARD Cooperative Test Programme," AGARD Report 732, Paris, France, 1988.

[16] Edwards, P. R. and Newman, J. C., Jr., "Short-Crack Growth Behaviour in Various Aircraft Materials," AGARD Report 767, Paris, France, 1990.

[17] Swain, M. H., Everett, R. A., Newman, J. C., Jr., and Phillips, "The Growth of Short Cracks in 4340 Steel and Aluminum-Lithium 2090," AGARD Report 767, Paris, France, 1990.

[18] Newman, J. C., Jr., "A Nonlinear Fracture Mechanics Approach to the Growth of Small Cracks," AGARD-CP-328, 1983, pp. 6.1–6.26.

[19] Leis, B. N., Kanninen, M. F., Hopper, A. T., Ahmad, J., and Broek, D., "Critical Review of the Fatigue Growth of Short Cracks," *Engineering Fracture Mechanics*, Vol. 23, 1986, pp. 883–898.

[20] Lankford, J., "The Growth of Small Fatigue Cracks in 7075-T6 Aluminum," Fatigue of Engineering Materials and Structures, Vol. 5, No. 3, 1982, pp. 233–248.

[21] Trantina, G. G. and Barishpolsky, M., "Elastic-Plastic Analysis of Small Defects-Voids and Inclusions," *Engineering Fracture Mechanics*, Vol. 20, No. 1, 1984, pp. 1–10.

[22] Brown, C. W. and Smith, G. C.: A Two Stage Plastic Replication Technique for Monitoring Fatigue Crack Initiation and Early Fatigue Crack Growth, *Advances in Crack Length Measurement*, C. J. Beevers, Ed., Engineering Materials Advisory Services LTD, West Midlands, United Kingdom, 1982, pp. 41–51.

[23] Ravichandran, K. S. and Larsen, J. M., "Growth Behavior of Small and Large Fatigue Cracks in Ti-24Al-11Nb: Effects of Crack Shape and Microstructure," presented at 22nd National Symposium on Fracture Mechanics, Atlanta, GA, 26–28 June, 1990.

[24] Mom, A. J. A. and Raizenne, M. D., "AGARD Engine Disc Cooperative Test Programme," AGARD Report 766, Paris, France, 1988.

[25] Pickard, A. C., Brown, C. W., and Hicks, M. A., "The Development of Advanced Specimen Testing and Analysis Techniques Applied to Fracture Mechanics Lifing of Gas Turbine Components," *Advances in Life Prediction Methods*, D. A. Woodford and J. R. Whitehead, Eds., ASME, New York, 1983.

[26] Swain, M. H. and Newman, J. C., Jr., "On the Use of Marker Loads and Replicas for Measuring Growth Rates for Small Cracks," AGARD CP-376, Paris, France, 1984, pp. 12.1–12.17.

[27] Raju, I. S. and Newman, J. C., Jr., "Stress-Intensity Factor for a Wide Range of Semi-Elliptical Surface Cracks in Finite-Thickness Plates," *Engineering Fracture Mechanics*, Vol. 11, No. 4, 1979, pp. 817–829.

[28] Newman, J. C., Jr. and Raju, I. S., "Stress-Intensity Factor Equations for Cracks in Three-Dimensional Bodies," *Fracture Mechanics: Fourteenth Symposium—Volume I, STP 791*, J. C. Lewis and G. Sines, Eds., American Society for Testing and Materials, Philadelphia, 1983, pp. 238–265.

[29] Pickard, A. C., "Stress-Intensity Factors for Cracks with Circular and Elliptic Crack Fronts, Determined by 3D Finite Element Methods," *Numerical Methods in Fracture Mechanics*, D. R. J. Owen and A. R. Luxmoore, Eds., Pineridge Press, Swansea, United Kingdom, 1980, pp. 599–619.

[30] Tan, P. W., "The Boundary Force Method for Stress Analysis of Arbitrarily Shaped Plates with Notches and Cracks," Ph.D. thesis, George Washington University, Washington, DC, 1986.

[31] Tan, P. W., Raju, I. S., Shivakumar, K. N., and Newman, J. C., Jr., "Evaluation of Finite-Element Models and Stress-Intensity Factors for Surface Cracks Emanating from Stress Concentrations," *Surface-Crack Growth: Models, Experiments and Structures, STP 1060*, W. G. Reuter, J. H. Underwood and J. C. Newman, Jr., eds., American Society for Testing and Materials, Philadelphia, 1990, pp. 34–48.

[32] Shivakumar, K. N. and Newman, J. C., Jr., "Stress-Intensity Factors for Large Aspect Ratio Surface and Corner Cracks at a Semi-Circular Notch in a Tension Specimen," submitted to *Engineering Fracture Mechanics*, Vol. 38, 1991, pp. 467–473.

[33] Zhao, W. and Wu, X. R., "Stress Intensity Factor Evaluation by Weight Function for Surface Crack in Edge Notch," *Theoretical and Applied Fracture Mechanics*, Vol. 13, 1990, pp. 225–238.

[34] Zhao, W. and Wu, X. R., "Stress Intensity Factors for Corner Cracks at a Semi-Circular Notch Under Stress Gradients," *Fatigue and Fracture of Engineering Materials and Structures*, Vol. 13, No. 4, 1990, pp. 347–360.

[35] Folias, E. S., "Some Remarks on Three-Dimensional Fracture," *Fracture Mechanics: Nineteenth Symposium, STP 969*, T. A. Cruse, Ed., American Society for Testing and Materials, Philadelphia, 1988, pp. 56–72.

[36] Hudak, S. J., Jr. and Chan, K. S., "In Search of a Driving Force to Characterize the Kinetics of Small Crack Growth," *Small Fatigue Cracks*, R. O. Ritchie and J. Lankford, Eds., The Metallurgical Society, Inc., Warrendale, PA, 1986.

[37] Chan, K. S., "Local Crack-Tip Field Parameters for Large and Small Cracks: Theory and Experiment," *Small Fatigue Cracks*, R. O. Ritchie and J. Lankford, Eds., The Metallurgical Society, Inc., Warrendale, PA, 1986.

[38] Minakawa, K. and McEvily, A. J., "On Near-Threshold Fatigue Crack Growth in Steels and Aluminum Alloys," *Proceedings of the International Conference on Fatigue Thresholds*, Vol. 2, Stockholm, Sweden, 1981, pp. 373–390.

[39] Lee, J. J. and Sharpe, W. N., Jr., "Short Fatigue Cracks in Notched Aluminum Specimens, *Small Fatigue Cracks*, R. O. Ritchie and J. Lankford, Eds., The Metallurgical Society, Warrendale, PA, 1986.

[40] Dugdale, D. S., "Yielding of Steel Sheets Containing Slits," *Journal of Mechanics and Physics of Solids*, Vol. 8, No. 2, 1960, pp. 100–104.

[41] Drucker, D. C. and Rice, J. R., "Plastic Deformation in Brittle and Ductile Fracture," Engineering Fracture Mechanics, Vol. 1, 1970, pp. 577–602.

[42] Rice, J. R., "A Path Independent Integral and the Approximate Analysis of Strain Concentration by Notches and Cracks," *Journal of Applied Mechanics*, Transactions of the ASME, June 1968, pp. 379–386.

[43] Tada, H., Paris, P. C. and Irwin, G. R., *The Stress Analysis of Cracks Handbook*, Del Research Corporation, Bethlehem, PA, 1985.

[44] Irwin, G. R., "Plastic Zone Near a Crack and Fracture Toughness," Proceedings of the 7th Sagamore Conference, 1960, pp. IV.63–IV.76.

[45] Barenblatt, G. I., "The Mathematical Theory of Equilibrium Cracks in Brittle Fracture," *Advances in Applied Mechanics*, H. L. Dryden and T. von Karman, Eds., Academic Press, New York, 1962, pp. 55–129.

[46] Elber, W., "The Significance of Fatigue Crack Closure," *Damage Tolerance in Aircraft Structures, STP 486*, American Society for Testing and Materials, Philadelphia, 1971, pp. 230–242.

[47] Newman, J. C., Jr., Swain, M. H., and Phillips, E. P., "An Assessment of the Small-Crack Effect for 2024-T3 Aluminum Alloy," *Small Fatigue Cracks*, R. O. Ritchie and J. Lankford, Eds., The Metallurgical Society, Warrendale, PA, 1986, pp. 427–452.

[48] Newman, J. C., Jr., "A Crack-Closure Model for Predicting Fatigue Crack Growth Under Aircraft Spectrum Loading, *Methods and Models for Predicting Fatigue Crack Growth Under Random Loading, STP 748*, J. B. Chang and C. M. Hudson, Eds., American Society for Testing and Materials, Philadelphia, 1981, pp. 53–84.

[49] Paris, P. C., Gomez, M. P., and Anderson, W. E., "A Rational Analytic Theory of Fatigue," *The Trend in Engineering*, University of Washington, Seattle, WA, Vol. 13, No. 1, Jan. 1961, pp. 9–14.

[50] Rice, J. R., "Mechanics of Crack Tip Deformation and Extension by Fatigue," *Fatigue Crack Propagation, STP 415*, American Society for Testing and Materials, Philadelphia, 1967, pp. 247–309.

[51] Newman, J. C., Jr. and Raju, I. S., "Prediction of Fatigue Crack-Growth Patterns and Lives in Three-Dimensional Cracked Bodies," *Proceedings of the 6th International Conference on Fracture*, New Delhi, India, 1984, pp. 1597–1608.

[52] Jolles, M. and Tortoriello, V., "Geometry Variations during Fatigue Growth of Surface Flaws," *Fracture Mechanics: Fourteenth Symposium—Volume 1*, J. C. Lewis and G. Sines, Eds., *STP 791*, American Society for Testing and Materials, Philadelphia, 1983, pp. 297–307.

[53] Landers, C. B. and Hardrath, H. F., "Results of Axial-Load Fatigue Tests on Electropolished 2024-T3 and 7075-T6 Aluminum Alloy Sheet Specimens with Central Holes," NACA TN-3631, March 1956.

[54] *FASTRAN—Fatigue Crack Growth Analysis of Structures—A Closure Model*, Computer Software Management and Information Center, University of Georgia, Athens, GA, Dec. 1984.

Mary H. Swain[1]

Monitoring Small-Crack Growth by the Replication Method

REFERENCE: Swain, M. H., **"Monitoring Small-Crack Growth by the Replication Method,"** *Small-Crack Test Methods, ASTM STP 1149*, J. M. Larsen and J. E. Allison, Eds., American Society for Testing and Materials, 1992, pp. 34–56.

ABSTRACT: The suitability of the acetate replication method for monitoring the growth of small cracks is discussed. Applications of this technique are shown for cracks growing at the notch root in semicircular-edge-notch specimens of a variety of aluminum alloys and one steel. Cracks were allowed to initiate naturally along the surface or at the corner of the notch root, a stress condition representative of a fastener hole or fillet in aircraft components. The calculated crack growth rate versus ΔK relationship for small cracks was compared to that for large cracks obtained from middle-crack-tension specimens. The advantages and limitations of the acetate replication method in comparison to other commonly used methods for small crack research are delineated. The primary advantage of this technique is that it provides an opportunity, at the completion of the test, to go backward in time towards the crack initiation event and "zoom in" on areas of interest on the specimen surface with a resolution of about 0.1 μm (0.0001 mm). The primary disadvantage is the inability to automate the process. Also, for some materials, the replication process may alter the crack-tip chemistry or plastic zone, thereby affecting crack growth rates.

KEY WORDS: fatigue (materials), crack propagation, short crack, replicas

Crack growth behavior of large fatigue cracks (>2 mm in length) can be documented using several standard fracture mechanics methods such as ASTM Test Method for Measurements of Fatigue Crack Growth Rates (E 647). Cracks in engineering components, however, may spend the major portion of their lives as physically small cracks on the order of 5 to 2000 μm in length. It has been demonstrated by numerous researchers in the last 20 years that the crack growth behavior of these cracks when they are "small" may not be describable by accepted linear elastic fracture mechanics principles, and that small cracks in fact grow more rapidly than large cracks when assessed on a stress intensity factor range basis. Because of the potential impact of this behavior on the total fatigue life of components in many engineering applications, it is important to develop reliable techniques to document early fatigue crack growth. One such technique, which has been used extensively, is the cellulose acetate replication method. This technique is both elegant in its simplicity and pedestrian in its tediousness. A sampling of materials, specimen configurations, and researchers involved with the replication method, as documented in the literature [*1–11*], is offered in Table 1.

This paper describes in some detail the replication procedure and typical results obtained using these procedures at National Aeronautics and Space Administration (NASA) Langley Research Center over the past eight years. In addition to independent work, the laboratory was involved in the organization and execution of three cooperative small-crack growth test

[1]Research engineer, Lockheed Engineering & Sciences Company, Hampton, VA 23666.

TABLE 1—*Some references on the use of the replication method for monitoring crack growth.*

Materials Tested	Specimen Type	Loading Conditions	Researchers
2090-T8E41, 2091-T351, 8091-T351	rectangular	4 point bend, $R = 0.1$	Rao and Ritchie [*1*]
8090-UA,PA,OA*	rectangular	3 point bend, $R = 0.1$	Birt and Beevers [*2*]
IMI318, IMI550, 7010	rectangular	4 point bend, $R = 0.1$	Bolingbroke and King [*3*]
IMI318	rectangular	4 point bend, $R = 0.1$	Brown and Smith [*4*]
Astroloy, Waspaloy	rectangular	3 point bend, $R = 0.1$	Brown et al. [*5*]
7075-T6, 4340 steel	hourglass	axial, $R = 0.1$	Lankford [*6,7*]
Ti-17	hourglass	bending, $R = -1$	Funkenbusch and Coffin [*8*]
A533B Steel	cylindrical	axial, $R = -1$	Dowling [*9*]
1026 Steel	rectangular	axial, $R = -1$	McClung and Sehitoglu [*10*]
2024-T3	notched	axial, $R = 0.5, 0, -1, -2$, Falstaff	Newman et al. [*11*]

[a]Under aged, peak aged, overaged.

programs in which a vast quantity of small-crack data was generated and analyzed using the replication method. Two of these programs were organized under the auspices of the Advisory Group for Aerospace Research and Development (AGARD) Structures and Materials Panel; the first program involved ten laboratories [*12*] and the second involved twelve [*13*]. The third program was a joint effort between NASA and the Chinese Aeronautical Establishment. Based on the experiences gained from this work, advantages and disadvantages of the replication method will be discussed.

Procedures

Specimen and Test Procedures

The replication method is applicable to a variety of specimen geometries. Replicas can be made from flat, cylindrical (convex) or notched (concave) surfaces. The examples cited in this work are from cracks that initiated at the notch surface or corner of a single-edge-notch tension specimen (SEN) containing a semicircular notch, with a radius r of 3.18 mm, as shown in Fig. 1. Specimens were machined such that the load axis was parallel to the rolling direction of the sheet (LT orientation). The width w of all aluminum specimens was 50 mm and of all steel specimens was 25 mm. This geometry, with a stress concentration factor K_T, of 3.11 for aluminum and 3.3 for steel specimens (based on gross section), was chosen because it served to localize the region of crack initiation, and it approximates the stress distribution of a fillet or fastener hole, two likely locations for crack initiation in airframe structures. All tests were conducted in lab air at a frequency of either 5 or 10 Hz. The growth of semi-elliptical surface cracks and quarter-elliptical corner cracks was monitored at the notch root by taking measurements of surface crack length, $2a$, or corner crack length a along the thickness direction of the sheet B as depicted in Fig. 2. The sheet thickness B is taken as $2t$ for the surface crack and t for the corner crack simply to make the equations for calculating ΔK consistent. Crack depth c is defined the same way in both cases.

Careful attention should be given to the surface condition of the specimens. Observation of crack initiation and crack growth is most easily done on specimens with a smooth surface finish. The presence of machining marks may obscure the fine details and is an indication of a mechanically deformed layer of material in an unknown state of residual stress. For these reasons, the small-crack studies conducted at NASA Langley always utilized specimens that were prepared by mechanical polishing, chemical polishing, or electropolishing.

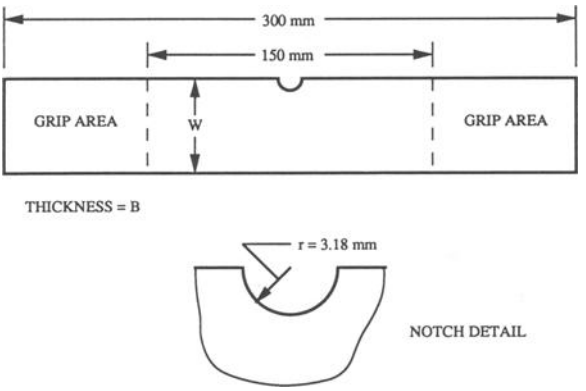

FIG. 1—*Single-edge-notch tension (SEN) specimen geometry.*

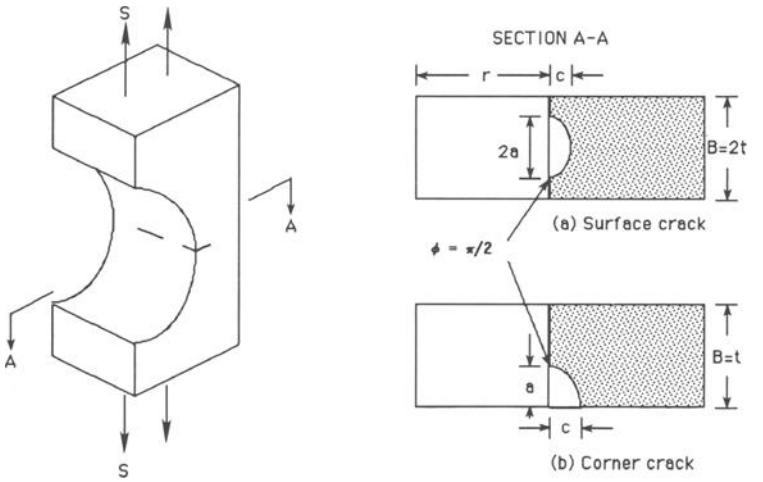

FIG. 2—*Schematic of surface and corner crack at notch root.*

Mechanical polishing was accomplished with 0.3-μm diamond paste applied to an adhesive-backed polishing cloth, which had been wrapped around a rod slightly smaller in diameter than the edge notch. The rod was inserted in the chuck of a drill press and rotated while the specimen notch surface was lightly pressed against the polishing compound. This resulted in a smooth notch surface with some fine scratches oriented at 90° to the nominal crack growth direction. Notch surface preparation was completed with a light etch (Keller's etch was used for aluminum specimens) to remove any residual stress introduced by the diamond paste polishing process and to delineate the grain boundaries.

Chemical polishing has also been used for 2000 and 7000 series aluminum alloys. The specimens were submerged for 5 min in a solution of 80% phosphoric acid, 5% nitric acid, 5% acetic acid, and water maintained at 105°C. After polishing the specimens were rinsed with water. A reddish cast on the specimen surface, caused by a copper-rich layer, was removed by dipping in a desmutting solution of 10% nitric acid in water for 20 s. A final water rinse and then an alcohol rinse completed the procedure. Grain boundaries were generally visible after this chemical polishing procedure, but were in some cases further enhanced by a light etch with Keller's etch.

Electropolishing of the localized notch region was used to prepare specimens of 4340 steel, but could also be used for a variety of alloys. The solution used for the steel consisted of 70% ethanol, 10% glycerin, and 20% perchloric acid maintained between 18 and 20°C. A stream of solution was directed through a 1.3-cm-diameter opening in the top of the polishing cell to flow over the notch root area for 4 min at a potential of 35 V. The polished area was cleaned in a solution of detergent and water, rinsed in water, then in alcohol. These three methods of notch preparation removed a surface layer between 20 and 100 μm in depth.

Monitoring crack initiation and growth via the acetate replica technique is a discontinuous process. Fatigue cycling is interrupted periodically and the specimen held under constant tensile load to maintain crack mouth opening while the surface or surfaces of interest are replicated. In order to select the cyclic interval at which replicas will be taken, the expected fatigue life must be determined from fatigue life tests conducted on the particular specimen geometry and loading conditions or otherwise estimated from available data. The objective is to have 20 to 50 replicas from each test, as this seems to document crack growth history with sufficient data from the small-crack regime to establish the similarities or differences from the large-crack behavior. Figure 3 shows fatigue life data for 2024-T3 aluminum SEN specimens under $R = -1$ loading. Stress levels selected for replica tests on this alloy were 105, 80, and 70 MPa. Lower stress levels were avoided because of the scatter in fatigue life near the "fatigue limit;" high stress levels were also excluded because of the increased tendency for multiple-crack initiation events and the resulting increased complexity of analysis of stress intensity factors at neighboring crack tips. Specific procedures for handling multiple cracks and excluding data when crack interaction effects are anticipated will be discussed in the following section. Once each stress level was selected, the corresponding fatigue life was divided by 50 (or 25, and so forth) to determine the cyclic interval that should be used for the small-crack tests to produce approximately 50 (or 25, etc.) replicas documenting crack initiation and growth.

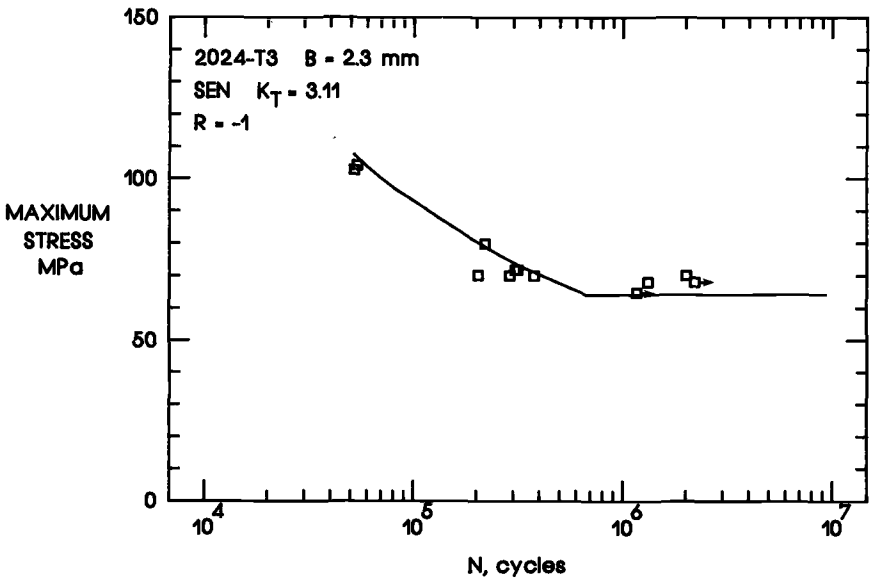

FIG. 3—*Fatigue life data for SEN specimens of 2024-T3 under* R = −1 *loading.*

Replication Procedures

The procedure by which the replica is made is straightforward. When the cyclic interval has been completed, the test is halted at mean load. A static load equal to 60 to 80% of P_{max} is then applied. This load is selected to be significantly above the closure level to assure that cracks (if present) will be open. The surface to be replicated is cleaned with reagent grade acetone. For the case of the SEN specimen, a section of cellulose acetate sheet, 0.04 mm thick, is cut slightly wider than the specimen thickness and longer than the circumference of the notch root. As shown in Fig. 4, the acetate is curved around a rod whose diameter is less than the notch diameter by somewhat more than two times the thickness of the acetate sheet. The notch surface is bathed with one or two drops of acetone from a hypodermic needle just before touching the acetate to the notch surface. Only gentle pressure from the rod is needed as capillary action will tend to draw the acetate against the notch surface and hold it there. The acetone softens the surface of the acetate sheet and allows it to conform to the notch surface topography, flowing into the mouth of any open cracks. The acetate dries to form the replica in less than 10 min and can be easily removed with tweezers, peeling away from one end of the notch. Clipping away the same corner from the margin of each replica facilitates orientation of the replicas for analysis. A cursory examination of the replica in a strong light or through a low power microscope should reveal the presence of undesirable bubbles or other artifacts that render the replica unusable. A bubble indicates that air was trapped at that location between the acetate and notch and, hence, no surface topography information was transferred. If necessary, a subsequent replica can be taken before continuing to cycle the specimen. The replica should be stored in a dry and dust free environment. For thin cellulose acetate, sealing in a small polyethylene bag works well, in that it tends to flatten the replica. The ends of the replica may be attached to the surface of a glass slide with adhesive tape for ease of handling when observing cracks in the optical microscope. For observation in the scanning electron microscope replicas must be clamped mechanically rather than using adhesive (because of vacuum considerations).

Depending on the particular specimen geometry, other forms of replica material may be more suitable. When replicating a flat surface a more rigid form of acetate, such as thicker

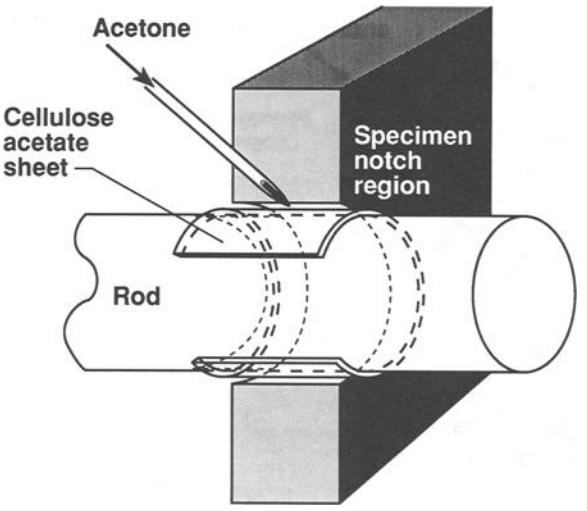

FIG. 4—*Schematic of replication procedure for semicircular edge notch.*

replicating tape or sheet material (on the order of 5 mm thick), can be readily used. In the case of thicker tape, the surface of the acetate is first softened with acetone and then firmly pressed against the surface to be replicated. A rolling pressure from one end of the tape to the other tends to force out trapped air. A detailed procedure for using 0.13-mm-thick tape to replicate flat fatigue specimen surfaces is given by Henry [*14*]. In order to use 5-mm-thick sheet to make a replica of a notch root, the rough shape of the notch is first cut into a block of acetate. The "notch shape" is then softened with acetone and pressed into the notch of the specimen. Because of its rigidity the thicker material is easier to handle and store.

Analysis of Replicas

Crack length measurement from replicas can be accomplished using an optical microscope (OM) or scanning electron microscope (SEM). Observation in an optical microscope can be made directly on the acetate surface. Although the replica is transparent, any features visible from the back surface are out of focus and, hence, do not impair the sharp image of cracks or notch surface features. In order to view replicas in the SEM, the surface must be sputter-coated with a thin layer (several 100 Å [10 nm]) of a heavy metal, such as gold or gold-palladium alloy. This provides the necessary conductive path for the electrons. The replica is a negative of the specimen surface, and the crack image appears as a thin ridge where softened acetate has penetrated into the open crack and remained attached to the replica sheet when it is removed from the specimen notch. A comparison of the crack images produced from a crack 130 μm in length and viewed using both OM and SEM is shown in Fig. 5. The fatigue specimen was 2024-T3 with a mechanically polished notch. The faint vertical lines are polishing scratches along the circumference of the notch and parallel to the loading direction. On the OM image, the hazy circles are from roughness on the back surface of the acetate. The image in the OM is reversed from left to right, whereas this is not the case for the SEM image (note the end points labeled A and B). The crack appears bright compared to the overall specimen surface when viewed in the SEM because many

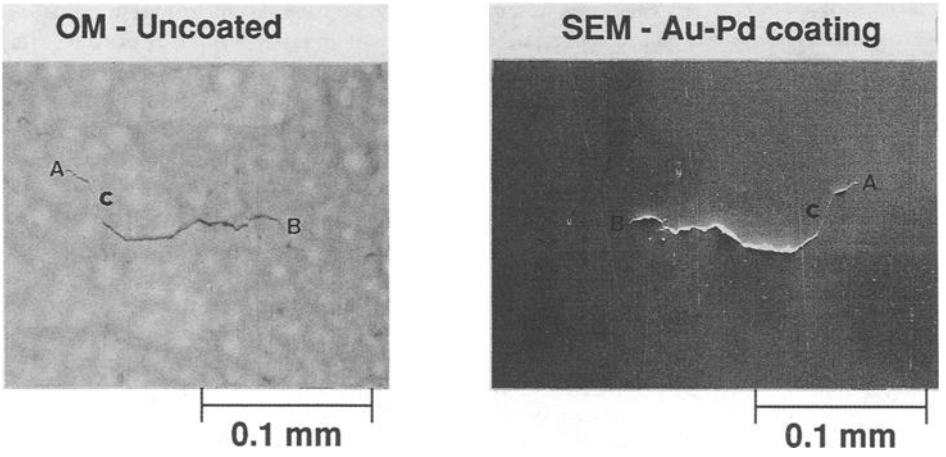

FIG. 5—*Comparison of crack replica image using* (a) *optical microscopy (OM) and* (b) *scanning electron microscopy (SEM).*

more secondary electrons (low-energy electrons that make up most of the intensity of the image) are produced near an edge than on a smooth surface. Secondary electrons can be created by (1) the beam electrons upon entering the specimen, (2) by backscattered electrons escaping the specimen through the entrance surface and the sides, and (3) by the electrons transmitted through the ridge [*15*]. This enhanced contrast is helpful in locating cracks when they are quite small, on the order of 5 μm. Replicas can be viewed at magnifications up to about 5000 times under selected electron beam conditions. The beam energy should be kept below 10 keV to keep the beam interactions near the surface of the coated replica. The beam spot size should be kept small in order to keep the beam current low and minimize heating effects. The beam diameter used in this work was approximately 40 nm.[2] Even when using these beam parameters care must be taken not to view an area of the replica at high magnification for more than about 1 min, otherwise damage to the replica from heating will result. The resolution, which can be obtained using this technique, is approximately 0.0001 mm (0.1 μm).

In the one-step replica process described above, the acetate replica remains intact and acts as the substrate. Other investigators have used two-step replicating procedures to produce a positive image of the specimen surface. Brown and Smith [*4*] vapor deposited a 0.3-mm layer of solder on the acetate replica and applied an epoxy backing. The acetate replica was then peeled away from the solder layer, forming the positive image. Lankford [*7*] coated the replicas with palladium, nickel plated the latter, and stripped away the acetate. These techniques, although more time consuming, allow examination of the positive metal replica in the SEM at high magnification with much less concern for damage from specimen heating.

At the conclusion of the fatigue test, replica analysis begins with the last replica, in this case the one taken just before the surface or corner crack becomes a through-thickness-crack. On this last replica, the identity of the critical crack or cracks is obvious. The crack length along the notch surface is measured directly from the SEM image or recorded photographically for later measurement. As each earlier replica is examined the crack image becomes smaller and would be more difficult to locate except that features on the notch surface, such as the edge of the notch, grain boundaries, inclusion particles, and scratches, can be used as points of reference to "zero in" on the proper area of the replica.

Shrinkage of the replica film by 5 to 10% as it dries on the specimen is a concern for thin replica material. This difficulty can be overcome by normalizing crack length measurements by a shrinkage factor. This factor is determined by comparing distances measured between several reference points on a specimen notch surface and on replicas made from that surface. An alternative solution is to take a montage of photographs of the notch surface along the crack path on one half of the fractured specimen and locate the position of the crack tips as noted in each successive replica on that montage. Jogs in the crack path and the location of surrounding grain boundaries and inclusion particle sites aid in the accurate placement of the crack tips on the montage. Crack-tip position is easily established on the fractured specimen photographs for most aluminum alloys, but is more difficult for materials, such as quenched and tempered steel, with few inclusion particles and a very fine tempered martensite microstructure.

In addition to examining the replicas to monitor the length of the crack or cracks present at the notch root, information on the relative position of multiple cracks is readily available. Knowledge of the proximity and size of neighboring cracks, either on the same plane or on a parallel plane, is necessary to evaluate the increase or decrease, respectively, in the stress intensity factor at the crack tip over that of a single, isolated crack. For the data presented in this work a set of "noninteraction" criteria was established to identify cases where the

[2]Private communication, Cambridge Instruments (Leica), Deerfield, IL.

stress intensity factor was thought to be influenced by neighboring cracks (see Appendix A). Crack growth data from these cracks were eliminated from the small-crack data presented in this work, but could be included in a subsequent analysis of the existing crack length-cycle data, if a stress intensity factor equation suitably modified for crack interaction effects was used.

Results

The initiation and growth of small surface and corner cracks in SEN specimens of 2024-T3, 7075-T6, 2090-T8E41, a clad Chinese aluminum alloy LC9-CS (similar to 7075-T6) and 4340 steel have been studied under both constant amplitude loading and several variable amplitude load spectra [*12*,*13*,*16*]. Selected results from these investigations are cited to illustrate typical results obtained with the replication method.

A series of replica SEM images typical for a single crack in 4340 steel is shown in Fig. 6*a*. It is clear from the 60 000-cycle replica that the fatigue crack initiated at a pit in the notch surface, possibly formed by a spherical inclusion particle removed by the machining or electropolishing process. This crack was located, however, by first examining the 160 000-cycle replica on which the crack image was approximately 70 times larger and then proceeding backwards consecutively to the replicas in the small-crack regime. After the specimen had undergone 160 000 cycles, it was pulled to failure in tension so that a measurement of fatigue crack shape (c/a) as a function of crack size (a/t) could be obtained. A micrograph of the fracture surface in Fig. 6*b* shows a semi-elliptical crack shape. The enlarged view of the crack initiation site shows the dimensions of the defect pit ($2a$ = 16 μm), which correlates with the pit (replica) dimension shown in Fig. 6*a*. The surface crack length, $2a$, measured directly from the fractograph can be compared with the value obtained from the replica taken after 160 000 cycles (just before the specimen was pulled apart) to verify the accuracy of the replica method.

Crack shape data sufficient to establish the relation between crack size and shape is necessary to the calculation of ΔK for small semi-elliptical cracks. For the 4340 steel tests, for example, a total of six specimens were pulled in tension to failure at a point in life when they contained semi-elliptical notch-surface fatigue cracks of varying sizes. Measurements from the fracture surface of surface crack length, $2a$, and crack depth c were plotted as c/a versus a/t, as shown in Fig. 7, and a visual best-fit line was drawn through the data points. The crack shape equation determined experimentally for 4340 steel and used in the ΔK calculations for this alloy was

$$c/a = 1.0 - 0.25(a/t) \quad \text{(for 4340 steel)} \tag{1a}$$

The crack shape relation obtained in a similar manner for 2024-T3 [*12*] and used for 2000 series aluminum alloys was

$$c/a = 0.9 - 0.25(a/t)^2 \quad \text{(for 2024-T3, 2090-T8E41)} \tag{1b}$$

and that determined for 7075-T6 was

$$c/a = 1.0 - 0.1(a/t) \quad \text{(for 7075-T6)} \tag{1c}$$

Once the relationship between measured crack length a and crack depth c has been established, a stress intensity factor at the point where the crack intersects the notch surface

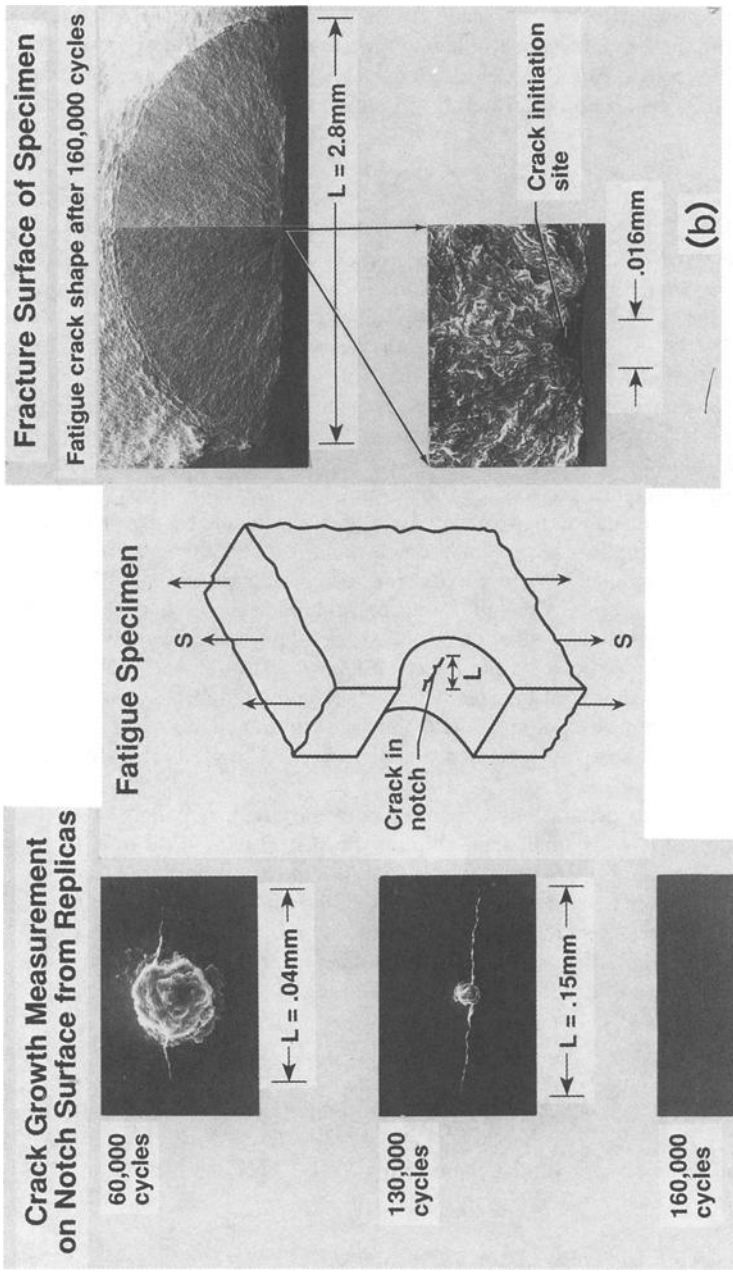

FIG. 6—*Small crack growth in 4340 steel:* (a) *SEM micrograph of replica showing crack growth sequence at surface flaw and* (b) *SEM micrograph of fatigue crack emanating from inclusion site shown in* (a).

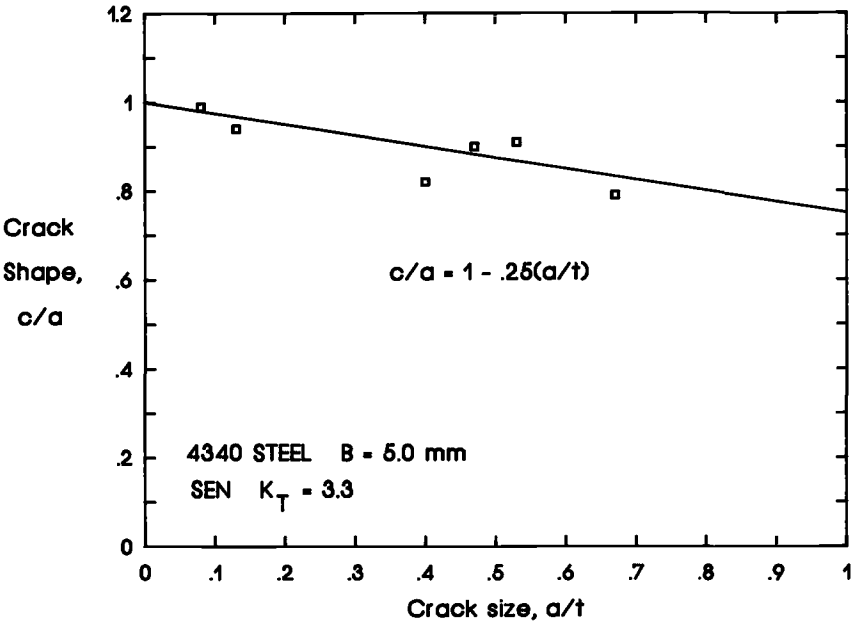

FIG. 7—*Experimental fatigue crack shape measurements for 4340 steel SEN specimens.*

($\phi = \pi/2$) can be calculated. In the interest of completeness, approximate stress-intensity factor equations for a surface crack or a corner crack emanating from a semi-circular edge notch developed by Newman and presented previously in the literature [*13*] are included in this work. These equations are used to compare crack growth rates measured for small cracks with those measured for large cracks as a function of the stress-intensity factor range. The calculation of stress-intensity factor assumes that either a semi-elliptical surface crack is located at the center of the edge notch or a quarter-elliptical corner crack is located at an edge, as was shown in Fig. 2. For a surface crack located at other locations along the bore of the notch, the calculation is adequate if the crack is small compared to thickness.

The stress-intensity factor range equation for a surface crack located at the center of the edge notch subjected to remote uniform displacement is

$$\Delta K = \Delta S\sqrt{(\pi a/Q)}\, F_{sn} \tag{2a}$$

for $0.2 < a/c < 2$ and $a/t < 1$. Equations for Q, the shape factor, and F_{sn}, the boundary-correction factor, are given in Appendix B.

For a corner crack, the stress-intensity factor is

$$\Delta K = \Delta S\, \sqrt{(\pi a/Q)}\, F_{cn} \tag{2b}$$

for $0.2 < a/c < 2$ and $a/t < 1$, where

$$F_{cn} = F_{sn}(1.13 - 0.09a/c) \quad \text{for } a/c \leq 1$$

$$F_{cn} = F_{sn}(1 + 0.04c/a) \quad \text{for } a/c > 1$$

The stress range (ΔS) is full range ($S_{max} - S_{min}$) for constant amplitude and spectrum loading. For example, $\Delta S = 2S_{max}$ for $R = -1$ loading. For spectrum loading, the highest peak stress is S_{max} and the lowest trough is S_{min}.

Crack growth rate results obtained by the replication method for 4340 steel SEN specimens under $R = -1$ loading for two constant amplitude stress levels are given in Fig. 8. The ΔK values given are for the full range in load. The heavy solid line in the figure represents a best fit to the large crack data from through-thickness cracks in standard middle-crack-tension (MT) tests, also conducted under $R = -1$ loading. Crack growth rates from the small crack tests (SEN specimens) are calculated as the difference in crack length observed on consecutive replicas divided by the cyclic interval. This rate is plotted for the ΔK calculated from the above equations for the average of the two crack lengths. Vertical lines indicate approximate crack size correlations with the ΔK values calculated for the SEN tests. For 4340 steel tested under $R = -1$ loading, small crack growth was observed below the large crack threshold over a range of crack growth rates. Small cracks grew faster than large cracks up to a stress intensity factor range of 15 MPa · $m^{1/2}$, which corresponds to a crack length, $2a$, of approximately 90 μm. For larger values of ΔK, crack growth rates measured in the small-crack tests using replicas agree with those measured on large-crack tests at the same stress ratio using standard methods. There is a larger variability in measured crack growth rates below a ΔK of 15 MPa · $m^{1/2}$ than above. This may be due, in part, to increased percent error in the measurement of crack length in this regime, since the cyclic interval between replicas was held constant throughout the fatigue test. For example, if the cyclic interval dN for a given test was 2000 cycles, a measured crack growth increment da of 1 μm results in a crack growth rate da/dN of 5×10^{-10} m/cycle, calculated by the secant method; whereas, a growth increment of 100 μm is necessary to obtain a growth rate of 5

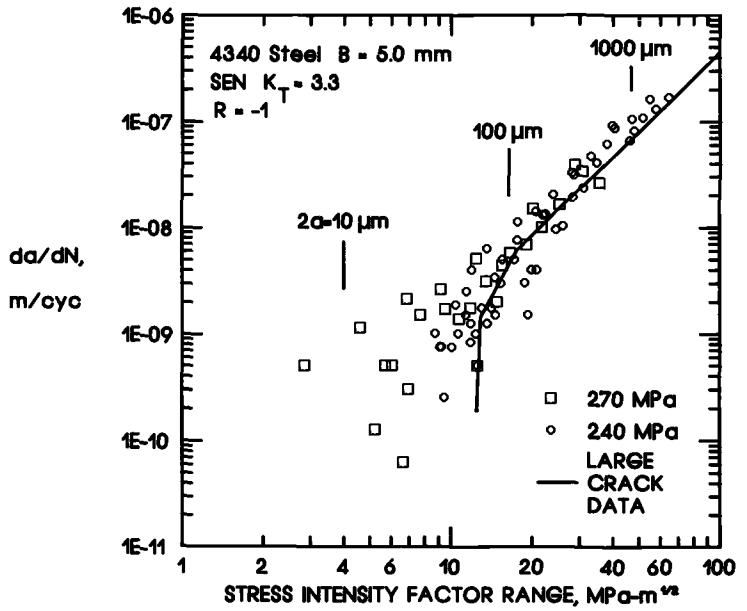

FIG. 8—*Small- and large-crack growth data for 4340 steel under* R = −1 *loading. Correlation of surface crack length and stress intensity factor range for the small-crack-test data points are indicated by the vertical line segments.*

$\times 10^{-8}$ m/cycle. The accuracy in crack length measurement using the replica technique was given previously as 0.1 μm, or 10% in the former case and 0.1% in the latter. Although the measurement error is larger for the smaller cracks, the variability in crack growth rates in this regime is much more than 10%, and thus is more likely attributable to changes in microstructural or closure contributions to crack growth.

Replication methods have also been used to study the effect of surface discontinuities (inclusions and pits) in fatigue crack initiation and small-crack propagation in aluminum alloys. Figure 9*a* shows a replica of a small crack in 7075-T6 aluminum, which has initiated at an inclusion particle pit. The inclusion particle sites in the aluminum alloys were approximately 6 μm in diameter on the notch surface, considerably smaller than those which initiated cracks in the steel. The replica shows the current crack length, as well as a number of inclusion particle sites and grain boundaries that can be matched to the features on the SEM photo of the notch surface in the lower part of Fig. 9*b*. The features on the replica

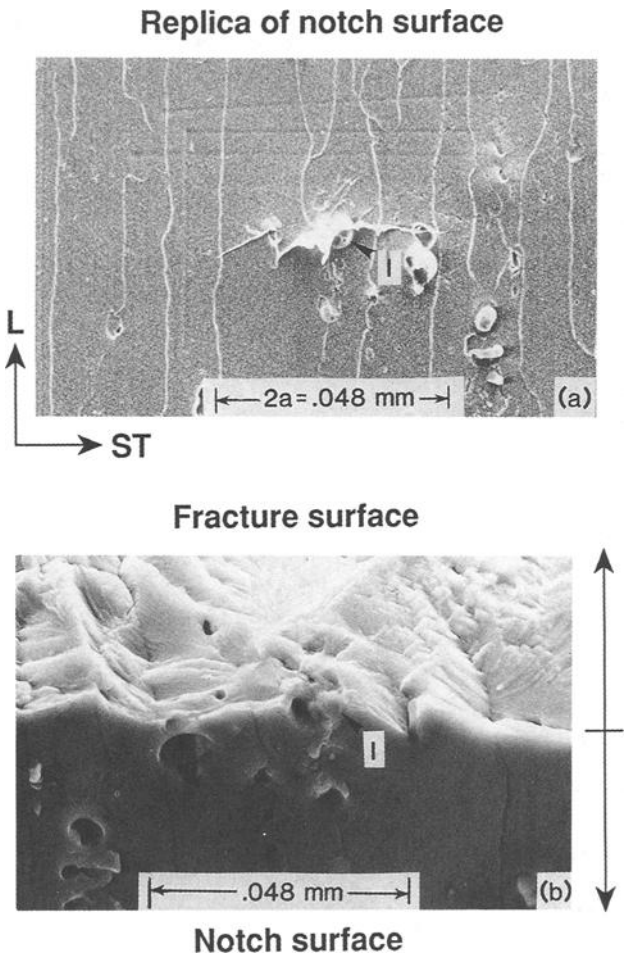

FIG. 9—*SEM micrograph of* (a) *replica of small-crack and* (b) *portion of SEN specimen fracture surface and notch root surface corresponding to replica region for 7075-T6 aluminum.*

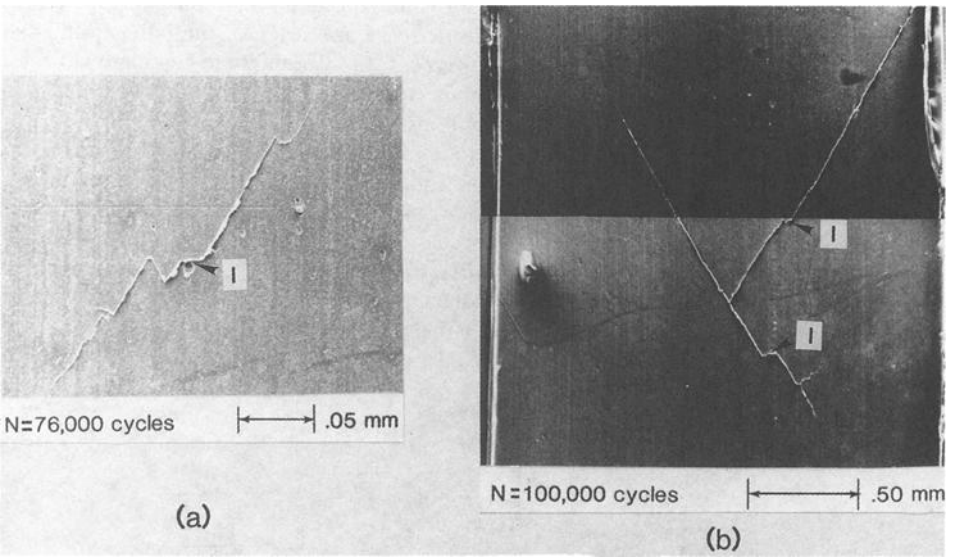

FIG. 10—*SEM replica micrographs of* (a) *small crack at inclusion particle site and* (b) *intersection of crack, from* (a), *with a second crack later in fatigue test. Material is 2090-T8E41 and points labeled T indicate crack initiation sites.*

appear reversed from left to right. The upper half of Fig. 9*b* shows a portion of the fracture surface near the crack initiation site. Tests conducted on the aluminum lithium alloy, 2090-T8E41, under $R = -1$ loading resulted in highly angled crack growth across the major portion of the notch root as illustrated by the replica photographs in Fig. 10. Crack initiation in most cases could still be associated with inclusion particle sites. The cracks propagated at an angle of about 35° to the load axis and were more difficult to observe on the replicas than cracks in other materials that grew essentially normal to the load axis. The difficulty was due to the decrease in local crack opening normal to the plane of the crack as the crack orientation rotated away from the plane normal to the load axis. Less acetate penetrates into this narrow opening, and the ridge left on the replica surface is less prominent. This effect is illustrated in region C of Fig. 5; this crack segment deviates substantially from the overall crack orientation normal to the load axis, and the crack image is less distinct. The 2090 specimen shown in Fig. 10*b* contained two cracks that initiated at the points labeled I. After 100 000 cycles the cracks are large (≈1 mm), and the crack-tip stress intensity factor levels are influenced by the presence of the other crack, as discussed in Appendix A. Earlier in the test, at 76 000 cycles, when the upper crack was about 175 μm long (see Fig. 10*a*), the crack growth rates would not be affected by crack interaction.

The target alloy in terms of strength for the development of 2090-T8E41 was the high strength 7075-T6. Despite differences in crack propagation orientation in the two alloys, the small-crack growth rates, when calculated in both alloys for crack lengths a measured normal to the load axis, were in good agreement, as previously reported by Swain et al. [*16*]. Results, da/dN versus ΔK, for the two alloys are given in Fig. 11 along with the large through-crack data from MT specimens, also tested under $R = -1$ loading. In the MT specimens of 2090-T8E41 the cracks grew normal to the loading axis. Note that the data from the SEN or small-crack specimens blends with data from the respective MT or large-crack specimens for large ΔK, above 10 MPa · $m^{1/2}$. For crack growth data from similar SEN specimens of

2090-T8E41 under $R = 0$ and -1 loading, Mazur and Rudd [*17*] calculated a mixed mode ΔK using equations for Mode I and Mode II and the actual length of the angled cracks. Their results show a poor correlation of the SEN data for angled cracks with MT data for ΔK above the large crack threshold; whereas, when the same data were analyzed using the crack length normal to the load axis and the Mode I equation for ΔK, good agreement was found. Although it is not fully understood why the Mode I and projected (or normal) crack length calculations give a better correlation for the highly angled cracks, it is a simpler calculation and allows for direct comparison with data for other aluminum alloys. Note that the replicas form a permanent record of crack growth and orientation, so that a future analysis using a different set of ΔK equations could be performed.

Replication Effects on Fatigue Life

For each of the alloys whose small-crack growth behavior was investigated, a number of preliminary fatigue life tests were conducted in advance on SEN specimens to aid in the selection of applied stress levels and replica intervals for the small-crack growth tests. A sample of this data for 2024-T3, for fatigue life tests and for replica tests, was presented in Fig. 3. In the small-crack growth tests, replicas were taken at intervals of load cycles until the crack grew across the root of the notch and became a through crack. Continued cycling of these specimens to failure yielded additional fatigue life data for the SEN specimens. As a general rule, these replica specimens had fatigue lives that fit into the scatter of life values determined from the preliminary *SN* tests. An example of this behavior is shown in Fig. 12 for 4340 steel under $R = -1$ loading. However, for Minitwist variable amplitude load

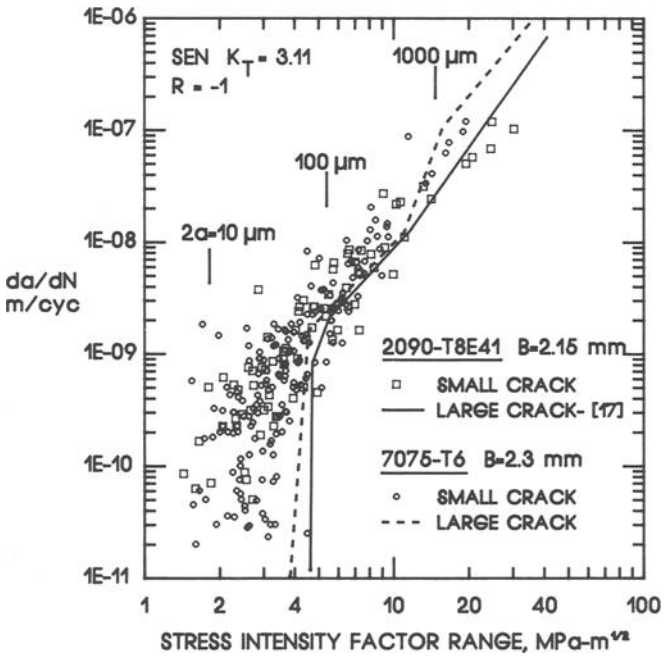

FIG. 11—*Small- and large-crack growth data for 2090-T8E41 and 7075-T6 under the Minitwist spectrum. Correlation of surface crack length and stress intensity factor range for the small-crack-test data points are indicated by the vertical line segments.*

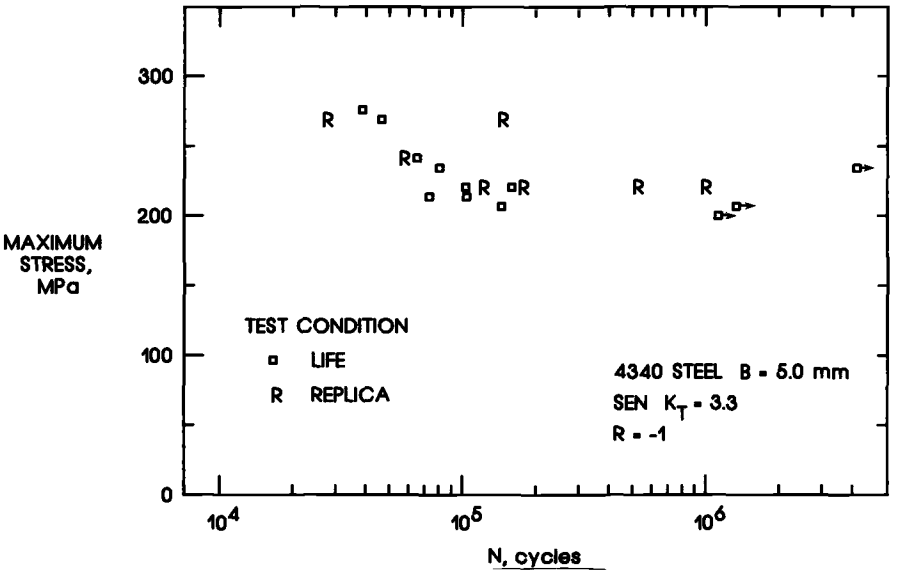

FIG. 12—*Fatigue life data for SEN specimens of 4340 steel under* R = −1 *loading.*

spectrum tests conducted on 7075-T6, fatigue life for replica tests did not agree with life for tests with no replicas.

Fatigue life data for 7075-T6 under the Minitwist spectrum are shown in Fig. 13 plotted as maximum stress level in the entire spectrum versus the number of load changes. A sequence of prescribed load changes (peaks and troughs) makes up the variable amplitude load spectrum. In addition to the eleven conventional fatigue life tests, a total of five small-crack growth tests were conducted at two stress levels. The latter tests, where replicas were taken, produced longer fatigue lives at both stress levels than were observed for tests where no replicas were taken. Additional tests were undertaken for this material under Minitwist loading at an S_{max} of 205 MPa in an attempt to understand the source of this increase in fatigue life. In two tests cycling was stopped periodically after the same cyclic interval used in the replica tests, and the load was held for 10 min at the replica load (approximately 60% of P_{max}), but no replica was made. The resulting lives were slightly less than those for the conventional fatigue life tests. For the remaining two specimens, the notch root was bathed with acetone twice during the 10 min the specimen was held at the replica load. The fatigue lives in this case agreed with those where replicas were taken. It appears that the increase in life exhibited by the replica test specimens in Fig. 13 is a result of a chemical effect connected with the presence of acetone, rather than a purely mechanical effect from holding the cracked specimen under a constant tensile load.

The sensitivity of fatigue life in 7075-T6 to elements of the replica process may well be attributed to environmental effects (the tests were all conducted nominally in lab air). Gao et al. [*18*] have reported an increase in crack growth rate for this alloy with increasing water vapor pressure. They also found crack growth rates in moist air to be greater than those in vacuum, argon, or oxygen. These increased crack growth rates in the presence of moisture were attributed to a hydrogen embrittlement mechanism. Given the sensitivity of 7075-T6 to water vapor, it is presumed that increased fatigue life by replication is due to a reduced environmental effect produced by the introduction of acetone. The fatigue life tests serve

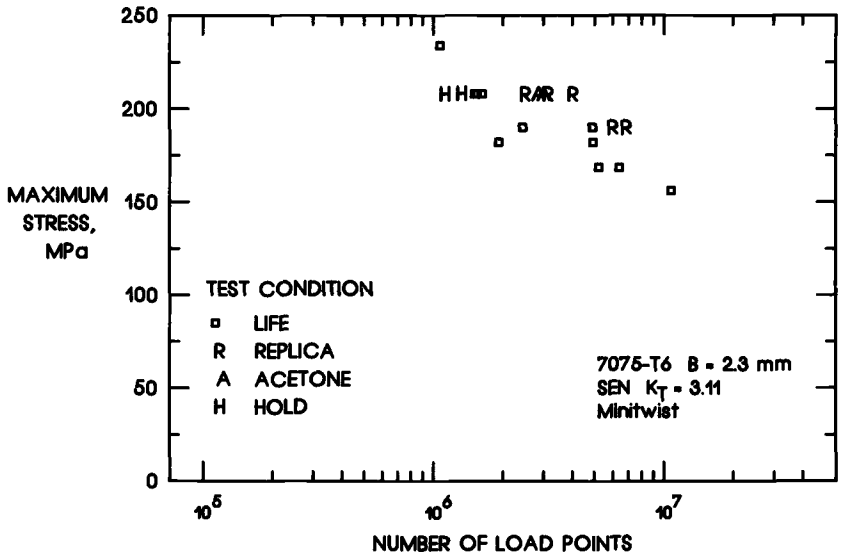

FIG. 13—*Fatigue life data for SEN specimens of 7075-T6 under the Minitwist spectrum.*

as a baseline condition of water vapor exposure. Tests with a hold time under load have equal or increased access of water vapor to the crack tip resulting in a slight decrease in life. In replica tests, or when the hold time includes bathing the notch surface in acetone, the water vapor concentration at the crack tip may be reduced, thereby slowing crack growth rates and increasing fatigue life.

Fatigue life tests, with and without taking replicas were also conducted under Minitwist loading on a clad Chinese alloy, LC9-CS. This alloy is nearly identical in composition and microstructure to 7075-T6 with the addition of a 50-μm cladding layer on each sheet surface. Crack initiation occurs from slip bands in the low-strength ductile cladding layer producing corner cracks, rather than the preponderance of surface cracks initiating at inclusion particle sites found in 7075-T6 (and all the other alloys tested). Figure 14 shows a crack which initiated in the cladding layer and has grown through several grains of the base alloy. Figure 15 gives fatigue lives (*SN* tests) and small-crack growth test lives (with replicas) for the clad material under the Minitwist spectrum. In this case, where corner cracks are prevalent, there is no consistent difference between cyclic life with and without replicas. The seeming indifference to the effects of acetone on the crack tip in LC9-CS may be due to corner crack geometry. Here, replication is performed on one surface allowing the crack tip to be exposed to water vapor environment through the side of the specimen. The increase in life for 7075-T6 using replicas may also be due to an increase in number of cycles to crack initiation at inclusion particles. This might not affect LC9-CS because crack initiation in this alloy always occurs in the ductile cladding layer.

Brown and Smith [*19*] reported on the effect of hold time on fatigue life of commercially pure titanium and of Ti-6Al-4V with various heat treatments. The hourglass specimens were electropolished then tested at 140 Hz under axial loading at $R = 0$. Testing was halted at mean load every 5% of expected life to take an acetate replica using acetone. For all materials fatigue life increased for specimens where replicas were taken. This follows the tendency shown by 7075-T6 under Minitwist loading. However, one test result, on as-received Ti-6Al-4V using hold times but taking no replicas, agreed with the replica test life. This result

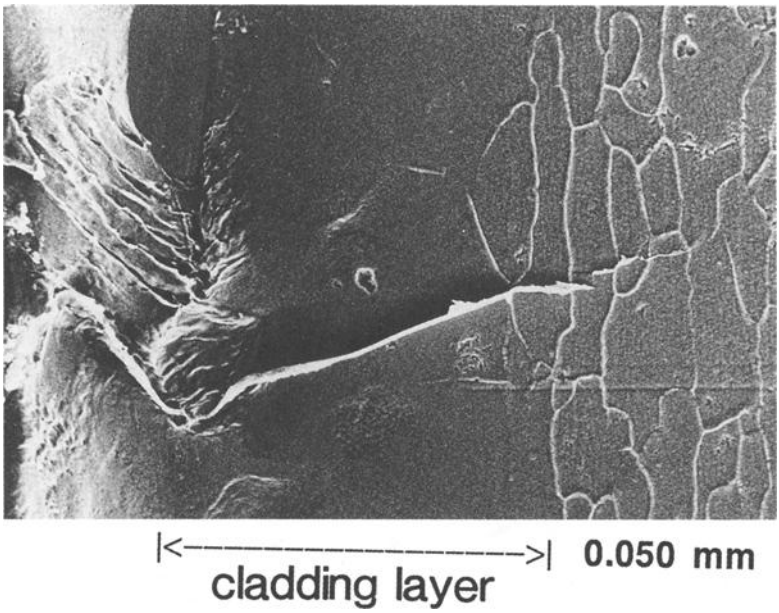

FIG. 14—*SEM micrograph of replica showing small corner crack in LC9-CS aluminum.*

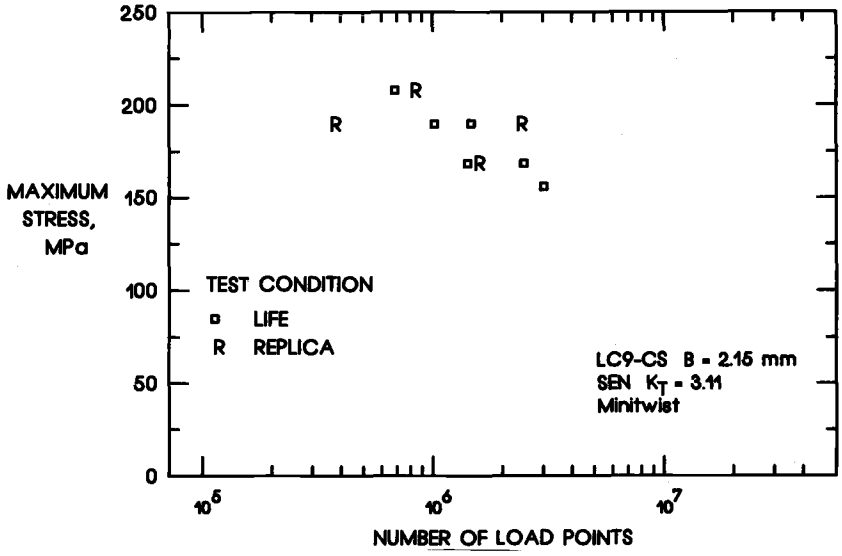

FIG. 15—*Fatigue life data for SEN specimens of LC9-CS under the Minitwist spectrum.*

indicates that the acetone itself played no part in the increased life. The authors attributed the increase in fatigue life, due to rest periods, to localized strain aging, brought on by increased oxygen or nitrogen pickup at surface slip bands, developed before crack initiation, and at the crack-tip plastic zone, developed during crack growth.

Summary Appraisal of Replication Method

In the course of the preceding discussion on procedures and results for the replication method, a number of strong and weak points have been highlighted. It seems desirable, however, to summarize those points and mention some additional features that should be considered before choosing to use this technique either as a primary or back-up crack growth monitoring tool.

Advantages

1. The growth of naturally initiating small cracks (as small as 5 μm) can be studied, as it is not necessary to know the crack location before it has grown to an easily detectable size.
2. Replicas can be made on specimens of various geometrical configurations, that is, notched, cylindrical, or flat.
3. Little specialized equipment is necessary to make or analyze the replica data, although better resolution of crack length is possible with the SEM than the OM.
4. Multiple-crack growth on a single specimen is easily monitored, and information concerning crack spacing is available for crack interaction analysis.
5. The replicas form a "permanent" record of the crack growth history, including crack length, orientation, and neighboring cracks.
6. Photomicrographs of the crack morphology indicate crack initiation mechanisms and interaction of the crack tip with microstructure.

Disadvantages or Limitations

1. Taking and analyzing the replicas is very labor intensive with no way to automate the process. The process of taking the replica is on the order of the time taken to run the intervening cyclic loading interval.
2. Crack growth information obtained from the replicas is only for the surface of the specimen. Information concerning growth below the surface is obtained independently by sectioning or breaking open specimens containing small cracks.
3. Testing in environments other than room temperature lab air is difficult.
4. The fatigue life of some materials under certain loading conditions, such as 7075-T6 cycled under Minitwist, has been shown to exhibit different total fatigue life behavior when the test is periodically interrupted so that replicas can be taken in comparison to a continuous fatigue life test. The reason for this behavior is not known, but the experimenter should take care to conduct both continuously cycled fatigue life tests and the replica (interrupted) fatigue life tests to establish any discrepancy.

Acknowledgments

The author wishes to acknowledge the support of the NASA Langley Research Center. This work was performed at the NASA facility under the Lockheed Engineering and Sciences Company contract. Thanks are also given to NASA technical support staff, C. D. Griffin, W. T. Howard, and O. White, for their efforts while conducting the replica test programs.

APPENDIX A

Noninteraction Criteria

The common occurrence of multiple cracks initiating and growing at the root of the notch in the SEN specimen prompted the development of the following criteria for flagging cases where the growth of one crack was likely to be influenced by the size and proximity of neighboring cracks [*12*]. The system for rejecting crack growth rate data as a result of crack interaction is described in Figs. 16 through 18. Three cases were considered when data are rejected:

1. When cracks are essentially collinear (such as Cracks 1 and 2) and when the distance $d_{1,2}$ between the adjacent crack tips is less than the length of the largest L_1, then subsequent data from both cracks are rejected. Here it is expected that as the crack tips approach each other the rate of growth of each would be accelerated.
2. When cracks intersect, the same line parallel to the loading axis of the specimen (such as Cracks 1 and 3) and when the distance between the two cracks $h_{1,3}$ is less than the length of the largest L_1, then subsequent data from Crack 3 is rejected. Here the larger crack L_1 would be expected to relieve stresses in the region of the shorter crack L_3 and, consequently, the rate of growth of Crack 3 would slow down.
3. After two collinear cracks have joined (such as Cracks 1 and 2), crack growth rate data are rejected from both cracks until the combined crack length L is twice the length of the combined crack immediately after joining $(L_1 + L_2)$, as illustrated in Fig. 17. This is to allow for the development of a full crack front for the combined crack.

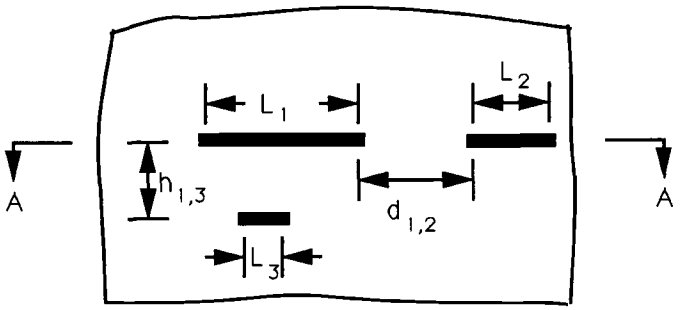

FIG. 16—*Multicracks at notch root.*

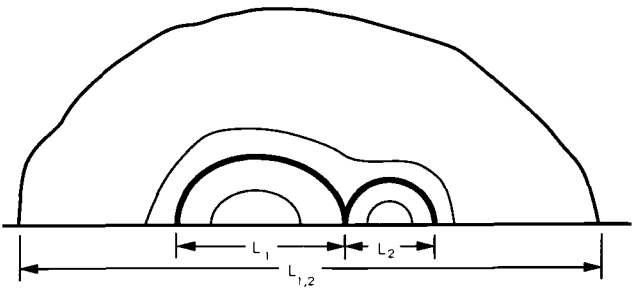

FIG. 17—*Definition of crack "noninteracting" criteria for coalescence and crack shadowing: interacting surface cracks for* $d_{1,2} = 0$ *(section A-A).*

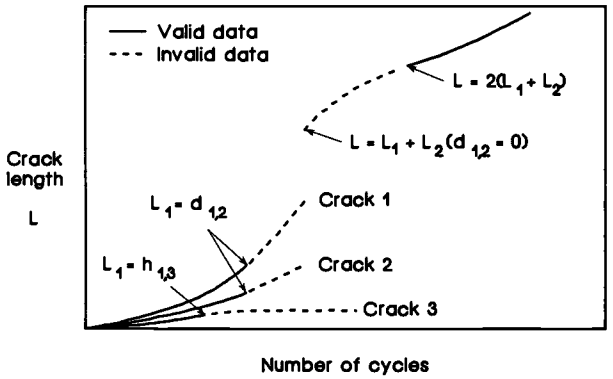

FIG. 18—*Definition of valid and invalid crack growth data.*

APPENDIX B

Approximate Stress-Intensity Factors for a Surface Crack and Through Crack at a Semi-Circular Notch

An approximate stress-intensity factor equation for a semi-elliptical surface crack located at the center of a semi-circular edge notch subjected to remote uniform displacement is

$$K = S\sqrt{(\pi a/Q)}\, F_{sn}\left(\frac{a}{c}, \frac{a}{t}, \frac{r}{t}, \frac{r}{w}, \frac{c}{w}, \phi\right) \tag{3}$$

for $0.2 < a/c < 2$, $a/t < 1$, $0.5 < r/t < 3$, $(c + r)/w < 0.5$, and $-\pi/2 \leq \phi \leq \pi/2$. (Note that here t is defined as one-half of the full sheet thickness for a surface crack and as full sheet thickness for a corner crack.) The shape factor Q is given by

$$Q = 1 + 1.464\left(\frac{a}{c}\right)^{1.65} \quad \text{for } \frac{a}{c} \leq 1 \tag{4a}$$

$$Q = 1 + 1.464\left(\frac{c}{a}\right)^{1.65} \quad \text{for } \frac{a}{c} > 1 \tag{4b}$$

and

$$F_{sn} = \left\{M_1 + M_2\left(\frac{a}{t}\right)^2 + M_3\left(\frac{a}{t}\right)^4\right\} g_1 g_2 g_3 g_4 f_\phi f_w \tag{5}$$

For $a/c \leq 1$

$$M_1 = 1 \tag{6}$$

$$M_2 = \frac{0.05}{0.11 + \left(\frac{a}{c}\right)^{3/2}} \tag{7}$$

$$M_3 = \frac{0.29}{0.23 + \left(\frac{a}{c}\right)^{3/2}} \tag{8}$$

$$g_1 = 1 - \frac{\left(\frac{a}{t}\right)^4 \left(2.6 - 2\frac{a}{t}\right)^{1/2}}{1 + 4\frac{a}{c}} |\cos\phi| \tag{9}$$

$$g_2 = \frac{1 + 0.358\lambda + 1.425\lambda^2 - 1.578\lambda^3 + 2.156\lambda^4}{1 + 0.08\lambda^2} \tag{10}$$

$$\lambda = \frac{1}{1 + \frac{c}{r}\cos(0.9\phi)} \tag{11}$$

$$g_3 = 1 + 0.1(1 - \cos\phi)^2\left(1 - \frac{a}{t}\right)^{10} \tag{12}$$

$$g_4 = K_T\left[0.36 - \frac{0.032}{\left(1 + \frac{c}{r}\right)^{1/2}}\right] \tag{13}$$

The finite-width correction f_w was

$$f_w = 1 + 2.7\gamma^2 - 3.5\gamma^4 + 3.8\gamma^6 \quad \text{for } h/w = 2 \text{ (aluminum specimen)} \tag{14a}$$

$$f_w = 1 + 3.93\gamma^2 - 5.59\gamma^4 + 5.93\gamma^6 \quad \text{for } h/w = 3 \text{ (steel specimen)} \tag{14b}$$

where

$$\gamma = \frac{c + r}{w}\left(\frac{a}{t}\right)^{1/2} \tag{15}$$

The function f_ϕ is given by

$$f_\phi = \left[\left(\frac{a}{c}\right)^2 \cos^2\phi + \sin^2\phi\right]^{1/4} \tag{16}$$

For $a/c > 1$

$$M_1 = \left(\frac{c}{a}\right)^{1/2} \tag{17}$$

The functions M_2, M_3, g_1, g_2, γ, g_3, g_4, and f_w are given by Eqs 7 through 14, respectively, and f_ϕ is given by

$$f_\phi = \left[\left(\frac{c}{a}\right)^2 \sin^2\phi + \cos^2\phi\right]^{1/4} \tag{18}$$

When the surface-crack half-length a reaches one-half sheet thickness t, the crack is assumed to be a through crack of length c. The stress-intensity factors for a through crack emanating from a semi-circular notch subjected to remote uniform displacement are then used. An equation fit to these results is

$$K = S\sqrt{(\pi c)}\, F_n\left(\frac{c}{w}, \frac{r}{w}\right) \tag{19}$$

for $(c + r)/w < 0.8$. The boundary correction factor F_n is

$$F_n = f_1 g_4 f_w \tag{20}$$

where g_4 and f_w are given by Eqs 13 and 14, respectively. The function f_1 is given by

$$f_1 = 1 + 0.358\lambda + 1.425\lambda^2 - 1.578\lambda^3 + 2.156\lambda^4 \tag{21}$$

where

$$\lambda = \frac{1}{1 + \frac{c}{r}}$$

References

[1] Venketeswara Rao, K. T. and Ritchie, R. O., "Mechanical properties of Al-Li alloys, Part 2-Fatigue Crack Propagation," *Materials Science and Technology*, Vol. 5, 1989, pp. 896–907.

[2] Birt, M. J. and Beevers, C. J., "The Fatigue Response of the Aluminum-Lithium Alloy, 8090," *Proceedings of the Fifth International Aluminum Lithium Conference*, T. H. Sander and E. A. Starke, Eds., 1989, pp. 983–992.

[3] Bolingbroke, R. K. and King, J. E., "The Effect of Microstructure on the Surface Crack Length: Crack Depth Relationship for Short Cracks," *Proceedings of the Third International Conference on Fatigue and Fatigue Thresholds*, R. P. Gangloff, R. O. Ritchie, E. A. Starke, and J. A. Wert, Eds., 1987, pp. 281–290.

[4] Brown, C. W. and Smith, G. C., "A Two Stage Plastic Replication Technique for Monitoring Fatigue Crack Initiation and Early Crack Growth," *Advances in Crack Length Measurement*, C. J. Beevers, Ed., Engineering Materials Advisory Services Ltd., 1982, pp. 41–52.

[5] Brown, C. W., King, J. E., and Hicks, M. A., "Effects of Microstructure on Long and Short Crack Growth in Nickel Base Superalloys," *Metal Science*, Vol. 18, 1984, pp. 374–380.

[6] Lankford, J., "The Growth of Small Fatigue Cracks in 7075-T6 Aluminum," *Fatigue of Engineering Materials and Structures*, Vol. 5, No. 3, 1982, pp. 233–248.

[7] Lankford, J., "Initiation and Early Growth of Fatigue Cracks in High Strength Steel," *Engineering Fracture Mechanics*, Vol. 9, No. 3, 1977, pp. 617–624.

[8] Funkenbusch, A. W. and Coffin, L. F., "Low Cycle Fatigue Crack Nucleation and Early Growth in Ti-17," *Metallurgical Transactions A*, Vol. 9A, 1978, pp. 1159–1167.

[9] Dowling, N. E., "Crack Growth During Low Cycle Fatigue of Smooth Axial Specimens," *Cyclic Stress-Strain and Plastic Deformation Aspects of Fatigue Crack Growth, STP 637*, American Society for Testing and Materials, Philadelphia, 1977, pp. 97–121.

[10] McClung, R. C. and Sehitoglu, H., "Closure Behavior of Small Cracks under High Strain Fatigue Histories," *Mechanics of Fatigue Crack Closure, STP 982*, J. C. Newman, Jr. and W. Elber, Eds., American Society for Testing and Materials, Philadelphia, 1988, pp. 279–299.

[11] Newman, J. C., Jr., Swain, M. H., and Phillips, E. P., "An Assessment of the Small Crack Effect for 2024-T3 Aluminum Alloy," *Small Fatigue Cracks*, R. O. Ritchie and J. Lankford, Eds., The Metallurgical Society, 1986, pp. 427–452.

[12] Newman, J. C., Jr. and Edwards, P. R., "Short Crack Growth Behaviour in an Aluminum Alloy–An AGARD Cooperative Test Programme," AGARD-R-732, 1988.

[13] Swain, M. H., Everett, R. A., Jr., Newman, J. C., Jr., and Phillips, E. P., "The Growth of Short Cracks in 4340 Steel and Aluminum Lithium 2090," *Short-Crack Growth Behaviour in Various Aircraft Materials*, P. R. Edwards and J. C. Newman, Jr., Eds., AGARD-R-767, 1990, pp. 7.1–7.30.

[14] Henry, M. R., "A Technique for Monitoring Time Dependent Surface Damage," General Electric Report 71-C-338, 1971, pp. 1–7.

[15] Goldstein, J. I., Newbury, D. E., Echlin, P., Joy, D. C., Fiori, C., and Lifshin, E., *Scanning Electron Microscopy and X-Ray Microanalysis*, Plenum Press, New York, 1981.

[16] Swain, M. H., Newman, J. C., Jr., Everett, R. A., and Phillips, E. P., "Fatigue Crack Initiation and Small Crack Growth in Several Airframe Alloys," *Third International Conference on Fatigue and Fatigue Thresholds*, Engineering Materials Advisory Services, Ltd., 1987, pp. 1079–1084.

[17] Mazur, C. J. and Rudd, J. L., "Determination of the Short Crack Effect in 2090-T8E41 Aluminum Lithium," *Short-Crack Growth Behaviour in Various Aircraft Materials*, P. R. Edwards and J. C. Newman, Jr., Eds., AGARD-R-767, 1990, pp. 2.1–2.11.

[18] Gao, M., Pao, R. S., and Wei, R. P., "Chemical and Metallurgical Aspects of Environmentally Assisted Fatigue Crack Growth in 7075-T651 Aluminum Alloy," *Metallurgical Transactions A*, Vol. 19A, 1988, pp. 1739–1750.

[19] Brown, R. and Smith, G. C., "A Note on the Influence of Rest Periods on the Fatigue Endurance of a Titanium Alloy," *Fatigue of Engineering Materials and Structures*, Vol. 7, No. 3, 1984, pp. 229–235.

James M. Larsen,[1] *Jay R. Jira,*[1] *and Kakkaveri S. Ravichandran*[1]

Measurement of Small Cracks by Photomicroscopy: Experiments and Analysis

REFERENCE: Larsen, J. M., Jira, J. R., and Ravichandran, K. S., "**Measurement of Small Cracks by Photomicroscopy: Experiments and Analysis,**" *Small-Crack Test Methods, ASTM STP 1149*, J. M. Larsen and J. E. Allison, Eds., American Society for Testing and Materials, Philadelphia, PA, 1992, pp. 57–80

ABSTRACT: A procedure for using photomicroscopy to record the growth of small fatigue cracks is presented. Using a specially designed fatigue specimen, the method is applicable to both naturally initiated cracks and cracks initiated from a small electro-discharge machined notch. Components of the experimental apparatus, which are low cost and readily available, include a standard metallurgical microscope, a 35-mm camera with bulk film capability, an electronic flash, and a microcomputer to control the fatigue machine and record test data. The photographic record provides a direct measurement of surface crack length and documents crack interactions with microstructural features; measurement precision less than 1 μm is possible. Following a test, the photographs of small cracks are projected on a computer digitizing tablet for convenient measurement of crack length. The crack length data are then combined with fatigue cycle-count data and reduced to the form of da/dN versus ΔK (or some other appropriate crack driving force). The capabilities of the photomicroscopic method are illustrated using typical data from specimens of the alloy Ti-6Al-2Sn-4Zr-6Mo, and an assessment is made of the practical advantages and limitations of the technique. Finally, some commonly unrecognized pitfalls that routinely arise in the analysis of small-crack data are discussed, and an alternative procedure for the analysis of such data is presented.

KEY WORDS: crack propagation, fatigue (materials), fracture mechanics, mechanical properties, microcracks, microscopy, short cracks, small cracks, test methods

A variety of imaging techniques have been used to acquire data on the growth of small fatigue cracks. Probably the most common approach involves the creation of an acetate replica of the specimen surface, which may be removed from the specimen and inspected using either optical or scanning electron microscopy (SEM) (see [Ref *1*] for a recommended replication practice). Since the replication process must be performed at periodic intervals throughout a small-crack fatigue test, the process is labor intensive, and if the replica is to be inspected using an SEM, the time involved in acquiring the small-crack data is significantly greater than with optical methods. Direct, in-situ observation of small cracks in fatigue has been performed in the SEM, including the use of stereoimaging to record details of the three-dimensional displacement fields surrounding a small crack (see [Ref *2*] for review). Although sophisticated, these experiments are time consuming and costly, and the level of detail they provide is often beyond the requirements of a given small-crack research project.

As an alternative to replication or SEM imaging methods, photomicroscopic techniques have been employed to record the initiation [*3*,*4*] and growth [*5*,*6*] of small fatigue cracks.

[1]Materials research engineer, materials engineer, and National Research Council research associate, respectively, Materials Directorate, Wright Laboratory, WL/MLLN, Wright-Patterson Air Force Base, OH 45433-6533.

This paper presents a recommended procedure for conducting small-crack experiments using photomicroscopy, including specific guidelines for specimen design and preparation, test execution, and data acquisition and analysis.

Experimental Procedure

Test Specimen

The use of photomicroscopy to record the growth of small fatigue cracks is greatly simplified by the design of a specimen specifically configured for easy microscopic examination of the surface. To simplify the testing procedure, the specimen should localize crack initiation within a relatively small, microscopically accessible region, and the region should be sufficiently flat to permit the formation of a well-focused image. Cylindrical or hourglass fatigue specimens, conventionally used for fatigue testing, are particularly unsuited for in-situ microscopic inspection and photography, because only a limited region of the specimen can be sharply focused at one time. Moreover, crack initiation can occur anywhere around the circumference of the specimen gage section, making it necessary to rotate the specimen or the microscope for complete inspection.

The small-crack specimen and testing procedure described in the following discussion were tailored to facilitate natural initiation of small surface cracks on a specimen surface that is free from residual stresses. Although corner cracks could be studied with photomicroscopy, the current discussion focuses on part-through cracks. The specimen, shown in Fig. 1, is a

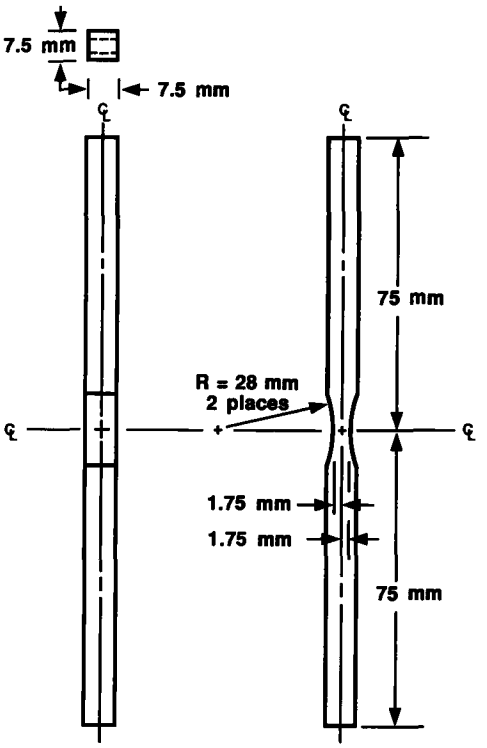

FIG. 1—*The small-crack fatigue specimen.*

square bar containing a mild notch with a stress concentration factor K_t equal to 1.037, as determined by two-dimensional finite-element stress analysis [5]. Thus, the through-thickness stress in the gage section is essentially uniform, while the reduced gage section serves to localize crack initiation within a small region. Initiation of cracks at specimen corners occurs occasionally and may be undesirable, if the objective of the research is to study surface cracks. Experience with this type of specimen on a variety of materials indicates that edge or corner cracks are responsible for specimen failure approximately 20% of the time. On these specimens it was often possible to acquire a significant amount of data on other small surface cracks within the gage section before the corner crack produced final failure. A recommended procedure, however, is to machine a number of additional specimens and discard the specimens having dominant corner cracks, rather than spending valuable test time on specimens with such undesirable cracks.

A key attribute of the specimen is its suitability for use with optical microscopy. The radius of curvature of the specimen notch is sufficiently gentle to allow sharply focused images to be formed at all microscope magnifications. Moreover, since the base of the notch is relatively flat, the image formed in a reflecting microscope is well illuminated across the entire field of view. Under such lighting, crack detection and the ability to distinguish between slip bands and cracks is greatly enhanced when the specimen is viewed under load, because the open crack appears black on the otherwise bright, reflective specimen surface. With oblique illumination, which produces a dark-field image, detection of the smallest cracks is much more difficult. In many instances, viewing under polarized light aids crack detection and enhances the ability to distinguish between slip bands and cracks.

Specimen Surface Preparation and Residual Stress Characterization

Preparation of the specimen surface involves a number of considerations, because the growth rates of small surface cracks may be significantly influenced by the surface condition [7,8]. If the intent of the research is to simulate crack initiation and growth for a surface that has undergone a specific manufacturing process, then the surface should be prepared by the same process, and the roughness and residual stress state of the surface should be thoroughly characterized for use in analysis of the data. To evaluate inherent material behavior, however, residual stresses and surface roughness caused by machining should be eliminated.

For example, it is well known [9,10] that the character (tensile or compressive) and magnitude of surface residual stresses resulting from a particular finish-grinding procedure depend strongly on parameters such as the type and microstructure of the grinding media, the grinding speed, and the grinding force. An alternative to grinding, or other mechanical machining methods, is to fabricate the specimens by electro-discharge machining (EDM). However, the EDM operation also induces surface residual stresses caused by local melting/solidification and phase transformations that occur in the surface layer of material [11].

To document the nature and the level of surface residual stresses produced by various fabrication practices, X-ray diffraction measurements of residual stresses were obtained on Ti-6Al-2Sn-4Zr-6Mo alloy specimens finished by a variety of methods. The level of residual stress was measured as a function of depth [12] on typical specimen surfaces prepared by four methods: low stress grinding, EDM, EDM followed by hand polishing, and EDM followed by electropolishing. The results are presented in Fig. 2, along with similar measurements on the same material prepared by careful milling [13]. As shown, the milling procedure produced the most extreme level, and the greatest depth, of residual stress. Milling, EDM followed by hand polishing, and low stress grinding processes produced successively lower levels of compressive surface residual stress, while the EDM-finished

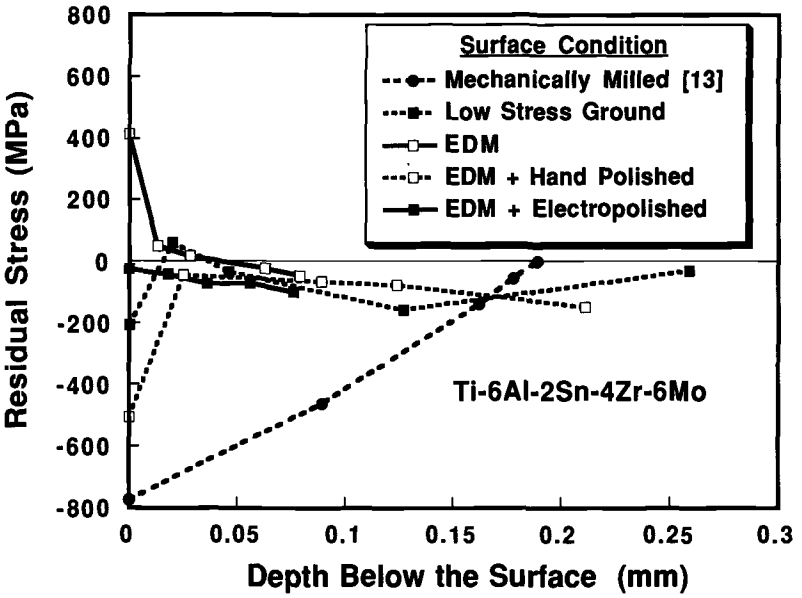

FIG. 2—*X-ray diffraction residual stress profiles obtained from the surface of specimens of Ti-6Al-2Sn-4Zr-6Mo produced by various machining methods.*

specimen exhibited a shallow tensile stress. The EDM followed by electropolishing operation essentially eliminated the surface residual stress.

Recognizing that surface residual stresses influence both the initiation and propagation of small fatigue cracks, and that such stresses appear to be produced by standard machining processes (chemical milling may be an exception), it is recommended that small-crack specimens be electropolished to a depth sufficient to remove the affected surface layer of the material. Since the depth of such a layer depends on many factors, it is recommended that surface residual stress be measured to determine the depth of electropolishing required. Moreover, to minimize the depth of the surface layer that must be removed by electropolishing, it is recommended that specimens be fabricated by electro-discharge machining. A recommended procedure for electropolishing small-crack specimens is presented in the Appendix.

In addition to eliminating surface residual stresses and machining marks, the electropolishing also produces a highly reflective surface, enhancing the detection and resolution of small surface cracks, while highlighting the material's microstructure. If desired, the gage section may be etched to further reveal the microstructure, but heavy etching often exacerbates the difficulties of crack detection and photography, because the small cracks may be camouflaged by detailed microstructural features. It is often desirable, therefore, to test unetched specimens.

Experimental Apparatus for Small-Crack Fatigue Testing

The equipment used by the authors for photomicroscopic recording of small cracks includes a metallurgical microscope, a 35-mm camera with a 250-frame film magazine, motor drive and power supply, an electronic flash, a microcomputer with analog-to-digital (A/D) and

digital-to-analog (D/A) interface electronics, and a standard servo-hydraulic testing machine with hydraulic grips. Figure 3 is a photograph of the camera and test machine. As shown, the microscope and camera are supported by a relatively rigid fixture. In spite of its rigidity, the stiffness of this fixture was found to be insufficient to prevent occasional vibrations from degrading the sharpness of photographs taken using a standard incandescent lamp. By using an electronic flash, which has a duration considerably less than 1/1000 s, sharp photographs were easily achieved, making a highly rigid camera support unnecessary. It is important, however, that the support be secure from permanent movement to avoid loss of focus of the microscope over time. In practice, fatigue cycling is interrupted for approximately 1 s, allowing test machine vibrations to subside, and the photograph is exposed. The hydraulic grips used to hold the specimen simplify test setup procedure and specimen design requirements. V-shaped grooves machined on the grip faces were used to center the specimen.

To automate the test procedure, a standard microcomputer was used to control the test machine, operate the camera, and collect pertinent data. Computerization of the testing process is not a necessity, but it eliminates much of the tedium involved in data acquisition and record keeping. With limited effort, computer software routinely used to control fatigue crack growth rate testing may be modified to accommodate the requirements of small-crack testing and photomicroscopy. The computer controls fatigue cycling and allows testing to be periodically interrupted, while the specimen is briefly held under tensile load and a photograph is taken. The software algorithm controls the camera by sending a signal to the camera's motor drive power supply, which triggers the camera and the synchronized electronic flash. The computer records the photograph frame number, fatigue cycle count, time,

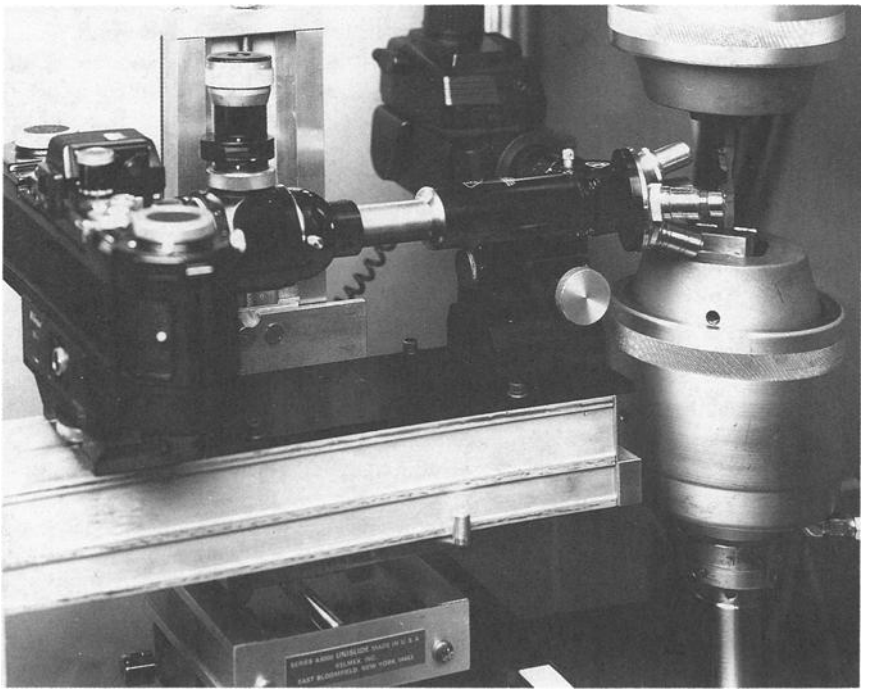

FIG. 3—*The photomicroscopic test system.*

and occasional notations by the operator. Thus, a detailed record of testing events is easily maintained to aid in subsequent analysis of the data.

Determination of Crack Shape

The photographic record of crack propagation provides a measurement of surface crack length ($2c$) but not crack depth (a), and thus the crack shape, or aspect ratio (a/c), remains unknown. To examine the shape of a small crack in some materials, selected spectrum loading events may be used to mark the position of the crack front for later fractographic inspection [*14*]. In other alloys, this may not be effective, and an alternative approach is required. In a variety of titanium alloys, crack shape can be delineated by a heat-tinting procedure wherein the test is temporarily interrupted, and the specimen is removed and heated in air to visibly oxidize the fracture surface of the existing fatigue crack(s). The specimen is subsequently fractured, revealing the shape of the heat-tinted crack, which is measured using a light microscope. The use of polarized light may significantly enhance the contrast of the oxidized fracture surface. The optimum time/temperature conditions for heat tinting a given alloy may be determined from trial thermal exposures of a series of cross-sectioned samples of the fracture surface of a large-crack fatigue specimen of the same material.

In some alloys, heat tinting can be accomplished without adversely affecting the material's microstructure or mechanical properties (for example, without aging). In this situation, heat tinting may be performed a number of times throughout the test by decreasing the temperature of each successive thermal exposure; this results in a series of progressively lighter fracture surface markings. Experience with titanium alloys, heat tinted for 1 hr at approximately 315°C, has shown no noticeable effect of heat tinting on the propagation of a small crack in an interrupted test. Recognizing, however, that heat tinting may influence subsequent growth of a small crack, it is advisable to heat tint a sample once only and avoid further fatigue testing. After heat tinting, the specimen is fractured under monotonic loading so that crack shape can be determined from optical measurements of the discolored surface. By collecting such data from a number of specimens, a relationship of crack shape as a function of crack size may be developed, which may be used as an indication of the shape of other cracks in the same material. As reported by a number of researchers [*15,16*], and shown in Fig. 4, the shapes of small surface cracks often remain approximately constant, independent of crack size. Although this may not be true for some large-grained or textured materials [*17*], or for cracks that initiate from inclusions [*18*], the crack-shape relationship provides valuable information for subsequent analysis of small-crack data.

Test Execution

Small cracks, whether they form on flat surfaces or within holes or notches, often initiate and propagate as surface cracks. Therefore, the following discussion will focus on a testing methodology developed for surface cracks, although, in principal, the photomicroscopic method is equally applicable to corner cracks. Moreover, the discussion will emphasize naturally initiated cracks, since these represent the smallest experimentally producible cracks.

Although photomicroscopy may be used to document crack initiation, the relatively large field of view that may be required limits the magnification that can be used (field of view = 1/magnification). For the specimen shown in Fig. 1, a 7.5-mm field of view corresponds to a magnification on the 35-mm film plane of 4.8 times. The usable resolution of the resulting image may be unsatisfactory for many small-crack research objectives. This problem may be diminished by reducing the specimen width, but to maximize resolution, the microscope

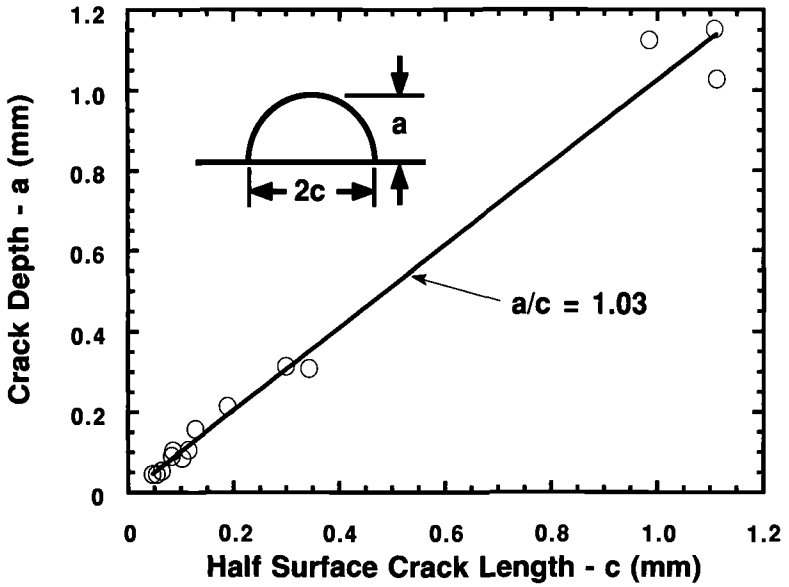

FIG. 4—*Crack-shape measurements from the heat-tinted fracture surfaces of a number of small-crack specimens of Ti-6Al-2Sn-4Zr-6Mo at different crack sizes.*

should be focused on a small crack to obtain a high-magnification image. This requires either that the crack initiation site be predetermined or that the small crack be visibly located before photographic data can be acquired. As will be discussed, the crack initiation site may be localized by positioning a small notch (or other stress riser, such as a laser weld bead) within the gage section. The smallest possible cracks, however, must be obtained by natural initiation, but visual detection of a small, naturally initiated crack may be a tedious process.

Visual detection of the initiation of a small crack is facilitated by inspection of the specimen under tensile load and the use of polarized light. By applying blocks of fatigue cycles and inspecting the specimen gage section under a tensile load (75% of maximum load is suggested), a small crack can usually be located relatively quickly, depending on the maximum stress and stress amplitude used. To aid in the initiation of small cracks at low levels of maximum stress, testing under tension-compression fatigue is recommended. Extensive experience with this approach on a number of materials has indicated that fatigue under a stress ratio, R ($\sigma_{min}/\sigma_{max}$), of -1.0 shortens the time required to initiate a small crack, without adversely influencing subsequent crack growth behavior when the specimen is tested under a higher (for example, positive) stress ratio. The tension-compression fatigue increases the strain range, which hastens crack initiation, but after the crack initiates, only the tensile portion of the stress range is effective in propagating the crack. A positive stress ratio may be used for crack initiation, but the resulting increase in the number of cycles required for crack initiation makes the crack detection process much more tedious.

To avoid load-history effects (for example, crack retardation), the maximum stress level used for crack initiation should not exceed the maximum stress chosen for subsequent fatigue testing. It is convenient to use maximum gage-section stress levels in the range $0.6 \leq \sigma_{max}/\sigma_y \leq 0.9$, where σ_y is the material's yield strength. Over this range the specimen is nominally elastic, while the number of fatigue cycles required to initiate a small crack is not excessive (in conventional titanium alloys tested under $R = -1.0$ fatigue with $\sigma_{max}/\sigma_y = 0.6$, 50-μm

cracks form within approximately 20 000 to 40 000 cycles). Lower stresses produce a few dominant cracks, while higher stresses tend to initiate multiple cracks. Obviously, depending on the objectives of the research, and the patience of the researcher, any stress level above the material's fatigue limit may be used.

As an alternative to natural crack initiation, a small notch formed by electro-discharge machining may serve as a crack initiation size. This eliminates the need to inspect the specimen surface, but the minimum size of the crack that forms is substantially larger than the minimum size of a naturally initiated crack. Typically, the smallest size of a naturally initiated crack that can be conveniently detected has a surface length of roughly 40 μm, and the initial size of a crack initiated from an EDM notch is limited by the notch dimension, which has a minimum practical length of approximately 100 to 200 μm. These practical limits on the notch size arise primarily from a desire to achieve a specific notch shape (for example, semicircular). Short, shallow notches may be easily produced, but the resulting cracks normally undergo a transient period of growth during which they attempt to reach a stable, approximately semicircular, shape. An additional factor limiting minimum notch size is the fact that, as the size of the crack starter is decreased, natural crack initiation tends to occur at sites away from the notch, and these remote cracks may dominate the fatigue process.

Photomicroscopy

The selection of a microscope magnification for photographing a small crack is based on the size of the crack being monitored and the required field of view. For example, film-plane magnifications of ×25 and ×400 result in a field of view of 1440 and 90 μm, respectively, with corresponding resolving powers of 3.7 and 0.42 μm (optical parameters for typical commercially available microscopes are presented in Table 1 [*19*]). Generally, a microscope aperture restricted to 70 to 80% of the numerical aperture of the objective is desirable for an optimum combination of resolution, contrast, and depth of focus. These factors are crucial, especially when photographing smaller cracks. Although higher magnifications offer improved resolution, the greatest sharpness can be achieved by choosing objectives with large numerical apertures. When accessibility to the specimen surface is limited, objectives with large working distances (typically 6 to 10 mm for a ×40 objective) can be used without significant loss in resolving power. Additional flexibility in terms of

TABLE 1—*Performance data for typical microscope objective lenses* [19] (*assumes that the eyepiece gives 10 times magnification at the camera's film plane* [*35-mm film image size = 36 mm wide by 24 mm high*]).

		Objective Lens Data				
Film Plane Magnification	Field of View (Width), μm	Magnification	Depth of Focus, μm	NA[a]	WD[b], mm	RP[c], μm
25	1440	2.5	125	0.075	28.2	3.7
50	720	5	56	0.1	20.0	2.8
100	360	10	10	0.25	9.0	1.1
200	180	20	3.5	0.4	3.0	0.69
400	90	40	1.2	0.65	1.0	0.42

[a]Numerical aperture.
[b]Working distance.
[c]Resolving power.

magnification and field of view can be achieved by employing different combinations of microscope objectives and eyepieces.

In some instances it may be desirable to take several hundred photographs during a single small-crack test. To complete the test without interruption, a 35-mm bulk film magazine is recommended. These are available in both 250 and 750 frame versions and may be purchased with a data imprinting capability to record test information on each frame of film. To maximize resolution, a fine-grain film, such as KODAK T-MAX 100® Professional Film, is recommended. This film has a resolving power of 63 lines/mm for a target object contrast (TOC) of 1.6:1 (200 lines/mm for a TOC of 1000:1) when processed with KODAK Developer D-76® [*20*]. (Although the typical image contrast for a small crack photographed using a reflecting-light microscope is very high, the TOC is probably less than 1000:1.) A standard electronic flash unit may be used for lighting, but it should be sufficiently powerful to permit good exposure using the microscope's standard light port. The intensity of the electronic flash should be manually controllable, or a camera/flash combination that has an automatic exposure capability should be used. Calibration of manual exposure may be accomplished by taking a series of test photographs of a specimen surface using a range of flash settings and selecting the best exposure conditions for testing.

At the conclusion of each test, the film is developed, and a standard photographic enlarger is used to project the images of the small crack(s) on a computer digitizing tablet for convenient determination of crack-tip positions. An enlarger magnification of approximately 15 times is commonly used, which when combined with the original microscope magnification, produces a total magnification in the approximate range of 300 to 1000 times after projection. The exact image magnification is determined from a photograph of a precision micrometer slide. The use of the micrometer slide as a reference standard for each magnification on a roll of film insures accuracy in the measurement of crack length and eliminates variations caused by differences in the experimental setup or photographic processing. After the digitizing process is complete, the cycle-count data acquired by the computer are merged with the crack length data to produce a computer file of surface crack length ($2c$) versus cycles N.

Example Data

The titanium alloy Ti-6Al-2Sn-4Zr-6Mo will be used to demonstrate the capabilities of the photomicroscopic system. This material, which is used for intermediate-temperature components in gas turbine engines, has a relatively high strength (yield strength = 1160 MPa; ultimate strength = 1230 MPa) and possesses a fine two-phase microstructure. Under nominally elastic fatigue loading, small surface cracks in this material remain nearly semicircular in shape and tend to produce relatively flat fracture surfaces. In addition, over a broad range of crack size, the growth rates (da/dN) of small cracks in this alloy correlate well with equivalent large-crack data when plotted against the applied stress intensity factor range ΔK [*21–24*]. Thus, data from this material exhibit minimal microstructural and "anomalous" small-crack "effects" and provide a clear illustration of the fundamental capabilities and limits of the photomicroscopic system. The system has been used for small-crack research on a number of other materials, reported elsewhere [*6,24,25,26,27*], which exhibit a more clearly defined small-crack "effect."

Figures 5 through 7 present example photographs of small cracks in Ti-6Al-2Sn-4Zr-6Mo tak,03en at various stages of crack growth. Figure 5 shows a crack, in a relatively featureless specimen, that was initiated and grown under $R = 0.1$ fatigue with $\sigma_{max}/\sigma_y = 0.8$. This series of photographs was taken using the same microscope magnification, and all but the first image were enlarged to the same magnification. The first image in the series is a more

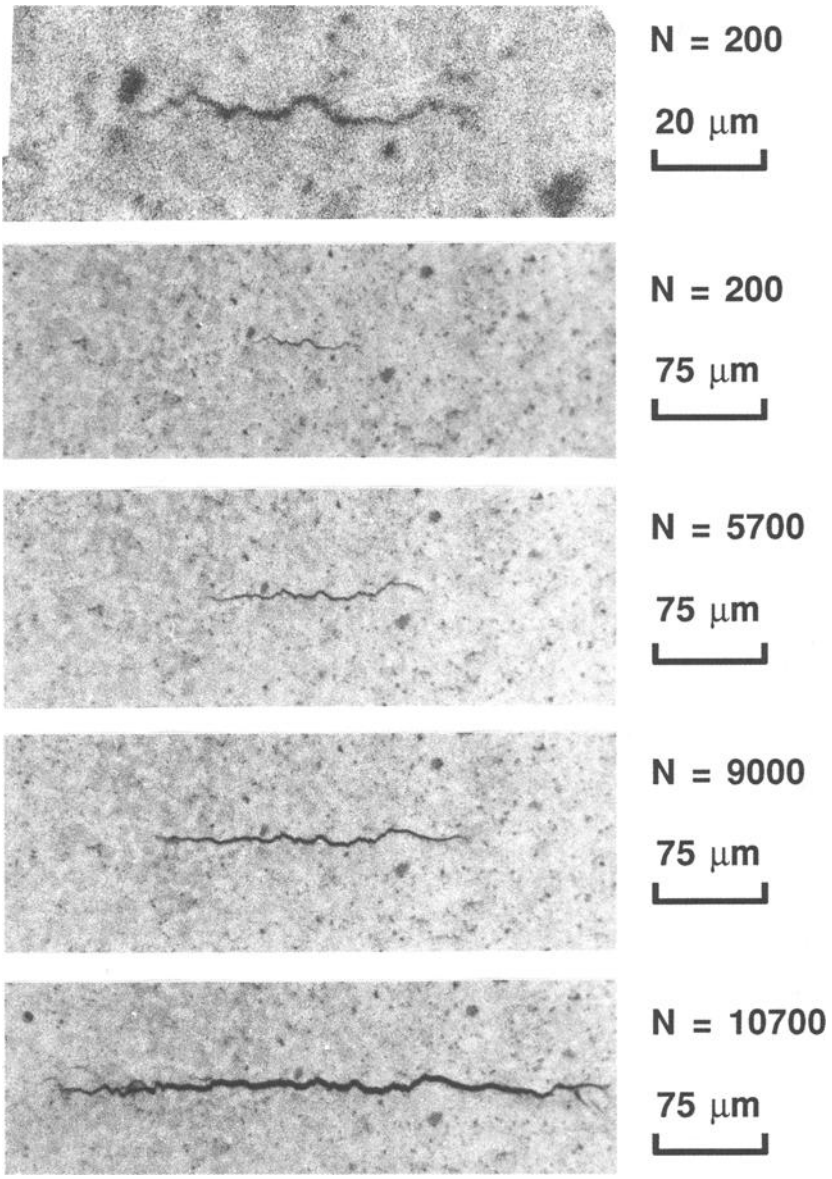

FIG. 5—*Representative photographs of a small crack in Ti-6Al-2Sn-4Zr-6Mo. Electropolishing conditions used to finish the specimen produced a nearly featureless surface.*

magnified enlargement of the second image. This first image, which begins to show the grain in the film, illustrates the resolution achieved in practice. The crack shown in Fig. 6 was initiated under $R = -1.0$ fatigue with $\sigma_{max}/\sigma_y = 0.6$, and the subsequent crack growth portion of the test was performed under $R = 0.1$ cycling. This series of photographs was taken using a range of microscope magnifications, but the same enlarger magnification was

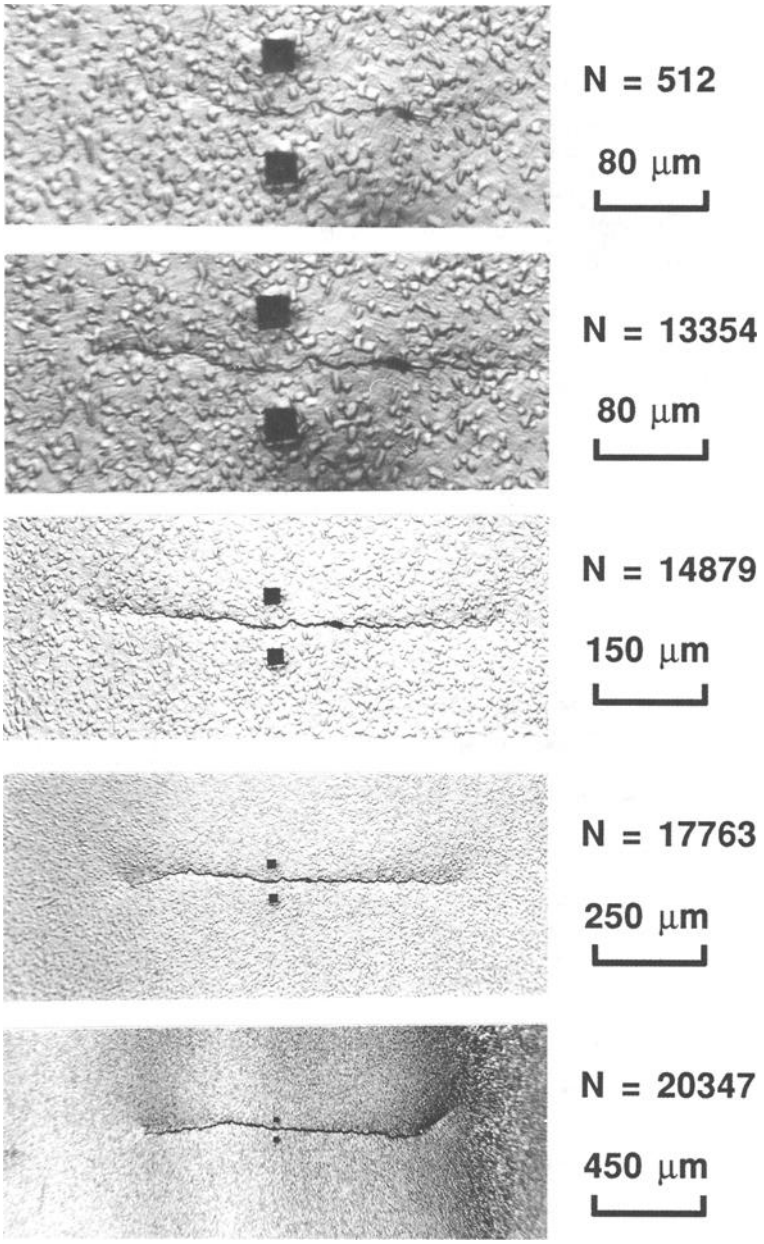

FIG. 6—*Representative photographs of a small crack in Ti-6Al-2Sn-4Zr-6Mo. Electropolishing conditions used to finish the specimen served to highlight microstructural features of the alloy. The Vickers hardness indentations were used for independent measurements of crack opening displacement* [27].

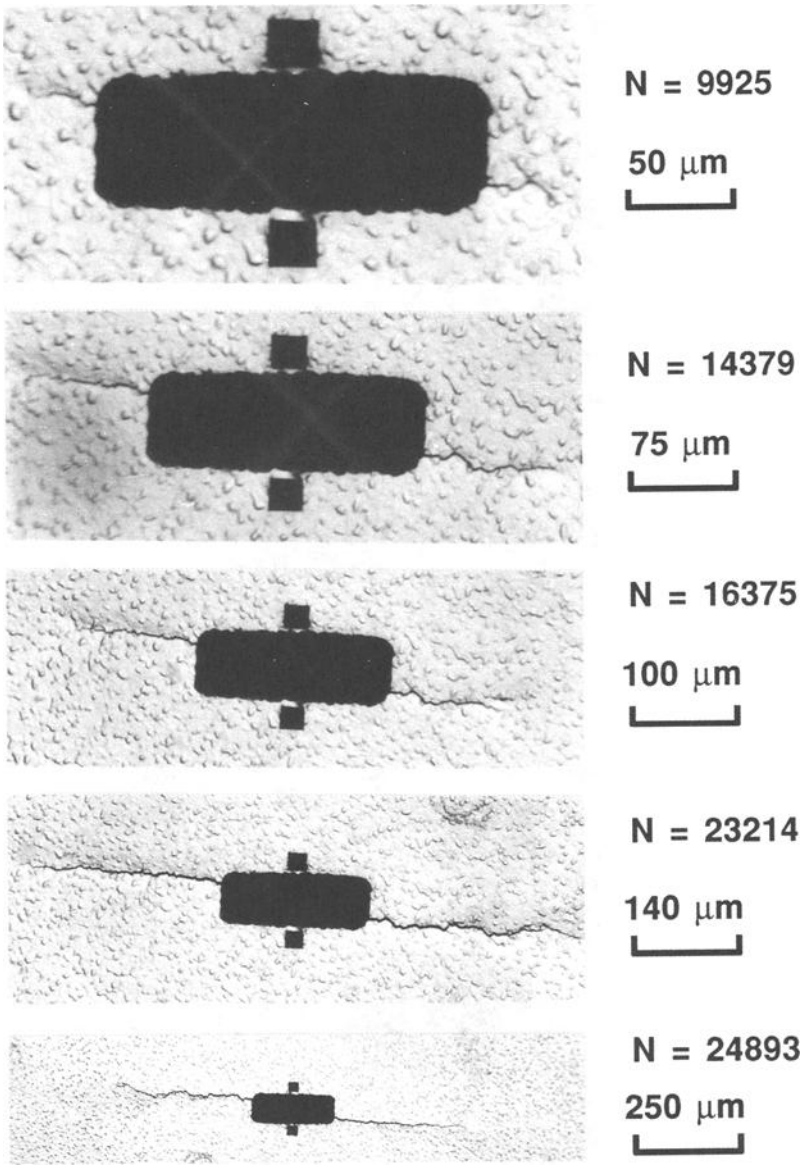

FIG. 7—*Representative photographs of a small crack growing from an EDM notch in Ti-6Al-2Sn-4Zr-6Mo. The Vickers hardness indentations were used for independent measurements of crack opening displacement* [27].

used for all prints. Electropolishing conditions used to prepare this specimen were tailored to highlight the material's microstructure. The small squares spanning the crack are Vickers microhardness indentations that were used independently to measure crack mouth opening displacement using laser interferometry [*27*]. The crack in the notched sample (Fig. 7) was initiated and grown under $R = 0.1$ fatigue with $\sigma_{max}/\sigma_y = 0.4$. Crack initiation occurred at the corners of the notch, and the crack eventually assumed a semicircular shape.

The crack growth data corresponding to the cracks pictured in Figs. 5 through 7 are presented in Fig. 8. The fatigue cycles represent data acquired following visual detection of the naturally initiated cracks, while data from the crack grown in the specimen containing the EDM notch include the crack initiation cycles. The initial "crack length" for the notched specimen is the notch length. The data from these three tests were reduced to the form of dc/dN versus ΔK using the surface-crack stress-intensity factor solution of Newman and Raju [*28*] and the modified incremental polynomial regression algorithm to be discussed later. The data from the cracks shown in Fig. 5 and 6 were reduced assuming that the aspect ratios of these cracks remained constant at a value of 1.03 (as indicated by the crack-shape measurements shown in Fig. 4). Data from the crack shown in Fig. 7 were reduced using a variable aspect ratio determined from independent measurements of crack opening compliance [*17*]. Figure 9 presents the small-crack $dc/dN - \Delta K$ data compared with a trend line representing large-crack data from tests on conventional $C(T)$ specimens of the same material. The small-crack data fall in a small scatter band, which agrees well with the large-crack behavior, and the test-to-test variability of the small-crack data is well within the variability in large-crack data observed in this material. The minimum observed small-crack growth rate ($dc/dN \approx 10^{-8}$ m/cycle) is a reflection of the minimum detectable crack size ($2c \approx 40$ μm), the applied stress, and the relatively low threshold stress-intensity factor ΔK_{th} of this material. Aside from the difficulty involved in locating an extremely slow growing small crack, there is no inherent growth-rate limit for use of the photographic method.

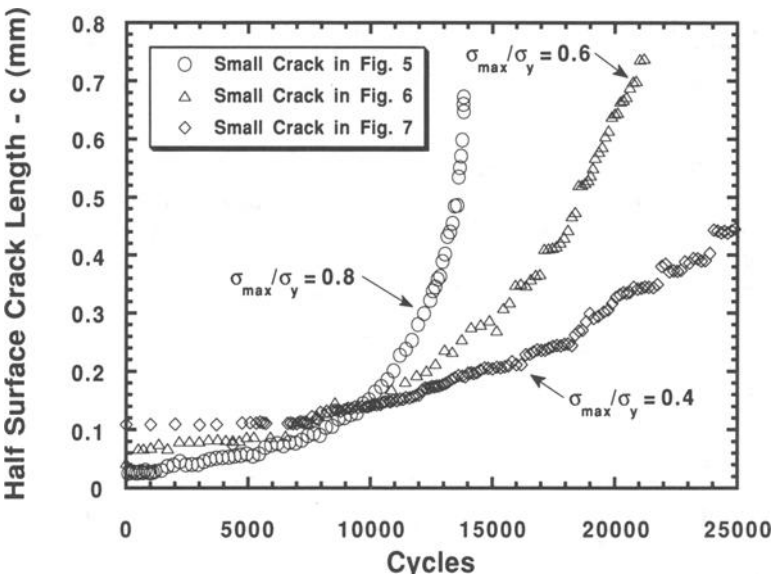

FIG. 8—*Typical crack growth data obtained from photomicrographs of small fatigue cracks. The small-crack data were taken from the cracks shown in Figs. 5 through 7, which were tested under* R = *0.1 fatigue and three different stress levels.*

Precision of Crack Length Measurement

The precision in crack growth rate data, apart from material variability effects, depends on the resolution of the measurement technique. For a given precision, decreasing the crack length interval between successive measurements is known to increase the accuracy and precision of the calculated crack growth rate data [*29,30*]. For the photomicroscopic system, the precision of crack length measurements depends on a variety of factors, such as surface condition of the specimen, microscope magnification, sharpness of focus, resolution of the film, photographic exposure conditions, and the digitizing process. In addition, interpretative factors such as the presence of deformation slip bands, microstructural features, and out-of-plane displacements at the crack tip in the presence of large plastic zones may reduce the precision that is otherwise possible with photomicroscopic measurements. Thus, the precision may depend on the specific test conditions and material being investigated.

To assess the precision of crack length measurements obtained from photographic negatives, several cracks in the Ti-6Al-2Sn-4Zr-6Mo alloy, photographed at different magnifications, were digitized repeatedly under routine measurement conditions. Each set of measurements (typically 30) on one crack was assessed based on the ASTM definition of precision, or repeatability (r), of a measurement (ASTM Practice for Use of Terms Precision and Bias in ASTM Test Methods [E 177])

$$r = 1.96\sqrt{2}\sigma \tag{1}$$

where r is defined such that there is 95% probability that any two arbitrary measurements on the same crack would differ by less than this value. σ is the standard deviation of the repeated measurements. Summaries of these statistics for several sizes of the cracks shown in Figs. 5 and 6 are presented in Tables 2 and 3, respectively. The data indicate that the standard deviation of the measured crack half-length c varies from a minimum of 0.35 μm at the highest magnifications to 2.72 μm at the lowest magnifications. The coefficient of variation (standard deviation/crack length) ranged from a maximum of 1.85% for the smallest crack to 0.22% for one of the larger cracks. For all measurements on all crack sizes, the average standard deviation was 1.2 μm and the average coefficient of variation was 0.63%.

Analysis of Crack Growth Rate Data

As indicated by the good correlation between the small- and large-crack growth rate data presented in the $dc/dN - \Delta K$ plot (Fig. 9), the surface-crack stress intensity factor solution of Newman and Raju appears to suitably represent the crack driving force for these particular experiments. However, it is well known that ΔK may be inadequate for small cracks under

TABLE 2—*Estimated precision of crack length measurements corresponding to the crack pictured in Fig. 5.*

Total Magnification After Projection	Mean Surface Crack Half-Length c, μm	Standard Deviation, μm	Coefficient of Variation, %	Repeatability r, μm
490	26	0.48	1.85	1.33
490	71	0.88	1.24	2.42
490	106	1.48	1.40	4.09
490	189	0.80	0.42	2.20
490	358	0.56	0.16	1.54
260	678	1.78	0.26	4.92

TABLE 3—*Estimated precision of crack length measurements corresponding to the crack pictured in Fig. 6.*

Total Magnification After Projection	Mean Surface Crack Half-Length c, μm	Standard Deviation, μm	Coefficient of Variation, %	Repeatability r, μm
910	69	0.43	0.62	1.19
455	160	0.35	0.22	0.97
455	275	0.83	0.30	2.30
305	353	1.76	0.50	4.89
305	414	2.58	0.62	7.15
195	528	1.18	0.22	3.28
195	672	2.72	0.40	7.52

a variety of conditions, and an alternative parameter may be required. Although discussion of these effects is beyond the scope of this paper, recommendations regarding the utility of stress-intensity-factor and J-integral solutions for small surface and corner cracks may be found in Ref *31*.

Regression analysis of crack-length data to determine crack growth rates also requires special consideration. To adequately document crack growth events at the smallest crack sizes (which are of primary interest), it is desirable to measure crack length at frequent intervals. However, as the crack length interval Δa between successive measurements decreases, the relative contribution of the measurement error to the calculated value of da/dN increases. For example, assume that a single crack length measurement is given by $\hat{a} = a + \varepsilon$, where $\hat{a}$ is the measured crack length, a is the "true" crack length, and ε is a normally distributed error inherent in the crack length measurement. A direct-secant cal-

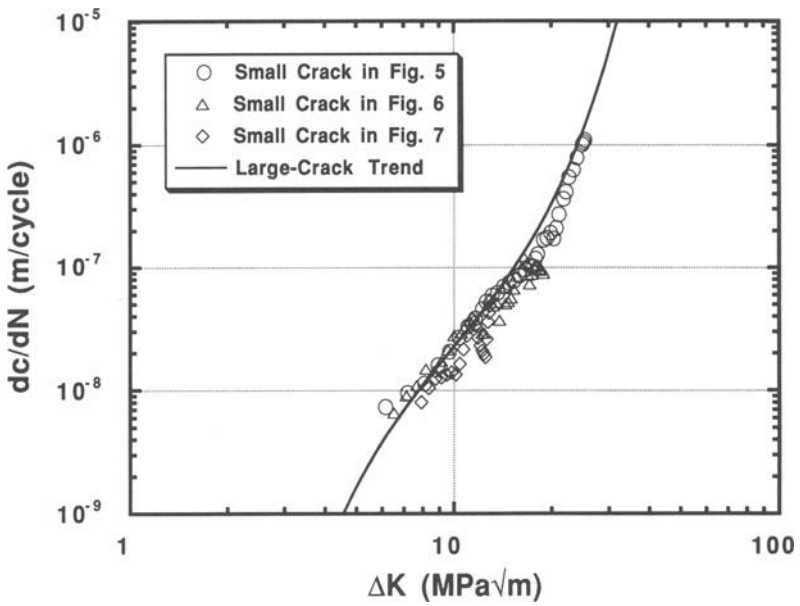

FIG. 9—*Crack growth rate data,* dc/dN – ΔK, *for the cracks shown in Figs. 5 through 7. The data are compared with a trend line representing data from a series of tests of large cracks in conventional* C(T) *specimens of width* W = *40 mm tested under* R = *0.1 fatigue.*

culation of crack growth rate between two successive crack length measurements (a_1 and a_2) is given by

$$\frac{\Delta \hat{a}}{\Delta N} = \frac{(a_2 + \varepsilon_2) - (a_1 + \varepsilon_1)}{\Delta N} = \frac{\Delta a}{\Delta N} + \frac{\Delta \varepsilon}{\Delta N} \tag{2}$$

Thus, as $\Delta a/\Delta N$ approaches zero, the error term $\Delta \varepsilon/\Delta N$ dominates the calculated value of $\Delta \hat{a}/\Delta N$. Since small-crack data are usually acquired at low growth rates (for example, in the large-crack near-ΔK_{th} region), much of the growth rate data may exhibit an unusually large variability because of measurement error.

Following ASTM recommendations for conventional large-crack fatigue tests (ASTM Test Method for Measurement of Fatigue Crack Growth Rates [E 647]), the minimum interval between successive crack length measurements should be 10 times the measurement precision, where the measurement precision is defined as "the standard deviation of the mean value of crack length determined for a set of replicate measurements." Thus, crack growth data must be acquired at specified intervals of crack length, or the *a-N* data must be edited to remove data to achieve the desired interval Δa. The inherent difficulty in this process is selecting the data points for removal. Small-crack measurement techniques often have measurement precision that is of the order of microstructural dimensions. As a result, discontinuities in the *a-N* (or 2*c-N*) data arise because of crack interactions with microstructure, as well as from inherent errors in the measurements. Thus, if a minimum level of Δa is used as a criterion for editing the data, then the selected data points will often be the first point after the crack has broken through a local microstructural obstacle, and the data exhibiting the crack retardation in the microstructure will be lost.

As an alternative to editing the data, regression analysis may be performed in such a way that the relative error in the crack growth rate calculations remains approximately constant. This modified incremental polynominal approach [*5*] is illustrated schematically in Fig. 10. Essentially, it is an implementation of the approach recommended by ASTM E 647, with a key modification. Rather than performing an incremental regression on each successive set of seven *a-N* data points, the modified approach uses crack extension as a criterion for the selection of data for inclusion in the regression interval. As illustrated, successive incremental regressions are performed on a body of data falling within an interval in crack length designated as Δa_{reg}, and the crack length and crack growth rate are calculated at the middle of the interval. Each successive local regression is incremented by an amount Δa_{inc} (where $\Delta a_{reg} \equiv 6\Delta a_{inc}$), and the process is repeated. If the number of data points within a local interval falls to seven or less, the computer algorithm extends the interval to include seven points. The final data set is a series of uniformly spaced crack growth rate calculations having an approximately uniform error in *da/dN*, and any perturbations in crack growth rate above this noise level reflect actual variations in the crack growth rate. A notable advantage of this approach is that the regression uses all of the data, and does not exclude information that may be lost if the data set is edited to remove data points.

To evaluate the capability of the modified incremental polynomial regression, an analytical data set was generated from a simple Paris-law regression of the Ti-6Al-2Sn-4Zr-6Mo large-crack data shown in Fig. 10. To simulate a typical photographic data set, the Paris expression was integrated to produce 200 *a-N* data pairs in the range of 0.020 mm $\leq a \leq$ 1 mm separated by equal intervals of ΔN (a is synonymous with surface crack half-length c). A normally distributed random error having a standard deviation σ_ε of 1 μm was added to each of the data points to produce the crack growth data shown in Fig. 11 ($a \equiv$ exact values of a; $a' \equiv a + \varepsilon$, where ε is the random error, as in Eq 2). These "data" were reduced by a variety of methods, using the Newman-Raju stress intensity factor solution for a semicircular surface

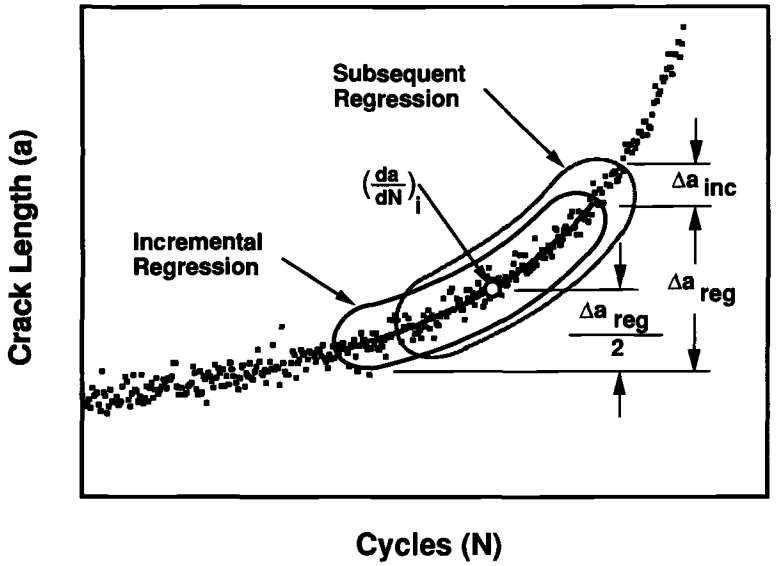

FIG. 10—*Schematic representation of the modified incremental polynomial method for reducing crack growth data.*

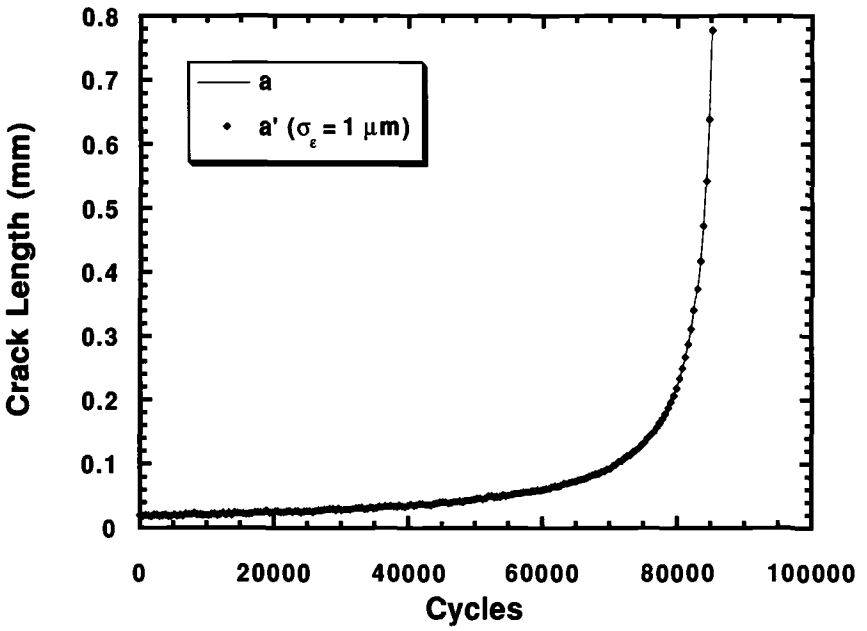

FIG. 11—*Analytically generated crack growth "data" used to demonstrate the influence of measurement error on the reduction of the data to the form of* da/dN *versus* ΔK.

crack to calculate ΔK. Reducing these data by a direct secant method, wherein crack growth rate is the slope of the line connecting successive points and the crack length is the average of the two points, produces the result shown in Fig. 12*a*. At the lowest ΔK values, the growth rates calculated for the data set containing the error term are as much as two orders of magnitude faster than the "actual" growth rate. A large number of the $da/dN - \Delta K$ data fell below 10^{-10} m/cycle (these are plotted along the ΔK axis), and many of these were actually negative. Obviously, the direct secant method is not appropriate for reducing the data in their unedited form.

As shown in Fig. 12*b*, the 7-point incremental polynominal method, suggested by ASTM E 647, reduces the variability in the calculations of da/dN, but this method is also inappropriate for reducing the data in the unedited state. Figures 12*c* and *d* show the same data reduced using the modified incremental polynomial method with Δa_{inc} set equal to 1 and 2 μm, respectively, which is 1 and 2 times the standard deviation of the error term σ_ε. As these two plots indicate, 1 times the standard deviation of the error significantly reduces the variability in the da/dN data, and 2 times the error almost eliminates the effect of the random error. Although not shown, a value of $\Delta a_{inc} = 3\sigma_\varepsilon$ brings almost all of the data points in contact with the underlying Paris line.

Advantages and Limitations of the Photomicroscopic Method

In selecting a technique for recording the growth of small fatigue cracks, a potential user may wish to consider the general attributes of this approach. Key characteristics of photomicroscopy as applied to small-crack research may be broken down into apparent advantages and limitations.

Aspects of photomicroscopy that may be considered advantages include the following:

1. The necessary equipment is relatively inexpensive and available in most fatigue laboratories.
2. Cracks may be initiated naturally.
3. The photographs provide a permanent record of crack growth, documenting crack interactions with microstructural features and with other cracks. In addition, the photographs provide a record of crack path, including crack branching, crack symmetry, and fracture surface asperities that may produce crack closure.
4. The precision of the measurement of surface crack length, $2c$, is of the order of 2 μm, although a precision of less than 1 μm is possible using higher microscope magnifications.
5. With the aid of a microcomputer, the experiment may be automated, making acquisition of a large number of data a routine task.
6. In principle, the method should be applicable to measurements at elevated temperature and in vacuum, although the limited standoff distances required for conventional long-focusing microscope objectives (≈10 mm) is a clear limitation.

Aspects of photomicroscopy that may be considered as disadvantages include:

1. To obtain the highest resolution of the photographs, naturally initiated cracks must be located visually before execution of the test.
2. The measurements of crack length are two-dimensional, requiring an independent determination of crack shape. In many cases, the assumption of a semicircular shape is reasonable, although there are examples where measurement of surface crack length alone can be misleading [*17*].

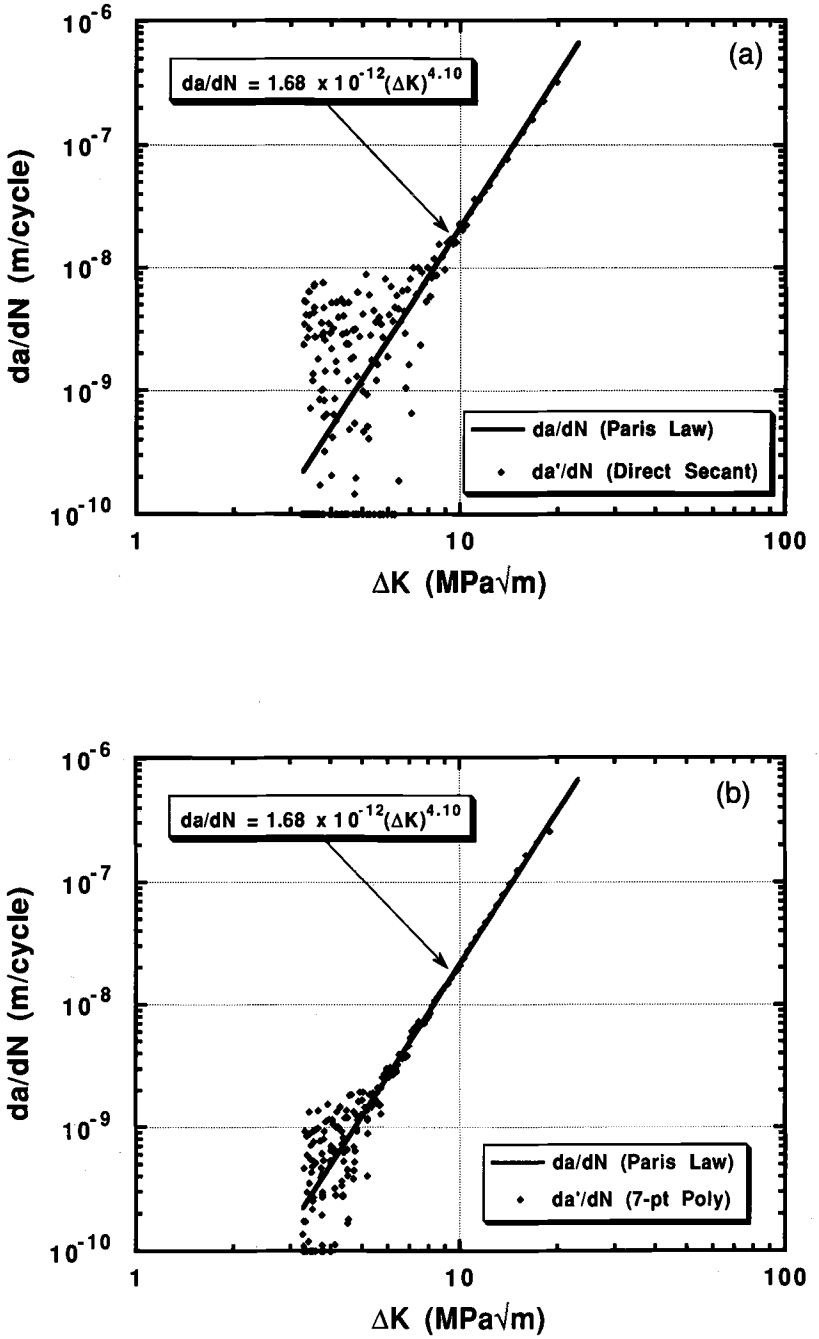

FIG. 12—*Plots of* da/dN *versus* ΔK *illustrating the influence of measurement error on the calculation of* da/dN *using various regression approaches:* (a) *the direct secant.* FIG. 12*b*—*the 7-point incremental polynominal.* FIG. 12*c*—*the modified incremental polynominal having* Δa_{inc} *set equal to the standard deviation of the measurement error.* FIG. 12*d*—*the modified incremental polynomial having* Δa_{inc} *set equal to 2 times the standard deviation of the measurement error.*

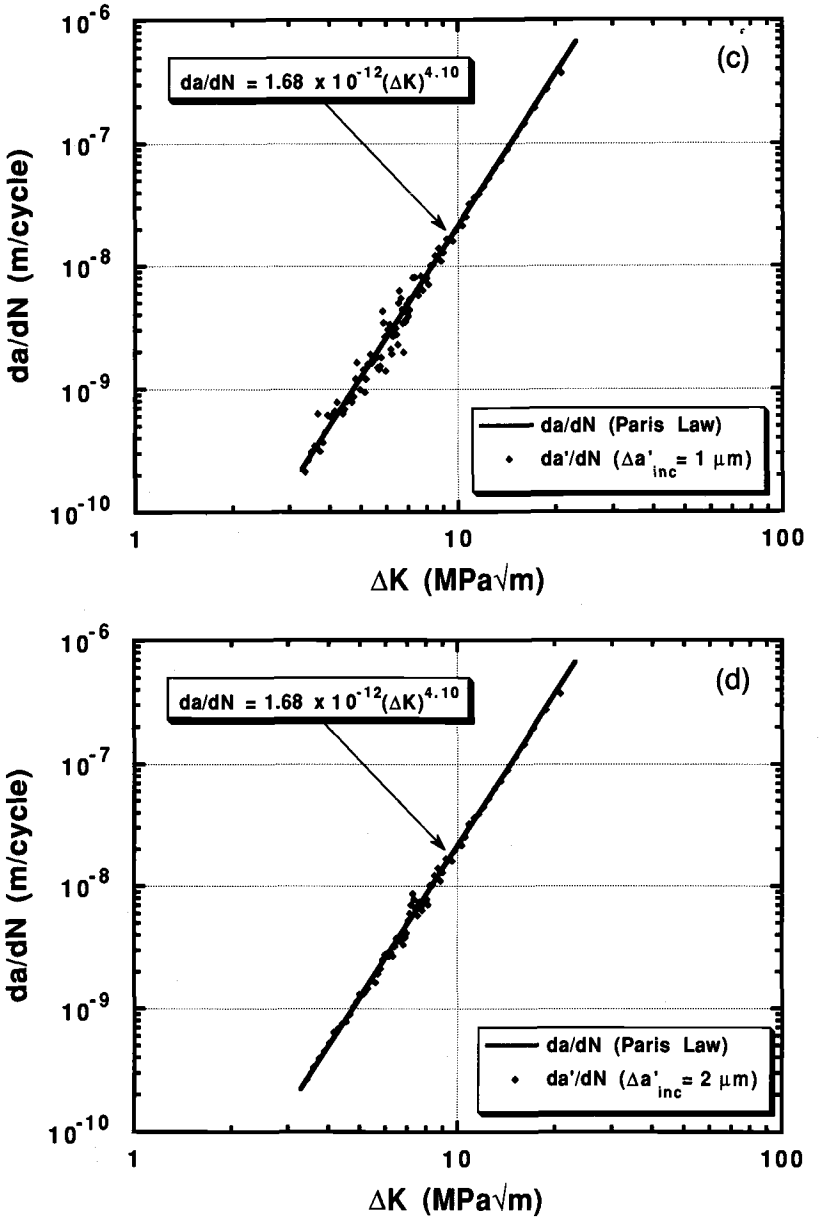

FIG. 12—*Continued.*

3. Approximately 20% of the specimens form corner or edge cracks, which limit the period from which data from other cracks may be obtained.
4. Useful measurements of crack opening displacement and crack closure cannot be made using the photomicroscopic system because of the inherent limit of resolution of light microscopy ($\approx$0.5 μm).
5. Photographs must be digitized to obtain crack length data; data cannot be analyzed in real time.

Concluding Remarks

In comparison with tests of conventional specimens containing large fatigue cracks, tests to study the behavior of small fatigue cracks are typically extremely labor intensive. The application of photomicroscopy to document the behavior of small cracks is an effort to reduce the tedium involved in the experiments. Photomicroscopy combines suitable resolution (optical resolution $\approx$ 0.5 μm; measurement precision $\approx$ 1 μm) and ease of use, facilitated by computer automation, to produce an experimental technique having a number of merits. Photomicroscopy is easy to implement and use, the necessary equipment is commercially available and relatively inexpensive, and a large number of data may be acquired quickly. The photographs provide a permanent record of the experiment and contain valuable information of crack-growth events, including interactions with microstructure. It was also shown, however, that the large number of crack growth data that may be acquired from a test should be analyzed with care. Although the photographic measurements are of relatively high precision, large variations in crack growth rates may result if the data are not edited to insure that sufficient crack growth occurs between successive crack length measurements. This problem, which has been recognized in the analysis of large-crack data, may be effectively circumvented by using a modified incremental polynomial method for the regression of crack growth data. This method uses all of the crack growth measurements to produce crack growth rate data that are not influenced by the original data acquisition interval.

Acknowledgments

This research was performed in the Materials Directorate, Wright Laboratory, Wright-Patterson Air Force Base, OH 45433-6533, under research project number 2302P101. One of the authors (KSR) gratefully acknowledges the support of the U.S. National Research Council for the award of a Research Associateship during the period this work was performed. The assistance of Mr. R. A. Kleismit and Mr. T. E. Johnson in the experimental portion of the research was invaluable and is deeply appreciated. We also wish to acknowledge R. K. Lewis, who prepared the electropolished fatigue specimens and S. D. Wampler for his efforts in revising the modified incremental polynominal algorithm.

APPENDIX

Electropolishing Procedure

Although there are a number of standard references on electropolishing (for example, Refs *32* and *33*), the procedure for electropolishing the gage sections of fatigue specimens requires special care. The following discussion outlines key aspects involved in such a procedure.

For a variety of titanium alloys, an effective electrolyte composition is 590-mL methanol,

350-mL ethylene glycol monobutyl ether, and 60-mL perchloric acid per litre of electrolyte. This electrolyte requires special attention, however, because of the explosive nature of perchloric acid at room temperature, and one should carefully follow handling instructions for this acid. To control the rate and quality of electropolishing, the electrolyte must be cooled to a temperature of approximately −40°C. At this temperature, and a constant current density of 0.01 A/cm^2, the rate of surface removal is approximately 25 μm/h. This rate is adjusted by balancing the combination of temperature and current density.

The apparatus used by the authors for electropolishing is shown schematically in Fig. 13 and discussed in detail elsewhere [*34,35*]. To restrict the electropolishing to the gage section, the ends of the specimen are coated with a standard chemical masking agent. The specimen is mounted in a rotating chuck and immersed in the electrolyte, which is contained in a stainless steel beaker that serves as the cathode. To insure that the electropolishing is uniform, the specimen is located at the center of the cathodic beaker and rotated at a rate of approximately 1 to 3 rpm. The circuit from the specimen to a constant-current power supply is completed using a slip-ring electric contact assembly. The temperature of the electrolyte is maintained constant by immersion of the beaker in a solution of isopropanol, which is cooled by a commercial cryogenic cooling ring. The isopropanol bath may be maintained at a relatively uniform temperature by the gentle motion of a magnetic stirring rod, but circular stirring normally is insufficient to eliminate the often severe vertical temperature gradient that develops in the electropolishing cell (ΔT as large as 15°C was observed). This thermal gradient results in a nonuniform electropolishing rate over the length

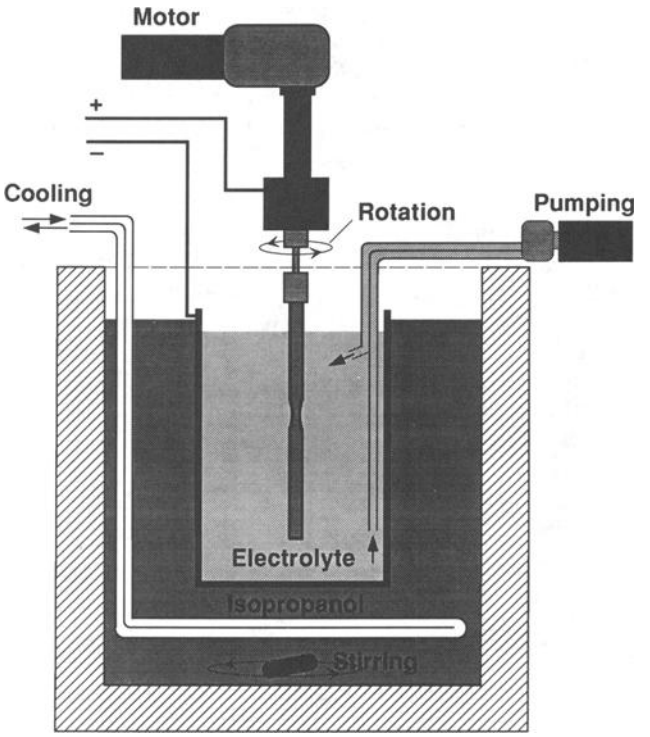

FIG. 13—*Schematic of the apparatus used in electropolishing the gage section of small-crack fatigue specimens.*

of the specimen gage section. The thermal gradient may be minimized by continuously recirculating the electrolyte as shown; the electrolyte is pumped from the bottom of the cell and returned to the top layer of the solution. This procedure provides a method to achieve consistent polishing from specimen to specimen.

References

[1] Swain, M. H., "Monitoring Small-Crack Growth by the Replication Method," *Small-Crack Test Methods, STP 1149*, J. M. Larsen and J. E. Allison, Eds., American Society for Testing and Materials, Philadelphia, 1992, pp. 34–56 (in this publication).

[2] Davidson, D. L., "The Experimental Mechanics of Microcracks," *Small-Crack Test Methods, STP 1149*, J. M. Larsen and J. E. Allison, Eds., American Society for Testing and Materials, Philadelphia, 1992, pp. 83–91 (in this publication).

[3] Papirno, R. and Parker, B. S., "An Automatic Flash Photomicroscopic System for Fatigue Crack Initiation Studies," *Cyclic Stress-Strain Behavior—Analysis, Experimentation, and Failure Prediction, STP 519*, American Society for Testing and Materials, Philadelphia, 1973, pp. 98–108.

[4] Cox, J. M., "*Pitting and Fatigue Crack Initiation of 2124-T851 Aluminum in 3.5% NaCl Solution*," M.S. thesis, University of Missouri, Columbia, MO, 1979, pp. 61–70.

[5] Larsen, J. M., "An Automated Photomicroscopic System for Monitoring the Growth of Small Fatigue Cracks," *Fracture Mechanics: Seventeenth Volume, STP 905*, J. H. Underwood, R. Chait, C. W. Smith, D. P. Wilhelm, W. A. Andrews, and J. C. Newman, Jr., Eds., American Society for Testing and Materials, Philadelphia, 1986, pp. 226–238.

[6] Larsen, J. M., "The Effects of Slip Character and Crack Closure on the Growth of Small Fatigue Cracks in Titanium-Aluminum Alloys," Ph.D. dissertation, Carnegie Mellon University, Pittsburgh, PA, 1987, also published as Wright Research and Development Center Report WRDC-TR-89-4094 (AD A220714), Wright-Patterson AFB, OH, 1990.

[7] Leverant, G. R., Langer, B. S., Yuen, A., and Hopkins, S. W., "Surface Residual Stresses, Surface Topography and the Fatigue Behavior of Ti-6Al-4V," *Metallurgical Transactions*, Vol. 10A, 1979, pp. 251–257.

[8] Hack, J. E. and Leverant, G. R., "Influence of Compressive Residual Stress on the Crack-Opening Behavior of Part-Through Fatigue Cracks," *Residual Stress Effects in Fatigue, STP 776*, American Society for Testing and Materials, Philadelphia, 1982, pp. 204–223.

[9] Johnson, G. A., "Generating Compressive Residual Stress by CBN Grinding," *Proceedings of ASM Conference on Residual Stress in Design, Process and Materials Selection*, American Society for Metals, Metals Park, OH, 1987, pp. 157–166.

[10] Koster, W. P., "Surface Integrity of Machined Structural Components," *U.S. Air Force Materials Laboratory Report 70-11*, Wright-Patterson Air Force Base, OH, 1970.

[11] Zlatin, N. and Field, M., "Procedures and Precautions in Machining Titanium Alloys," *Source Book on Titanium Alloys*, M. J. Donachie, Jr., Eds., American Society for Metals, Metals Park, OH, 1982, pp. 342–357.

[12] Private communication, Lambda Research Inc., Cincinnati, OH, 1990.

[13] Pardee, W. J., Morris, W. L., and Addison, R. C., "Quantitative Nondestructive Evaluation (NDE) for Retirement-for-Cause," *Annual Technical Report 1 on Defense Advanced Research Projects Agency Contract MDA903-80-C-0641*, Rockwell International Science Center, Thousand Oaks, CA, 1981, p. 9.

[14] Hicks, M. A. and Pickard, A. C., "A Comparison of Theoretical and Experimental Methods of Calibrating Electrical Potential Drop Technique for Crack Length Determination," *International Journal of Fracture*, Vol. 20, 1982, pp. 91–101.

[15] Tokaji, K., Ogawa, T., and Aoki, T., "Small Fatigue Crack Growth in a Low Carbon Steel Under Tension-Compression and Pulsating-Tension Loading," *Fatigue Fracture of Engineering Materials Structures*, Vol. 13, 1990, pp. 31–39.

[16] Suh, C. M., Yuuki, R., and Kitagawa, H., "Fatigue Microcracks in a Low Carbon Steel," *Fatigue Fracture Engineering Materials Structure*, Vol. 8, 1985, pp. 193–203.

[17] Ravichandran, K. S. and Larsen, J. M., "Behavior of Small and Large Fatigue Cracks in Ti-24Al-11Nb: Effects of Crack Shape, Microstructure, and Closure," in press: *Fracture Mechanics: 22nd Symposium, Volume I, STP 1131*, H. A. Ernst, A. Saxena, and D. L. McDowell, Eds., American Society for Testing and Materials, Philadelphia, 1992, pp. 727–748.

[18] Pineau, A., "Short Fatigue Crack Behavior in Relation to Three-Dimensional Aspects and Crack Closure Effect," *Small Fatigue Cracks*, R. O. Ritchie and J. Lankford, Eds., The Metallurgical Society, Warrendale, PA, 1986, pp. 191–211.

[19] Nikon Metallurgical Microscope, OPTIPHOT, *Instruction Manual*, Nippon Kogaku K. K., Japan.
[20] KODAK publication F-32, Eastman Kodak Co, Rochester, NY, 1988.
[21] Larsen, J. M., Jira, J. R., and Weerasooriya, T., "Crack Opening Displacement Measurements on Small Cracks in Fatigue," *Fracture Mechanics: Eighteenth Symposium, STP 945*, D. T. Read and R. P. Reed, Eds., American Society for Testing and Materials, Philadelphia, PA, 1988, pp. 896–912.
[22] Jira, J. R., Weerasooriya, T., Nicholas, T., and Larsen, J. M., "Effects of Closure on the Fatigue Crack Growth of Small Surface Cracks in a High-Strength Titanium Alloy," *Mechanics of Fatigue Crack Closure, STP 982*, J. C. Newman, Jr. and W. Elber, Eds., American Society for Testing and Materials, Philadelphia, 1988, pp. 617–635.
[23] Jira, J. R., Nicholas, T., and Larsen, J. M., "Fatigue Thresholds in Surface Flaws in Ti-6Al-2Sn-4Zr-6Mo," *Fatigue 87, Vol. IV*, E. A. Starke, Jr. and R. O. Ritchie, Eds., Engineering Materials Advisory Services, Ltd., West Midlands, United Kingdom, 1987, pp. 1851–1860.
[24] Larsen, J. M. and Jira, J. R., "Small-Crack Closure Measurements in Titanium Alloys," *Experimental Mechanics*, March 1991, pp. 82–87.
[25] Larsen, J. M., Nicholas, T., Thompson, A. W., and Williams, J. C., "Small-Crack Growth in Titanium-Aluminum Alloys," *Small Fatigue Cracks*, R. O. Ritchie and J. Lankford, Eds., TMS-AIME, Warrendale, PA, 1986, pp. 499–512.
[26] Larsen, J. M., Williams, J. C., and Thompson, A. W., "Crack-Closure Effects on the Growth of Small Surface Cracks in Titanium-Aluminum Alloys," *Mechanics of Fatigue Crack Closure, STP 982*, J. C. Newman, Jr. and W. Elber, Eds., American Society for Testing and Materials, Philadelphia, PA, 1988, pp. 149–167.
[27] Sharpe, W. N., Jira, J. R., and Larsen, J. M., "Real-Time Measurement of Small-Crack Opening Behavior Using an Interferometric Strain/Displacement Gage," *Small-Crack Test Methods, STP 1149*, J. M. Larsen and J. E. Allison, Eds., American Society for Testing and Materials, Philadelphia, PA, 1992, pp. 92–115 (in this publication).
[28] Newman, J. C., Jr. and Raju, I. S., "Stress-Intensity Factor Equations for Cracks in Three-Dimensional Finite Bodies," *Fracture Mechanics: Fourteenth Symposium—Volume I: Theory and Analysis, STP 791*, J. C. Lewis and G. Sines, Eds., American Society for Testing and Materials, Philadelphia, 1983, pp. I-238–I-265.
[29] Clark, Jr., W. G., and Hudak, Jr., S. J., "The Analysis of Fatigue Crack Growth Rate Data," *Application of Fracture Mechanics to Design*, J. J. Burke and V. Weiss, Eds., Vol. 22, Plenum Press, 1979, pp. 67–81.
[30] Wei, R. P., Wei, W., and Miller, G. A., "Effect of Measurement Precision and Data Processing Procedure on Variability in Fatigue Crack Growth-Rate Data, *Journal of Testing and Evaluation*, Vol. 7, 1979, pp. 90–95.
[31] Newman, J. C., Jr., "Fracture Mechanics Parameters for Small Fatigue Cracks," *Small-Crack Test Methods, STP 1149*, J. M. Larsen and J. E. Allison, Eds., American Society for Testing and Materials, Philadelphia, 1992, pp. 6–33 (in this publication).
[32] American Society for Metals, "Electropolishing," *Metals Handbook*, 9th Ed., Vol. 5, American Society for Metals, Metals Park, OH, 1982, pp. 303–309.
[33] Vander Voort, G. F., *Metallography, Principles and Practice*, McGraw-Hill Inc., New York, 1984, pp. 119–125.
[34] Rowe, M. S., Harper, C. E., Jr., and Jackson, A., "A Computer Controlled Electropolishing System," *Microstructural Science*, Vol. 16, H. J. Cialoni, M. E. Blum, G. W. E. Johnson, and G. F. Vander Voort, Eds., pp. 555–564.
[35] Rowe, M. S., Harper, C. E., Jr., and Underwood, C. R., "Computer Controlled Electropolishing System," United States Patent No. 4,935,865, 1990.

David L. Davidson[1]

The Experimental Mechanics of Microcracks

REFERENCE: Davidson, D. L., **"The Experimental Mechanics of Microcracks,"** *Small-Crack Test Methods, ASTM STP 1149*, J. M. Larsen and J. E. Allison, Eds., American Society for Testing and Materials, Philadelphia, 1992, pp. 81–91.

ABSTRACT: The experimental mechanics of small cracks require high spatial resolution measurements that are only obtained by using the scanning electron microscope. This paper describes how cyclic loading stages developed for the scanning electron microscope have been used successfully to study growing microcracks, both at ambient and elevated temperatures. In addition, the stereoimaging technique has been used to measure crack-tip parameters that characterize the mechanics and driving force for small fatigue cracks.

KEY WORDS: cracks, microcracks, measurements, scanning electron microscope, crack-tip mechanics

As has been demonstrated by numerous investigators, for example, Ref *1*, small fatigue cracks grow at rates faster than anticipated, based on existing correlations between crack growth rate and calculated cyclic stress intensity factor ΔK for large fatigue cracks. There have been many hypotheses given for the effect of crack size on crack growth rate, including (1) a change in the mechanism of crack advance, (2) differences in crack closure level, (3) difficulties in computing stress intensity factor, (4) loss of similitude, and (5) influence of microstructure.

To understand the reasons small cracks have enhanced growth rates, to test the hypotheses advanced for this phenomenon, and to find a suitable method for describing the growth of small cracks in terms similar to those used for large cracks, it has been necessary to characterize growing small cracks in great detail. New tools were required for this task, and it has been necessary to bring new interpretations to the parameters that describe the mechanics of crack tips. This paper describes techniques first developed for the study of large fatigue cracks and illustrates their use in understanding the growth of small fatigue cracks; the paper is an extension of an earlier paper describing the study of small fatigue cracks in aluminum alloys [*2*].

Dynamic Observations

Two cyclic loading stages have been developed for the scanning electron microscope (SEM) in the course of studying fatigue crack growth. The SEM has both the resolution necessary for the study of fatigue crack tips and the depth of field required to accommodate the specimen movement inherent in the application of large loads. Both of the cyclic stages were developed by Southwest Research Institute for the ETEC scanning electron microscope. The ambient temperature stage became operational in 1978 [*3*], and a similar stage for experiments up to about 850°C was constructed in 1984 [*4*]. The loading capacity of these stages is 4440 N, which is sufficient to allow the study of small cracks in high strength

[1]Institute scientist, Southwest Research Institute, P.O. Box 28510, San Antonio, TX 78228.

materials. Loading is hydraulic and control is through a closed-loop feedback system with a load cell. The crack tip remains relatively stationary beneath the scanning electron beam because loading is applied to each end of the specimen.

Fatigue cracks, both large and small, have been observed dynamically as loading is applied, and videotapes made during these experiments have been extensively studied for information related to the mechanisms of growth. Both videotapes and a film made from them have been presented as part of numerous lectures and seminars. A videotape of crack growth in large fatigue cracks presented at an ASTM meeting in 1978 is described in Ref *5*.

Dynamic observation showed that large fatigue cracks under constant amplitude loading in the near threshold region do not grow on each loading cycle [*6–8*]. Subsequent study of small cracks under similar conditions in aluminum alloys [*2,9*], a nickel based superalloy [*10*], and a Ti_3Al alloy [*11*] have shown the same result for most cracks. Thus, for all the metallic systems studied, it must be concluded that conditions exist that require application of a number of loading cycles between increments of crack growth, independent of crack size.

Stereoimaging

The technique devised for making measurements of useful crack-tip parameters, stereoimaging [*12*], compares two photographs made under different conditions, usually different load levels. When two photographs are compared in a stereoviewer, the visual system can detect very small differences between the fields, much smaller than can be seen without the stereoviewer. For many years, photogrammetric methods were used for measuring the displacements between photographs. Strains are determined by computing gradients from measured displacements [*13*]; the three elements of the in-plane symmetric strain tensor thus determined, are the axial, or normal, strains and the shear strain. By rotating the axes (Mohrs circle construction) the principal strains and maximum shear strain can be computed. Stereoimaging has now been automated using the methods of image processing [*14*] so that quantitative information may be obtained quickly and inexpensively. A small crack typical of many of those studied is shown in Fig. 1, together with displacements and the distribution of maximum shear strain resulting from the applied stress. Strains near the tips of this small crack are the largest approximately along the direction of loading (the x axis). This strain distribution is very different than would be exhibited by a large crack at the same level of ΔK. Maximum shear strains for a large crack have been found to occur along a line approximately ahead of the crack tip. This behavior, which is very unlike that computed for a mathematical crack, probably reflects the large Mode II crack-opening displacement also a characteristic of most large cracks.

Crack-Opening Sequence

The most direct use of stereoimaging is for measurement of fatigue crack closure. Fatigue cracks of all sizes are almost always tightly shut at minimum load. With increasing load P_i, they begin to open from near the crack mouth, for large cracks, or approximately from the center, for small cracks. By making a series of photographs of the crack as load is increased, the distance between the actual crack tip and the point where the crack is open d_i may be directly determined. The degree of crack opening in Mode I is determined by comparing a photograph made at minimum load to one made at P_i, with the photographs oriented so that the eye axis coincides with the loading axis; the measurement of d_i is made simply with a ruler [*15*]. For large cracks in some alloys under near threshold conditions, crack opening in Mode II has been detected at a load below crack opening in Mode I.

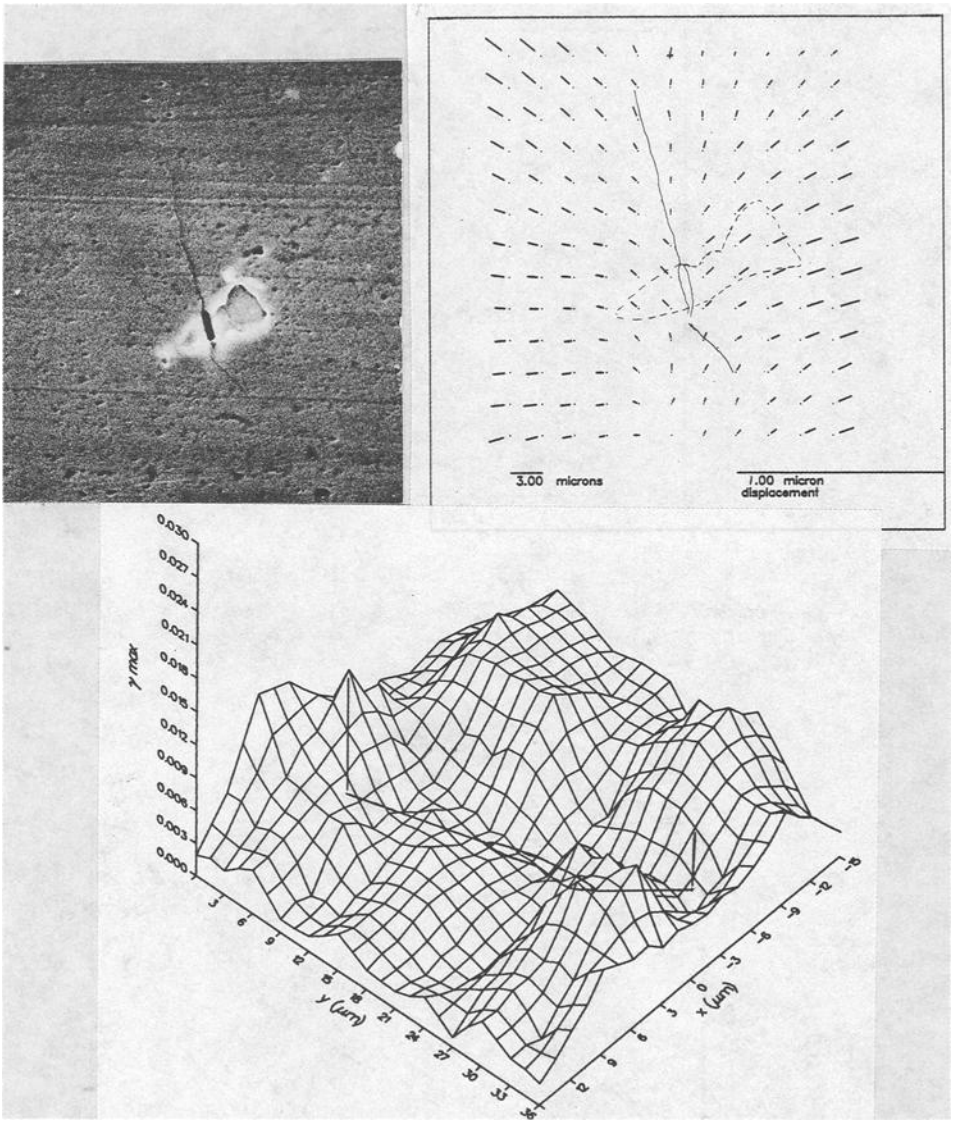

FIG. 1—*Small fatigue crack in 2024-T351 initiated from inclusion growing under a stress of 287 MPa in air. Loading (x axis) was in the direction of the scratches:* (a) *photograph of the crack,* (b) *displacements surrounding the crack, and* (c) *distribution of maximum shear strain in the same region as shown for displacements. Crack is shown schematically on the plane of zero strain.*

The dependence of crack opening on applied load for several small cracks in 2024-T351 is shown in Figs. 2 and 3. These cracks were initiated and grown from surface inclusions at a maximum tensile cyclic stress of approximately 80% of the 0.2% offset yield stress, with $R = 0.1$, in an environment of humid air (50% relative humidity [RH]). The shapes of a few small cracks initiated and grown in aluminum alloys using the same technique were examined and found to be approximately semicircular [*16*].

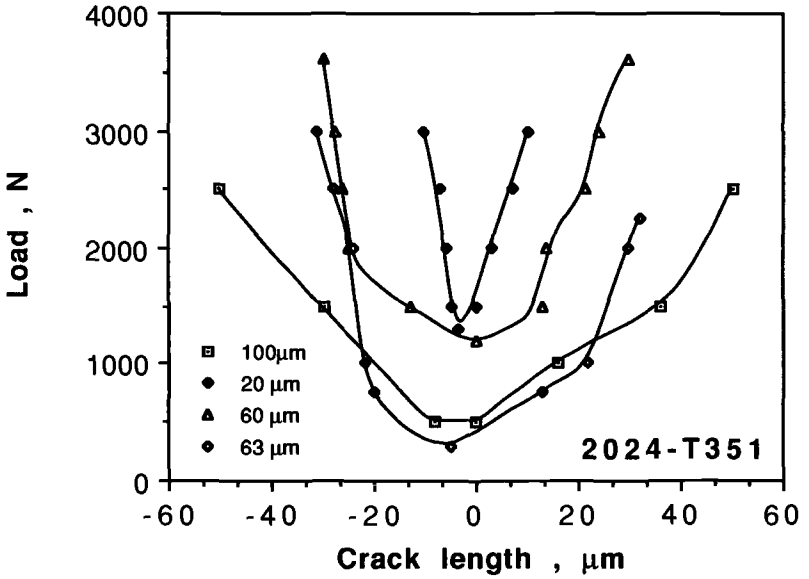

FIG. 2—*Open crack length as a function of applied load for four surface cracks in 2024-T351. The cracks opened with near symmetry about the center line of the crack, and opened to each tip at about the same load, except for the 63-μm crack.*

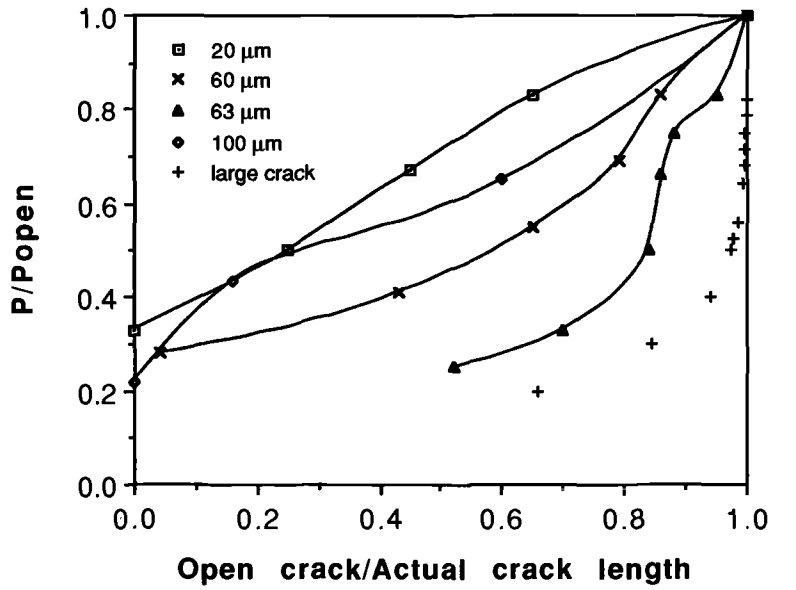

FIG. 3—*Open crack length normalized by total crack length as a function of applied load, normalized by crack opening load, for the four small cracks of Fig. 2. Also shown for comparison is the crack opening for a large crack 6 mm long.*

All the cracks studied in detail opened almost symmetrically about the centerline of the crack and were fully open at approximately the same load at each end of the crack (the 63-μm crack was the exception). This behavior is illustrated in Fig. 2. Note that no opening occurred until about 20% of the opening load had been applied, even for the smallest (20 μm) crack. These same data are shown normalized by crack length and opening load in Fig. 3; on this basis there is remarkable similarity between the 20- and 100-μm-long cracks. For comparison, the opening characteristic of a large fatigue crack (≈6000 μm long) in a center cracked specimen of 7091 aluminum alloy is also shown. Clearly, there are differences in the way small and large cracks peel open with increasing load.

Crack-Opening Load Magnitude

Extensive use has been made of stereoimaging for measuring the loads at which fatigue cracks, both large [*15*,*17*,*18*] and small [*10*,*19*] become fully open. In order to present these data in compact form, the ratio of opening load to maximum load (P_o/P_{max}) was used to determine $\Delta K_{eff}/\Delta K$ using the relationship

$$U = \Delta K_{eff}/\Delta K = (1 - P_o/P_{max})/(1 - R) \tag{1}$$

where ΔK for small cracks (applied) is computed from the half crack length a and the range of applied stress $\Delta\sigma$ using the formula [*9*]

$$\Delta K = 1.32\Delta\sigma\sqrt{a} \tag{2}$$

For large fatigue cracks, a systematic change in U with K and R ($0 < R < 0.9$) was discovered by Hudak [*17*], giving the relation

$$U = 1 - K_h/K_{max} \tag{3}$$

Measured values of U for small cracks are plotted versus $1/K_{max}$ in Fig. 4. The data in these figures include the 4 small cracks in 2024-T351 shown in Fig. 2, measurements from 14 cracks in 7075-T651 and 14 cracks in Astroloy, all at $0 < R < 0.3$. The large scatter seen for the aluminum alloys is believed to result from two factors: (1) Opening load is usually measured to within ±100 N (out of 3000 N, typically, for an error of about ±3%). (2) Opening loads change from cycle to cycle, just as do crack opening displacements and crack-tip strains. These changes in crack-tip parameters occur because of the discontinuous nature of the crack growth process [*6*,*7*]. For the cracks in Astroloy, more care was taken in making the measurements (±50 N), and there was not so much crack-tip variation from cycle to cycle for this material.

The data in Fig. 4 indicate that U is not likely to be a function of K for most of the small cracks studied, and that small cracks in fine grained Astroloy exhibit closure similar to large cracks; thus a line having the form of Eq 3 is drawn through the fine grained Astroloy data.

The results in Figs. 3 and 4 indicate that closure is different for small and large fatigue cracks, as hypothesized. The data show that ΔK_{eff} is a constant fraction of ΔK (that is, crack length) from initiation to some crack size that apparently depends on the grain size, after which the closure behavior assumes the characteristics found for large cracks.

Crack-Opening Displacement

The displacements caused by cyclic load variation, as measured by stereoimaging, allow direct determination of crack-opening displacement (COD). All three modes of crack open-

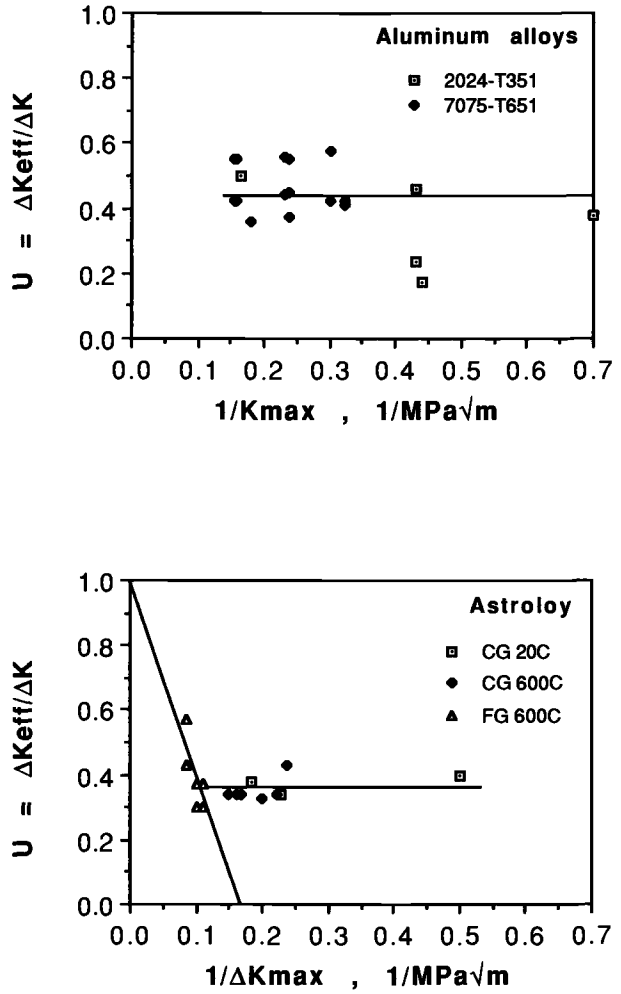

FIG. 4—*Crack closure versus* $1/K_{max}$ *for aluminum alloys and Astroloy. The line shown for Fine Grained Astroloy is given by Eq 3.*

ing can be measured, with Mode III being the most difficult. For Mode I and Mode II, there is great similarity between small and large fatigue cracks in the change of COD with distance behind the crack tip d. The Mode I COD generally varies with d as

$$\text{COD} = C_o\sqrt{d} \tag{4}$$

This behavior is illustrated in Fig. 5 for the small crack of Fig. 1. The COD function given by Eq 4 is the same as for an elastic mathematical crack where C_o is proportional to the stress intensity factor; however, it has been determined that this crack opening behavior cannot be used to accurately determine K for large fatigue cracks [*19*]. Furthermore, there are significant plastic strains at the tips of these cracks, indicating that an elastic analysis is

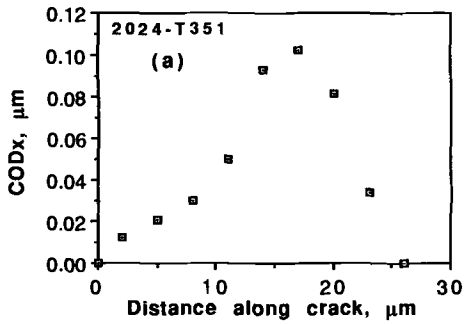

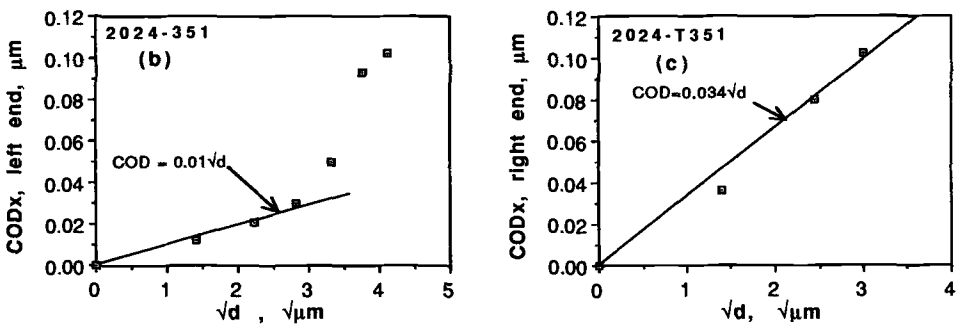

FIG. 5—*Crack-opening displacements for the small crack shown in Fig. 1:* (a) *crack opening for the entire crack.* (b) *and* (c), *crack opening versus square root of the distance from the crack tip for each end.* COD_x *is the opening displacement in the direction of loading (≈ Mode I COD).*

inappropriate. Monotonically loaded cracks blunt with the application of load, so the question arises as to why similar blunting does not occur for fatigue cracks. The answer is not known with confidence, but it is likely that the lack of blunting is another manifestation of crack closure. Either compressive residual stresses within the plastic zone or deformed material at the crack tip, or both, probably cause this behavior.

Most small cracks, as well as large cracks, also have a COD in Mode II. The prospect of this behavior is increased if the crack plane is at an angle to the loading axis. For this case, it may be desirable to either measure or resolve the COD into the directions parallel and perpendicular to the crack plane. An example of this is given for the small crack shown in Fig. 6.

Crack-Tip Strains

For the materials studied, strains at the tips of small cracks are well into the plastic range [*2,9,10*]. For large cracks, crack-tip strain is proportional to the crack-tip opening displacement (CTOD), defined as C_o in Eq 4 [*6,7*]. The strain distribution ahead of large cracks also scales with the magnitude of crack-tip strain [*20*]. Both of these factors indicate that large cracks exhibit similitude. For small cracks, this proportionality between C_o and strain

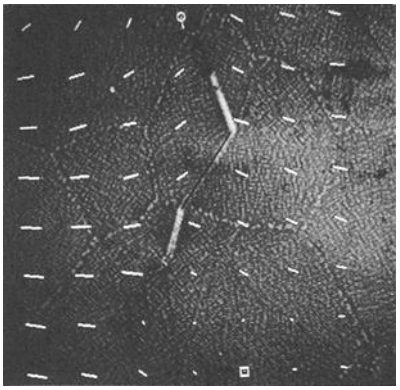

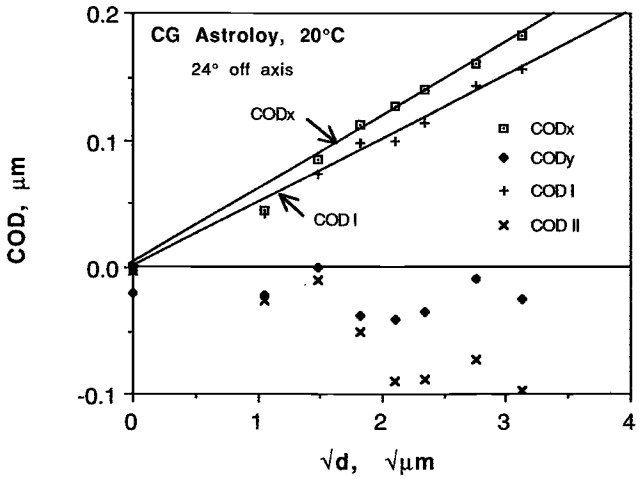

FIG. 6—*Small crack in coarse grained Astroloy showing the effect of resolving crack opening displacements from axial to normal to the crack plane:* (a) *photograph with overlay of displacements measured each 10 μm, loading axis horizontal (x-axis)* (b) *crack-opening displacements of the upper end of the crack parallel and perpendicular to the loading axis and resolved parallel and perpendicular to the crack plane.*

does not exist, and the strain distribution is different for small cracks [*9*], as illustrated in Fig. 1. Thus, also in agreement with hypothesis, small cracks do not exhibit similitude.

Plastic Zone Size

Strains derived by stereoimaging may also be used to determine plastic zone sizes through extrapolation of the strain distribution function to the elastic/plastic boundary. For small cracks in Astroloy, it was found that the average ratio of plastic zone size ahead of the crack tip to half-crack size was 0.68 ± 0.25 for the 21 cracks studied ($45 < 2a < 230$ μm).

Therefore, plastic zone size is thus a much larger fraction of the crack size than for large fatigue cracks [*21*].

Determination of Crack Driving Force from Measured Parameters

The measured crack-tip parameters can be used to determine a driving force, or local stress intensity factor, for small cracks, and that can be compared to the stress intensity factor computed from crack length and stress. This method is based on the work of Hudak and Chan [*22*] and uses the concept of ΔJ as determined by the equation

$$\Delta J = C_o \Delta\sigma \tag{5}$$

where C_o is the CTOD. The stress range experienced by the material element at the crack tip is $\Delta\sigma$, which may be estimated as twice the yield stress or computed from crack-tip strain via the cyclic stress strain curve. For purposes of correlation, ΔJ may be converted to stress intensity using the relation

$$\Delta K_{eq} = (E\Delta J)^{1/2} \tag{6}$$

When computed in this way, the resulting stress intensity factor accounts for the plastic response of the material as well as the influence of crack closure. Based on this method of determining crack driving force and the direct measurement of crack closure, the value of applied (computed) ΔK, Eq 2, may be adjusted so that the $da/dN - \Delta K$ correlation approximately matches that for large cracks [*10*,*11*,*19*]. This analysis requires the use of an additional term ΔK_i to describe ΔK for small cracks; this term was attributed to the excess plasticity found at the tips of small cracks, when compared to large cracks at the same computed value of ΔK_{eff}, and a method has been demonstrated for estimating the magnitude of this term [*19*].

Discussion

The results given above, taken with those already published, can be used to examine the hypotheses listed in the Introduction as possible reasons for unusual small crack behavior: (1) Direct observation of growing cracks has failed to discern any differences in the mechanisms by which small and large fatigue cracks grow. Further consideration of this hypothesis should be discarded. (2) There are considerable differences in the level and behavior of crack closure, which must be accounted for in correlating the growth rates of small and large fatigue cracks. The similarity in behavior for cracks 20 and 100 μm long is indicative that closure behavior is relatively insensitive to crack length. Closure appears to be one of the most significant factors separating small- and large-crack behavior and warrants further study. (3) The loss of similitude for small cracks has been clearly demonstrated by the change in relationship between CTOD and crack-tip strain and by the size of the plastic zone, relative to large cracks. These differences in crack-tip parameters have a significant effect on crack driving force. (4) The change in similitude has led to unexpectedly large magnitudes of plasticity at the tips of small cracks, as compared to large cracks, which contributes to the problems of accurate determination of stress intensity factor for small cracks. (5) The influence of microstructural effects on small-crack growth rates has been unquestionably demonstrated, but it remains unclear just what microstructural characteristics exert this influence. For planar slip materials, grain size is important, but is much less important in materials with multiple slip. Texture is another microstructural factor likely to be important.

Further study of microstructural effects on crack growth is required.

The techniques developed to study small-crack behavior described in this paper are capable of measurements that determine the effects of the many variables related to the unexpectedly high growth rates for small fatigue cracks. Spatial resolution, strain resolution, and crack-opening load measurements are all sufficiently accurate for characterizing small cracks; however, none of these techniques can be classified as suitable for routine laboratory, engineering measurements.

Crack growth for small fatigue cracks is, for some materials, nearly as well understood as for large fatigue cracks; the problem is that there are still many phenomena associated with fatigue that are poorly understood. Many of the experimental problems in making measurements from small cracks are in initiating and growing small cracks under conditions of interest, and in finding these cracks while they are still very small physically.

Conclusions

The ability to load small cracks in tension under high resolution conditions in the SEM and make displacement measurements using stereoimaging provide adequate tools for measuring the characteristics of small cracks that are likely to be responsible for their unexpected crack growth characteristics. With these capabilities, it has been possible to examine some of the issues related to small cracks, but a complete understanding of their general behavior in a variety of alloys is still lacking because of the important influence of microstructure. Further experimental work is required on a wider variety of microstructures to test current understanding. Even though we have the ability to measure crack-tip parameters, there is still the problem of interpreting these parameters in terms of crack growth rate. This is particularly true when stress state is complex, causing cracks to assume nonsemicircular shapes, that is, to grow at different rates along the surface and perpendicular to it. More work on relating the models developed by theoretical mechanics to experimental results is also needed. Fatigue crack closure is an important parameter that is different for small and large cracks, and requires further investigation, both experimentally and theoretically, in a variety of microstructures.

Acknowledgments

Preparation of this manuscript was supported by Air Force Contract F49620-89-C-0032, while crack-tip parameter measurements on Astroloy were made under Contract F33615-85-C-5051. The author appreciates the many helpful discussions with his colleagues on the fracture mechanics of small fatigue cracks.

References

[1] Ritchie, R. O. and Lankford, J., Eds., *Small Fatigue Cracks*, The Metallurgical Society, Warrendale, PA, 1986.

[2] Davidson, D. L. and Lankford, J., "High Resolution Techniques for the Study of Small Cracks," *Small Fatigue Cracks*, R. O. Ritchie and J. Lankford, Eds., The Metallurgical Society, Warrendale, PA, 1986, pp. 455–470.

[3] Davidson, D. L. and Nagy, A., *Journal of Physical Environment*, Vol. 11, 1978, pp. 207–210.

[4] Nagy, A., Campbell, J. B., and Davidson, D. L., *Review of Scientific Instruments*, Vol. 55, 1984, pp. 778–782.

[5] Davidson, D. L. and Lankford, J., "Dynamic, Real-Time Fatigue Crack Propagation at High Resolution as Observed in the Scanning Electron Microscope," *Fatigue Mechanisms, STP 675*, J. Fong, Ed., American Society for Testing and Materials, Philadelphia, 1978, pp. 277–284.

[6] Davidson, D. L. and Lankford, J., *Fatigue of Engineering Materials and Structures*, Vol. 6, 1983, pp. 241–256.
[7] Davidson, D. L. and Lankford, J., *Fatigue of Engineering Materials and Structures*, Vol. 7, 1984, pp. 29–39.
[8] Davidson, D. L. and Lankford, J., *Metallurgical Transactions A*, Vol. 15A, 1984, pp. 1931–1940.
[9] Lankford, J. and Davidson, D. L., "Near-threshold Crack Tip Strain and Crack Opening for Large and Small Fatigue Cracks," *Fatigue Crack Growth Threshold Concepts*, D. L. Davidson and S. Suresh, Eds., TMS-AIME, Warrendale, PA, 1984, pp. 447–463.
[10] Hudak Jr., S. J., Davidson, D. L., Chan, K. S., Howland, A. C., and Walsch, M. J., "Growth of Small Cracks in Aeroengine Disc Materials," AFWAL-TR-88-4090, Wright-Patterson Air Force Base, OH, June 1988.
[11] Davidson, D. L., Cambell, J. B., and Page, R. A., "The Initiation and Growth of Fatigue Cracks in a Titanium Alloy," *Metallurgical Transactions A*, Vol. 21, 1990, pp. 377–391.
[12] Davidson, D. L., "The Observation and Measurement of Displacements and Strain by Stereo-imaging," in *Scanning Electron Microscopy/1979/II*, SEM Inc., AMF O'Hare, IL, 1979, pp. 79–86.
[13] Williams, D. R., Davidson, D. L., and Lankford, J., *Experimental Mechanics*, Vol. 20, 1980, pp. 134–139.
[14] Franke, E. A., Wenzel, D. J., and Davidson, D. L., "Measurement of Micro-*dis*placements by *ma*chine vision *p*hotogrammetry (DISMAP)," *Review of Scientific Instruments*, Vol. 62, 1991, pp. 1270–1279.
[15] Davidson, D. L., *Mechanics of Fatigue Crack Closure, STP 982*, J. C. Newman and W. Elber, Eds., American Society for Testing and Materials, Philadelphia, 1988, pp. 44–61.
[16] Lankford, J. and Davidson, D. L., "The Role of Metallurgical Factors in Controlling the Growth of Small Fatigue Cracks," *Small Fatigue Cracks*, R. O. Ritchie and J. Lankford, Eds., The Metallurgical Society, Warrendale, PA, 1986, pp. 51–71.
[17] Hudak, S. J., Jr. and Davidson, D. L., *Mechanics of Fatigue Crack Closure, STP 982*, J. C. Newman and W. Elber, Eds., American Society for Testing and Materials, Philadelphia, 1988, pp. 121–138.
[18] Davidson, D. L., "Fatigue Crack Closure," *Engineering Fracture Mechanics*, Vol. 38, 1991, pp. 393–402.
[19] Davidson, D. L., *Acta Metallurgica*, Vol. 32, 1984, pp. 707–714.
[20] Davidson, D. L., *Engineering Fracture Mechanics*, Vol. 25, 1986, pp. 123–132.
[21] Davidson, D. L. and Lankford, J., *Fatigue of Engineering Materials and Structures*, Vol. 3, 1980, pp. 289–303.
[22] Hudak, S. J., Jr. and Chan, K. S., *Small Fatigue Cracks*, R. O. Ritchie and J. Lankford, Eds., The Metallurgical Society, Warrendale, PA, 1986, pp. 455–470.

William N. Sharpe, Jr.,[1] *Jay R. Jira,*[2] *and James M. Larsen*[2]

Real-Time Measurement of Small-Crack Opening Behavior Using an Interferometric Strain/Displacement Gage

REFERENCE: Sharpe, W. N., Jr., Jira, J. R., and Larsen, J. M., **"Real-Time Measurement of Small-Crack Opening Behavior Using an Interferometric Strain/Displacement Gage,"** *Small-Crack Test Methods, ASTM STP 1149*, J. M. Larsen and J. E. Allison, Eds., American Society for Testing and Materials, Philadelphia, 1992, pp. 92–115.

ABSTRACT: A procedure for real-time measurement of the opening displacement of small fatigue cracks is reviewed. The method employs a computerized, laser-based, interferometric strain/displacement gage (ISDG) to monitor the relative displacement between two tiny indentations placed across small surface cracks. Complete load versus crack opening displacement curves are obtained for surface cracks of length ranging from 50 μm to several millimetres. The method is applicable to naturally or artificially initiated cracks in smooth or notched specimens. The load-displacement measurements provide a detailed record of crack closure behavior, and estimates of crack size are obtained from measurements of elastic compliance. The resolution of the opening displacement measurements is on the order of 5 nm. Computerization of the system allows measurements to be obtained in real time, facilitating feedback control of testing.

Four versions of the ISDG that are used in different laboratories are described. The instrument's characteristics are presented along with some practical considerations associated with its use. Examples from studies of a number of materials are included to demonstrate applications of the ISDG to the measurement of closure, crack shape, and to automation of small-crack testing.

KEY WORDS: automation, crack propagation, displacements, fatigue, materials, fracture mechanics, interferometry, lasers, mechanical properties, microcracks, short cracks, small cracks, test methods

Of the various test techniques that have been used to record the growth of small fatigue cracks, only a few can provide useful measurements of small-crack closure. Moreover, many methods give only post-test information, making real-time interpretation of crack behavior impossible. From an experimental perspective, it is desirable to not only measure crack length and the closure behavior of small fatigue cracks, but to do so in real-time in order to provide feedback control of the test.

Although measurements of crack length may be obtained by a variety of methods, the observation of crack closure behavior is much more difficult, which accounts for the relatively small quantity of such data reported in the literature. In general, observation of small-crack closure requires some method to measure crack opening displacement. Initially, scanning electron microscopy (SEM) was used by Morris et al. [*1–5*] and Davidson et al. [*6–8*] to

[1]Professor, Department of Mechanical Engineering, The Johns Hopkins University, Baltimore, MD 21218.

[2]Materials engineer and materials research engineer, respectively, Wright Laboratory, Materials Directorate, WL/MLLN, Wright-Patterson Air Force Base, OH 45433-6533.

obtain detailed measurements of crack opening and closing events. While such methods continue to be attractive for a number of key studies [*9*], they are time consuming, and the data are not easily converted from image to digital form. As an alternative to SEM methods, Tanaka et al. [*10,11*] mounted strain gages across sharp notches to monitor closure of short, through-thickness cracks growing in the root of the notch. Although strain-gage methods are not generally applicable to small surface cracks, the use of the notched through-crack specimen made this approach viable. Clement et al. [*12*] used a clip-gage extensometer to monitor the development of closure of through-thickness cracks as short as approximately 0.4 mm. Although this method produced valuable data, it also does not appear to be applicable to very small cracks. As shown by Iyyer and Dowling [*13*], acetate replicas can be used to monitor small-crack closure, although this approach is laborious and time consuming. Recently, Resch and Nelson [*14*] have used ultrasonic methods to monitor small-crack closure. While this method has thus far been applied on a limited basis, it has a number of attractive features, including the ability to detect crack initiation.

The interferometric strain/displacement gage (ISDG) developed by Sharpe [*15*] has been shown to be an effective alternative to the various small-crack test methods—providing real-time crack length and closure data in digital form. Larsen et al. [*16*] demonstrated the utility of the ISDG for small-crack testing on an advanced titanium alloy and have since applied this technique to a number of other alloys [*17–19*]. Lee and Sharpe [*20*] and Sharpe and Su [*21*] have used the ISDG to investigate small-crack behavior in aluminum alloys, while James and Sharpe [*22*] have used it for steel. Jira et al. [*23*] have used the ISDG for feedback control of small-crack fatigue tests, and Ravichandran and Larsen [*24*] have used the method to monitor shape effects for surface cracks in fatigue. Recently, modified ISDG systems have also been used in small-crack testing by Ebi and Neumann [*25*] and by Akiniwa et al. [*26*]. This paper discusses the characteristics of the various ISDG systems that have been applied to small-crack testing, and example data are presented to illustrate the capabilities of the method.

Measurement Principles and Techniques

The ISDG is very simple in concept, and the basics are briefly described in this section. A more thorough explanation is available in Ref *27*. As with any experimental method, there are techniques and procedures that are learned through experience, and this section also presents some of those.

Principles

The basic optical principle underlying the ISDG is illustrated schematically in Fig. 1. Two tiny indentations are made in the surface of a specimen at positions A and B with a Vickers microhardness tester. When a coherent, monochromatic light source is incident upon them, the reflected light is diffracted because of the small size of the indentations. The two cones of light emanating from A and B intersect and form interference fringes in space at positions C and D. Two other interference patterns are formed since the indentations have four sides, but these are not used. As the distance between A and B changes because of loading of the specimen, the fringes at C and D move, and this motion is related to the relative displacement between the two indentations.

Two typical indentations are shown in Fig. 2 along with a photograph of a fringe pattern such as would be seen at C or D in Fig. 1. If the indentations are placed on a smooth surface (as in Fig. 2), then strain will be measured. If they are placed across a crack (see Fig. 3 below), then crack opening displacement will be measured. The indentations in Fig. 2 are

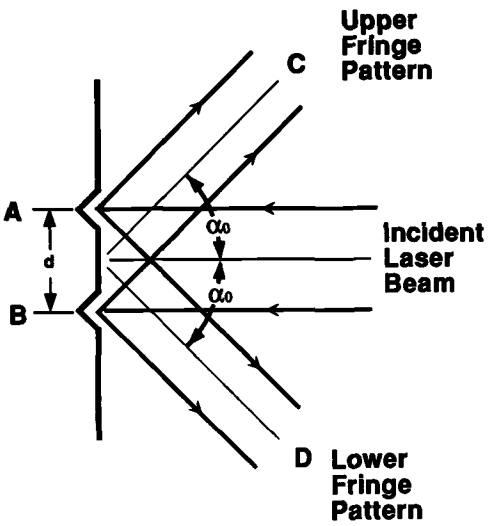

FIG. 1—*Schematic of the ISDG.*

25 μm square and the distance between them is 100 μm (0.004 in.). It is this small size of the "gage" that enables the ISDG to be used for crack opening measurements of small cracks.

The optical principle is simply Young's Two-Slit Interference phenomenon from elementary optics [*28*] except that it is in reflection instead of transmission through two slits or pinholes. Both diffraction and interference are involved to create the fringes. First, the impinging light is diffracted by the reflecting sides of the indentations. The wavelength of a helium-neon (He-Ne) laser is 0.6328 μm, whereas a representative dimension of a reflecting side is about 15 μm; this ratio of wavelength to "slit width" of ~0.04 is small enough to cause appreciable spreading by diffraction (in fact, the angle would be 2.3°). Second, these reflected rays of light interfere because they are coherent and have been shifted along the lines between B and C or A and D by an amount $d \sin \alpha$ where d is the distance between the indentations and α is the angle between the incident laser beam and the observation positions C or D. If one places screens at C or D, one will see straight, parallel fringes because the angle α changes slightly as one moves to different positions on the screen. The governing equation is therefore

$$d \sin \alpha = m\lambda \tag{1}$$

where λ is the wavelength of light, and m is a positive or negative integer.

The shape and structure of the fringe pattern in Fig. 2 show these two aspects of the optical phenomenon. The triangular overall shape of the pattern arises from diffraction from the triangular reflecting sides of the pyramidal indentations. The fringe pattern inside it arises from the interference effect. If one were to observe the pattern as the distance between the indentations changes, one would see the fringes move within the stationary triangular outline. This point is important; it is the motion of the fringes and not the change in spacing between them that is monitored in the ISDG. The spacing between fringes does change somewhat as the indentations move, but that is considered in the calculations of relative displacement from fringe motion.

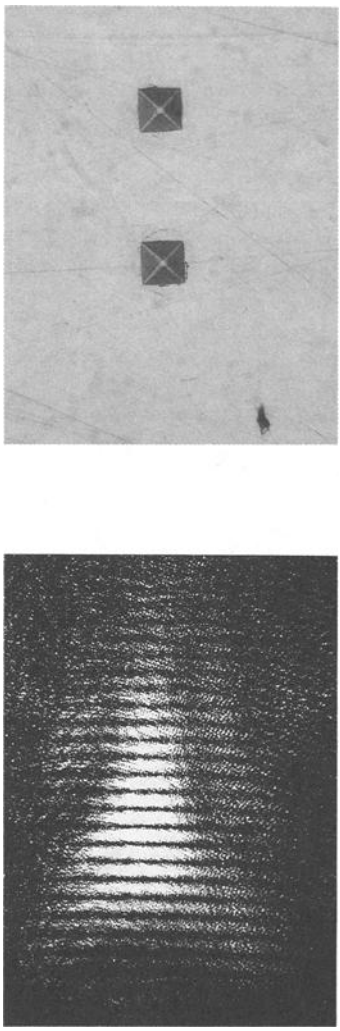

FIG. 2—*Photomicrograph of a set of indentations and photograph of an interference fringe pattern. The centers of the indentations are 100 μm apart.*

The equation giving the relative displacement Δd from the fringe movements Δm is

$$\Delta d = \Delta m \frac{\lambda}{\sin\alpha_0} \tag{2}$$

The angle α_0 is the angle between the incident laser beam and a fixed measurement position (at C or D in Fig. 1) and is approximately 42° because of the shape of the Vickers diamond. So the "calibration factor," $\lambda/\sin\alpha_0$, is ~1 μm. A fringe shift of one, that is, a fringe moving to occupy the position of a neighbor, corresponds to a relative displacement between the two indentations of ~1 μm.

It is obvious that if the specimen moves in a rigid-body manner, the fringes will also move. It is very difficult to construct a test machine in which the specimen does not move vertically as the load is applied, so that motion must be accounted for. If the specimen moves up (Fig. 1), then the fringe pattern at C moves away from the incident laser beam and the one at D moves toward the incident beam. If one defines fringe motion toward the incident laser beam as positive, then the vertical rigid body effects can be averaged out. This definition of sign means that increasing distance between the indentations is recorded as positive. Other rigid-body motions are not averaged out and can lead to errors; however, the results to follow show that these errors are small in a carefully aligned test machine.

So, the equation that is used with the ISDG is

$$\Delta d = \frac{\Delta m_1 + \Delta m_2}{2} \frac{\lambda}{\sin\alpha_0} \tag{3}$$

where Δm_1 and Δm_2 are the fringe movements at the two observation positions.

Larger displacements, say more than 5 or 10 μm, can be measured simply by recording the fringe motions versus load on an *X-Y* plotter, determining the loads at which maxima and minima occur, and plotting the load-displacement curve. The basic resolution is therefore 0.5 μm, which is too coarse for use with small cracks. Computer-controlled measurement systems with resolutions as small as 0.005 μm are described later, but first some practical aspects of the measurement technique are presented.

Practical Considerations

Although only the sides of the indentations need to be smooth and reflective, a polished specimen surface will produce better fringe patterns. If the surface is rough, then some of those features may be impressed into the sides of the indentation and degrade the reflected diffraction pattern. But the most serious consequence of a rough surface is the reflection of the incident beam into the fringe pattern. This can be avoided by making the last polishing motions along the line between the indents; reflections from the surface marks will then go into the side interference patterns and not the two that are monitored. Surfaces with a final polish using 600 grit paper have been used, but a final polish with 1-μm slurry or paste is normally used for small crack testing. Better surfaces can be prepared by electropolishing [*29*]; this produces a scratch-free surface and also delineates the material's microstructure.

Of course the main problem is finding the small crack so that indentations can be placed across it. Acetate replicas [*21*] and direct optical microscopic observation [*29*] have been used; once the crack is found, the specimen can be removed from the test machine and indents applied. Surface cracks as small as 50 μm long have been studied this way [*21*]. Such cracks require very small indentations, 7 μm square, so that the act of applying the indent does not distort the crack surface and cause a falsely high closure measurement.

Indentations can be applied with any of the commercially available microhardness testers. The shape of the Vickers diamond indenter is convenient, and one can place indentations within a micrometre of a desired location without any problem. Figure 3 is a photomicrograph of indentations across a short crack in 2024-T3 aluminum; it illustrates a problem with crack opening displacement measurements. The crack is not straight and perpendicular to the loading direction—as is assumed in most analyses. It tends to follow the grain structure on the surface, which in this case is elongated in the direction of loading with grains roughly 25 by 100 μm.

The smaller the indentation the less intense the individual fringes, so that a larger laser is needed for small-crack studies. Indentations 20 μm square in a reflective metal give good

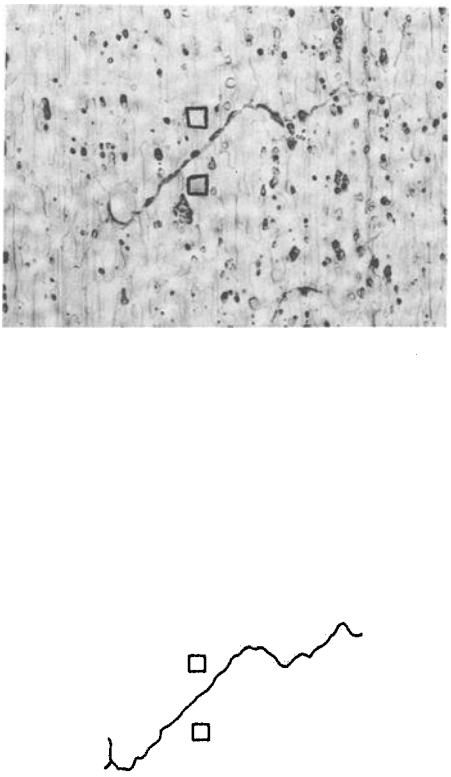

FIG. 3—*Photomicrograph of a set of indentations across a small fatigue crack in 2024-T3 aluminum. The crack is 210 μm long and the indentations are 50 μm apart. The sketch at the bottom is a tracing from the photomicrograph.*

fringe patterns (bright enough to produce a high signal-to-noise ratio from a detector) when illuminated with a 5-mW He-Ne laser. Higher power lasers, 15 mW or more, are routinely used, but safety then becomes more of a concern. Even a low-power laser can cause discomfort or damage if reflected from a polished surface directly into the eye. A dim room is required for observing the fringes and aligning the laser and detectors. The human eye is very sensitive and, in a dark room, can easily see fringe patterns that are too weak to produce a good signal from most detectors. If a higher power laser is used, it is recommended that a filter be inserted in the incident beam during the alignment process and then removed for testing. Detectors can be covered with interference filters so that tests can be conducted in ordinary room light. Optical masks of black cardboard are very helpful in reducing stray reflections that may shine on the detector or into the eye of an operator.

Computer Controlled Systems

The resolution of the ISDG technique can be significantly increased by using computer controlled methods to measure fractional fringe motion. Several different strategies for tracking fractional fringe motion have been developed, and the salient features of each is briefly described in the following sections. Common to each of these methods is an underlying

software strategy that controls the ISDG systems and provides realtime testing capability. This strategy is briefly outlined below, four different existing systems are described, and typical characteristics of one of them are given. Currently there are no commercial manufacturers of ISDG systems; the key components are readily available.

Software Strategy

The basic steps in obtaining a single displacement data point are as follows: (1) acquire fringe data, (2) process the fringe data to obtain current positions of the fringes, (3) compare the current fringe positions with the previous ones, (4) compute the change in displacement and the total displacement, and finally, (5) store the data. Normally, these steps are repeated hundreds of times in order to construct a complete load-displacement trace. Unfortunately, the appropriate software is not currently commercially available, and establishing the software should not be considered a trivial task.

To acquire the fringe data, standard analog to digital (A/D) converters are used. In addition, digital to analog (D/A) converters are required to control functions such as loading and synchronization. Software must be established to control the A/D and D/A utilities and to acquire the data. The basic control software for the A/D and D/A hardware is usually supplied by the manufacturer, but this software must be tailored to accomplish the objectives of a specific ISDG system.

Processing of the fringe data consists of searching the fringe data arrays and determining the current position of several fringes. Typically, fringe positions are determined by searching for maxima or minima in the fringe signal. To simplify processing, it is advantageous to provide software that will smooth the fringe data before processing. Actual changes in displacements are calculated using Eq 3, and the accumulation of the displacements provides the total displacement.

There are two types of data that are of interest. These are (1) the digital displacement information for each loading cycle and (2) the test history. The test history information includes quantities such as the cycle count, crack length, maximum load, time, and date. The digital displacement data can be used to compute the elastic compliance and the closure load, which can be calculated in real time, or the displacement data can be saved for post-test analysis.

The software code for a real-time ISDG system can become lengthy and complex; a FORTRAN program for the diode array system is included in Ref *27*. It is advantageous to off-load specific tasks from the software into laboratory peripherals, which may be controlled through the software. An example of this technique is the use of a programmable function generator to develop a command signal for a fatigue machine. Although the load control signal could be generated through the computer software, a dedicated function generator will provide considerable flexibility and simplicity to the system. This general idea can be used throughout any particular ISDG control system to simplify and reduce the software requirements.

Scanning Mirror System

Figure 4 presents a schematic of the original scanning mirror system [*30*]. The fringe pattern falls on a small servo-controlled mirror that receives its control signal either from the microcomputer or from a function generator. The fringes are directed onto a slit in front of a photomultiplier tube (PMT); this slit is narrower than the spacing between the fringes. The motion of the mirror has a backward sawtooth shape causing the fringes to move across the slit at a uniform rate. The PMT voltage is sampled at a uniform rate also, with the result

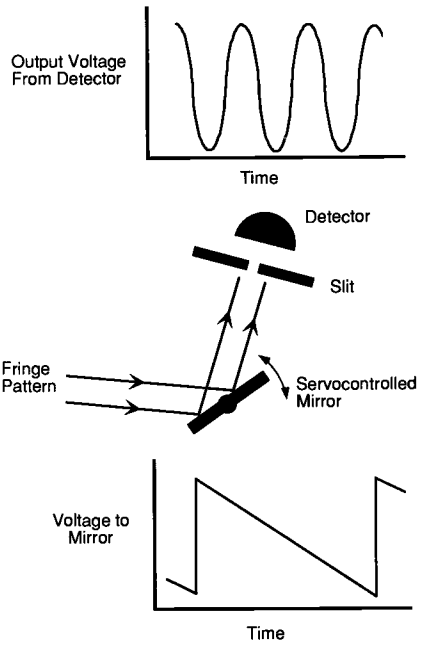

FIG. 4—*Schematic of the scanning mirror system.*

that the digital signal acquired by the microcomputer is effectively the fringe intensity versus angle.

If the mirror-controlling signal is generated in digital form within the microcomputer, then synchronization of the mirror position and the PMT signal is ensured. However, this requires a D/A channel for each mirror, and since many A/D, D/A boards have only two D/A channels, another strategy must be used. (One D/A must be used to send out the load signal, and it is convenient to use one to drive a plotter or oscilloscope.) A digital function generator with a trigger signal at the start of each cycle can serve as the master controller of a system—the trigger signal starts the A/D conversion of each PMT signal. In practice, a triangular waveform is used instead of the sawtooth because it introduces a smaller transient into the mirror. The period of the waveform is chosen so that signal acquisition occurs within the rising portion and computation, data storage, and so forth, occur before the next cycle starts. This period is about 90 ms, with roughly half devoted to acquisition and half devoted to computation.

Figure 5 is a plot of two load-displacement records from the crack shown in Fig. 3. The first is when the crack is 0.21 mm long—as measured perpendicular to the load axis and as shown in Fig. 3. The second is after the crack has grown to 1.23 mm long; by that time it was fairly straight overall and perpendicular to the load axis. Both plots show the hysteresis commonly found in local crack-opening displacement (COD) measurements; the loading part of the curve is on the top.

The high resolution of the COD obtained with this system is shown in Fig. 5. The "least count" or displacement value corresponding to one bit in the digital signal varies between 0.005 and 0.010 μm depending upon the particular setup. It should also be noted that this is a real-time measurement, that is, the plots of Fig. 5 could have been displayed on a plotter as they were being taken.

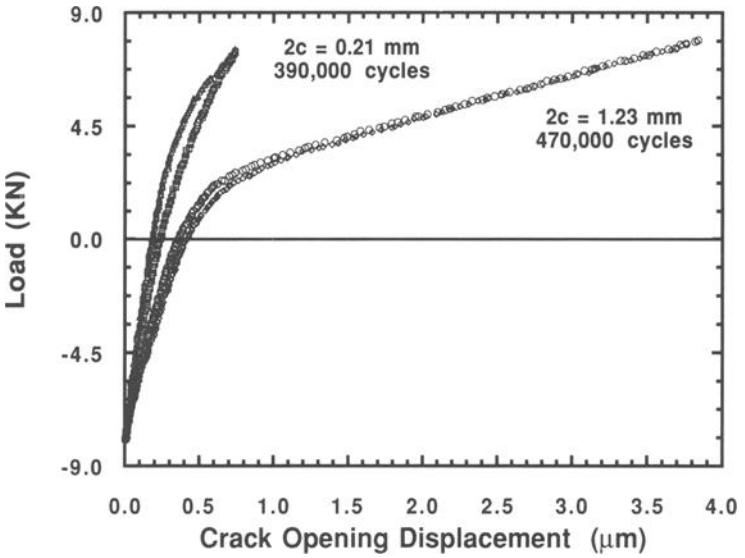

FIG. 5—*Load versus COD plots for the microcrack of Fig. 3 at two stages in its growth.*

Diode Array System

Recent advances in solid state line-image sensors (linear diode arrays) have made them very attractive for acquiring fringe data. A fractional fringe monitoring ISDG system using linear arrays was originally developed by Hartman and Nicholas [*31*], and a later version was constructed by Sharpe [*27*]. The scanning mirror and PMT are replaced by a single detector composed of a series of closely spaced elements. By sequentially addressing each element, a digital representation of the fringe pattern can be conveniently obtained for computer analysis. Through this solid-state approach, several advantages over the scanning mirror approach have been achieved.

The key component to this system is the detector array. Several different types of arrays have been used, although they typically contain 500 to 1000 detector elements equally spaced along an axis. Originally, the arrays were charge coupled devices (CCD) with aperture dimensions 13 μm square. This relatively small aperture made them very sensitive to small variations in fringe intensity. Currently, better results have been obtained using a photodiode detector array with apertures 13 μm high and 2.5 mm wide. The wider aperture averages out more of the speckle of the fringe pattern than the original CCD detectors. Also, the additional light gathering area of the photodiode detectors provides a higher signal-to-noise ratio and thus produces better fringe resolution.

A significant enhancement to this system has been obtained through the use of cylindrical lenses. Appropriate mounting hardware holds the lenses and allows precise alignment to focus the fringe pattern onto the aperture of the array. The lenses do not distort the fringes in the direction of the fringe spacing, but instead condense the fringes in the transverse direction thus channeling the available fringe intensity into the detectors. This technique can be useful in low fringe intensity situations.

A mounting plate is needed for the laser, the beam alignment mirror, and the diode arrays; this is usually fastened to the test machine although it may be mounted on a tripod. The support electronics continually scan the diode arrays and produce voltage versus time sweeps representing the light intensity. The interface electronics package contains amplifying and filtering circuits to condition the output signals from the detectors. The signals produced by the interface package are captured by the computer, which processes and stores the information.

A typical data acquisition sequence consists of 100 scans from each of two diode arrays during a loading cycle. Each scan typically contains 512 digitized points representing the light intensity across the array and is essentially a digital "snapshot" of the fringe position at a given load. To obtain fringe position data from each fringe pattern, an algorithm starts at the data point representing the center of the detector array and searches forward and backward to find the first fringe minimum on either side of the center of the detector. The motion of the fringe pattern is computed by comparing the current position of the fringe minimums to their previous positions. The current fringe spacing is used in the computations.

Mechanically, the linear array approach is much simpler than its predecessor, the scanning mirror approach. Without the mechanical limitations imposed by the scanning mirrors, the system can acquire data at a much faster rate. Currently linear arrays operate at 250 to 500 scans per second, and therefore data acquisition rates are limited only by the speed at which the data can be digitized and processed. In addition, the overall hardware costs for an array system are about half the cost of a scanning mirror system. On the other hand, an array system is electronically more complicated than a scanning mirror system and implementation requires considerable expertise.

Tracking Diode System

A completely different approach with slightly higher sensitivity has been developed by Ebi and Neumann in Germany [25]. The interference fringe pattern shines through a coarse linear grating, which generates Moiré fringes. These fringes impinge on a photodiode, which is mounted on a servocontrolled translation stage. The result is that a small motion of the interference fringes produces a large motion of the Moiré fringe. The controlling microcomputer moves the photodiode to keep it at the midpoint of the intensity of the Moiré fringe (the slope of intensity versus angle is highest there), and the position of the photodiode is proportional to the displacement of the indentations.

The system has a high resolution of 0.003 μm; however, it is slower than the two systems described above, taking 2 s for each data point. Figure 6 is a load-displacement plot from a crack 274 μm long in austenitic stainless steel.

Pulsed Laser System

An ISDG system for use on specimens cycled at 30 Hz has been developed by Akiniwa et al. [26]. A specimen is cycled until a crack is found, and then indentations are applied. The test is then continued at a low-stress-intensity factor range while monitoring the load-displacement curves.

A 30-mW pulsed laser with wavelength of 0.788 μm is used to illuminate the indentations. This laser, which requires cooling for stability of the wavelength, has a diverging beam, which is collimated with a lens. A microcomputer controls the entire test and triggers the laser to produce a fringe pattern at a particular load value. The width of the pulse is 0.33 ms, 1/100th of the period of the loading cycle. The fringe pattern is recorded with a diode

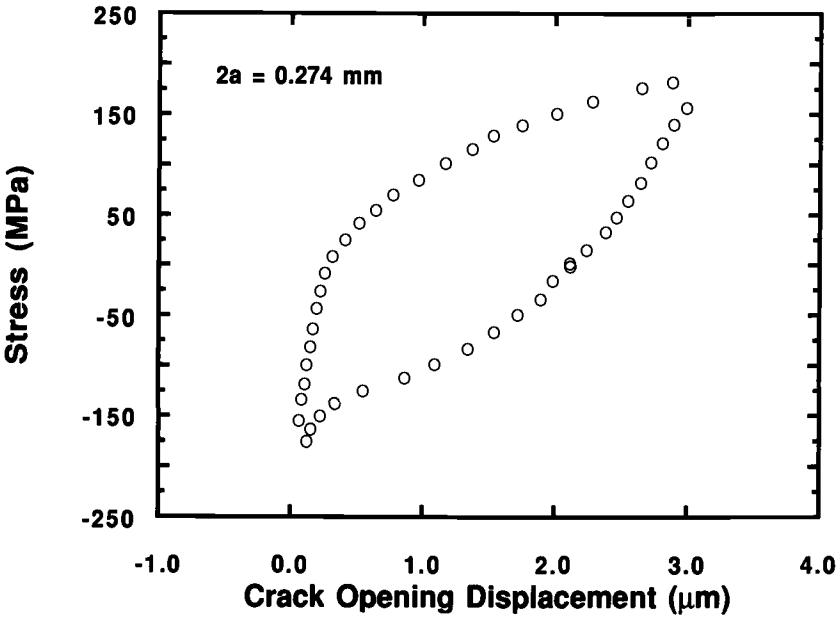

FIG. 6—*Load versus COD obtained with the tracking diode system* [25].

array, and it may be necessary to sample at the same load value for several consecutive cycles to build up an acceptable signal on the diodes. (However, this repetition may be avoided by using cylindrical lenses to concentrate the fringes onto the diodes.) Once the fringe pattern for a particular load value is obtained, the timing of the laser pulse is shifted to another load value. In this way, a complete load-displacement record is built up by sampling consecutive load cycles. The approach is analogous to that used in sampling oscilloscopes.

The approach of Akiniwa et al. is to store all the fringe data for one record and then do the computations to produce a load-displacement curve. The diode array has 512 elements, so 51 200 data points are temporarily stored. Typically, 5 consecutive cycles are needed to produce a good signal on the diode arrays, so it takes 500 cycles or 16.67 s to acquire that data. The computations take another 18 s, so a load-displacement record is produced every 35 s, approximately every 1000 cycles. If one is conducting high-cycle crack growth tests, this sampling rate is adequate. A plot of one of their load-displacement curves is shown in Fig. 7.

Instrument Characteristics

The instrument characteristics, such as range, resolution, and accuracy, are rarely reported in papers and reports where the ISDG is described; emphasis is on the results. Usually if the elastic modulus measured when the crack is fully closed, or the compliance measured when the crack is fully open, agrees reasonably well with expectations, the measurement system is assumed to be sufficiently accurate. It may be useful to look at the results of a calibration as presented in Fig. 8 in order to get a more quantitative feel for the capabilities of an ISDG measurement system.

The problem in conducting a calibration is generating a suitable "true value" or measur-

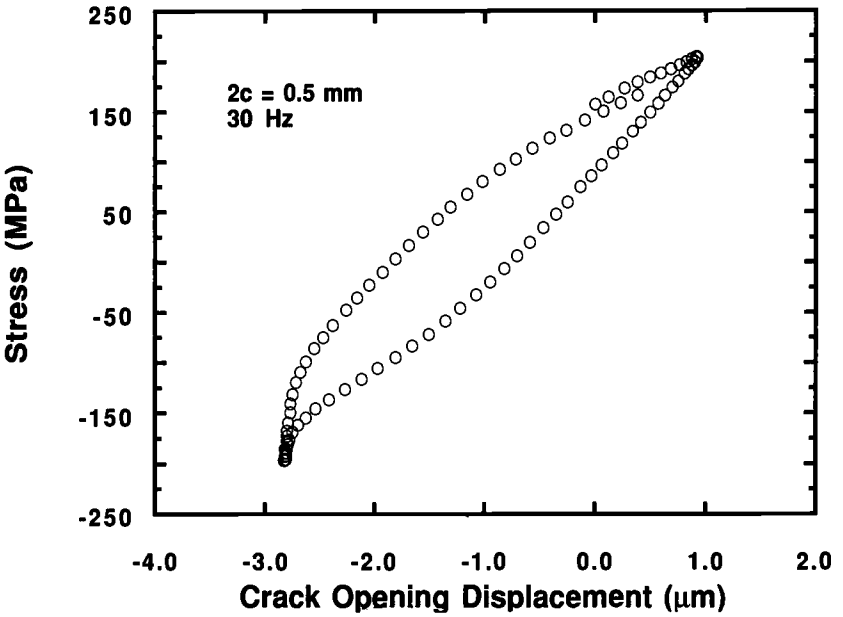

FIG. 7—*Load versus COD obtained with the pulsed laser system* [26].

and; this is especially difficult when one wants to move two indentations that are a few 100 μm apart. The test setup used for the current example was a smooth flat aluminum specimen in a tension test machine with foil resistance strain gages on the two flat sides. A pair of indentations, 200 μm apart, was placed on one edge and a clip gage placed on the other edge. All four gages read very similar values as the specimen was loaded elastically; the alignment was well within the specifications of ASTM Practice for Verification of Specimen Alignment Under Tensile Loading (E 1012).

The plot in Fig. 8 was produced by multiplying the averaged foil gage readings (which were practically identical) by 200 μm to produce a displacement in nanometers; the displacement as measured by the ISDG is plotted on the ordinate. Zero displacement corresponded to zero load, and the calibration was run in tension-compression for one cycle. A straight line was fitted by least-squares to the data, and the standard deviation of the ordinate differences from the straight line was computed.

The slope was 0.96 with the intercept being 1.91 nm. The resolution of the ISDG was 5.2 nm, that is, one bit in the digital output corresponded to that displacement. The standard deviation σ is 3.1 nanometers, and the error bands drawn in Fig. 8 are at $\pm 3\sigma$ or ± 9.3 nm. The error band here is approximately twice the resolution. The range here is 140 nm (although it could be much larger; in principle there are no nonlinearities in the ISDG measurements). The width of the error band is really a measure of the accuracy or precision—here these are nearly the same since the slope is almost 1.0. It is customary to state accuracy as a percent of full scale; in that case, the accuracy of the ISDG is 6.9%. But that is based on an error band of $\pm 3\sigma$. If one uses the probable error (0.674σ, which means that 50% of the points lie within the error bands) then the accuracy is $\pm 1.5\%$ of full scale.

This is a calibration on a single setup and illustrates the best that the scanning mirror ISDG system can do. However, other systems would probably exhibit similar characteristics under ideal circumstances.

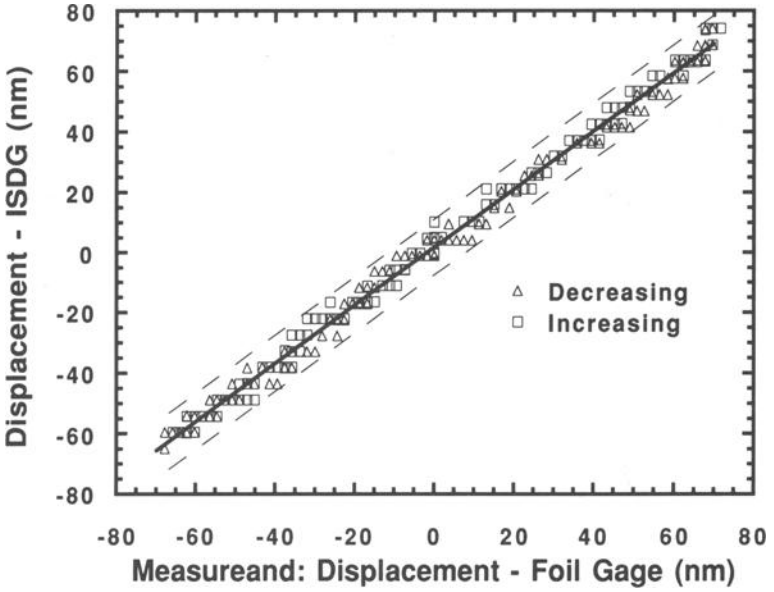

FIG. 8—*A calibration of the scanning mirror ISDG system.*

Applications of the ISDG

The ISDG has been used to measure the COD of small surface cracks in several alloys. Examples from studies on titanium alloys that illustrate the capabilities of the technique are presented here. Compliances measured after the crack is fully open can be used to determine crack length and shape, and use of this information to automate crack-growth testing is described.

COD Data from Small Cracks in Titanium

The ISDG has been used by the authors to acquire data on small fatigue cracks in various materials, including a number of titanium [*16–19,22,23*] and aluminum alloys [*20,21*] having different small-crack, closure, and crack topography characteristics. Data from two of the titanium alloys represent extremes in small-crack behavior and have therefore been selected to represent the capabilities of the ISDG system as applied to small-crack testing. These alloys are Ti-6Al-2Sn-4Zr-6Mo in the heat treated and aged condition and Ti-8Al in the solution treated and quenched condition. Ti-6Al-2Sn-4Zr-6Mo is a fine-grain, high-strength alloy used in turbine engine components, and the solution-heat-treated Ti-8Al is a research material that demonstrates high levels of crack closure. Photographs of small surface cracks in each of these materials are shown in Figs. 9 and 10; the Vickers microhardness indentations used for crack opening displacements are visible.

Typical load-displacement data for the two materials are presented in Figs. 11 and 12. The differential load-displacement data that are also shown were obtained by fitting a line to the upper linear portion of the load-displacement data and subtracting the resulting linear-

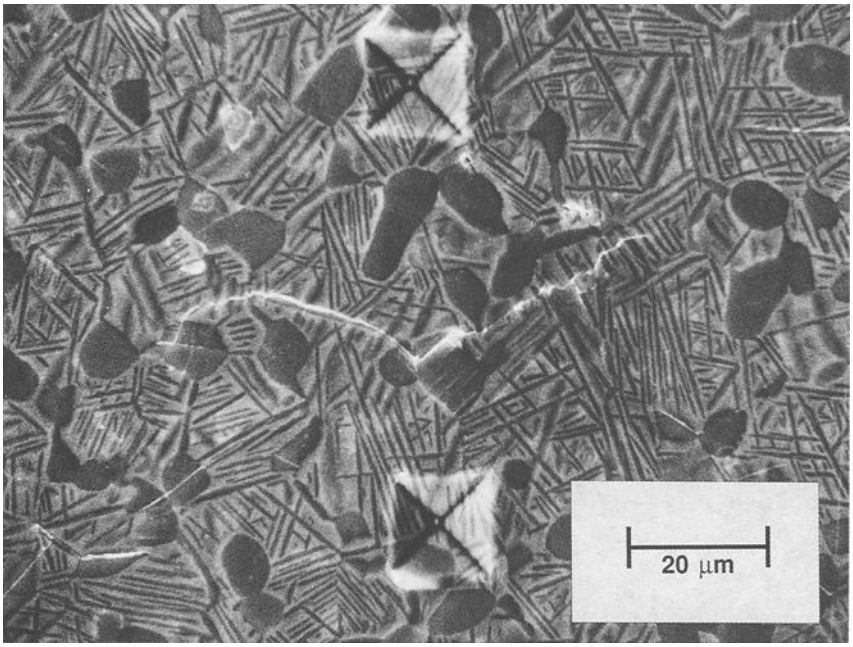

FIG. 9—*Microcracks and indentations of Ti-6Al-2Sn-4Zr-6Mo.*

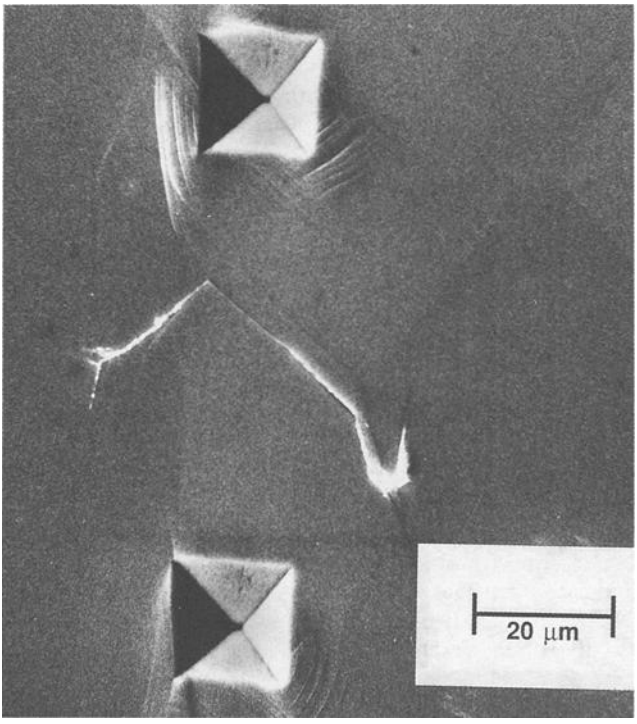

FIG. 10—*Microcracks and indentations of Ti-8Al.*

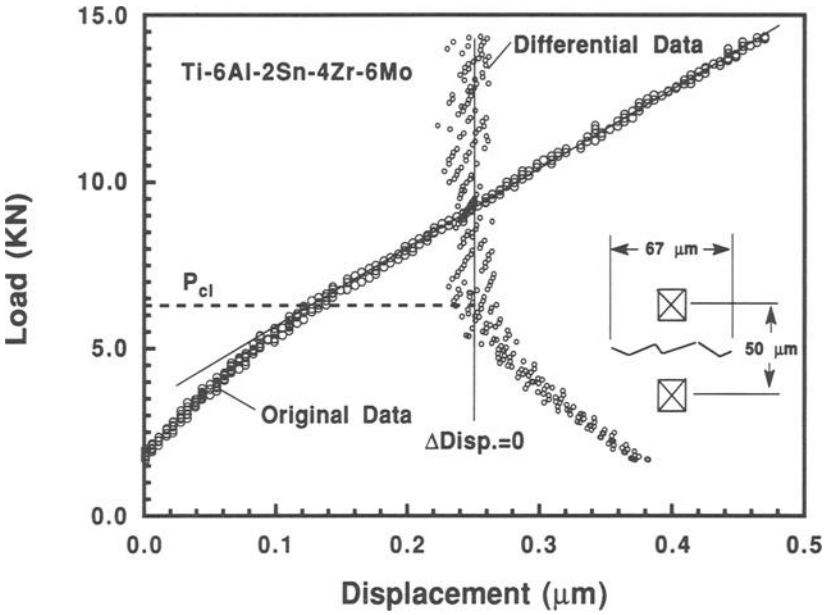

FIG. 11—*Load versus COD for the Ti-6Al-2Sn-4Zr-6Mo alloy of Fig. 12a. The differential load-COD data are also shown.*

elastic component of crack opening displacement from the measured displacement. The Ti-6Al-2Sn-4Zr-6Mo data shown in Fig. 11 demonstrate the high resolution of the ISDG system. These data were acquired from a surface crack of length $2c = 67$ μm. For this case, the total crack mouth opening displacement measured under maximum load was approximately 0.5 μm, and the complete load-displacement trace exhibits no detectable hysteresis. In this material, the crack closure load P_{cl} and crack opening load P_{op} are indistinguishable and are marked by a well-defined break from linearity in the load-displacement data. For the data in both Figs. 11 and 12, P_{cl} has been defined by the deviation from linearity in the unloading load-displacement data. It should be noted, however, that computer storage of the load-displacement data allows post-test closure analysis to be conducted using any of the alternative methods proposed in the literature.

In contrast to the behavior exhibited by the small crack in the Ti-6Al-2Sn-4Zr-6Mo, Fig. 12 presents data from the Ti-8Al alloy, which clearly show load-displacement hysteresis. These data were acquired from a crack of length $2c = 122$ μm. Inspection of the data indicate that, although similar, $P_{op} \neq P_{cl}$. The ability to record such details is a particular strength of the ISDG.

The calculation of crack length from compliance may be accomplished using expressions developed by Mattheck et al. [*32*] or Fett [*33*]. Each of these expressions is a function of crack aspect ratio, a/c, requiring an estimate of crack shape. For example, in Ti-6Al-2Sn-4Zr-6Mo, small-crack aspect ratios were documented by heat tinting experiments, which showed an approximately constant value of $a/c = 0.9$. Assuming that a/c remains constant, the relationship between crack length c and compliance may be examined and compared with the analytical prediction, as shown in Fig. 13. The solid line represents the relationship predicted using the Mattheck expression, while the symbols represent optically measured crack length versus experimental measurements of compliance using the ISDG. The general agreement is excellent. Most of the variability of the experimental data about the predicted

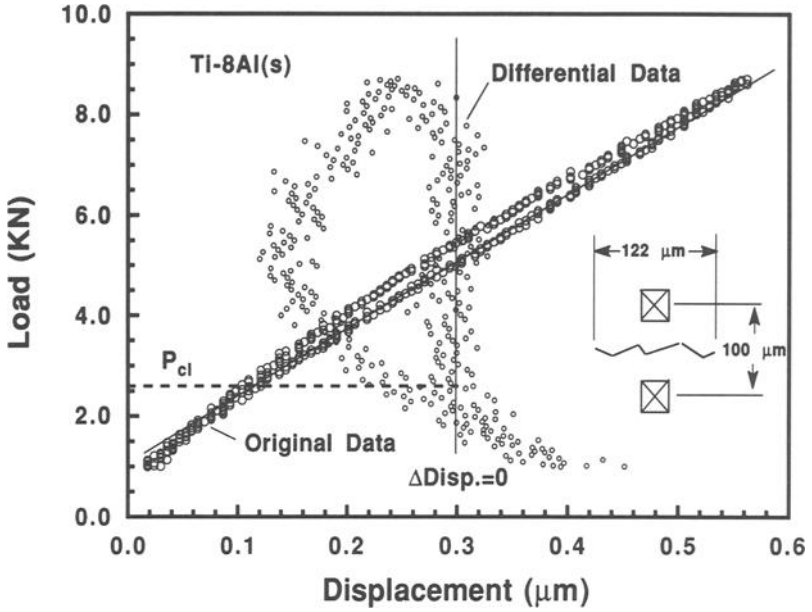

FIG. 12—*Load versus COD for the Ti-8Al alloy of Fig. 12*b. *The differential load-COD data are also shown.*

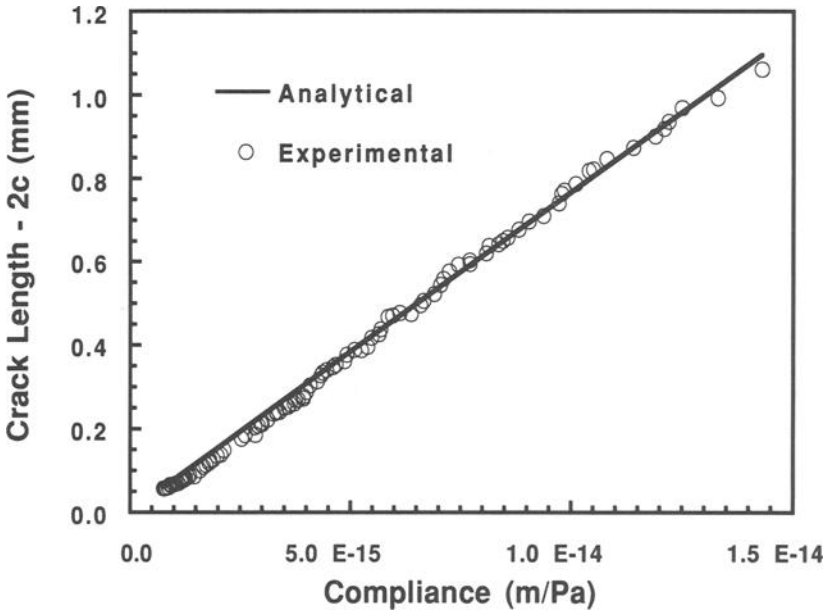

FIG. 13—*Crack length versus compliance for a small surface crack.*

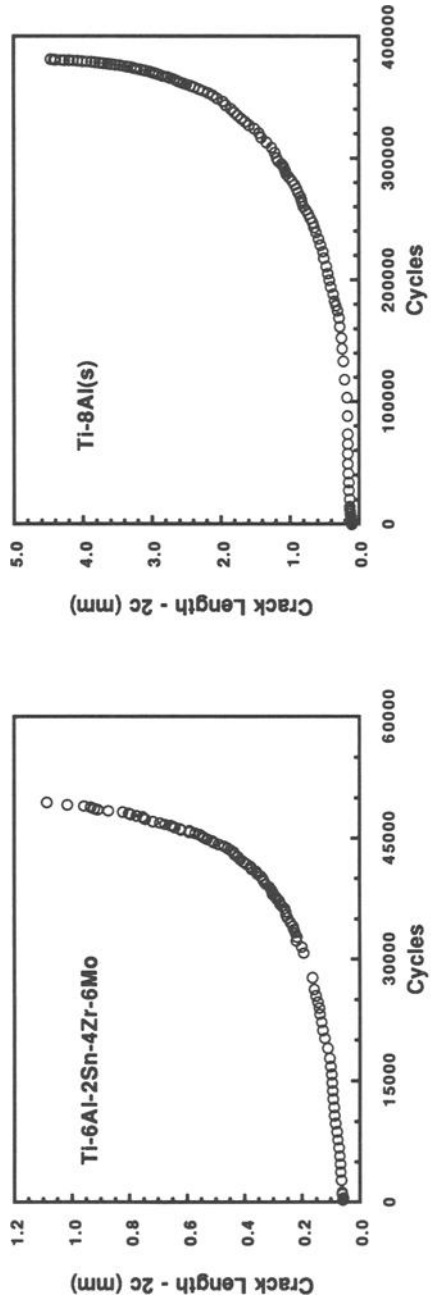

FIG. 14—*Crack length versus number of cycles for the two titanium alloys:* (a) *Ti-6Al-2Sn-4Zr-6Mo and* (b) *Ti-8Al.*

line are due to variations in the optically measured crack length. The optical measurements may be expected to be more variable, because they represent observations on a two-dimensional surface, and the resulting crack length measurements reflect the interaction of the crack tip with discrete microstructural features. The compliance data represent the behavior of the three-dimensional crack and tend to average crack length variations along the semielliptical crack front.

Typical data of crack length calculated from ISDG measurements versus cycle count N are presented in Fig. 14 for the two materials. In each case, optical measurements of surface crack length were in good agreement with compliance calculations of crack length. Because of accentuated interactions of the small crack with microstructural fractures in Ti-8Al, this material demonstrates significantly more discontinuous crack growth behavior than does the Ti-6Al-2Sn-4Zr-6Mo. Figure 15 presents the corresponding $da/dN - \Delta K$ plots for the example data sets. In each plot, the solid line represents data from large cracks in conventional C(T) specimens. The Ti-6Al-2Sn-4Zr-6Mo data from small and large cracks are in excellent agreement. These data are typical of a body of related ISDG small-crack data acquired in this material. This agreement tends to validate the surface flaw stress intensity factor solution [*34*], as well as validating the accuracy of the experimental methodology for the small surface cracks.

In contrast to the good agreement between large- and small-crack data found for the Ti-6Al-2Sn-4Zr-6Mo alloy, similar data from the Ti-8Al show a distinct crack-size effect. In this material, the small-crack data fall well above the large-crack trend, and the small-cracks grow under conditions that are well below the large-crack threshold stress intensity factor range ΔK_{th}.

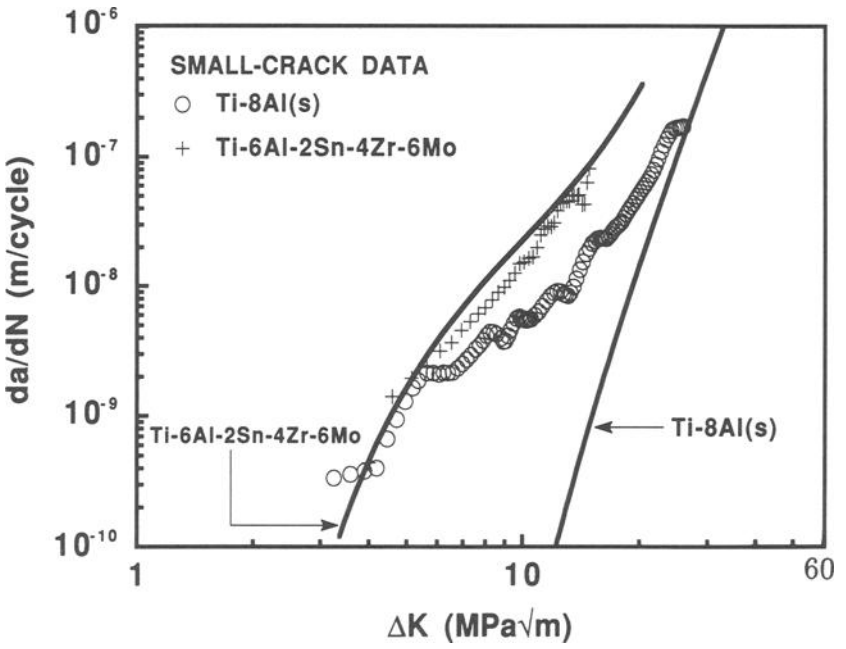

FIG. 15—*Crack-growth-rate versus* ΔK *for the Ti-6Al-2Sn-4Zr-6Mo and the Ti-8Al alloys. The solid line is long-crack data from conventional CT specimens.*

A key difference between the two materials lies in their respective closure behavior, as shown in Fig. 16, which presents large- and small-crack closure measurements plotted as a function of K_{max}. For both materials, the large-crack closure levels are approximately constant, while the respective small-crack closure levels initially increase with increasing K_{max} (increasing crack size) and ultimately tend to assume a level that agrees with the large-crack trend. When these crack closure data are used to calculate values of $\Delta K_{eff} = K_{max} - K_{cl}$, the large- and small-crack data are consolidated into narrow bands as shown in Fig. 17. Thus it appears that crack closure effects are largely responsible for the observed differences between large- and small-crack $da/dN - \Delta K$ data. Detailed discussion of the behavior of small cracks in these and other titanium alloys is available elsewhere [*16–19,22,23*].

Applications to Crack Growth Studies

In the previous section, it was shown that real-time measurements of crack length can be made using ISDG compliance measurements. This single capability opens a myriad of potential applications for small-crack research, because it provides a source of feedback for computer control of small-crack fatigue tests. Recently, this capability has been applied to automated small-crack testing in a manner similar to conventional large-crack methods. The following discussion presents some of these applications.

The examples of small-crack data shown previously were acquired under computer controlled fatigue. During fatigue testing, the computer periodically generated crack length and closure data from the ISDG measurements. Using these data, the computer made test control decisions and controlled the fatigue machine. For example, every time a cycle of load-displacement data was taken, the crack length was calculated from the compliance and stored with the corresponding fatigue cycle count. This information was used to estimate

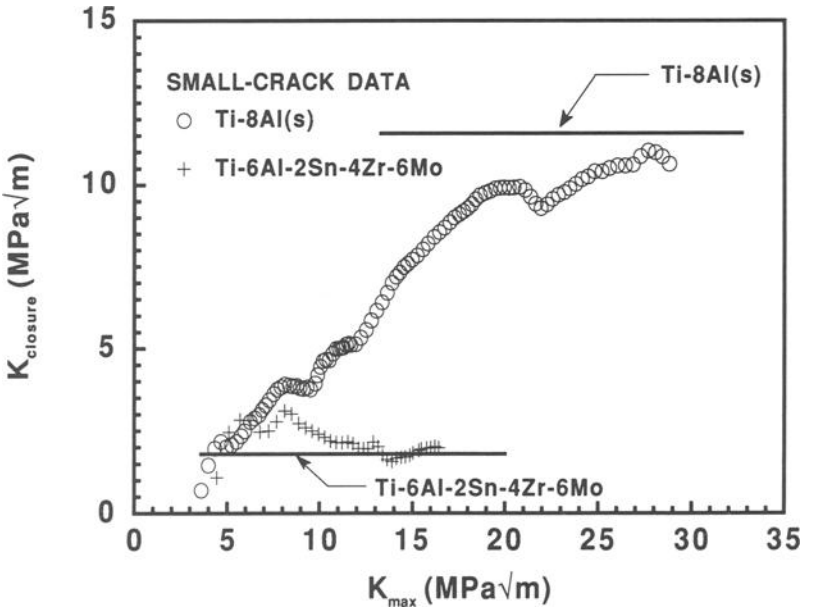

FIG. 16—*Load versus COD for the Ti-6Al-2Sn-4Zr-6Mo alloy of Fig. 12*a. *The differential load versus COD data are also shown.*

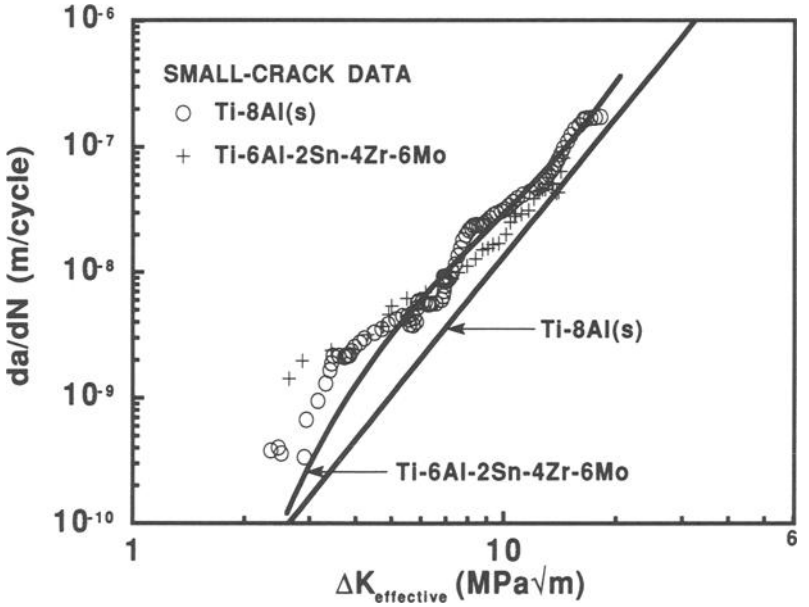

FIG. 17—*Crack-growth-rate versus* ΔK_{eff} *for the Ti-6Al-2Sn-4Zr-6Mo and the Ti-8Al alloys. The solid line is long-crack data from conventional CT specimens.*

the current growth rate and to determine the number of fatigue cycles before the next data was taken. This minimizes the volume of data required to define the growth rate behavior throughout the fatigue life. In addition, with real-time knowledge of the growth rate, tests can be aborted prior to final fracture, which allows post-test analysis of the unfailed specimens.

The ISDG technique has been used to control the fatigue amplitude of small-crack tests. Jira et al. [*23*] used this approach to investigate the effects of load history on fatigue crack growth thresholds ΔK_{th} in small cracks. During fatigue crack growth testing on small cracks, the applied load amplitude was adjusted based on a prescribed stress intensity history and the crack length determined from ISDG compliance. In this manner, four different load histories were applied to small surface cracks to achieve growth rates near threshold. The load histories included both increasing and decreasing stress intensity factor range ΔK tests. Throughout testing, crack closure was monitored using the ISDG to establish the effect of closure on the growth rates. The investigation established a history-independent threshold stress intensity in surface cracks and illustrated a unique capability for automated material testing through the use of an ISDG.

In a separate application of the ISDG, the opening compliance of small cracks was used to investigate shape changes of small fatigue cracks. As discussed earlier, the opening compliance of a surface crack is a function of crack size and crack shape. Normally, small-crack shape can be shown to be approximately constant, allowing crack size to be calculated from compliance. However, some alloy microstructures are sufficiently coarse, or exhibit a sufficiently intense microstructural or crystallographic texture, as to dramatically affect crack shape. In these instances, measurement of crack shape becomes important, because local changes in crack shape can result in appreciable variations in apparent crack growth rate. Recently, Ravichandran and Larsen [*24*] combined the capabilities of the ISDG with direct photographic measurements of the surface length of small cracks to obtain an estimate of

crack shape. By using independent crack length and compliance measurements, crack depth (crack shape) was calculated directly using the appropriate compliance expression. The accuracy of the crack shape calculations was verified by direct optical measurements on heat-tinted fractures surfaces. For a number of measurements on small cracks of shapes in the range $1.0 \leq a/c \leq 2.0$, the difference between calculated and actual crack shape was less than 13%.

Another key advantage of the ISDG lies in its extremely high resolution for displacement measurements. This becomes apparent in research involving the study of very slow or "threshold" growth rates. The extreme resolution of displacement provided by the ISDG, produces a corresponding high resolution of crack length from compliance. Since the amount of crack length extension required to determine growth rate is directly related to the ability to resolve crack length, an ISDG system will permit the determination of very slow growth rates in a relatively short time. For example, a typical resolution of compliance crack length using conventional extensometry is approximately 50 μm. To measure a growth rate of 1×10^{-10} m/cycle with this resolution, requires the application of at least 500 000 fatigue cycles. In contrast, a crack length resolution of 1 μm is typical of an ISDG system. With this resolution, the measurement of the same growth rate would require as few as 10 000 cycles. The significance of this difference becomes apparent when these are converted to testing times. At 10 Hz, the application of 500 000 cycles would require 14 h, while 10 000 cycles would require only 15 min. Thus, the measurement of threshold crack growth rates becomes much more economical using an ISDG.

Advantages and Disadvantages

The ISDG is a specialized laboratory technique valuable for measuring displacement (and strain, although examples are not given here) over very short gage lengths. It has now been used enough by various laboratories to permit an evaluation of its strengths and weaknesses. It is useful to conclude by listing some of the advantages and disadvantages related to small-crack testing.

Attributes which may be viewed primarily as advantages of the ISDG for small-crack research:

- It is a noncontacting extensometer, which may be applied to naturally initiated surface cracks of length $2c$ greater than approximately 40 μm.
- It may be applied to cracks emanating from starter slits with lengths $2c \geq 200$ μm; cracks as large as $2c = 10$ mm have been studied by this method.
- Digital load-displacement data are produced and may be analyzed in real time to obtain measurements of three-dimensional crack size and crack closure load.
- The displacement resolution ranges from approximately 3 to 10 nm, depending on the specific ISDG approach that is used.
- Test control and data acquisition may be automated, significantly reducing the manpower requirements for testing.
- The ISDG closely resembles large-crack extensometry and can be utilized as such to provide real-time control of test parameters (for example, load-shed ΔK_{th} testing, constant K_{max} testing, and controlled ΔK_{eff} testing).
- Feasibility of use of the ISDG at high temperatures has been demonstrated on large cracks in certain materials; usage for high-temperature small-crack research should be readily achievable.
- The long-term stability of the diode-array version of the ISDG make it attractive for creep crack-growth studies.

Attributes which may be viewed primarily as disadvantages of the ISDG for small-crack research:

- It is necessary to locate a small crack before placement of the Vickers indentations used for displacement measurements.
- Purchase of the ISDG components may be costly, and assembly of the components into an operating system may be time-consuming.
- Once an ISDG system is operational, knowledgable technical personnel are needed to assure optimum utilization of the equipment's capabilities.
- Although the ISDG can be used at elevated temperatures, the specimen surface must be able to retain reflectivity at high temperature; for some materials this requires that a coating be applied to the specimen.
- For cracks of length $2c$ significantly less than the indentation spacing, displacement sensitivity is reduced. Thus, the finite size and spacing of the indentations limit the minimum measurable crack size.
- As a small crack extends, the distance from crack tip to measurement location increases. In some materials, this has been reported to influence closure measurements, although the full significance of this effect is still unknown.
- To enhance reflectivity of the indentations, the specimen surface must normally be polished.
- The specimen design and load train must limit rigid body motion to prevent movement of the indentations out of the incident laser beam; specimen out-of-plane displacements must be avoided.

The purpose of this paper has been to describe the ISDG and present some applications so that a reader can decide whether or not to use it. Reference *27* is a detailed description of an ISDG system and may be regarded as a "handbook." The other references describe various applications.

References

[*1*] Morris, W. L., "A Comparison of Microcrack Closure Load Development for Stage I and II Cracking Events for Al 7075-T651," *Metallurgical Transactions*, Vol. 8A, 1977, pp. 1087–1093.

[*2*] Morris, W. L., "Microcrack Closure Phenomena for Al 2219-T851," *Metallurgical Transactions*, Vol. 10A, 1979, pp. 5–11.

[*3*] Morris, W. L. and Buck, O., "Crack Closure Load Measurements for Microcracks Developed During the Fatigue of Al 2219-T851," *Metallurgical Transactions*, Vol. 8A, 1977, pp. 597–601.

[*4*] Morris, W. L., "The Early Stage of Fatigue Crack Propagation in Al 2048," *Metallurgical Transactions*, Vol. 8A, 1977, pp. 589–595.

[*5*] Morris, W. L., "Crack Closure Load Development for Surface Microcracks in Al 2219-T851," *Metallurgical Transactions*, Vol. 8A, 1977, pp. 1079–1085.

[*6*] Davidson, D. L. and Lankford, J., "Fatigue Crack Tip Strains in 7075-T6 Aluminum Alloy by Stereoimaging and Their Use in Crack Growth Models," *Fatigue Mechanisms: Advances in Quantitative Measurement of Physical Damage, STP 811*, J. Lankford, D. L. Davidson, W. L. Morris, and R. P. Wei, Eds., American Society for Testing and Materials, Philadelphia, 1983, pp. 371–399.

[*7*] Davidson, D. L. and Lankford, J., "High Resolution Techniques for the Study of Small Cracks," *Small Fatigue Cracks*, R. O. Ritchie and J. Lankford, Eds., The Metallurgical Society, Inc., Warrendale, PA, 1986, pp. 455–470.

[*8*] Lankford, J. and Davidson, D. L., "Near-threshold Crack Tip Strain and Crack Opening for Large and Small Fatigue Cracks," *Fatigue Crack Growth Threshold Concepts*, D. Davidson and S. Suresh, Eds., TMS-AIME, Warrendale, PA, 1984, pp. 447–463.

[*9*] Davidson, D. L., "The Experimental Mechanics of Microcracks," in this publication, pp. 81–91.

[10] Tanaka, K. and Nakai, Y., "Propagation and Non-Propagation of Short Fatigue Cracks at a Sharp Notch," *Fatigue and Fracture of Engineering Materials and Structures*, Vol. 6, 1983, pp. 315–327.
[11] Tanaka, K. and Akiniwa, Y., "The Propagation of Short Fatigue Cracks at Notches," *Basic Questions in Fatigue, Volume 1, STP 924*, American Society for Testing and Materials, Philadelphia, 1988, pp. 281–298.
[12] Clement, P., Angeli, J. P., and Pineau, A., "Short Crack Behavior in Nodular Cast Iron," *Fatigue and Fracture of Engineering Materials and Structures*, Vol. 7, 1984, pp. 251–265.
[13] Iyyer, N. S. and Dowling, N. E., "Opening and Closing of Cracks at High Cyclic Strains," *Small Fatigue Cracks*, R. O. Ritchie and J. Lankford, Eds., The Metallurgical Society, Inc., Warrendale, PA, 1986, pp. 213–223.
[14] Resch, M. T. and Nelson, D. V., "An Ultrasonic Method for Measurement of Size and Opening Behavior of Small Fatigue Cracks," in this publication, pp. 169–196.
[15] Sharpe, W. N., Jr., "Interferometric Surface Strain Measurement," *International Journal of Nondestructive Testing*, 1971, pp. 59–76.
[16] Larsen, J. M., Jira, J. R., and Weerasooriya, T., "Crack Opening Displacement Measurements on Small Cracks in Fatigue," *Fracture Mechanics: Eighteenth Symposium, STP 945*, D. T. Read and R. P. Reed, Eds., American Society for Testing and Materials, Philadelphia, 1988, pp. 896–912.
[17] Larsen, J. M., Williams, J. C., and Thompson, A. W., "Crack-Closure Effects on the Growth of Small Surface Cracks in Titanium-Aluminum Alloys," *Mechanics of Fatigue Crack Closure, STP 982*, J. C. Newman, Jr. and W. Elber, Eds., American Society for Testing and Materials, Philadelphia, 1988, pp. 149–167.
[18] Larsen, J. M., "The Effects of Slip Character and Crack Closure on the Growth of Small Fatigue Cracks in Titanium-Aluminum Alloys," Ph.D. dissertation, Carnegie Mellon University, Pittsburgh, PA, 1987; also published as Wright Research and Development Center report WRDC-TR-89-4094 (AD No. A220714), Wright-Patterson AFB, OH, 1990.
[19] Larsen, J. M. and Jira, J. R., "Small-Crack Closure Measurements in Titanium Alloys," *Experimental Mechanics*, Vol. 31, pp. 82–87.
[20] Lee, J. J. and Sharpe, W. N., Jr., "Closure Measurements on Short Fatigue Cracks," *Mechanics of Fatigue Crack Closure, STP 982*, J. C. Newman, Jr. and W. Elber, Eds., American Society for Testing and Materials, Philadelphia, 1988, pp. 270–278.
[21] Sharpe, W. N., Jr. and Su, X., "Closure Measurements of Naturally Initiating Small Cracks," *Engineering Fracture Mechanics*, 1988, pp. 275–294.
[22] James, M. N. and Sharpe, W. N., Jr., "Closure Development and Crack Opening Displacement in the Short Crack Regime for Fine and Coarse Grained A533B Steel," *Fatigue and Fracture of Engineering Materials and Structures*, 1989, pp. 347–361.
[23] Jira, J. R., Nagy, D., and Nicholas, T., "Influences of Crack Closure and Load History on Near-Threshold Crack Growth Behavior in Surface Flaws," *Surface-Crack Growth: Models, Experiments, and Structures, STP 1060*, American Society for Testing and Materials, Philadelphia, 1990, pp. 303–314.
[24] Ravichandran, K. S. and Larsen, J. M., "Microstructural Aspects of the Growth of Small and Large Fatigue Cracks in Titanium Aluminide: Ti-24Al-11Nb," *Fracture Mechanics: Twenty Second Symposium (Volume I), ASTM STP 1131*, American Society for Testing and Materials, Philadelphia, 1992, pp. 727–748.
[25] Ebi, G. and Neumann, P., "Closure Behavior of Small Cracks," *Proceedings of Fourth International Conference on Fatigue*, H. Kitagawa and T. Tanaka, Eds., *Materials and Component Engineering Publications*, Birmingham, United Kingdom, 1990, pp. 1033–1042.
[26] Akiniwa, Y., Harada, S., and Fukushima, Y., "Dynamic Measurement of Crack Closure Behaviour of Small Fatigue Cracks by Interferometric Strain/Displacement Gage with a Laser Diode," in *Fatigue and Fracture of Engineering Materials and Structures*, Vol. 14, 1990, pp. 317–328.
[27] Sharpe, W. N., Jr., "An Interferometric Strain/Displacement Measurement System," NASA Technical Memorandum 101638, Aug. 1989.
[28] Jenkins, F. A. and White, H. E., *Fundamentals of Optics*, McGraw-Hill Book Company, 1957.
[29] Larsen, J. M., Ravichandran, K. S., and Jira, J. R., "Measurement of Small Cracks by Photomicroscopy: Experiments and Analysis," in this publication, pp. 57–80.
[30] Guillot, M. W. and Sharpe, W. N., "A Technique for Cyclic Plastic Notch Strain Measurement," *Experimental Mechanics*, Vol. 23, 1983, pp. 354–360.
[31] Hartman, G. and Nicholas, T., "An Enhanced Laser Interferometer for Precise Displacement Measurements," *Experimental Techniques*, 1987, pp. 24–26.

[32] Mattheck, C., Morawietz, P., and Munz, D., "Stress Intensity Factor at the Surface and at the Deepest Point of a Semi-Elliptical Surface Crack in Plates Under Stress Gradients," *International Journal of Fracture*, Vol. 23, 1983, pp. 201–212.

[33] Fett, T., "The Crack Opening Displacement Field of Semi-Elliptical Surface Cracks in Tension for Weight Functions Applications," *International Journal of Fracture*, Vol. 36, 1988, pp. 55–69.

[34] Newman, J. C., Jr. and Raju, I. S., "Stress-Intensity Factor Equations for Cracks in Three-Dimensional Finite Bodies," *Fracture Mechanics: Fourteenth Symposium—Volume I: Theory and Analysis, STP 791*, J. C. Lewis and G. Sines, Eds., American Society for Testing and Materials, Philadelphia, 1983, pp. I-238–I-265.

Richard P. Gangloff,[1] *Donald C. Slavik,*[1] *Robert S. Piascik,*[2] *and Robert H. Van Stone*[3]

Direct Current Electrical Potential Measurement of the Growth of Small Cracks

REFERENCE: Gangloff, R. P., Slavik, D. C., Piascik, R. S., and Van Stone, R. H., "**Direct Current Electrical Potential Measurement of the Growth of Small Cracks,**" *Small-Crack Test Methods, ASTM STP 1149*, J. M. Larsen and J. E. Allison, Eds., American Society for Testing and Materials, Philadelphia, 1992, pp. 116–168.

ABSTRACT: This paper demonstrates the successful application of the direct current electrical potential difference method for continuous in-situ monitoring of the growth of short (50 to 5000 μm) fatigue cracks in a variety of metallic alloys exposed to various environments. Crack initiation site and crack shape must be known a priori. Instrumentation includes a constant current power supply, relay circuit, 10^4 gain amplifier, and computer analog to digital board with controlling software. A closed-form analytical model accurately relates crack size to measured potential, as a function of crack shape and probe position local to the growing crack. Analytical calibrations are experimentally confirmed for small through-thickness edge cracks, surface semielliptical and semicircular cracks, and corner cracks in steels, nickel-based superalloys, titanium and aluminum alloys. Micron-level average crack advance resolution, long-term stability, continuous measurement, simplicity, compatibility with aggressive environments, and programmed stress intensity loading are attributes of the electrical potential method. Crack length versus load cycles and growth rate versus stress intensity range data demonstrate the power of this method for studies of the effects of microstructure, environment (elevated temperature, high purity gases, vacuum and aqueous solutions) and loading variables on the growth kinetics of small and short fatigue cracks. Additional work is required for electrical potential monitoring of fatigue cracks sized below 75 μm, cracking not associated with a defined initiation site and thermal-mechanical fatigue.

KEY WORDS: fatigue crack propagation, fracture mechanics, corrosion fatigue, steels, aluminum alloys, nickel based superalloys, environmental effects, crack growth measurements, small cracks, electrical potential instrumentation

Introduction

Small-Crack Problem

Extensive data from the literature establish the rapid growth of small cracks, compared to typical fracture mechanics test-pieces containing long cracks, when correlated based on applied stress intensity range, ΔK ($\Delta K = K_{max} - K_{min}$) [*1–7*]. It is important to measure and utilize the correct small crack growth behavior to avoid predicting nonconservative

[1]Professor and graduate student, respectively, Department of Materials Science and Engineering, University of Virginia, Charlottesville, VA 22903.

[2]Research scientist, Mechanics of Materials Branch, NASA Langley Research Center, Hampton, VA 23665.

[3]Research engineer, Life Methods Group, General Electric Aircraft Engines, Cincinnati, OH 45215.

service lives for components. The mechanisms for the rapid growth of small fatigue cracks include: (a) limited crack wake closure contact, (b) a typically large crack tip plastic strain range, not ΔK-based, caused by the single crystal character of deformation, (c) compromised small-scale yielding caused by high applied stress or large plastic zone size, and (d) unique crack environment chemistry [*6*]. Limited crack closure results in Paris behavior below the long crack threshold, ΔK_{th}, while enhanced crack tip plasticity promotes subthreshold growth at high rates compared to long crack kinetics [*8*]. The definition of the limiting small crack size depends on the dominant mechanism.

Rapidly growing fatigue cracks are classified according to shape and size relative to the surrounding microstructure [*6*]. "Small" refers to 3-dimensional cracks of length and depth on the order or smaller than alloy grain size. Such cracks are often nearly semicircular and are sized between 1 and 5000 μm. A "short" 2-dimensional crack intersects many grains along a crack front that is large relative to the microstructure, but has a depth that is limited to between 5 and 5000 μm. Cracks may be either naturally initiated at inclusions, pores, pits, grain boundaries, or persistent slip bands; or artificially nucleated at notches. Grain boundaries may retard the growth of a microstructurally small crack, but do not affect short cracks.

An experimental method to monitor the growth of small/short fatigue cracks in metals should have several attributes. The technique should provide a continuous indication of crack extension, with micron-scale resolution, and in two dimensions for 3-dimensional cracks. The method should be applicable to both naturally and artificially nucleated fatigue cracks, and to single and multiple surface or internal cracks in a variety of specimen and component geometries. Crack monitoring should not interrupt load cycling and steady state fatigue crack propagation (FCP). Cyclic crack length data should be interfacable with a computer to enable real-time programmed stress intensity loading. The method should monitor cracks in thermal, gaseous, vacuum and aqueous environments, and during prolonged loading periods.

Direct Current Electrical Potential Monitoring of Small Cracks

The objective of this paper is to review the analytical and experimental elements of the direct current electrical potential difference (dcEPD) method for monitoring the growth kinetics of small and short fatigue cracks. Successful applications in studies of FCP are documented.

The principle of dcEPD monitoring of a small/short fatigue crack is illustrated in Fig. 1. An artificial defect, for example, a 1-mm-long and 100-μm-deep electrospark discharge machined (EDM) surface micronotch, locates the site of cracking (Fig. 1*a*). A constant direct current of 5 to 50 A is passed through the specimen, and the voltage difference on the order of 100 μV is measured between two probe points, above and below the midplane of the micronotch. The voltage difference increases with crack growth because current density about the crack is intensified. Measured voltage versus load cycles data (Fig. 1*b*) are converted to cyclic crack depth data (Fig. 1*c*) by a calibration equation, which is derived either empirically by experiment or from analysis of the electric field. Crack depth is defined along the short axis of the ellipse and for a known aspect ratio. The results in Fig. 1*c*, for constant load range cycling of Renè 95 at 538°C, were analyzed by fracture mechanics to yield an average crack growth rate (da/dN) versus ΔK relationship or da/dN versus crack length. Electrical potential monitoring of small/short fatigue cracks follows from the instrumentation and analytical techniques that were developed over the past 25 years for large cracks in typical fracture mechanics specimens [*9–12*].

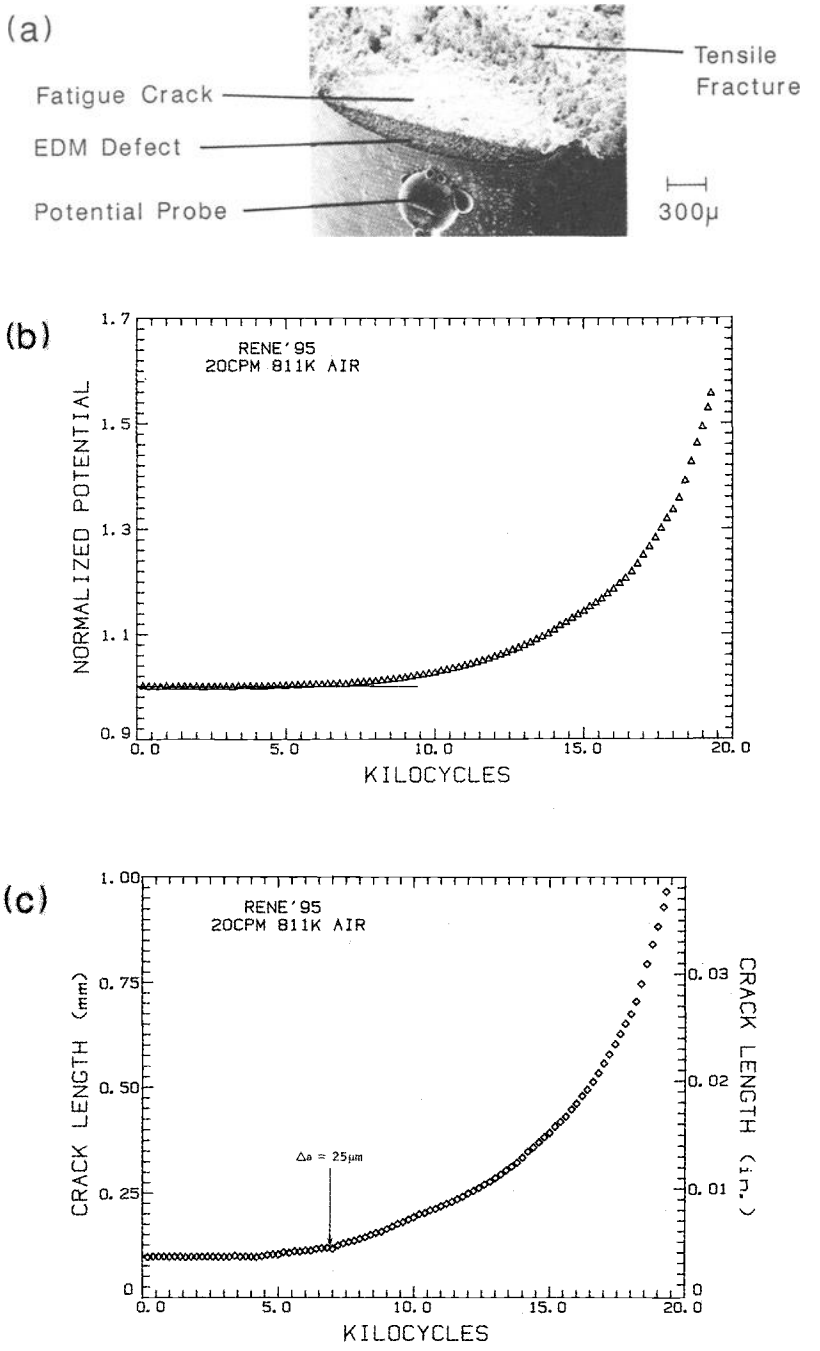

FIG. 1—(a) *SEM micrograph of a small/short fatigue crack from an EDM defect with an adjacent potential probe,* (b) *measured voltage versus load cycles, and* (c) *analytically calculated crack length versus cycles.*

Benefits—The dcEPD method has been successfully employed in a large number of short/small fatigue crack studies over the past 10 years. Analyses and results, summarized in ensuing sections, indicate the following benefits of the method:

- High resolution (1 to 4 μm) monitoring of 75 μm to 5 mm small and short cracks; continuously without loading interruption for ferrous, nickel, titanium, and aluminum alloys.
- Experimentally confirmed analytical voltage-crack size calibration relationships that quantitatively account for varying crack geometry (surface elliptical, semicircular, corner, and through thickness edge cracks), and voltage probe location.
- The capability for small/short crack length feedback control and programmed constant ΔK or K_{max} loading.
- An in-situ monitoring technique applicable to aggressive environments.
- Capability to measure low crack growth rates at low loading frequencies for prolonged test times.
- Capability to resolve growth rate transients in response to mechanical, microstructural, and chemical changes.
- Inexpensive to implement and simple to use based on modifications of a pending annex to an ASTM Standard Test Method for Measurement of Fatigue Crack Growth Rates (E 647).
- Confirmed by extensive $da/dN - \Delta K$ data.

Limitations—There are several limitations to the dcEPD method, including:

- The experiment typically employs a preexisting machined defect to locate crack initiation for probe attachment. Naturally nucleated or multiple cracks have not been monitored.
- DcEPD measurements provide no interpretable information on crack closure.
- Errors produced by plastic deformation effects on resistivity, voltage probe displacement during loading, and thermally induced voltages may be significant and require post-test correction.
- Crack surface electrical contact requires maximum load voltage readings and post-experiment correction.
- Electrical noise, ground loops, and laboratory temperature variations complicate voltage stability.
- Rapid changes in chemical, mechanical, and thermal variables may destabilize the electrical potential signal.
- A crack length-voltage calibration may have to be developed or an existing result verified.
- Crack shape must be defined by multiple probes, empirical aspect ratio data or specimen geometry.

Along with surface replication, electrical potential monitoring has impacted small/short crack research. The following review of work at several industrial and university laboratories demonstrates these conclusions and updates previous reviews [*13–16*].

Analytical Electrical Potential Calibration Relationships

The determination of crack size from electrical potential or resistance measurements is not, in principle, complicated. For a uniform direct current field, the potential V between two fixed locations that contain a crack is described by a function of current density, resistivity, crack size and shape, and voltage probe location. Current and metal resistivity are often unknown, but constant for a particular experiment. For this reason potential solutions are referenced to the result for an initial or otherwise known crack size a_o or notch size a_n, where the potential is referred to as V_o or V_n

$$V/V_n = f(a, a_n, L_p) \tag{1}$$

where L_p describes the voltage probe position. If a notch of depth a_n is employed to define V_n, rather than a sharp crack, then the calibration must specifically account for this three dimensional geometry, as described in the Appendix [*17*]. Examples of analytical potential-crack size relationships are described for both two- and three-dimensional cracks. Two-dimensional cracks are through thickness edge or center cracks in a panel, while three-dimensional cracks are semielliptical surface or corner cracks.

Potential Solutions for Two-Dimensional Cracks

A widely accepted potential solution for single edge or center cracks was reported by Johnson [*12*]. Based on an analytical method of conjugate functions suggested by Irwin, Johnson derived the electrical potential equation for a center crack of length, $2a$, in a panel of finite width W. V is measured between two positions on the centerline of the specimen at a distance L_p above and below the crack

$$V \sim \cosh^{-1}[\{\cosh(\pi L_p/W)\}/\{\cosh(\pi a/W)\}] \tag{2}$$

The proportionality is eliminated by dividing the solution for any crack size by that of the initial crack size a_o

$$\begin{aligned} V/V_n = {} & \cosh^{-1}[\{\cosh(\pi L_p/W)\}/\{\cosh(\pi a/W)\}] \\ & \div \cosh^{-1}[\{\cosh(\pi L_p/W)\}/\{\cosh(\pi a_o/W)\}] \end{aligned} \tag{3}$$

This expression can be rearranged to specify crack size a

$$\begin{aligned} a = {} & (2W/\pi)\cos^{-1}\{\cosh(\pi L_p/W)\} \\ & \div \cosh\{(V/V_n)\cosh^{-1}[\{\cosh(\pi L_p/W)\} \div \cosh(\pi a_o/W)\}]\} \end{aligned} \tag{4}$$

Although not trivial, the Johnson solution is a closed-form relationship for relatively easy calculation of potential for a given crack size or vice-versa. The latter capability permits the use of this solution in real-time K-control crack growth experiments, as discussed in an ensuing section.

Johnson's solution can also be used for the single edge crack (SE(T)) geometry, where potential is measured on the edge of the specimen containing the crack. The solution is identical to Eq 3, however, the total width of the SE(T) specimen is $W/2$. This specimen, specific terms in the calibration equation, and a voltage-crack depth prediction for a two-dimensional crack in a 10-mm-wide plate (filled circles) are shown in Fig. 2.

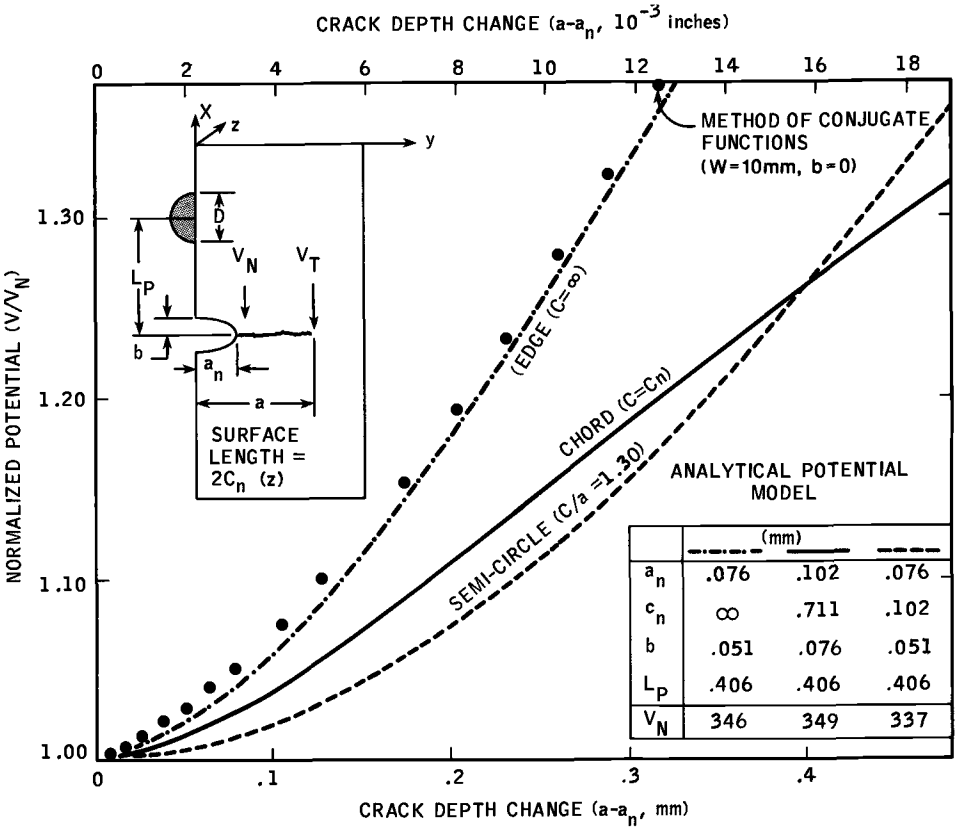

FIG. 2—*Voltage versus crack depth relationships, predicted from the analytical electrical potential model in the Appendix, for edge, semicircular, and chord defect nucleated cracks. The filled circles are predicted from Johnson's equation* (W = *10 to 500 mm). (After Gangloff* [14].)

Potential Solutions for Three-Dimensional Cracks

The voltage solution for a three-dimensional crack in a uniform current field is complicated because the crack has two dimensions, depth a and surface length, $2c$. Roe and Coffin derived a potential solution for a semielliptical surface notch, with height $2b$, in an infinite body under a uniform current [*18*]. This solution was based on a fluid flow analysis by Milne-Thompson [*19*], and was extended and verified by Gangloff, Van Stone and Heubaum, as summarized in the Appendix [*13,20,21*]. As in the two-dimensional solution, it is necessary to normalize the Roe-Coffin potential solution by that for a reference crack or notch geometry. Similar to Eq 1, this results in

$$V/V_n = f(a, b, c, a_n, b_n, c_n, L_p) \tag{5}$$

The detailed form of Eq 5 is presented in the Appendix. Example calculations of normalized potential versus crack depth are presented in Fig. 2 for several typical small crack geometries. The analysis can be employed for surface elliptical and semicircular cracks, for a corner crack caused by a symmetry conditions and providing that the potential probes are located along the corner containing the crack, and for the single-edge crack with c_n and c equal to infinity.

For the edge crack, model predictions are in excellent agreement with Johnson's equation [*12*], as indicated by the dashed line and filled circles in Fig. 2. The solutions agree exactly if the notch height is taken as zero in the three-dimensional model. Johnson's equation is only strictly applicable to the two-dimensional crack problem ($b = 0$) and under predicts crack length. The model in the Appendix more accurately accounts for the effect of the notch on the voltage-crack size relationship, an issue first noted by Li and Wei [*17*]. The agreement in Fig. 2 is only applicable for $a/w < 0.25$ [*22*]. The Johnson equation includes the effect of finite specimen width W as a boundary condition and should be accurate to substantial crack lengths. The Johnson equation predictions in Fig. 2 were calculated for a typical short crack specimen width of 10 mm; V/V_n at fixed crack length increases mildly as W increases to several 100 mm. The analytical model in the Appendix is derived for an infinitely wide plate, a reasonable assumption for the small/short crack problem.

The application of an analytical potential solution to a three-dimensional crack is significantly more complicated than the through crack case because crack shape frequently changes as the crack grows [*13,16,20*], and the equations require an iterative solution. Because of this complexity, tables of V/V_n versus crack depth must be calculated and then employed in a "lookup" mode for computerized ΔK-controlled experiments.

An alternate approach to the closed-form analytical model is the use of the finite-element method (FEM) to numerically determine the potential solution for a given crack geometry and probe location. Figure 3 shows such calculations for a corner crack of radius a in a square section with side of length W [*23,24*]. The FEM results agree with a closed-form analytical solution [*23*]

$$V/V_{\text{remote gradient}} = (4a/\pi) + L_p - 2L_p \sin^{-1}[(a^2 - L_p^2)/(a^2 + L_p^2)] \tag{6}$$

particularly for small crack sizes. As the crack becomes large relative to specimen size, the discrepancy between the analytical and FEM solutions increases. The finite-element solution models the finite geometry, while this is not considered in Eq 6. Similar good agreement was reported between an FEM calibration and the analytical model in the Appendix [*21*]. For the case of small/short cracks in uniform current fields, either the closed-form analytical or FEM solutions can be used to determine the crack size-potential relationship.

The major weakness of the FEM solutions is that they are developed for a specific voltage probe location and crack aspect ratio. For applications to crack growth experiments, it is necessary to have a number of FEM relationships to cover the range of experimental observations, as well as a verified technique to interpolate between these solutions. This may preclude the use of the FEM solutions to perform K-control tests.

Small-Crack Geometry Design by Potential Solutions

By predicting the relationship between crack size and voltage with the model in the Appendix, it is possible to assess the applied direct current and voltage resolution necessary for any small/short crack geometry, specimen size, and alloy. A single voltage, measured for a specific crack and probe geometry, is employed with model calculations to define absolute voltages for any crack size and probe location. To establish the effect of material, potential values linearly scale with known electrical resistivity values. Voltage also linearly scales with current density, given by the applied current and specimen cross-sectional area.

A significant factor in using the dcEPD method to monitor cracking is the location and spacing of the potential probes. Increasing L_p increases the magnitude of the potential and the signal to noise ratio, but diminishes the voltage sensitivity ($dV/d\Delta a$) to small changes in crack size. For example in Fig. 3, the potential solution for the corner crack shows that, as

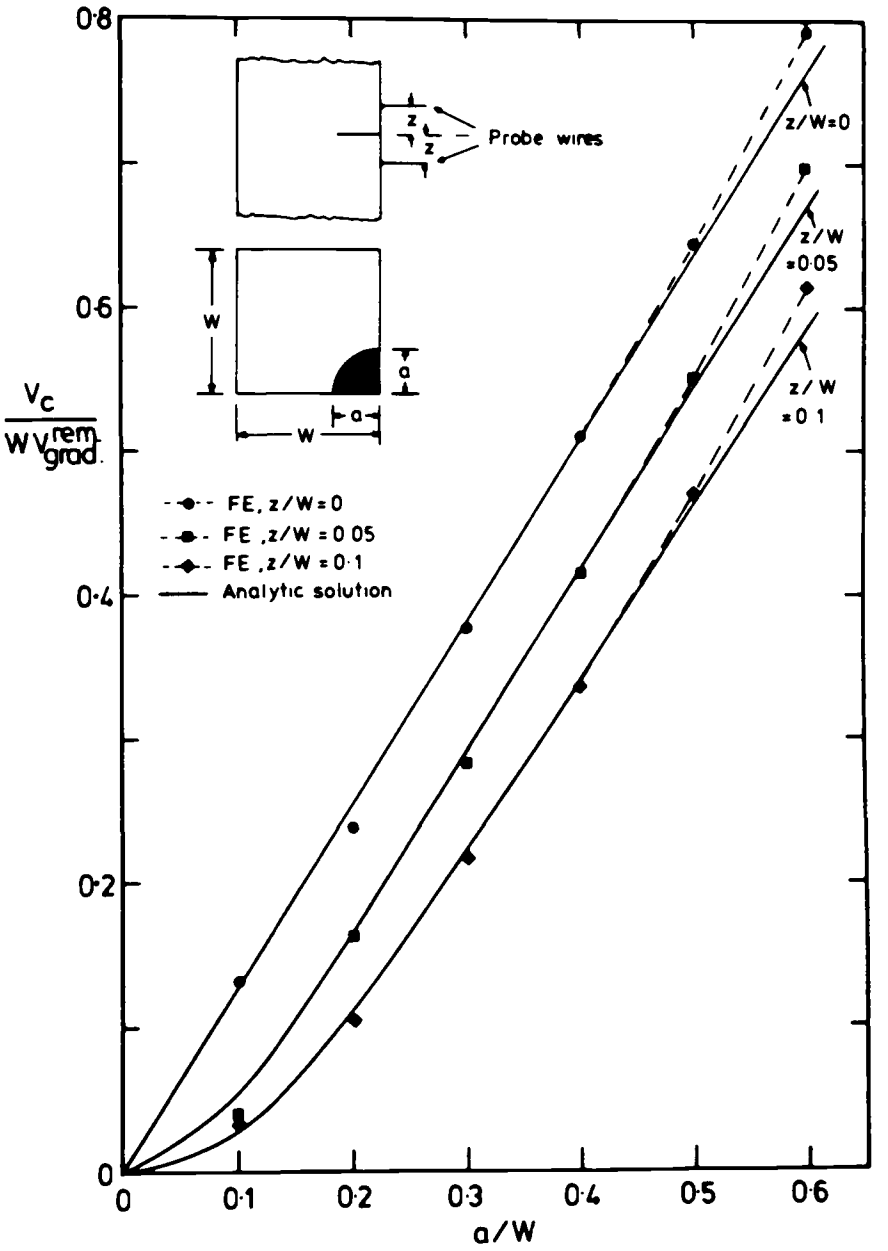

FIG. 3—*Comparison of the potential solutions for a constant radius corner crack, determined using the FEM and a closed-form analytical solution (Eq 6 or the Appendix) for three probe spacings. (After Hicks and Pickard* [23].)

L_p increases ($L_p = z$), there is a smaller potential increase with crack growth, especially when a/W is less than 0.1. Figure 4 illustrates the effect of probe spacing (L_p) on the potential-crack depth solutions for a surface crack that is initially 0.1 mm deep and 1.5 mm long [*13*]. These solutions were calculated based on the model in the Appendix for the case where the crack increases in depth at a fixed surface length. It is advantageous to use the smallest possible probe spacing. Since the potential wires and tip beads commonly have diameters on the order of 0.1 mm, probes contact a specimen (Fig. 1*a*) over an area. The magnitude of this contact range is shown by the ±0.05-mm bar in Fig. 4. (The bar is located along the 0.40-mm probe spacing solution because this spacing is used as a compromise between $dV/d\Delta a$ sensitivity and a significant voltage.) Over this range of L_p, the voltage-crack size relationship varies significantly. Accordingly, the equations in the Appendix were employed to integrate crack and notch potentials over the contact area of the potential probe [*13,15*].

Crack geometry significantly effects the potential response, as shown in Fig. 2 [*14*]. This example illustrates the effect of surface crack aspect ratio for small/short cracks emanating from notches with depths ranging from 0.076 to 0.102 mm and with a ±0.4-mm probe spacing. Through thickness, semielliptical chord, and nearly semicircular crack geometries are represented. Dimensionless values of the notch voltage V_n are indicated. The model in the Appendix can employ any constant or crack-depth-dependent surface length to depth aspect ratio. The results in Fig. 2 illustrate the decreased potential sensitivity associated with small three-dimensional cracks as compared to edge through cracks. Empirical or FEM solutions are not well suited for sensitivity studies of crack geometry and probe spacing effects on the voltage-crack size relationship.

Experimental Methods

High resolution dcEPD methods for determining crack length have been developed for the study of small and short crack growth kinetics in engineering alloys. A pending annex to an ASTM standard, on dcEPD monitoring of large cracks, provides a basis for small crack experimental methods (ASTM Test Method for Measurement of Fatigue Crack Growth Rates [E 647]). Details of specific experimental procedures are reviewed here.

DcEPD Equipment

The electronic instrumentation necessary to implement the dcEPD method is easily assembled for about $6000. A constant direct-current low-voltage power supply (10 to 50 A, constant to better than ±0.05% at 10 to 20 V) with minimal short-term noise (0.05%) and long-term stability is required. Either a nanovoltmeter or a high (for example, 10^4) gain amplifier is used to measure the dcEPD signal. The response time of such highly filtered instruments is typically on the order of 0.3 s; more rapid changes in dcEPD will not be accurately measured. A typical requirement is to measure 0.2 μV changes in an initial signal of 200 μV; with this voltage increasing to about 600 μV during fatigue crack growth. With 10^4 gain, this requirement is 2 mV changes in a base signal of 2 V and a final signal of 6 V.

Figure 5 shows a schematic diagram of a typical dcEPD circuit coupled with a computer-based data acquisition system and a servo-hydraulic test machine. It is not necessary to measure the applied current, however, an appropriately sized known resistance shunt can be employed for this purpose and interfaced with the computer if desired. A power relay circuit is employed to switch the polarity of the applied current to eliminate thermally induced voltages, as discussed in an ensuing section. The current switching interval is dictated by experimental conditions and is automatically controlled by a digital-to-analog signal from

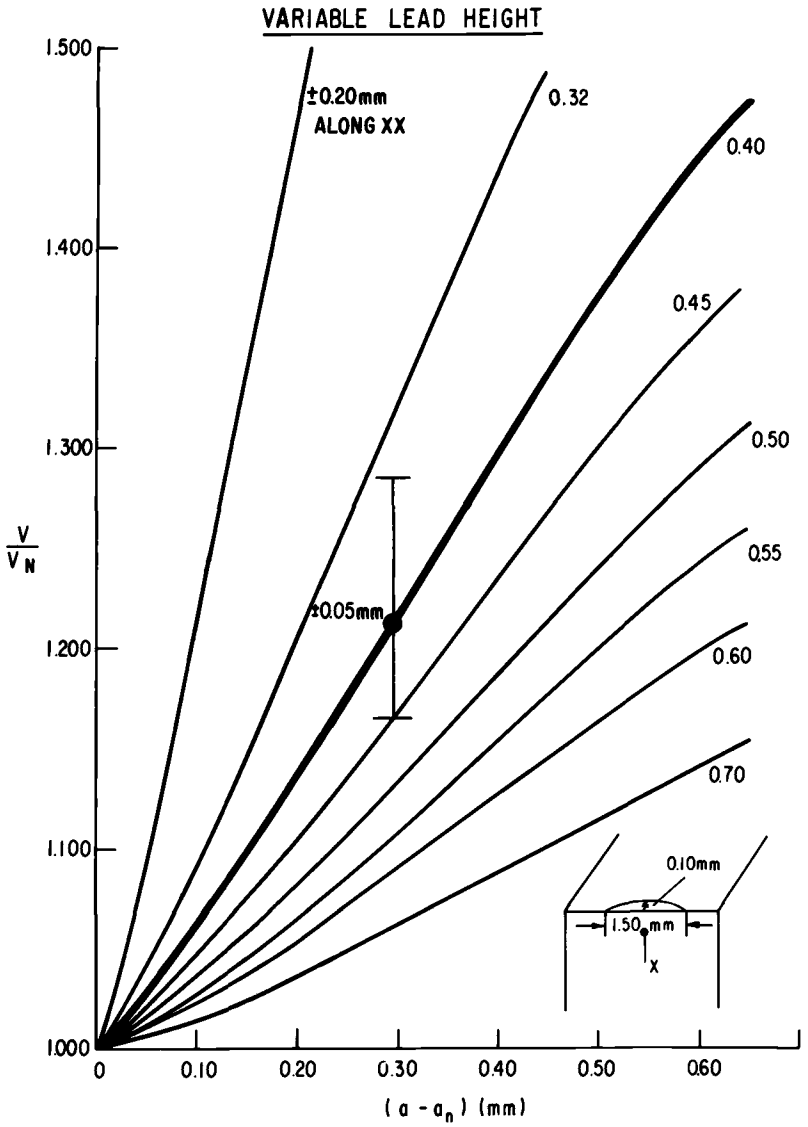

FIG. 4—*Variation of normalized potential* (V/V_n) *with semi-elliptical crack depth at constant surface length for several probe spacings (after Gangloff* [13]*).*

the computer. Alternately, this operation can be manually performed, or the current simply switched between zero and the test value. DcEPD signals from both the active crack and inactive reference probe pairs (see ensuing section), amplified by 10 000 times, are at an acceptable level for most analog-to-digital boards. The amplified signal may also be measured with a recorder or digital voltmeter. Crack lengths calculated from measured dcEPD values may be employed for computer control of the servohydraulic machine, for example, to alter load as necessary to control stress intensity.

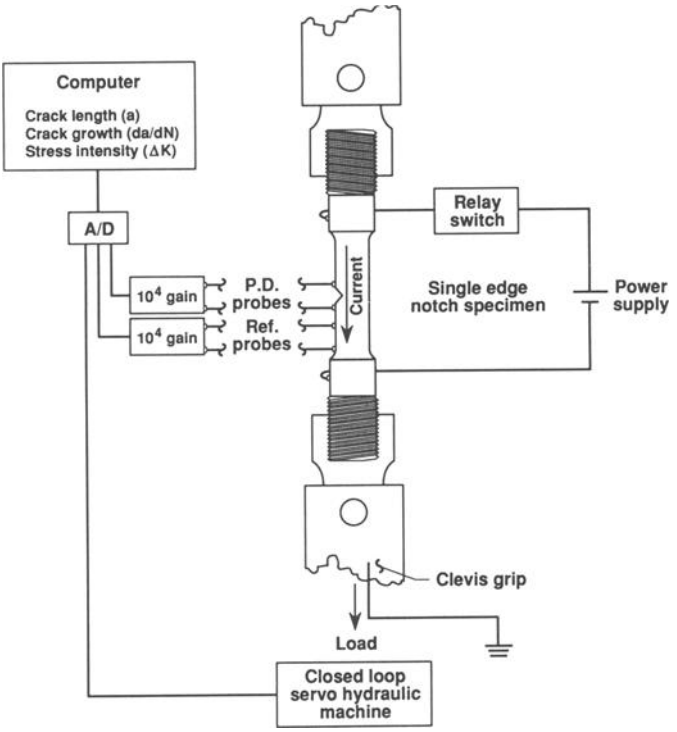

FIG. 5—*The computer controlled reversing dcEPD method applied to a micro-notched SE*(T) *specimen.*

Auxiliary Equipment

DcEPD monitoring has been successfully conducted in conjunction with auxiliary equipment, particularly that necessary for specimen environment control. Experiments in aqueous chloride electrolytes demonstrated that potentiostatic application of an anodic or cathodic electrochemical current to the specimen working electrode had no resolvable influence on measured dcEPD values for crack monitoring [*22*,*25*–*27*]. The main consideration in this experiment is to ground the specimen and to employ a potentiostat that is capable of controlling a grounded working electrode.

DcEPD resolution and stability were not adversely affected by either radio frequency (RF) [*13*,*28*] or resistance heating [*29*] of the fatigue specimen, at least for Paris regime crack growth rates above about 10^{-5} mm/cycle and loading frequencies as low as 0.1 Hz. For this case, computerized acquisition and averaging of a large number of dcEPD values for a single-load cycle, coupled with cycle-block averaging discussed in an ensuing section, minimizes the impact of random electrical noise. For measurements of small/short crack growth rates within the near threshold regime (10^{-6} mm/cycle or lower), unpublished data indicate that resistance heating imparts less noise and is superior to RF heating [*29*].

There have been no published accounts of adverse interactions between dcEPD instrumentation and other equipment, including servohydraulic electronics, vacuum system pumps, attached strain gage extensometers or linear variable differential transformers. The user of the dcEPD method should, however, be on guard for unexpected effects. For example, a

low resistance alternate current path provided by a crack mouth displacement gage should be avoided so as not to alter the current flowing through the uncracked portion of the specimen [*21*].

Specimen Fabrication

Several specimen attributes facilitate quantitative dcEPD monitoring of small/short fatigue cracks. Specimen cross-sectional area must be limited, typically on the order of 50 mm^2, for sufficient current densities with reasonably sized power supplies. The specimen must contain a known crack initiation site, or "micronotch," for accurate voltage probe location. The stress intensity solution should be known if a $da/dN - \Delta K$ correlation is desired. The specimen should be containable in a variety of gaseous, aqueous, and thermal environments. Additionally, the specimen may be monitored to measure temperature, electrode potential, average longitudinal or diametral strain, crack opening displacement, crack closure, and applied load.

Crack Initiating Defect—The need to study a variety of small and short crack growth issues using the dcEPD method prompted the development of several specimen geometries, as described in Table 1 and Fig. 6. Each geometry is based on a uniaxial tension specimen containing an artificially introduced surface flaw. Micronotches include the through-thickness single edge notch, semicircular flaw, chord notch, and corner flaw geometries [*15,16,21,22,25,26,28,30–32*]. Typical notch dimensions in Table 1 include depth a_n, mouth opening b, and surface length c_n. Current is applied to the specimen, far from the crack. Potential difference is measured by probes that are attached in close proximity to the micronotch, typically separated by a distance equalling 4 to 12 notch depths, as indicated in Fig. 4.

Other unique specimens containing surface flaws have been used with the dcEPD method. For example, the multiple single-edge cracked tension specimen, containing six through thickness edge cracks in series along a uniaxial tension specimen was employed to study corrosion fatigue in steels [*33*]. The growth of small semicircular cracks in large diameter austenitic stainless steel pipe exposed to high-temperature water was investigated using the DC potential difference method [*34*].

The growth of small/short cracks emanating from surface flaws can be influenced by specimen fabrication methods. To minimize residual stress, special machining techniques are used, including electrospark discharge machining (EDM) and cutting or grinding with limited material removal on each pass. Potentially useful methods based on acid string sawing, localized corrosion, hardness indentation or laser melting have not been employed. An advantage associated with electrospark discharge machining is that surface notch geometries can be easily and accurately fabricated. Figure 7 shows optical micrographs of metallographic cross sections through small surface flaws that were electrodischarge machined in Renè 95 using machined tungsten, tantalum foil, and Fe-Ni-Cr razor blade electrodes [*15*]. Notch root radii on the order of 25 μm are readily produced.

Crack growth within 30 μm of the notch is affected by notch bluntness, notch stress concentration, and the brittle layer formed by EDM [*14*]. For example, a 2- to 5-μm-thick melted and alloyed layer is formed on the notch surface due to EDM. Initial growth is not analyzed by fracture mechanics, and in the case of the EDM melt region is not representative of parent material and is typically ignored. To avoid notch effects, more elaborate fabrication methods can be employed; for example, the surface flaw can be introduced by precracking followed by careful machining of the specimen to the required dimensions. Alternately, to study initiation at the root of the micronotch, the EDM surface can be removed by mechanical or electropolishing.

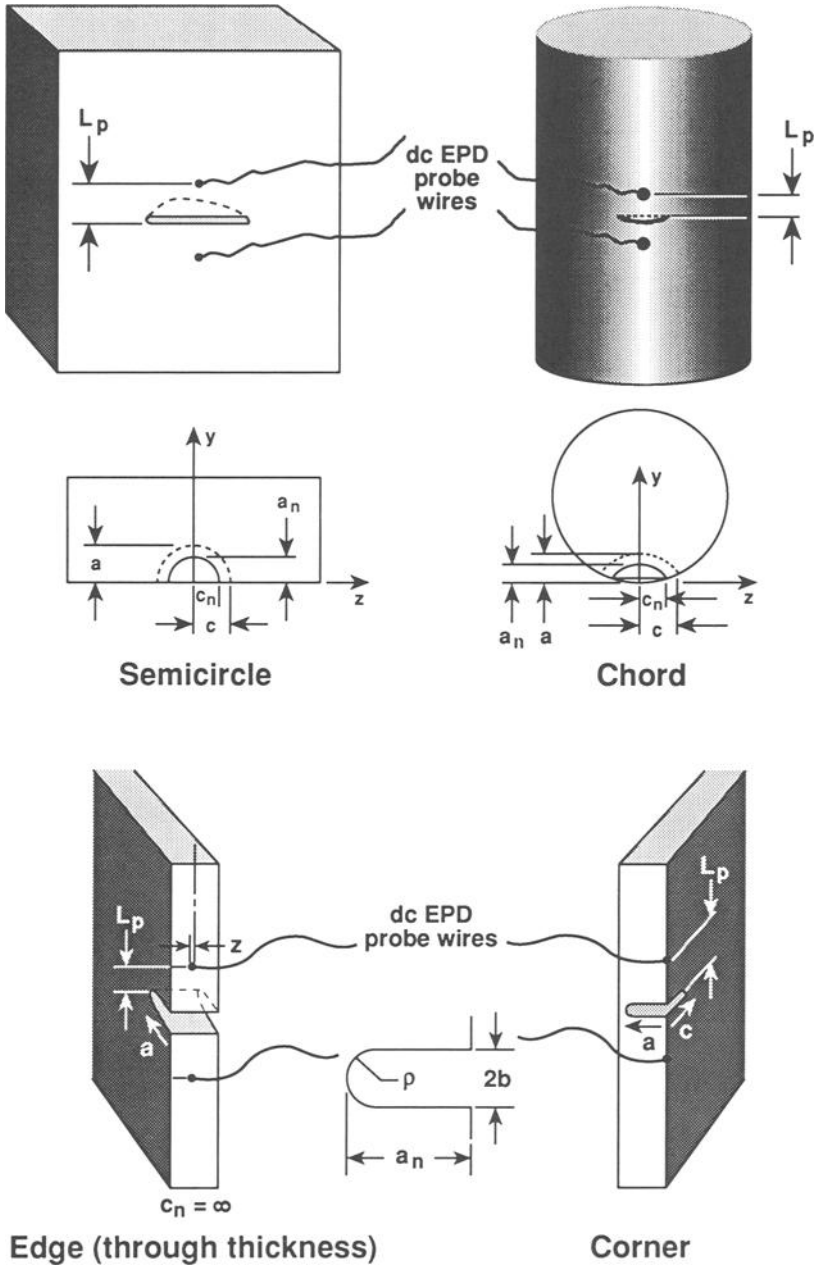

FIG. 6—*Semicircular, chord, through thickness edge, and corner notch geometries for dcEPD monitoring.*

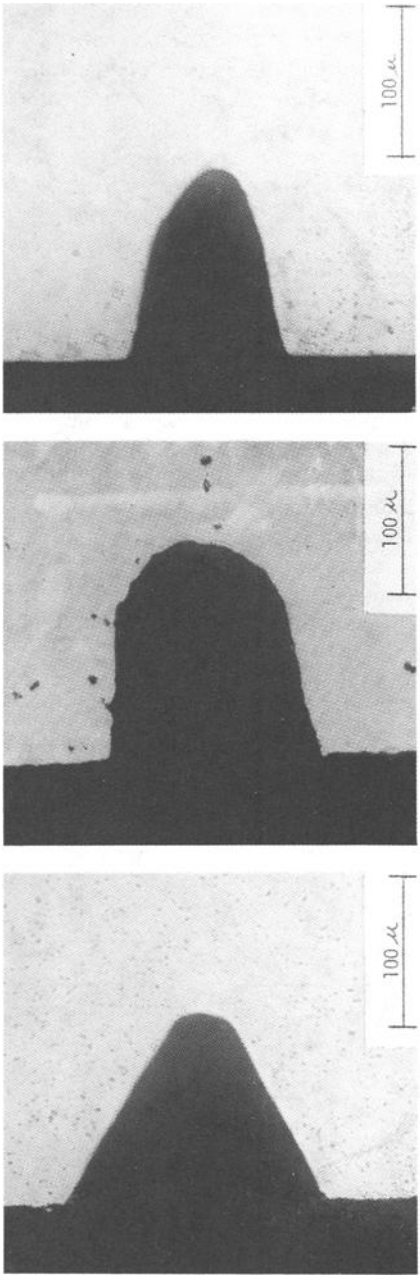

FIG. 7—*Optical micrographs of cross sections through EDM surface defects produced by:* (a) *machine shaped tungsten,* (b) *tantalum foil, and* (c) *razor blade (Fe-Ni-Cr alloy) electrodes (after Van Stone et al.* [15]).

Current and Voltage Leads—Typically, copper current leads of the appropriate size to carry up to 50 A are attached to the specimen by silver soldering, mechanical clamping, or a threaded fastener. Ideally, current leads are directly placed on the specimen, but sufficiently far from the surface flaw to provide a uniform current density and so as not to initiate fatigue cracking (Figs. 5 and 6). To prevent measurement errors caused by current variations, it is essential that the resistance to current flow through the specimen is several orders of magnitude less than other current paths. As a precaution, the specimen-grip interface, or some other element in the load train, can be insulated to guarantee that all applied current flows through the specimen. In practice the several ohm resistance typical of the current path through the grips, loading rods, load cell, test machine, and servohydraulic actuator, is about six orders of magnitude higher than the specimen resistance. Alternate current paths are unlikely; this conclusion should be confirmed by test machine resistance measurements. It is acceptable to apply the current to the specimen grips, provided that the grip-specimen resistance is on the order of 10^{-3} Ω or less and does not change with load or increase during prolonged fatigue loading. Current shunting problems are not present when similar dcEPD measurements are observed before and after mounting the specimen in the loading fixture.

It is generally advisable to ground the specimen at the lower current attachment point. Ground loop electrical noise is often specific to ancillary equipment, such as an RF heater or electrochemical potentiostat; a discussion of ground loops is beyond the scope of this paper.

Critical to dcEPD measurement is the attachment of two probes to measure the small (0.05 to 0.10 μV) increase in potential associated with crack extension. Accurate placement of the potential leads relative to the micronotch, with reliable electrical conductivity and structural integrity, is typically achieved by resistance spot welding. The attachment method must not introduce a metallurgical heterogeneity or stress concentration that could initiate fatigue cracking. Alumel and copper wire, ≤0.15 mm in diameter, is commonly used as potential leads as noted in Table 1. A strain relief may secure the probe wires beyond the spot weld contact point.

Enhanced resolution of the potential difference measurement is obtained by optimum placement of the potential probes, as dictated by the analytical calibration relationships discussed earlier. Spot welding methods, often employing a micrometer mounted specimen holder, a fine tipped electrode, and a stereomicroscope, have been successfully employed to precisely locate potential probes. As an example, Fig. 8 is an optical micrograph showing

TABLE 1—*DcEPD specimen configurations.*

Specimen		Probe	Flaw Size, mm	
Type	Material	Material/Diameter, mm	$a_n/b/c_n$	Reference
SE(T)[a]	4340	alumel/0.12	0.10/0.06/1.90	*25,30*
SE(T)[a]	aluminum	copper/0.12	0.25/0.08/2.54	*22,26*
Chord[b]	10Ni Steel A286 Renè 95	alumel/0.12	0.10/0.06/0.70	*25,31*
Semi-circle[c]	Renè 95	alumel/0.12	0.08/0.04/0.10	*15,16,28*
	aluminum	copper/0.08	0.13/0.02/0.13	*32*
Corner	A537 Steel	alumel/0.10	0.10/0.25/0.10	*21*

[a]Though-thickness single edge crack.
[b]Hourglass specimen containing chord surface flaw.
[c]Semicircular surface flaw.

a corner notch in a single tempered martensite grain of A537 steel [*21*]. Here, fatigue crack growth is monitored by Teflon® coated alumel probes spot welded adjacent to the corner notch. Similar methods have been successfully applied to nickel, titanium, and aluminum alloys [*15,16,22,32*]. A variety of problems, such as weld galvanic, crevice, and pitting corrosion, must be considered when testing in aqueous environments. Such potential problems have not been typically encountered in experiments with steels and aluminum alloys in aqueous chloride [*22,25–27*]. Insulated potential leads (for example, Teflon coated) are used to prevent electrical shorting and environmental damage. The leads should be as short as possible and twisted (if insulated) to limit interfering voltages induced by stray magnetic or RF fields.

The dcEPD level depends on micronotch/crack geometry, probe location, applied current, and specimen cross section (current density), alloy resistivity, and temperature. Results in Table 2 indicate typical potentials that are associated with variably sized and shaped micronotches in different alloys. These data guide the selection of specimen cross section, power supply capacity, and potential amplification needs. The data in Table 2 can be used in conjunction with the analytical electrical potential model (Appendix) to predict absolute voltages associated with any notch/crack geometry and probe position. The challenge to monitor the growth of small cracks in aluminum alloys near room temperature is apparent.

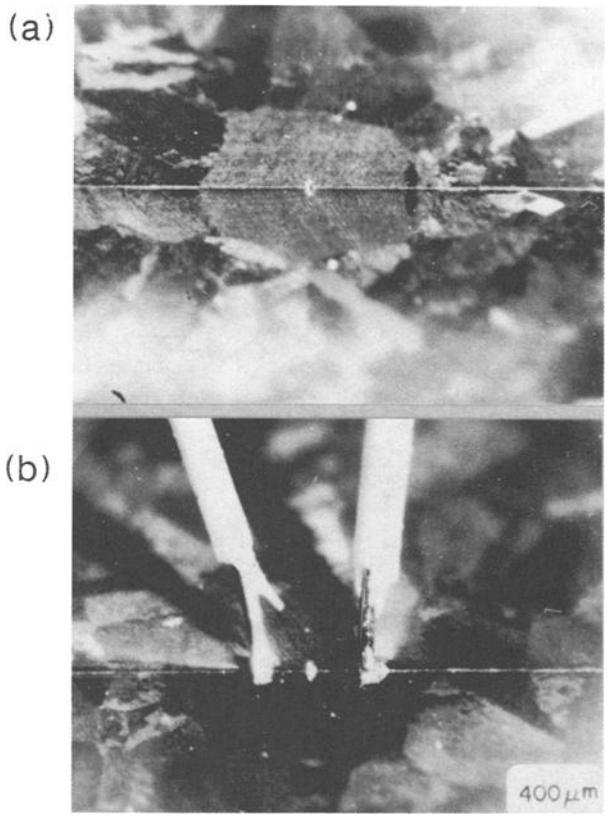

FIG. 8—*Optical micrographs showing:* (a) *a corner notch in a single grain of martensitic A537 steel and* (b) *75-μm diameter alumel dcEPD probes spot welded adjacent to the corner notch in* (a) *(after Heubaum* [21]*).*

TABLE 2—*Electric potential values for alloys and micronotches.*

Alloy	Temperature, °C	Notch Size, μm	Total Probe Separation, μm	Notch Voltage/Current Density, μV cm²/A
10 Ni steel	23	100[a], 1500[b] chord	800	4.0
MP35N	538	"	"	12.8
304 stainless	538	"	"	8.4
A286	538	"	"	10.2
Renè 95	23	"	"	10.8
Renè 95	538	"	"	12.3
Renè 95	538	75[a], 200[b] semicircle	760	13.0
AA 2090	23	300[a] SE(*T*)	1200	1.3

[a]Notch depth.
[b]Notch surface length.

Requirements for dcEPD Accuracy

Apart from precisely measuring the potential difference with constant applied current, several factors must be considered to guarantee accurate crack lengths from dcEPD measurements.

Thermally Induced Voltage—Associated with each electrical connection in the dcEPD circuit is a thermally induced voltage that varies with temperature during testing and that contributes to erroneous crack length measurements. A net voltage develops, for example, between the two potential probes, if these probes make dissimilar metal contacts with the specimen and if the contact points are at different temperatures. Although thermal voltage effects are minimized by limiting the number of electrical connections and by maintaining a constant temperature during testing, procedures are desirable to eliminate these interfering voltages.

The thermally induced voltage is measured at frequent test intervals by switching the applied current to zero [*13*]. The true crack potential ($dcEPD_{corr}$) is the algebraic difference between the total measured *V* and the thermally induced voltage. Alternately, the reversing dcEPD method employed by Coffin et al. eliminates thermal effects by reversing the polarity of current flow [*35*]. $DcEPD_{corr}$ is determined by averaging the voltage measurements obtained at each polarity of current; $dcEPD_{corr} = [(PD^+) + (PD^-)]/2$, where PD^+ and PD^- are the potential values for each polarity of applied current. The reversing current approach has the claimed advantage that the magnitude of the measured potentials are large relative to the current-off value, which is typically near zero [*35*]. While reversing method voltages are substantially above amplifier noise, the use of computerized averaging methods are likely to result in a similar error for each approach. Accordingly, the reversing and on-off current methods are equivalent.

Temperature Dependent Alloy Resistivity—The use of so-called reference probes can yield accurate determination of crack length by compensating for changes in crack potential caused by changes in specimen electrical resistivity produced by temperature variations and by fluctuations in applied current and PD amplification [*33,34*]. (For aluminum alloys, a 3°C increase in temperature results in a 1% increase in resistivity and measured potential.) This procedure is important for long-term experiments, when instrument stability problems and subtle thermal fluctuations arise, or for cases where temperature is intentionally varied during crack growth as in thermal-mechanical fatigue.

Using attachment methods identical to the dcEPD leads across the micronotch, a pair of reference potential leads is attached to the test specimen in a region where the potential is not affected by crack growth (Fig. 5). Potential difference measurements are corrected

($dcEPD_{corr}$) by dividing the actual (active) dcEPD signal by the ratio of the current reference probe voltage ($dcEPD_r$) and the initial reference value ($dcEPD_{ro}$); $dcEPD_{corr} = dcEPD/[dcEPD_r/dcEPD_{ro}]$. Both active crack and reference voltages are corrected to eliminate thermally induced voltages before this normalization.

Crack Surface Shorting—Crack surface contact causes substantial errors in crack length by reducing the level of the electric potential if the surfaces are electrically conducting [*14*]. Crack length, inferred from measured voltage by an empirical or analytical calibration, can be significantly less than the true size because of shorting-reduced potential. Anomalous dcEPD behavior caused by crack surface shorting was observed for alloys in both inert and reducing environments; for example, steels and aluminum alloys in vacuum and helium, or steels in aqueous sodium chloride (NaCl) at open circuit or cathodic potential. Specific instances were reported for both long [*36–38*] and short [*25,30,39*] crack specimens.

Figure 9 reveals the cyclic load dependence of dcEPD for a short chord surface crack in 4130 steel loaded in 3% NaCl at room temperature and a frequency of 0.01 Hz [*14*]. Shown in Fig. 9 is the tensile load history (3 cycles) and the corresponding dcEPD signal variation. Increased dcEPD, caused by decreased crack surface contact and electrical conduction, occurs as the crack surfaces move apart with higher tensile loads. Interestingly, the maximum dcEPD signal contains a reproducible structure that probably represents secondary surface asperity contact caused by local Mode I and Mode II or III displacements. When the surface flaw was exposed to a film producing environment such as moist air, the load dependence was eliminated and a constant dcEPD of approximately 280 μV was observed within 2 load cycles.

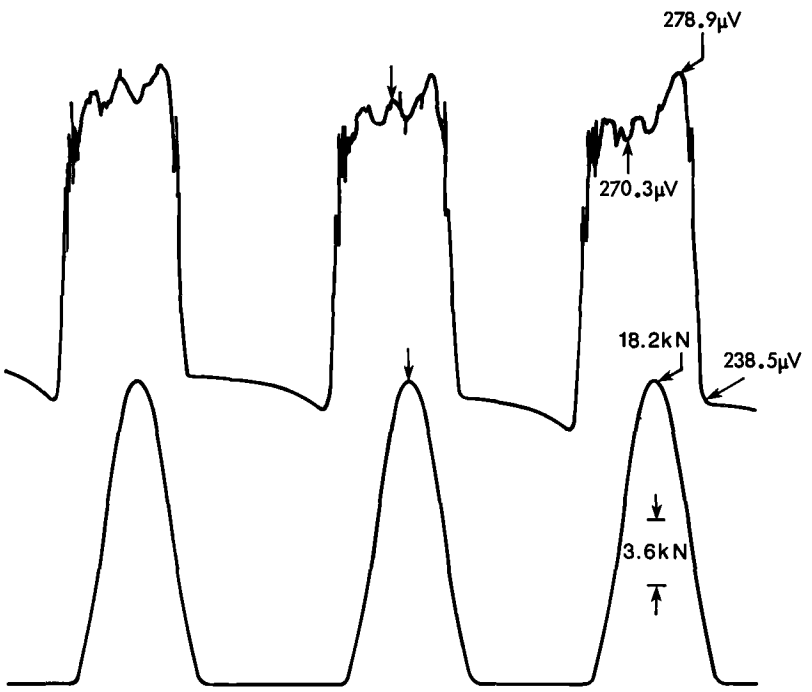

FIG. 9—*Measured changes in dcEPD signal caused by crack surface electrical contact during cyclic loading at 0.01 Hz; 400-μm-deep surface chord crack in 4130 steel exposed to 3% NaCl at the free corrosion electrode potential (after Gangloff* [14]*).*

Crack surface shorting phenomena are partially eliminated by measuring potential at maximum load. If surface contact persists at this point, crack length errors occur and post-test correction is required. To date, crack surface electrical contact has not been exploited to gain mechanistic insight regarding surface films. Attempts to infer crack closure information from data of the sort presented in Fig. 9 failed [*36*,*37*]. Electrical contact on unloading is typically indicated at loads that are well above crack closure levels inferred from nonlinear compliance behavior.

DcEPD Data Acquisition and Reduction

Crack and reference potentials are ideally measured during the maximum portion of the tensile load cycle. Synchronization with load is accomplished with a computerized system. Computerized data acquisition and averaging techniques are used to reduce data scatter due to system noise. A specific example is as follows:

- A large number of voltages (for example, 500) are rapidly read near maximum load in a single cycle and averaged. (This analysis calculates the mean of the potential signal that varies due to random high frequency noise on the output of the nanovoltmeter or amplifier. The true value of the voltage does not change during the period of this rapid data acquisition because of the slow response time of typical nanovoltmeters or filtered amplifiers.)
- The voltage average is repeatedly obtained for a programmed number of loading cycles (for example, 50) and the resulting values are averaged to a single dcEPD.
- The polarity of the current is switched, and the above averaging is repeated for the programmed number of load cycles.
- A single thermally corrected potential is calculated from the plus and minus current polarity averages.
- This voltage value may be printed and stored, or additional block averaging can be conducted and the resulting value reported.
- A reference potential can be obtained in parallel with the above measurements to correct the averaged active crack potential.
- Crack length is calculated from the resulting thermally corrected and normalized potential.

The number of cycles for block averaging and optimum crack length resolution depends on crack growth rate. A variety of strategies are conceivable for specific applications, be it high-frequency near-threshold or low-frequency Paris regime FCP. As a precaution, if crack surface shorting is present, the change in voltage with load must be measured at a sufficiently slow loading frequency so that the time dependent potential will not be attenuated by the slow response time of typical high gain amplifiers or nanovoltmeters. A frequency of less than 0.5 Hz is adequate. A computer controlled test system can slow the loading frequency periodically to obtain accurate voltage measurements near maximum load.

Averaged voltages may be converted to crack lengths, either in real time or after an experiment. Real-time crack length calculations may employ either a closed-form equation or a lookup table for complex voltage-crack geometry relationships. For computation of crack growth rate (da/dN), the modified secant method is typically used; the fatigue crack growth rate at initial crack length a_i is based on increments of crack length and load cycles between a_{i-1} and a_{i+1} (as stated in ASTM Test Method for Measurement of Fatigue Crack Growth Rates [E 647]). Crack tip stress intensity is calculated based on known crack size and the specimen stress intensity equation. An example calculation of $da/dN - \Delta K$ is provided for the chord crack in a round bar [*31*].

A computer controlled servohydraulic system provides continuous increases or decreases in applied load for programmed ΔK and R. In addition to a known stress intensity equation, the following expression can be employed with small/short crack specimens and dcEPD crack length [*40,41*]

$$K = K_0 \exp[C(a - a_o)] \tag{7}$$

where

K = the maximum, minimum or range stress intensity,
K_0 = the initial stress intensity at a_o,
a_o = initial crack length,
a = current crack length, and
C = a constant with dimensions of reciprocal length.

Qualifying Results

Resolution of Fatigue Crack Depth and Growth Rates

Perhaps the best way to assess the resolution and long-term stability of the dcEPD method is to consider the extensive data presented in ensuing sections on applications for small and short fatigue cracks. These results indicate that uniform crack growth increments of less than 3 μm are resolvable, and that growth rates below 10^{-6} mm/cycle can be determined at moderately slow frequencies between 0.5 and 25 Hz. Higher crack growth rates can be measured for extremely low frequencies, on the order of 10^{-4} Hz.

The average crack advance resolution of the dcEPD method is determined from the analytical calibration for a specific crack geometry and voltage probe location, instrumentation resolution, and material resistivity. From Figs. 2 through 4, a typical sensitivity $(d(V/V_n)/d\Delta a)$ for the chord, corner, and semicircular cracks is 0.8 $(\mu V/\mu V)$ mm^{-1}. (This value varies with probe location, crack shape, and crack depth.) The instrumentation and data averaging method discussed in a previous section enable the detection of 0.10 to 0.30 μV changes in dcEPD. From Table 2, the voltage associated with a 75-μm-deep semicircular crack in a nickel-based superalloy at 538°C is 13.0 μV cm^2/A. For a specimen cross-sectional area of 0.3 cm^2 and an applied direct current of 10 A, the absolute value of the crack voltage is 430 μV. Combining these values establishes that a voltage uncertainty of 0.25 μV results in a crack depth resolution of 0.7 μm.

Similarly, it is possible to calculate an average crack length resolution for any current, specimen cross-sectional area, and material resistivity; these factors linearly influence resolution. Additionally, the analytical calibration can be employed to determine the voltage sensitivity to crack length increases for any crack and probe geometry. As a second example, the above calculation leads to an average crack length resolution of 5.8 μm for the same conditions as the nickel based superalloy, but assuming that the crack is in an aluminum alloy at 23°C. (The resistivity of the aluminum alloy is eight times less than that of the superalloy.) To improve this resolution, current could be increased to 20 A, cross-sectional area could be reduced to 0.15 cm^2, and the dcEPD resolution could be improved to 0.15 μV. The resulting crack length resolution for the aluminum alloy is 0.9 μm.

Calculated resolutions represent an idealized lower bound. The analysis assumes that crack growth occurs uniformly along the crack perimeter. This assumption is confirmed for Paris regime crack growth, but is questioned for near threshold cracking [*13*]. Secondly, the analysis assumes that voltage resolution is constant with time. In fact variations in average voltage occur during a prolonged fatigue experiment, due to thermal voltages and thermal

effects on instrumentation. The user of the dcEPD method should establish the long-term variation in V/V_n; for the specific crack geometry, probe position, material, specimen environment, and laboratory environment of interest; and during load cycling without crack growth. Measured changes in dcEPD can be converted to apparent crack growth rates through the analytical calibration. An example of this procedure was presented for a 100-μm-deep surface chord crack in Renè 95, loaded cyclically at 538°C (RF heating) [*13*]. Over a 48-h period of loading at 0.33 Hz, V/V_n varied by between -1×10^{-7} $(\mu V/\mu V)$ cycle^{-1} and $+3 \times 10^{-7}$ $(\mu V/\mu V)$ cycle^{-1}. For this specimen, the analytical model indicated a crack length sensitivity of 1 $(\mu V/\mu V)$ mm^{-1}. The apparent crack growth rates are between -1×10^{-7} mm/cycle and $+3 \times 10^{-7}$ mm/cycle. While such variations are small compared to typical Paris regime crack growth rates, a reference probe pair would most likely further improve the dcEPD signal stability and crack growth rate resolution necessary for near-threshold experiments [*29*].

Confirmation of Analytical Calibrations

Extensive experiments have been conducted to confirm the accuracy of the analytical model (Appendix) that relates measured voltage to crack length or depth. A large number of artificially defected specimens were cyclically loaded to grow small/short cracks to varying depths. Crack position was marked by either heat tinting or rapid fracture; true crack size (a_{measured}) was measured by optical or scanning electron microscopy and compared to the prediction ($a_{\text{predicted}}$) of the analytical model. Voltage probe location and crack aspect ratio were measured inputs for each specimen. For over 500 specimens examined to date, predicted and measured crack sizes agree to within ±15%. The adverse impact of such differences, and associated effects on da/dN and ΔK, are effectively minimized by linear correction based on one or more known crack lengths.

Through Thickness Edge Crack—Piascik applied the electrical potential model to short, through thickness single edge cracks in aluminum alloys [*22*]. The results from 40 fractured specimens are presented in Fig. 10, with 100-μm-deep micronotches employed for steel [*14*] and 300-μm-deep notches for lower resistivity aluminum alloys [*22*]. Specimen width W equalled 10.2 mm. Therefore, the infinite plate analytical model is tested for a/W ratios up to 0.7. In the majority of cases, including cracks as small as 100 μm ahead of the notch, total measured and predicted crack lengths differ by less than ±15%. The data in Fig. 10 indicate that the model tends to slightly underpredict the length of the edge crack.

Surface Chord Crack—Extensive work has been conducted with a short surface fatigue crack, emanating from an EDM chord notch in a 6-mm round bar [*13,14,25,28,31*]. The initiating flaw is typically 1.5 mm long and 100 μm deep. For the fine grain size (10 to 40 μm) alloys examined, the fatigue crack was short, of depth between 100 and 1000 μm, and intersected many grains along the crack perimeter.

Measured and dcEPD predicted surface crack lengths are compared in Fig. 11 [*14*]. Crack length change represents the depth of fatigue cracking ahead of the micronotch. Results of 90 experiments are presented, including data for two high-strength steels, an austenitic stainless steel, and iron, nickel, and cobalt-based superalloys. Room and elevated temperature (RF heated), moist air, and ultra-high vacuum environments are represented. In all cases $\Delta a_{\text{predicted}}$ differed from $\Delta a_{\text{measured}}$ by less than ±20%. The error is randomly distributed about the line for equal predicted and measured crack lengths.

Corner Crack—Heubaum applied the analytical calibration equation to small and short corner cracks, initiated at a 100-μm-deep corner notch in several HSLA steels [*21*]. Crack length was measured optically at 200 times magnification with 3 μm resolution and on each side of the corner cracked specimen. Averages of these two measurements are plotted in

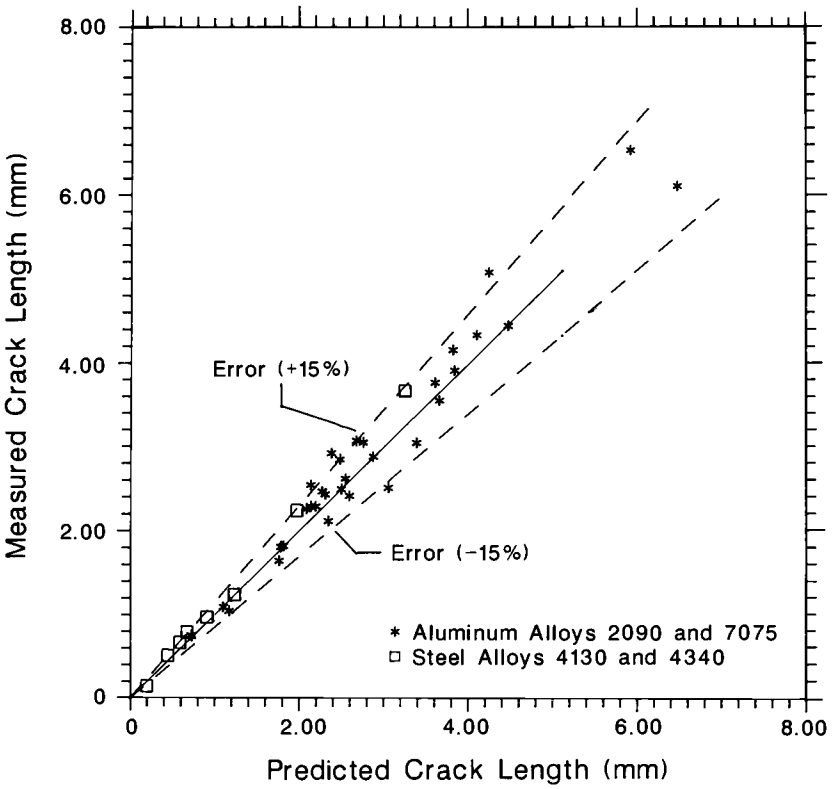

FIG. 10—*Analytically predicted (Appendix) versus optically measured short SE*(T) *crack lengths in fractured individual specimens of aluminum alloys and steels (after Piascik* [22]*).*

Fig. 12 for two replicate experiments with Hiform-60 steel of 200-μm grain size. The accuracy of the analysis is demonstrated by the excellent agreement between the dcEPD predicted and optically measured total crack lengths (notch + fatigue crack). The accuracy of the dcEPD model was not affected by the fact that the fatigue crack interacted with a limited number of prior austenite grains.

Pickard and Hicks employed a finite-element method to relate electrical potential to the size of short corner cracks [*23*,*24*]. The initiating corner notch was 250 μm deep, and the test piece was 10 mm square. The data in Fig. 13 demonstrate that optical measurements of beachmarked corner crack lengths are in excellent agreement with the numerical calibration analysis of the electric field for cracks, sized between 500 and 7000 μm long, in steel [*23*]. Additional data for several alternate crack geometries in steel and titanium indicate similar good agreement between the FEM voltage-crack depth calibration and optical measurements.

Semicircular Surface Crack—Van Stone and coworkers conducted extensive experiments to establish the accuracy of the analytical calibration for nearly semicircular surface cracks in nickel based superalloys [*15*,*16*,*42*]. The grain size of these alloys was between 20 and 100 μm. Heat tint experiments with Renè 95 showed that predicted and measured fatigue crack depths, between 75 and 1500 μm ahead of a 100-μm-deep semicircular notch, differed by less than ±15% [*15*]. Measured mean crack depth at the completion of 73 fatigue

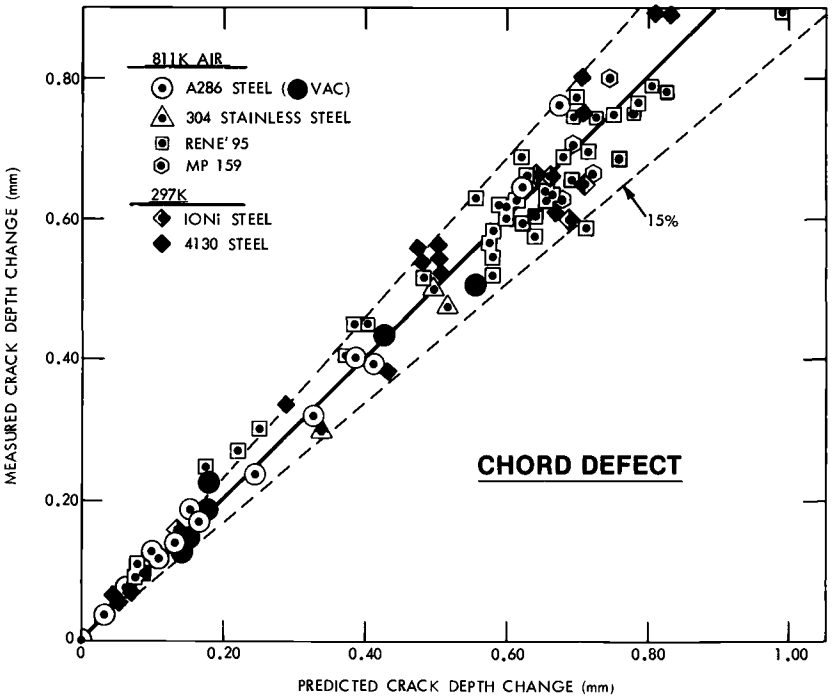

FIG. 11—*Predicted versus measured depths of short chord cracks in individual fractured specimens of steels and superalloys. Chord fatigue cracks were grown at room and elevated temperatures in air and in vacuum. (After Gangloff* [14].*)*

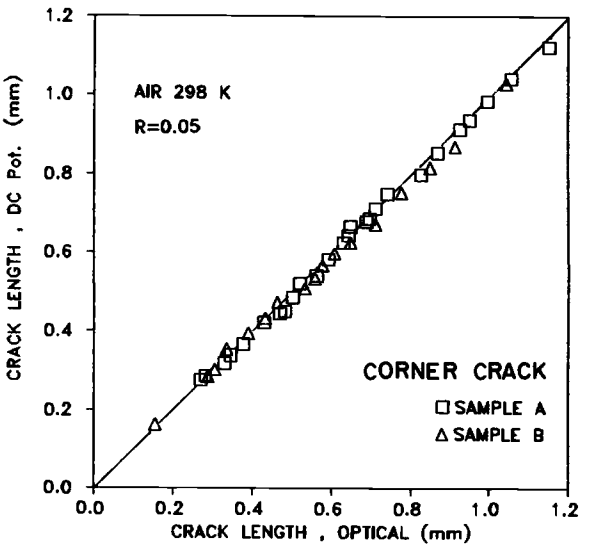

FIG. 12—*Predicted versus optically measured corner crack depths for two specimens of Hiform-60 steel, fatigue cracked in moist air at room temperature (after Heubaum* [21]*).*

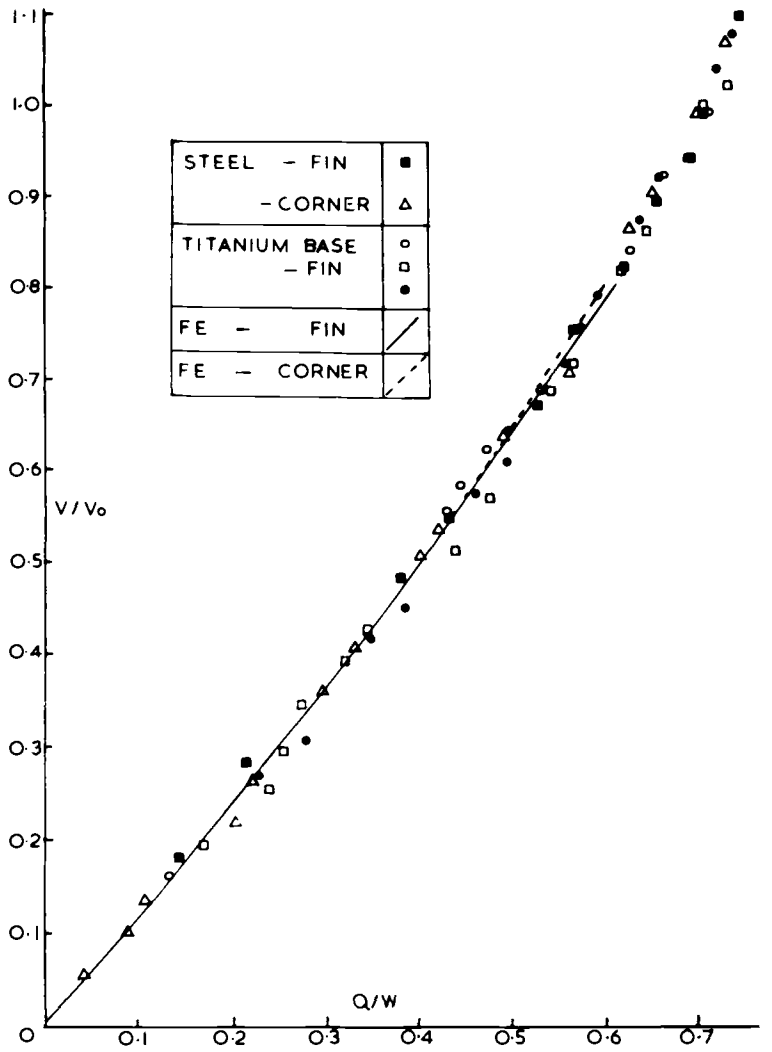

FIG. 13—*Finite element calculated versus beachmark measurements of corner fatigue crack length in a steel (after Hicks and Pickard* [23]*).*

experiments equalled 1.059 mm and the mean ratio of $a_{\text{predicted}}$ to a_{measured} equalled 1.0028 with a range of from 0.768 to 1.165.

Recent data, summarized in Table 3 and Fig. 14*a*, further demonstrate the accuracy of the analytical electrical potential model [*42*]. Test conditions and statistics are given in Table 3, and $a_{\text{predicted}}$ versus a_{measured} data are plotted in Fig. 14*a* for nickel and titanium based alloys. Several specimen designs are represented; including a rectangular bar K_b, a doubly notched rectangular bar with an elastic stress concentration of 1.76 ("DEN" or DE(T)) and a plate with a hole of elastic stress concentration equal to 2.54 ("BH"). The K_b and DE(T) specimens contained 100-μm-deep semicircular micronotches, and the BH specimen contained a corner crack, each produced by EDM. Fatigue experiments were conducted at

constant temperature, over the range indicated in Table 3. For the majority of the 63 experiments, predicted and measured crack depths differ by less than ±15%, as indicated by the dashed lines in Fig. 14*a*. Average errors in terms of the ratio of measured to predicted crack depth, Table 3, are 0.97 for 46 K_b specimens, 1.092 for 12 DE(T) specimens and 1.260 for 5 BH specimens.

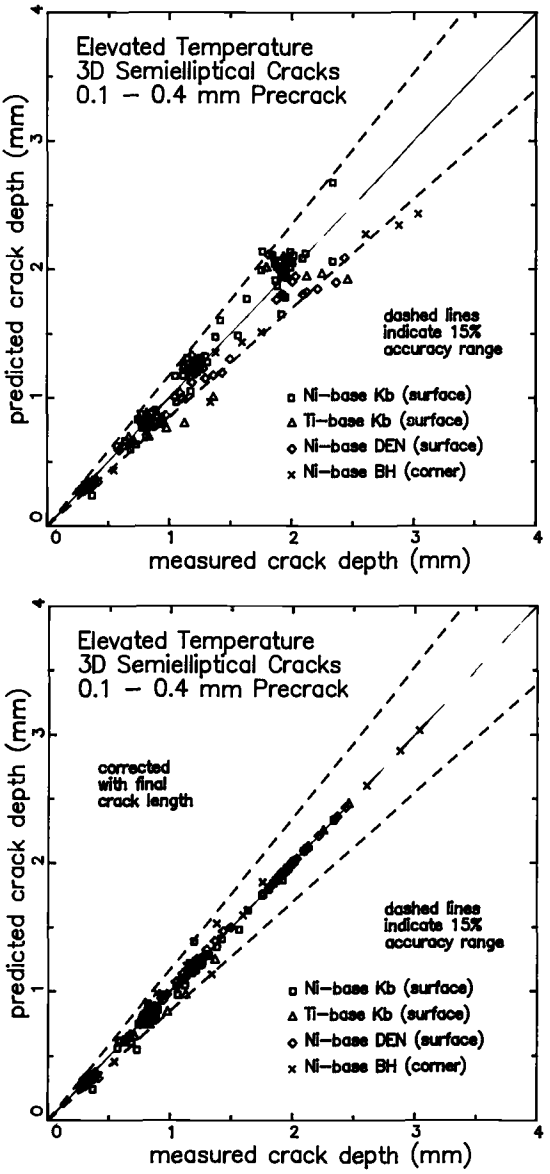

FIG. 14—*Comparison of analytically predicted and optically measured fatigue crack depths in nickel and titanium alloy specimens under uniform stress; and including surface crack* (K_b), *double edge notch (DEN or DE*(T)*) surface crack, and bolt hole (BH) corner crack specimens:* (a) *without and* (b) *with final crack size correction.*

TABLE 3—*Three-dimensional surface cracks under isothermal fatigue loading.*[a]

Test Type	Number of Tests	Temperature Range, °C	$\Delta a_m/\Delta a_p$ Range	Average, $\Delta a_m/\Delta a_p$	Standard Deviation, $\Delta a_m/\Delta a_p$
Ni-base K_b simple cycle	11	204 to 677	0.804 to 0.995	0.930	0.064
Ni-base K_b mission cycling	21	454 to 593	0.855 to 1.146	0.961	0.069
Ti-base K_b mission cycling	14	149 to 316	0.874 to 1.143 (one at 1.325)	1.020	0.129
Ni-base DE(T) simple cycle	7	399 to 649	1.057 to 1.272	1.062	0.019
Ni-base DE(T) mission cycle	5	593 to 621	0.836 to 1.219	1.122	0.161
Ni-base BH simple cycle	3	593 to 649	1.149 to 1.289	1.236	0.076
Ni-base BH mission cycle	2	343 to 593	1.168 to 1.399	1.283	0.163
	63				

[a]Nucleated at 100-μm deep semicircular micronotch.

Crack Length Correction Procedures

The up to ±20% differences between predicted and measured crack lengths for the various geometries are essentially eliminated by employing a post-test linear correction procedure. Crack length and crack front shape are measured by optical or scanning electron microscopy of any beachmarks and the crack geometry after fast fracture. Differences between dcEPD predicted and measured crack lengths are utilized to calculate a correction factor that is linearly apportioned to all crack lengths during the test. An example of the effectiveness of linear correction is indicated in Fig. 14*b*. Final measured crack lengths in Fig. 14*a* were employed to correct shorter crack lengths for each specimen.

The linear correction procedure is effective for post-test data analysis, however, crack length errors result in departures from programmed ΔK during a fatigue experiment. If measured and predicted crack lengths differ by more than about 10%, then programmed stress intensity conditions may not be achieved during loading. This problem is particularly important to constant stress intensity experiments conducted with small/short cracks in either vacuum or reducing environments. For such cases, large errors (for example, $a_{predicted} = 0.6\ a_{measured}$) may be associated with crack surface electrical contact, microscopically rough crack wake surfaces, and potentials measured at low crack openings. When shorting is suspected, voltage must be measured at high K and low loading frequency, linear correction must be employed, and resulting $da/dN - \Delta K$ data should be confirmed by replicate experiments. Complex analytical procedures were proposed to account for the crack opening shape dependence of electrical shorting [*38*]. This procedure is cumbersome and not typically employed.

Three-Dimensional Crack Shape

DcEPD monitoring of the growth of three-dimensional cracks is complicated if the surface length to depth ratio varies during crack extension. Electrical potential solutions for three-dimensional cracks (Appendix) describe an infinite number of crack sizes and shapes for a given value of potential. It is necessary to know the crack aspect ratio in order to uniquely determine crack depth.

Crack aspect ratio depends on the material, specimen, and crack geometry, environment, and in some cases on stress level. Figure 15 shows such behavior for small surface cracks

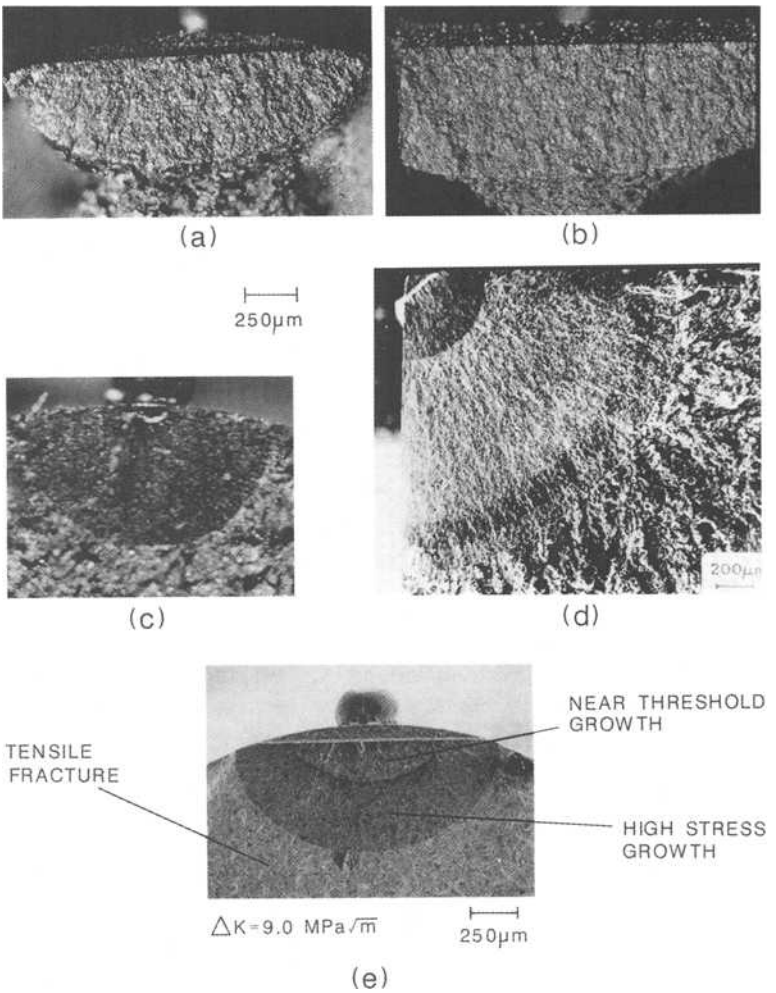

FIG. 15—*Micrographs showing fatigue crack shapes in specimens containing:* (a) *and* (e) *chord shaped surface,* (b) *through thickness edge,* (c) *semicircular surface, and* (d) *constant radius corner initiation micronotches.*

initiated from (a) chord, (b) edge, (c) surface semicircular, and (d) corner micronotches. For these cases, cracks tend to grow from high *c/a* aspect ratios to nearly semicircular shapes. The example in Fig. 15*e* shows that irregular crack shapes can sometimes develop, particularly for near-threshold FCP where da/dN varies strongly with ΔK and ΔK varies with position about the crack perimeter. Environment can also cause novel crack shapes, as discussed elsewhere [*14*]. If the crack shape is well behaved, then dcEPD method is quantitatively accurate. Fortunately, aspect ratio is predictable for a large number of micronotch geometries.

The single-edge crack typically grows uniformly with the crack front parallel to the initiating notch [*22*]. The shape of the fatigue crack emanating from the chord micronotch in a round specimen is predictably shaped. Qualitative examples are shown in Figs. 15*a* and *e*. Figure 16 shows the change in surface crack length for a 100-μm-deep by 1.42-mm-long

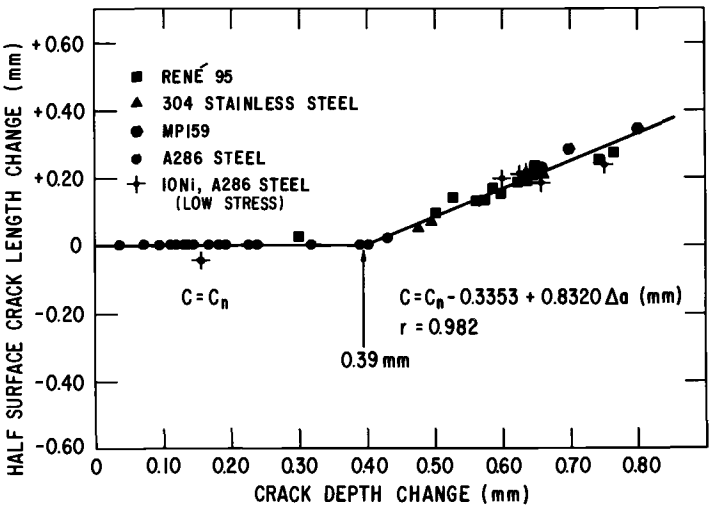

FIG. 16—*Empirical relationship between changes in crack depth and surface length for a range of materials containing a chord initiation notch (after Gangloff* [14]*).*

chord defect in a 5.1-mm-diameter axisymmetric test specimen for a variety of materials. The crack does not grow along the surface until the depth increases by 0.39 mm, after which the crack grew in both the depth and surface directions.

Cracks, initiated at semicircular surface or corner notches, grow with a constant aspect ratio because stress intensity is nearly constant at all crack perimeter locations. Larsen reported that naturally initiated cracks in titanium-aluminum alloys maintain a *c/a* ratio of approximately 0.9 [*43*]. Van Stone et al. showed that the *c/a* ratio of semicircular notch (c_n/a_n = 1.0) nucleated surface cracks in nickel-base superalloys moderately decreases with increasing crack length, according to an empirical relationship [*15,16*]

$$c = c_n + A_2(a - a_n) + A_3(a^2 - a_n^2) \tag{8}$$

Least squares analyses summarized in Table 4 establish the values for A_1, A_2, and A_3. The magnitude of the aspect ratio decrease depends on the applied stress level, as shown in Table 4 [*16*]. Heubaum reported that quarter-circle corner notch nucleated fatigue cracks in an HSLA steel grew with *c/a* equal to 1.0 [*21*].

The influence of changing crack shape is combined with the analytical potential solution in one of two ways. The crack shape can be assumed to evolve by a specific empirical relationship, similar to that shown in Fig. 16 for the chord defect. This relationship must accurately apply over a wide range of experimental conditions. An alternate approach is to monitor the change in crack shape at several times during each test, using a technique such as heat tinting [*16*]. These data can be used to develop a crack shape relationship and to analyze the results of that test. This technique is more applicable to situations where the crack shape is sensitive to the experimental conditions being evaluated such as stress level, temperature, environment, residual stress, or stress gradient.

In order to determine crack shape, Coffin and coworkers employed multiple pairs of potential probes bracketing a surface notch [*35*]. The voltage output from each probe pair was simultaneously analyzed by the model in the Appendix to yield a best fit for crack depth and surface length. This method was only applied to large (10 to 30 mm) surface notches.

TABLE 4—*Summary of Renè 95 K_b specimen experiments.*

Parameters	Specimen 2	3	4	5	A_5
Maximum Stress, ksi	100.0	120.0	100.0	100.0	150.0
a_n	0.0042	0.0043	0.0041	0.0041	0.0030
c_n	0.0040	0.0040	0.0040	0.0041	0.0030
a_f	0.0375	0.0515	0.0747	0.0638	0.0930
c_f	0.0383	0.0473	0.0725	0.0615	0.0705
c_f/a_f	1.02	0.92	0.97	0.96	0.76
	Number of Heat Tints				
	3	3	3	4	2
A_1, in.	−0.001006	−0.000695	−0.000467	−0.000370	−0.000711
A_2, in./in.	1.210076	1.112276	1.096120	1.099421	1.087968
A_3, 1/in.	−4.319042	−3.508373	−1.589179	−2.220452	−3.465136
Correlation coefficient	1.00000	0.99940	0.99997	0.99461	1.00000

NOTE: a_n, c_n, a_f, and c_f are in units of inches. 1 ksi = 6.89 MPa; 1 in. = 25.4 mm.

Ultra-fine probes, perhaps on the order of 20 μm diameter, and precision low power spot welding are required to array multiple probes along a 500 μm long surface flaw. Multiple probing of 50-μm-size flaws is probably not possible.

Quantitative Crack Growth Rate-Stress Intensity Range Data

Gangloff demonstrated the accuracy of the dcEPD method for physically short cracks by determining *da/dN* versus ΔK for a high strength martensitic steel [*31*]. FCP in this 10Ni steel was previously characterized by ASTM round-robin experiments with standardized long crack compact tension specimens [*44*]. Surface chord cracks, 100 μm deep and 1.5 mm long, were employed for the short crack study. From work on the small crack problem, equal fatigue crack growth rates were expected for equal applied ΔK for the short chord and compact tension cracks. Applied maximum stresses were less than the monotonic yield strength (σ_{max} was between 0.3 and 0.8 of σ_{ys}), the crack tip plastic zone at K_{max} was small compared to crack length (between 0.11 and 0.01 of *a*), and the chord crack length was always large compared to the 15-μm grain size and the Topper length parameter for the 10Ni steel.

Da/dN − ΔK data in Fig. 17 confirm that electrical potential monitoring of short surface elliptical cracks in 10Ni steel provides identical crack growth kinetics compared to the extensive compact tension data reported in the ASTM round-robin program [*44*]. Each of the five short crack experiments was conducted at a different constant applied load range [*31*]. Surface crack depth was measured as a function of load cycles by the dcEPD method, and the aspect ratio was empirically defined by the data in Fig. 16. *Da/dN* − ΔK were calculated by an incremental polynomial method and the appropriate stress intensity solution [*31*]. Excellent agreement is observed between the results of the five short crack experiments (symbols) compared to the compact tension data base (solid lines with ± 1 standard deviation of *da/dN*). Even better agreement is achieved if the short crack data in Fig. 17 are calculated based on a plastic zone correction of crack length.

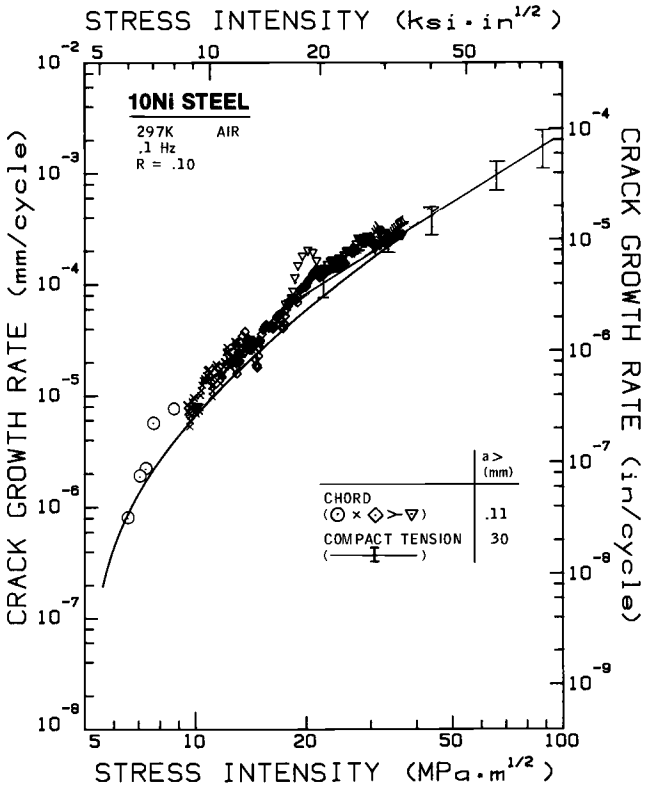

FIG. 17—da/dN – ΔK *data for short surface semielliptical chord cracks in 10Ni steel* (σ_{ys} = *1300 MPa)* [31], *compared to compact tension results (solid line with ±1 standard deviation on* da/dN*) for the same steel, produced by an ASTM round robin program* [44].

Applications of dcEPD Monitoring to Small/Short Fatigue Crack Problems

Programmed Stress Intensity Control for Small/Short Cracks

The dcEPD method provides the important capability to study the growth of small and short cracks under programmed stress intensity. For example, if crack length nonlinearly increases with loading cycles for constant applied ΔK, then calculated stress intensity is not governing crack growth. Continuously recorded crack length data from dcEPD experiments will indicate crack size dependent wake closure contact, crack environment chemistry, or crack tip-microstructure interaction mechanisms.

Heubaum, and later Piascik and Gangloff, conducted computer controlled constant and decreasing ΔK experiments with short cracks monitored by the dcEPD method [*21,22*]. Programmed ΔK was maintained by continuous load adjustments based on dcEPD crack length input to a computerized servohydraulic test machine. This approach follows from automated experiments with long cracks in standard fracture mechanics specimens, where the rate of change of K with crack length C is selected to guarantee a constantly increasing or decreasing plastic zone size, Eq 7 [*40,41*]. (Also see the ASTM Test Method for Measurement of Fatigue Crack Growth Rates [E 647].) If the small/short crack stress intensity solution is complex, a predetermined table of $\Delta K/\Delta P$ as a function of crack length may be employed in a real-time "lookup" mode. (ΔP is applied load range.)

Heubaum and coworkers conducted constant ΔK ($C = 0$) and decreasing ΔK ($C < 0$) FCP experiments at constant stress ratio with well characterized 10Ni steel [*21,39*]. Figure 18 provides an example of dcEPD measurements of the growth of a short through thickness edge crack from a 125-μm-long micronotch in the 10Ni steel, under constant ΔK (6.4 MPa · $m^{1/2}$) and R (0.10) loading. After an initial number of load cycles for crack formation at the root of the 25-μm-radius micronotch, crack length linearly increases with load cycles, as expected based on ΔK similitude for this steel. The resolution of the dcEPD measurements in Fig. 18 is better than 4 μm. Figure 19 contains the results of 16 constant ΔK and R experiments with the 10Ni steel. Both through thickness edge cracks, sized between 125 and 1500 μm, and short corner cracks between 125 and 1000 μm long were successfully monitored and grown under constant ΔK. Each data point, resulting from linear regression analysis of crack length versus cycles data (for example, Fig. 18), is in good agreement with the extensive long crack database for this 10Ni steel, as represented by the line in Fig. 19 and replotted from Fig. 17. Similar good agreement was observed between the results of a short crack decreasing ΔK experiment (ΔK decreased from 15 to 9 MPa · $m^{1/2}$ at $R = 0.10$ as the edge crack grew from 1.9 to 2.2 mm) and the long crack trend line. While this crack length was greater than 1 mm, experience with the 10Ni steel indicates that decreasing ΔK experiments can be conducted with short cracks sized between 50 and 1000 μm.

Piascik and coworkers employed constant ΔK and constant K_{max} methods for both small and short cracks, 300 μm to 4000 μm long, in aluminum alloys [*22,26,32*]. The growth of an edge crack in Al-Li-Cu alloy 2090, from 300 to 4400 μm at constant ΔK and R (2.9 MPa · $m^{1/2}$ at $R = 0.75$), is illustrated by over 200 data points in Fig. 20. Figure 21 contains a similar result for a smaller semicircular surface crack also in alloy 2090 [*32*]. The semicircular fatigue crack grew from 100 to 310 μm under four constant ΔK segments, each at a constant high K_{max} and hence at R above 0.65. Piascik reported similar results for constant K_{max}

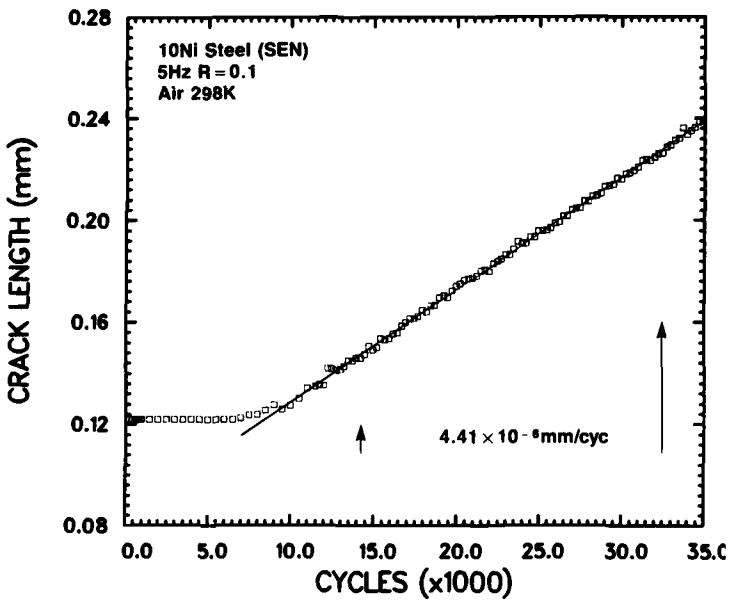

FIG. 18—*Short crack length versus load cycles for a through thickness edge crack in 10Ni steel (σ_{ys} = 1300 MPa) under computer controlled constant* ΔK *and* R [39]. *Note the demarkation between fatigue crack formation at the notch root and steady state crack growth.*

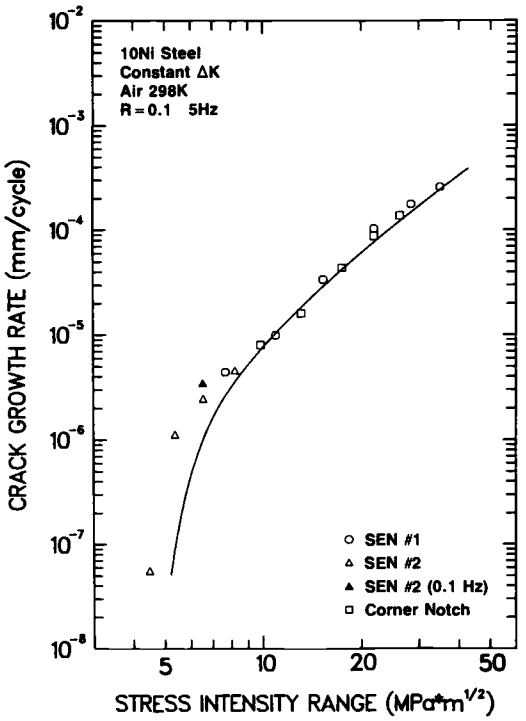

FIG. 19—da/dN – ΔK *from constant* ΔK *experiments with short single edge and corner cracks in 10Ni steel* [21]. *The solid line represents extensive compact tension data for this steel, replotted from Fig. 17* [44].

experiments with edge cracks in several aluminum alloys [*22*]. Linear crack growth indicates that ΔK governed fatigue for each case, as amplified in an ensuing section. There is no evidence of delay retardation after any ΔK decrease in Fig. 21, consistent with constant K_{max} loading. Critically, note the excellent resolution of the dcEPD measurements, as indicated by the insert in Fig. 20 and the data in Fig. 21. Aluminum alloys provide a particular challenge to the dcEPD method because of low resistivity, and hence low voltage for a given crack size, and because of problems in resistance welding fine probe wires to aluminum.

Microstructurally Small Crack Monitoring by dcEPD

The lower limit on the size of the fatigue crack that can be accurately monitored by dcEPD depends on material and temperature (resistivity), probe location, probe attachment stress concentration, and the electrical noise characteristics of the amplifier and laboratory surroundings. Semicircular cracks, of radius as low as 75 μm and 100 μm long through thickness edge cracks, have been accurately monitored. Whether such cracks are microstructurally small depends on grain size. The successes to date indicate opportunities for applications of improved dcEPD methods to naturally and artificially nucleated microstructurally small fatigue cracks.

Ni-based Superalloys—Work with nickel-based superalloys provided the first demonstration of dcEPD monitoring of physically small three-dimensional fatigue cracks between 23°C and 750°C. This system is ideal because of the high electrical resistivity of nickel alloys.

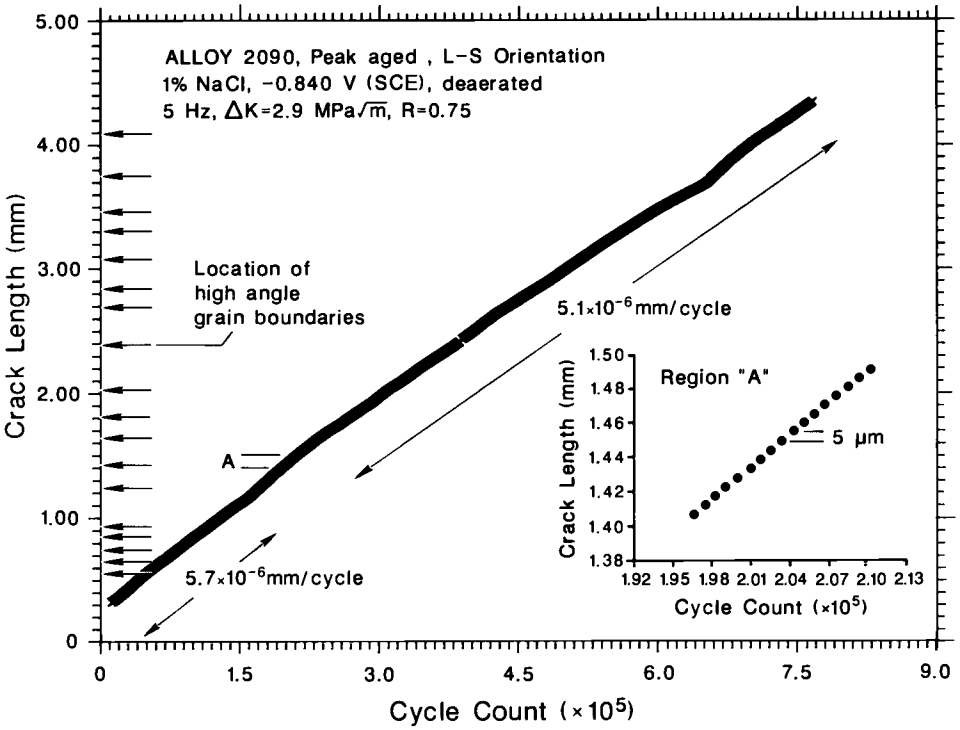

FIG. 20—*DcEPD measured* a(N) *for a short edge crack growing in the LS orientation in alloy 2090 for constant* ΔK *and* R *loading in aqueous NaCl. Arrows indicate the positions of single high angle grain boundaries (after Piascik* [22]*).*

Owing to the small (5 to 50 μm) grain size of such alloys, microstructurally small cracks have not been examined by the dcEPD method.

An initial study of fatigue cracking from 75 μm deep and 200 μm surface length EDM defects (380-μm probe half-height) in 40-μm grain size Renè 95 at 538°C demonstrated that growing crack depth is accurately monitored [*13*]. A crack advance of 240 μm produced a 2% increase in notch potential. Van Stone and coworkers extensively investigated short semicircular surface cracks in nickel-based superalloys [*15,42*]. Specimens with 50-μm-deep semicircular micronotches failed at the probe attachment points, which were marked by shallow EDM dimples to facilitate spot welding. Experiments with 100-μm-deep notches were successful, as indicated by the data in Fig. 14*a* and Table 3. For the probe spacings employed (either 250-μm or 380-μm half-height), 75-μm fatigue crack extension corresponded to a 2% increase in notch potential. Given the 0.05% resolution and long-term stability of the electrical potential signal, crack growth ahead of the 100-μm notch tip was monitored with 1- to 2-μm sensitivity for prolonged loading times.

Van Stone and coworkers investigated wrought and powder metallurgy superalloys including IN718 and Renè 95 with 20- to 50-μm grain sizes [*15,16,28,42*]. This case does not represent a microstructurally small crack because the 100- to 1000-μm semicircular fatigue crack intersected several grains. Accordingly, crack growth rates correlated with ΔK, and crack interactions with grain boundaries were not observed [*45*]. These studies indicate, however, that improved instrumentation, artificial or natural defecting, and probe attachment techniques can be developed for dcEPD monitoring of semicircular cracks sized on

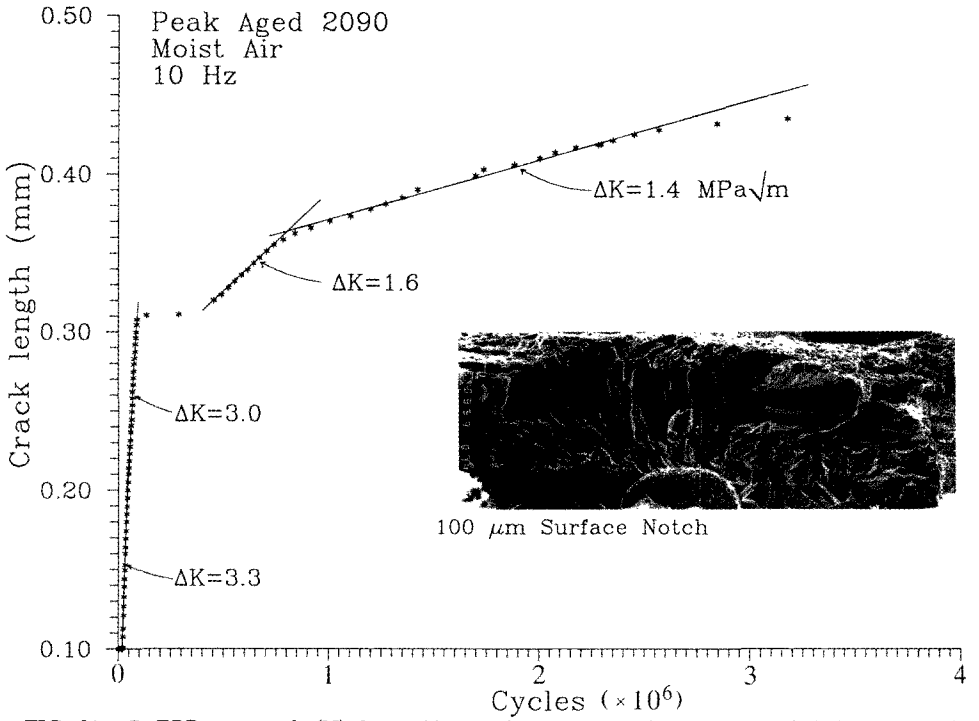

FIG. 21—*DcEPD measured* a(N) *for a 100- to 400-μm semicircular surface crack (LS orientation) in aluminum alloy 2090 (*S *grain size = 110 μm), loaded at several constant* ΔK *constant* K_{max} *(*R > *0.65) in moist air (after Coppin* [32]*).*

the order of 25 μm in superalloys. An alternate approach is to monitor the growth of 50- to 500-μm semicircular cracks in single large grains or in superalloy single crystals.

C-Mn Steel—Heubaum employed the dcEPD method to monitor the growth of microstructurally small fatigue cracks in a tempered martensitic steel [*21*]. Semicircular corner notches, 75 to 100 μm deep, were electrospark discharge machined in single 600-μm-diameter grains of quenched and tempered C-Mn A537 steel (Fig. 8) that was austenitized at a high temperature for grain growth. Stress intensity range was maintained constant by computer control of ΔP with increasing crack length. Typical crack length versus load cycles data are presented in Fig. 22. The continuous decrease in da/dN at constant ΔK is associated with the development of crack wake closure. Based on these and other data, the crack depth resolution of the potential measurement was better than ±2 μm. The results in Fig. 22 establish that the dcEPD method can characterize the growth of small cracks within single grains and sized on the order of 100 to 500 μm in steels.

Heubaum examined several important issues associated with the data in Fig. 22. Corner cracks were located in single lath martensite packets so as to vary the angle between the notch plane (perpendicular to the applied Mode I load) and lath martensite interfaces [*21*]. Specimens were loaded at constant ΔK and R (7.7 MPa · $m^{1/2}$ and 0.05) in moist air. For notch plane-lath angles between 0° and 65°, the small fatigue crack propagated parallel to (and probably within) the interface between two martensite laths within a single packet. The crack plane reverted to a Mode I normal orientation for notch-lath angles in excess of 65°. (The data in Fig. 22 are for a fatigue crack oriented at an angle of 36° to the martensite

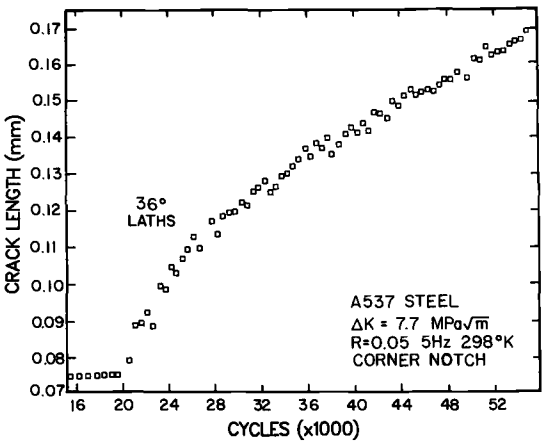

FIG. 22—*DcEPD measured crack length versus load cycles for a microstructurally small 75-μm-deep corner micronotch nucleated fatigue crack in a single 600-μm grain of martensitic A537 steel. Load range was continually adjusted to maintain constant* ΔK *(7.7 MPa · m$^{1/2}$) and* R *(0.05) (after Heubaum* [21]*).*

interfaces.) Heubaum employed a mixed mode analysis of ΔK to successfully explain the observation that *da/dN*, under constant applied Mode I ΔK, decreased by a factor of 2.3 with increasing crack-lath angle.[4] On this basis excellent agreement was observed between *da/dN* for lath interface (small) cracks in single martensite packets and the simple Mode I growth of short cracks in a fine grain size microstructure of the same A537 steel. It is remarkable that equal crack growth rates are observed for small interlath and long translath fatigue cracks.

Heubaum observed that lath interface cracking only occurred in moist air [*21*]. Experiments with small fatigue cracks in single grains of A537 steel, grown in ultra high vacuum, established that crack propagation was always translath and along a plane normal to the applied load (Mode I), independent of the notch-lath interface angle. Vacuum crack growth rates were always less than values typical of fatigue in moist air. These results were obtained because of the compatibility of the dcEPD method with FCP experiments in vacuum.

Replication studies on microstructurally small fatigue cracks in titanium and aluminum alloys typically indicate that surface growth in rapid in a single grain, but is retarded or halted by crack intersection with a high angle grain boundary [*6,8,46*]. In limited beach-marking studies, crack shape has been shown to be reasonably constant, with growth locally retarded when the three-dimensional crack front intersects a grain boundary [*47*]. The electrical potential method is applicable to studies of small crack-boundary interactions. In experiments of the type represented in Fig. 22, Heubaum observed no indication of growth retardation or arrest when the interlath crack intersected a grain boundary in large grain size A537 steel [*21*]. Substantial changes in martensite interface orientation across packet or prior austenite grain boundaries had no significant effect on FCP. On average, cracking progressed along the interface in the next grain, at a rate dictated only by the appropriate mixed mode ΔK level.

An alternate example is presented in Fig. 23. A corner fatigue crack in 200-μm-grain size steel is retarded (200% reduction in *da/dN*) as it crosses the first grain boundary in front of the notch tip, as observed on the corner surfaces (arrow), and changes orientation from laths that are normal to the applied load to inclined interfaces [*21*]. Crack deflection was

[4]The electrical potential model in the Appendix is not strictly applicable to a crack growing out of the plane of the notch. None-the-less, surface measured and dcEPD predicted corner crack lengths differed by less than ±10%, indicating that the simple analysis is accurate [*21*].

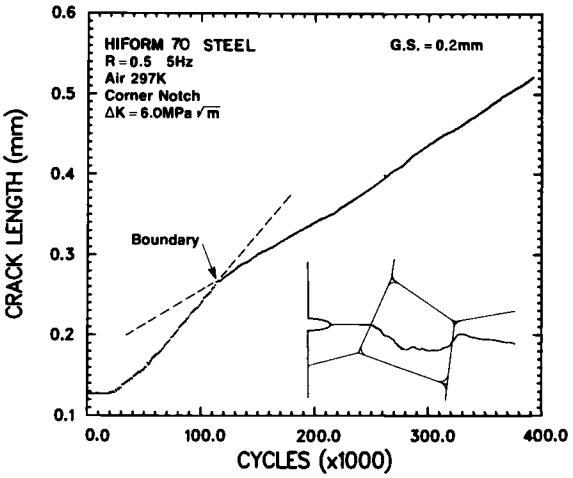

FIG. 23—*DcEPD measured* a(N) *for a small corner crack in a single 200-μm-diameter grain in martensitic A537 steel at constant applied Mode I* ΔK *(6.0 MPa* · $m^{1/2}$) *and* R *(0.5) (after Heubaum* [21]*).*

boundaries can locally arrest FCP, but the more general increase in fatigue crack area is not substantially affected by grain boundary-crack interactions at single points [*21*]. Retardation may be more pronounced if a significant portion of the crack front intersects a grain boundary.

Aluminum Alloys—The dcEPD method was successfully applied to measure the growth of microstructurally small fatigue cracks in aluminum alloys, with better than 3-μm resolution [*22*]. Good long-term stability enabled near-threshold growth rate measurements in controlled gaseous and aqueous environments.

Two small crack geometries, nucleated at micronotches and ranging in depth from 100 μm to 5 mm, were employed to study the effect of microstructure and grain boundaries on intrinsic fatigue crack growth [*22*]. For highly textured unrecrystallized aluminum alloy 2090 (Al-Li-Cu-Zr) plate, dcEPD crack length measurements are presented in Figs. 20 [*22*] and 21 [*32*] for growth from either a through thickness 300-μm-long single-edge notch and or a 100-μm-deep semicircular defect, respectively. Specimens were loaded at constant applied ΔK. Given the LS orientation, each growing fatigue crack is essentially contained within a single high angle grain (L grain size = 10 to 20 mm, T grain size = 3.3 mm, and S grain size = 110 μm). These fatigue cracks encounter grain boundaries with propagation in the through thickness direction S every 100 to 300 μm. The excellent 3 μm resolution of the dcEPD method is evident in Figs. 20 and 21.

The SE(T) data in Fig. 20 indicate a constant rate of fatigue crack advance, with no resolvable effect of high angle boundaries (noted by arrows) for 2090 in aqueous NaCl. Similar results were observed for edge cracks in this alloy in moist air [*22*]. A different result was obtained for the semicircular flaw in 2090, loaded at four constant ΔK levels in moist air (Fig. 21). The crack grew from 100 to 310 μm, across a high angle grain boundary during the initial two high constant ΔK segments, with no resolvable retardation. At the lowest ΔK (1.4 MPa · $m^{1/2}$) the crack grew at an essentially constant rate, but was slowed by a grain boundary. The shape of the crack indicates that growth continued as the leading point of the perimeter was arrested at the grain boundary. The boundary altered crack shape, but did not generally arrest cracking, as would be inferred from surface optical measurements. DcEPD measurements indicate the increase in crack area; however, calculated crack lengths for the last segment in Fig. 21 are not precise because of the change in crack shape. The

not sufficient to explain this change in da/dN based on mixed mode ΔK; rather roughness induced crack closure was important. Experiments with C-Mn steels indicate that grain contributions of ΔK level, crack shape, and grain microstructure/crystallographic orientation to the different crack-boundary interactions indicated in Figs. 20 and 21 are not understood.

DcEPD based-crack growth rate data for small and short cracks in Al-Li-Cu alloys in moist air do not indicate the rapid growth of microstructurally small cracks. Figure 24 contains da/dN data from dcEPD measurements during constant ΔK and K_{max}-high R loading of alloy 2090 [*22,26,32*]. Each dcEPD based data point represents the least squares fit of a large sampling of $a(N)$ data at constant ΔK (for example, Figs. 20 and 21). Similar intrinsic growth rates are observed for edge cracks in both multiple grain (LT with 20 to 30 grains along the crack front) and single grain (LS) orientations, and for the semicircular flaw (LS). For ΔK levels above an apparent threshold of 1.4 to 1.6 MPa · $m^{1/2}$, dcEPD results are in good agreement with standard compact tensile data [*22*], and with the results of a replication study of cracks initiated at surface constituent particles in alloy 2090 [*48*]. Coppin obtained identical results for unrecrystallized, textured aluminum-lithium alloy 2091 [*32*]. Other than the crack arrest indicated in Fig. 21, the data in Fig. 24 suggest that high angle grain boundaries have little effect on closure-free FCP in textured aluminum alloys.

Electrical potential and replication based crack growth rates differ for the near threshold regime of FCP. Edge and semicircular notch nucleated cracks in alloys 2090 and 2091 did not grow at ΔK levels below about 1.4 MPa · $m^{1/2}$ at any stress ratio [*22,32*]. In contrast replication based growth rates for inclusion nucleated fatigue cracks are finite at ΔK levels

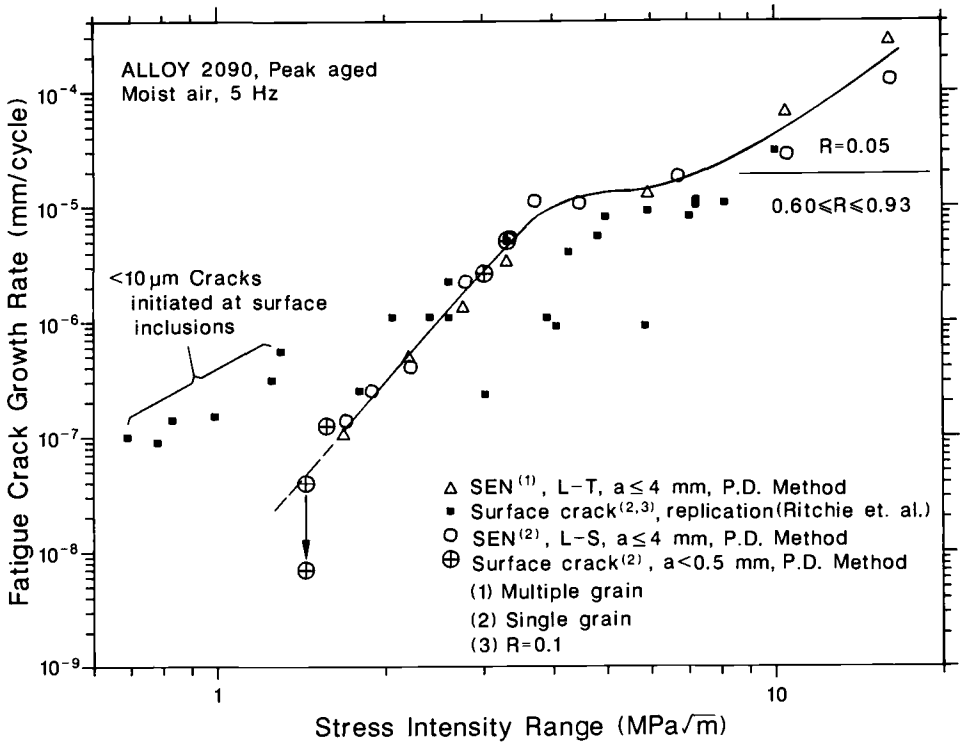

FIG. 24—*Comparison of the FCP rates of microstructural small surface flaws (a < 500 μm), monitored by replication and dcEPD, and through thickness multiple (LT) and single (LS) grain edge cracks of length ≤ 3 mm (dcEPD monitored) (after Piascik* [22]).

well below 1.4 MPa · $m^{1/2}$ [*8,46,48,49*]. This "small crack effect" is not evident from electrical potential results, despite the fact that the latter dealt with microstructurally small cracks in single grains of alloy 2090. Accelerated *da/dN* associated with small surface cracks, <10 μm in depth and initiated at surface constituents, may be due to residual stress or notch effects produced by the inclusion, or to an artifact of surface crack length measurement. Comparative studies involving dcEPD, surface replication and perhaps interferometric displacement measurements are required to resolve the inconsistency illustrated in Fig. 24.

Small/Short Crack-Environment Interactions

DcEPD monitoring of cracking from artificial micronotches is particularly effective for studies of small/short FCP kinetics for alloys in aggressive environments. Results identified novel chemical crack size effects [*7*], and the unique high resolution and constant ΔK capabilities of the method yielded new understanding of corrosion fatigue [*50*].

High Strength Steels in Aqueous Chloride: The Chemical Crack Size Effect—Gangloff demonstrated that physically short fatigue cracks grow at unpredictably fast rates in aqueous chloride environments because of a so-called "chemical crack size effect" [*7*]. *da/dN* – ΔK data are presented in Fig. 25 for high-strength tempered martensitic 4130 steel in aqueous 3% NaCl [*25*]. Experiments with 100- to 1000 μm-deep surface chord cracks, 100 to 3000 μm long through thickness edge cracks and 25 to 40 mm long compact tension specimen

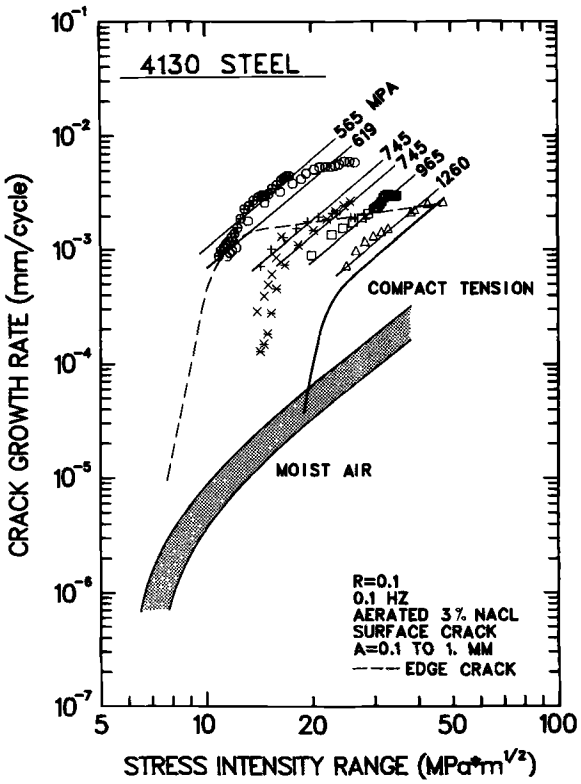

FIG. 25—*The effect of crack size and shape on corrosion fatigue crack propagation kinetics in a high strength steel in aqueous NaCl (after Gangloff* [25]*).*

cracks, demonstrate that applied ΔK uniquely correlates da/dN, independent of crack size and applied stress range, but only for FCP in vacuum or moist air. Crack growth in NaCl is not described by ΔK. While compact tension results indicate the deleterious environmental effect compared to FCP in vacuum, the short chord and edge flaws grow at substantially higher corrosion fatigue crack growth rates. Furthermore, da/dN for the short cracks decreases with increasing applied stress at constant ΔK. Long cracks at all ΔK and short cracks at high stresses grow by a transgranular mechanism, while rapid short crack growth is intergranular.

The results in Fig. 25 are interpreted in terms of crack size and opening shape dependent changes in the local chemistry of the occluded fatigue crack [*7,25*]. For steels in chloride, increased levels of embrittling hydrogen are produced at the tips of small and short cracks because of a complex interplay between convective mixing, ionic diffusion, and surface electrochemical reactions [*51,52*]. Stress intensity based similitude does not describe this effect. The environment within cracks sized above about 5 mm is essentially constant with varying length and opening; ΔK similitude is obeyed in long crack corrosion fatigue [*50*].

Chemical crack size effects have not been broadly reported for other material-environment systems. The effect indicated in Fig. 25 is observed for a range of ferritic and martensitic C-Mn and alloy steels, however, the magnitude of the growth rate increase for short cracks decreases with decreasing steel yield strength [*7*]. Additional studies of crack size effects in corrosion fatigue are required [*50*]. The DcEPD method provides an effective method for such work.

DcEPD Monitoring of Aluminum Alloys in Gases and Electrolytes—The dcEPD method was successfully applied to measure the growth of small and short fatigue cracks in aluminum alloys stressed in controlled gaseous and aqueous environments [*22,26,27,53*]. The through thickness edge crack geometry was employed, with crack lengths between 350 μm and 5 mm. This work exploited the capabilities of the dcEPD method for 3-μm or better average crack length resolution, long-term stability for near-threshold cracking, environmental compatibility, and constant ΔK loading to resolve the effects of environment chemistry and loading frequency changes. Environmental effects were quantified in short increments of crack growth (<250 μm) at constant ΔK, and small changes in a versus N behavior were resolved. Intrinsic crack closure free growth rates were measured by coupling short edge cracks, and accordingly limited wakes, with fracture mechanics based constant $\Delta K/K_{max}$, high R experiments.

Shown in Fig. 26 are the results of dcEPD short crack (SE(T)) experiments performed on alloy 2090 in several aqueous NaCl environments [*22,26,27*]. Data for cracking in moist air are replotted from Fig. 24. For all SE(T) experiments at R above 0.05, K_{max} was maintained constant at 17 MPa · $m^{1/2}$. Saltwater experiments were conducted in flowing deaerated 1% NaCl solution at 23°C, contained in an O-ring sealed plexiglass chamber, and with applied polarization of either -840 mV_{sce} (anodic) or -1240 mV_{sce} (cathodic). The effects of various gaseous environments (dynamic vacuum, helium, oxygen, and water vapor) on intrinsic small/short crack propagation kinetics were characterized by similar experiments [*53*]. Purified gas experiments were performed in a stainless steel ultra high vacuum chamber.

The data in Fig. 26 demonstrate that the dcEPD method successfully monitors the growth of small/short fatigue cracks in aluminum alloys immersed in aggressive environments. Spot welded probe connections were not corroded during 1- to 10-day experiments. These experiments indicate the lack of a chemical crack size effect in the aluminum/NaCl system, in contrast to the behavior of steels (for example, Fig. 25). Stress intensity range accurately describes the growth rates of short edge cracks and long compact tension cracks in 2090 and 7075 aluminum alloys exposed to aqueous NaCl [*22,26,27*]. From the corrosion fatigue perspective, the data in Fig. 26 indicate the good environmental cracking resistance of the

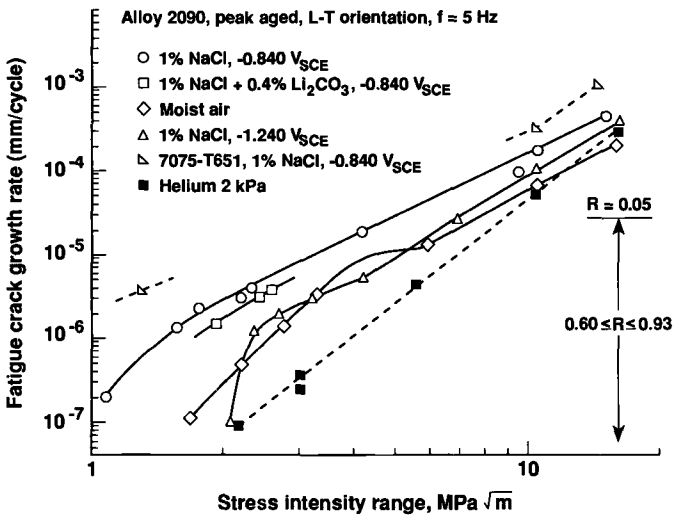

FIG. 26—*The FCP behavior of Al-Li-Cu alloy 2090 in aqueous 1% NaCl at constant anodic (−0.840 V_{SCE}) and cathodic (−1.240 V_{SCE}) potentials, in 1% NaCl + 0.4% Li_2CO_3 (−0.840 V_{SCE}), in moist air, and in helium environments; and of alloy 7075 in aqueous 1% NaCl at constant anodic (−0.840 V_{SCE}) potential (after Piascik and Gangloff* [22,26,27]).

advanced Al-Li-Cu alloy, compared to 7000 series alloys and similar to the behavior of alloys such as 2024. Increased near threshold *da/dN* in water vapor containing gases and aqueous NaCl is thought to be due to hydrogen embrittlement [*22,26*]. The time required for these corrosion fatigue experiments was substantially reduced because of the high resolution and small crack growth increments typical of small/short crack measurements by the dcEPD method.

Several problems must be dealt with when employing the dcEPD method to characterize environmental FCP in aluminum alloys. Electrical resistance is low and voltages are relatively small (Table 2). Specimen heating in vacuum results from applied direct current of 5 to 10 A; temperature must be monitored by a thermocouple attached directly to the specimen and is controlled by limiting the current and testing time [*22,53*]. Heat is dissipated by helium, oxygen, and water vapor. Crack length measurement errors, associated with fracture surface shorting in vacuum, helium, and NaCl, are minimized by measuring voltages at maximum tensile loads and by high *R* loading.

The applied direct current, necessary for dcEPD monitoring, does not influence fatigue crack growth rates for aluminum alloys and steels in NaCl. Experiments were performed using alloy 2090 micronotched SE(*T*) specimens, fully immersed in deaerated 1% NaCl at −0.840 V_{SCE} [*22*]. At a constant ΔK of 1.6 MPa · $m^{1/2}$ and an applied direct current of 14 A (6×10^5 A/m^2), a constant fatigue crack growth rate of 1.5×10^{-6} mm/cycle was obtained for crack depths ranging from 0.70 to 0.89 mm (Fig. 27). The potential difference current was eliminated for 155 000 load cycles; continued cycling produced a crack depth increase from 0.89 to 1.13 mm as noted in Fig. 27. During this period, load was maintained constant, but ΔK only mildly increased with crack length. The average "measured" *da/dN* ($\Delta a/\Delta N$) for alloy 2090 with no applied electrical current was 2.0×10^{-6} mm/cycles. Considering the small increase in ΔK, this rate is consistent with the growth behavior indicated by the data in Fig. 26, which were obtained with an applied current. The experiment was continued at 1.13 mm (Fig. 27), the DC current of 14 A was reapplied, and ΔK was immediately adjusted

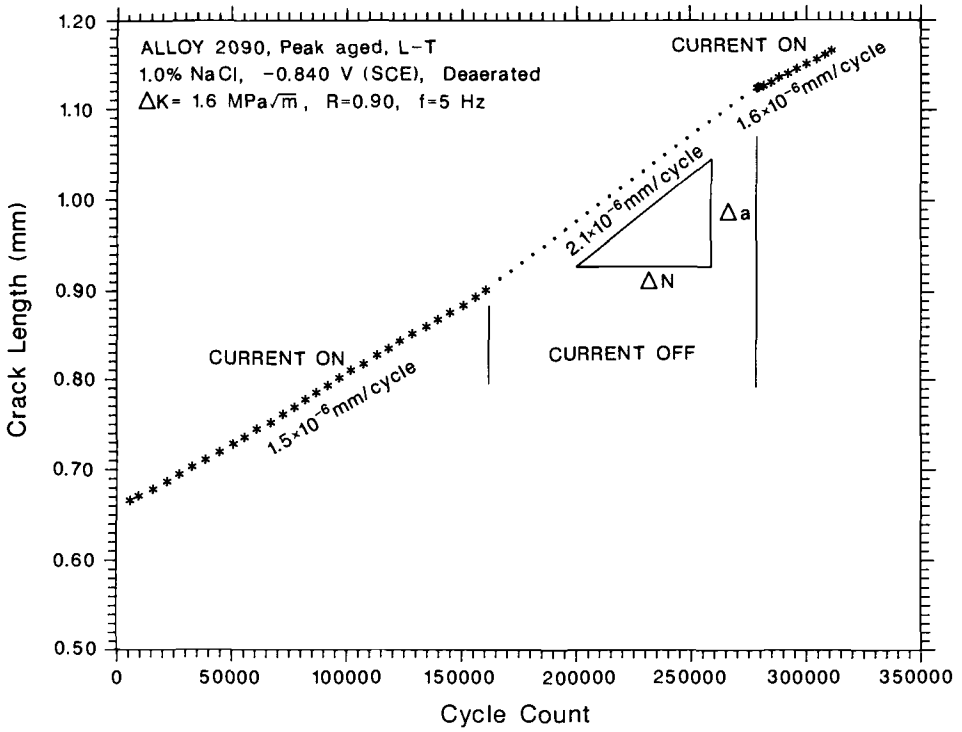

FIG. 27—*The lack of an effect of the applied dcEPD current on fatigue crack growth in alloy 2090 in an aqueous NaCl environment (after Piascik* [22]*).*

to the initial constant level of 1.6 MPa · $m^{1/2}$. Little difference in *da/dN*, 1.5 × 10^{-6} and 1.6 × 10^{-6} mm/cycle, is observed for the initial and final crack length intervals, suggesting that no chemical history effects are present. Crack tip environment was not altered by eliminating the electrical current.

Results clearly show that aluminum alloy corrosion fatigue crack growth rates are not altered by an applied direct current. A similar result was reported for a steel in NaCl [*25*]. In both cases dcEPD current switching has no effect on measured anodic or cathodic electrochemical currents for constant working electrode potential. To date, there have been no reports of an applied direct current for dcEPD monitoring affecting fatigue crack growth rates. Presumably, the applied current only passes through the low resistivity metal and does not enter the higher current path associated with the electrolyte in the fatigue crack.

Corrosion Fatigue at Ultra Low Loading Frequencies—A particularly important aspect of the dcEPD method for small/short crack monitoring is the capability to resolve environment sensitive *da/dN* at extremely slow loading frequencies. Low frequency loading enhances rates of FCP for aggressive environments, however, data are limited because of the prolonged times required for conventional experiments with long crack fracture mechanics specimens [*50*].

Crack length data in Fig. 28 indicate the effectiveness of the dcEPD method [*39*]. A short edge crack in a C-Mn steel exposed to aqueous NaCl is propagated at constant ΔK and R (23 MPa · $m^{1/2}$ and 0.1) at an ultra low loading frequency of 2.4 × 10^{-4} Hz. Crack length increased by 100 μm, at a constant rate of 4.9 × 10^{-4} mm/cycle, during 200 loading cycles

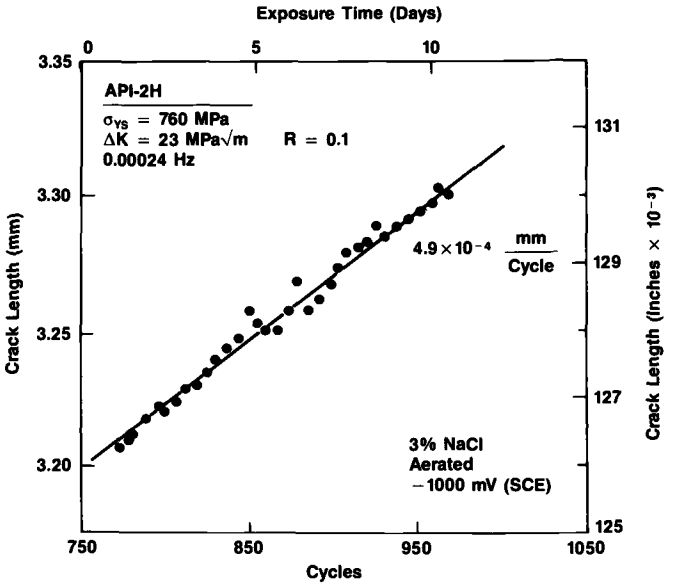

FIG. 28—*DcEPD measured* a(N) *for a short edge crack in a C-Mn steel in NaCl and subjected to very slow frequency loading (0.00024 Hz) at constant* ΔK, R, *and electrode potential.*

over a period of 9.6 days. The resolution and stability of the dcEPD measurements are obvious, and the crack growth rate is quantitatively defined. The results in Fig. 28 were obtained with a relatively long crack, however, similar data have been obtained for cracks sized below 1000 μm [*39*]. Since crack growth increments of 25 to 100 μm are readily defined by dcEPD monitoring, the number of cycles and time required for the *da/dN* determination are reduced.

Van Stone and coworkers employed dcEPD monitoring of short (250 μm to 1.5 mm) through thickness edge cracks to measure near-threshold growth rates at very low loading frequencies [*54*]. For Renè 95 at 593 and 649°C, growth rates between 2×10^{-8} and 1×10^{-3} mm/cycle were measured for 20 cycles per minute (cpm) continuous cycling. FCP rates as low as 8×10^{-8} and 8×10^{-7} mm/cycle were obtained with 30 and 300 s K_{max} hold periods, respectively. Similar results were previously reported by Gangloff, as summarized in Fig. 29 [*14*]. Here, a surface chord notch nucleated fatigue crack propagated from 100 to 750 μm at constant applied load (increasing ΔK), during either continuous load cycling at 0.1 Hz or with a 15-min hold period at K_{max}. This latter case required loading for 7.8 days. The dcEPD method provided a stable and high resolution output of crack length throughout each experiment and in spite of the fact that the Renè 95 specimen was RF heated to 538°C.

Effect of Environment Chemistry—DcEPD monitoring is well suited to define crack growth rates associated with changes in the surrounding chemical environment. The use of constant ΔK and small/short crack methods enhances this capability for both steady state and transient cracking cases.

DcEPD based chord crack depth data in Fig. 30 demonstrate the effect of applied cathodic polarization on corrosion fatigue crack initiation at the micronotch root and on subsequent short crack propagation for high-strength 4130 steel in 3% NaCl [*55*]. With crack initiation and early growth operationally defined as the load cycles required for 125 μm of crack

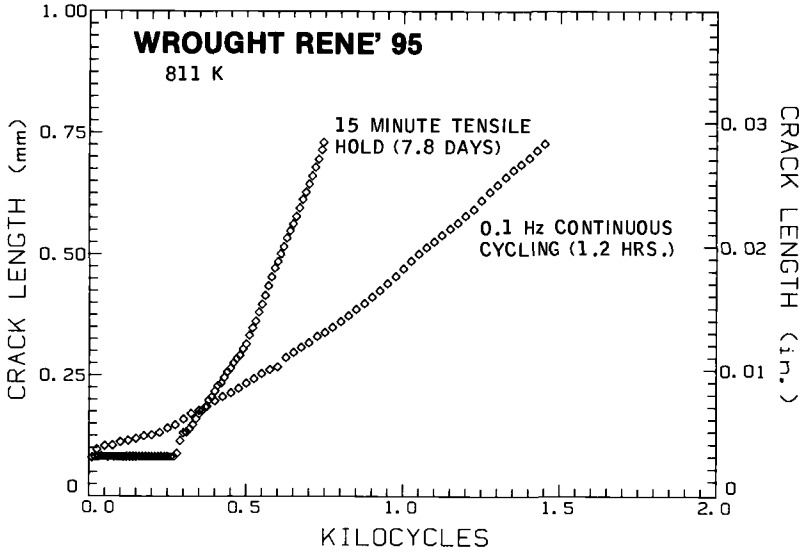

FIG. 29—*DcEPD measured crack lengths for chord micronotch nucleated fatigue cracks in cast and wrought Renè 95, RF heated to 538°C, under constant applied load range cycling at either 0.1 Hz or with a prolonged hold period at* K_{max} *(after Gangloff* [14]*).*

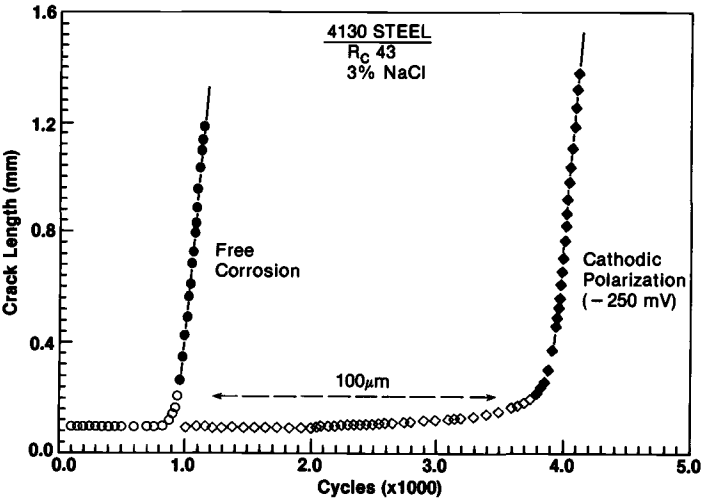

FIG. 30—*DcEPD measured* a(N) *for high strength steel in NaCl, under free corrosion or applied cathodic polarization (after Gangloff* [55]*).*

growth ahead of the 125-μm-deep chord notch, applied cathodic potential retards the deleterious environmental effect. (The crack initiation life in moist air is about 4000 cycles at this applied "ΔK" level.) Crack growth rates are enhanced by cathodic polarization. Data of the sort presented in Fig. 30 are relevant to the use of cathodic protection on marine structures.

Near-threshold fatigue crack growth transients, resulting from changes in bulk and crack environment chemistry, were resolved by the dcEPD method for aluminum alloys in NaCl [*22,26,27*]. Short edge cracks, between 350 and 5 mm deep, were grown at constant ΔK and high R. Such experiments, involving changes in applied electrode potential, lithium carbonate (Li_2CO_3) additions and varying loading frequency, demonstrated that chemical conditions favoring crack surface film formation retarded crack growth rates at constant ΔK because of reduced hydrogen production and uptake efficiency [*22,26*].

Two studies employed dcEPD monitoring of short cracks to investigate the effect of gaseous environment chemistry on fatigue crack propagation in steels. Data in Fig. 31 were obtained with constant ΔK and R (8.2 MPa · $m^{1/2}$ and 0.05) loading of short corner cracks (400 to 1100 μm deep) in fine grain size (20 μm) martensitic A537 steel exposed to various gas environments [*21*]. Initial cracking in purified H_2 occurred at a constant rate of twice that observed for vacuum. The gas within the vacuum test chamber was then sequentially changed from H_2 to moist air to pure oxygen to pure water vapor to O_2 + H_2O. Faster crack growth rates were observed relative to H_2, with each environment similarly enhancing *da/dN*. These data indicate that both the oxygen and water vapor constituents of moist air increase rates of FCP. While hydrogen embrittlement is typically invoked to explain the effect of water vapor on FCP in steels, surface oxide effects are also suggested by these data [*50*]. A similar study demonstrated the important effects of hydrocarbon molecules, such as ethylene, in inhibiting the otherwise strong gaseous hydrogen embrittlement of steel [*30*]. The dcEPD/constant ΔK/short crack method is equally effective in characterizing the effect of aqueous environment chemistry changes; for example, the effect of solution oxygen for chloride corrosion FCP in steel [*55*].

As a caution, rapid environmental changes (for example, hydrogen to vacuum) or loading variations (for example, a frequency or R change) may alter the electric potential because of thermal effects on specimen resistivity and changes in crack surface electrical conductivity. Under constant ΔK control, apparent crack length changes result in applied load changes and hence varying ΔK. The importance of these effects depends on the severity of the environmental change and on specific ΔK, R, and loading frequency levels. Guidelines, beyond an awareness of the complication, cannot be given.

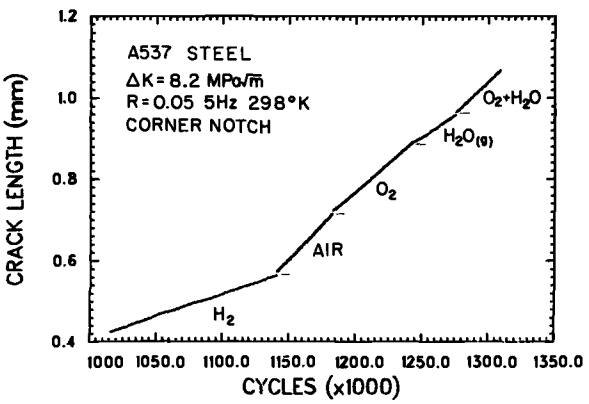

FIG. 31—*DcEPD measured cyclic crack length data for A537 steel in various high purity gaseous environments during constant* ΔK *loading of a short corner crack (after Heubaum* [21]*).*

Applications to Elevated Temperature Gas Turbine Materials

Lankford et al. reported on the importance of microstructurally small fatigue cracks to the performance of nickel and titanium alloy gas turbine disks [*56,57*]. Experiments based on surface replication demonstrated that inclusion nucleated fatigue cracks in alloys, such as Waspaloy, grow at finite rates, below the apparent long crack threshold ΔK_{th}, for both ambient and elevated temperature cycling [*58*]. An extrapolation of the Paris power law to low ΔK levels reasonably described the growth of such cracks.

The dcEPD method has been routinely used to monitor the growth of short cracks in nickel and titanium alloys. During the past 12 years, over 2000 specimens have been tested, as summarized below. This research generally demonstrates that the propagation behavior of short cracks, sized between 75 μm and 1 mm, is well described by linear elastic fracture mechanics similitude based on ΔK; anomalous crack size dependent FCP was not observed [*45*].

The dcEPD method has not been applied to microstructurally small cracks, naturally nucleated at inclusions or pores, and contained within a single grain. Nonetheless, dcEPD based experiments have provided important insight regarding the fatigue behavior of gas turbine disk alloys. For example, it was not possible to a priori assume that elastic stress intensity similitude describes the growth of submillimeter sized fatigue cracks. Additionally, many of the studies, summarized in the following sections, could not have been conducted with conventional long crack methods.

Effect of Stress Ratio—Fatigue crack growth rates for extruded and isothermally forged Renè 95 were measured at 399°C and 0.33 Hz with R ranging from -1.00 to 0.75 [*59*]. The on-off dcEPD technique was applied to short surface semicircular and SE(T) through thickness cracks sized between 100 and 1000 μm. This approach provided extensive and highly reproducible data in a cost efficient manner. Typical growth rate laws were defined by several 100 $da/dN - \Delta K$ data pairs covering up to five orders of magnitude in da/dN. These data demonstrated that the influence of stress ratio is accurately treated with a Walker model [*59,60*].

Effect of Microstructure—Direct current potential monitoring of short crack growth permits the rapid and automated evaluation of microstructural influences on FCP. The effects of superalloy grain size and aging condition were studied for wrought Inconel 718 [*61,62*]. $da/dN - \Delta K$ data were measured in specimens with through thickness edge cracks, sized between 100 μm and 2 mm, and tested at 428°C. Results for Inconel 718 at elevated temperatures show that increasing grain size increases ΔK_{th} and decreases Paris regime crack growth rates, and that slip reversibility controls da/dN. Van Stone and Gangloff studied the effects of powder size and hot isostatic processing conditions on FCP in powder metallurgy Renè 95, based on experiments with small surface chord cracks [*28*].

Effect of Temperature—DcEPD monitoring of 100- to 3000-μm-deep through thickness edge cracks demonstrated that increasing test temperature increases both the fatigue crack growth threshold and Paris regime crack growth rates for IN 718 [*20,59*]. There is almost a factor of two increase in ΔK_{th} with increasing temperature from 149 to 538°C. Experiments at high and low R suggested that differences in the threshold were not caused by oxide induced closure and may result from creep-induced stress relaxation in the vicinity of the crack tip [*59*]. Experiments at 149°C are an excellent illustration of the long-term stability of the on-off dcEPD monitoring system [*59*]. A typical experiment was conducted at a constant frequency of 0.33 Hz and lasted six weeks; no difficulties were encountered. The test was terminated because an additional six weeks was required to reduce ΔK by only 0.5 MPa · $m^{1/2}$. Such data are not obtainable, in a reasonable time, with conventional long crack methods.

Creep-Fatigue-Environment Interactions—It is well known that elevated temperature crack growth in nickel-base superalloys is accelerated by slow load cycling, prolonged hold times at K_{max}, and the moist air environment [*45*]. The dcEPD technique, applied to short cracks, is invaluable for studies of such effects. Figure 32 shows $da/dN - \Delta K$ results for 100 to 1000 μm long through thickness edge cracks in Renè 95, subjected to 0.33 Hz (20 cpm) or 300 s hold time cycles at 649°C in moist air and ultra high vacuum [*59*]. Note that the hold time at K_{max} accelerates crack growth rates for both air and vacuum, with particularly rapid crack growth rates observed for the former environment. These experiments demonstrate that FCP is governed by a complex interaction between creep, fatigue, and environment [*20,59*]. The dcEPD method is well suited to monitor the growth of fatigue cracks in vacuum; no extra space is required in the test chamber, the electrical method is noncontaminating, and artifacts and delays caused by repeated loading interruptions are avoided. The excellent resolution of the small crack dcEPD technique enables growth rate measurements for low frequencies and prolonged hold times, as previously discussed with regard to Fig. 29 [*54*]. As a caution, crack surface shorting often occurs in vacuum; voltages must be measured at maximum load, high K_{max} experiments are least prone to errors, and post-test crack length corrections may be required.

Life Prediction Studies—The dcEPD technique was used to monitor the growth of short cracks in test specimens, with the objective of verifying the accuracy of fatigue life prediction methods. Such specimens have stress gradients or are cycled with stress-time histories that are representative of gas turbine components, or both [*45,63,64*]. Typical test specimens are

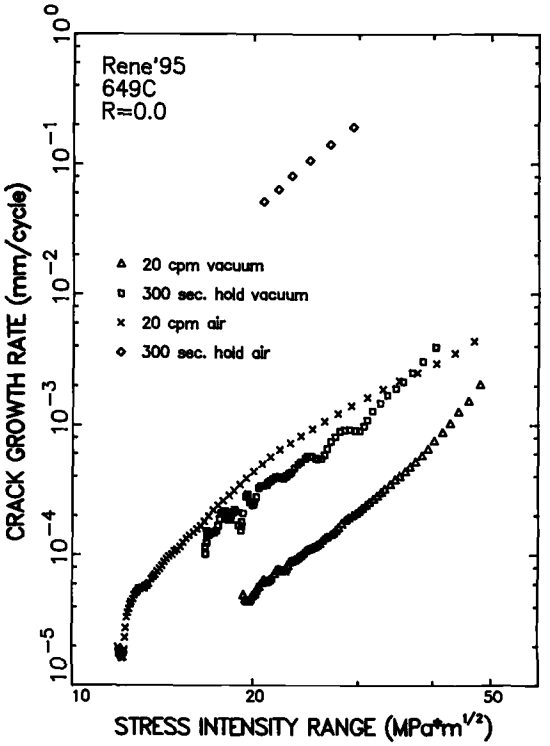

FIG. 32—*Variation of crack growth rates in extruded and isothermally forged Renè 95 at 649°C with 0.33 Hz and 300 s hold time cycling conditions in laboratory air and high vacuum.*

the surface crack K_b bar [65], the double edge notch tensile (DEN or DE(T)) specimen with a K_t value of 1.7 used to evaluate a surface crack growing in a stress gradient [59], and the "bolt hole" (BH) specimen used to evaluate corner cracks emanating from holes with the associated stress gradient [64].

The data in Fig. 14 and Table 4 show that the dcEPD solution (Appendix), with final crack size corrections, accurately established the growth of small cracks under isothermal conditions. The ability of the three-dimensional solution to predict crack lengths in the DE(T) and BH specimens is notable because the large notch or hole results in a nonuniform current density in the location where the small crack grows. The analytical solution is based on uniform current density.

The growth of cracks in a thermal gradient or during thermal-mechanical fatigue (TMF) cycling is not explicitly treated in the electrical potential solutions because of the change in electrical resistance with temperature. A series of displacement controlled Alloy 718 crack growth tests were performed with SE(T) specimens under nonisothermal conditions in order to evaluate nonlinear fracture mechanics parameters [66]. These tests were cycled at 0.01 Hz, the current-on potential was measured at the time of maximum displacement, and the current-off potential was measured one second later. The dcEPD technique predicted most crack lengths within 15% accuracy, as shown in Table 5.

Needs and Future Directions

The limitations of the dcEPD method for small/short crack monitoring, listed in a previous section, indicate the direction for future research. The most important arena for such work is that of microstructurally small cracks in small grain size alloys. For artificially nucleated fatigue cracks, improvements in signal amplification are required for increased signal to noise sensitivity and faster measurement speed. This later capability is particularly important when dealing with a load dependent voltage, typical of crack surface shorting, and frequencies above about 0.5 Hz. Improved methods for voltage probe attachment are required for monitoring of cracks sized below 75 μm. Current methods with indexing dimples and resistance spot welding produce a crack initiation site that is preferred compared to 50 μm sized EDM micronotches.

Alternate methods for producing small crack nucleating defects are required. Since the EDM method produces a damaged zone of 2 to 5 μm, this method should be applicable to producing precisely located 25-m-scale defects. Alternate methods for producing defects,

TABLE 5—*Two-dimensional single-edge crack under complex thermal-mechanical fatigue loading.*[a]

Test Type	Number of Tests	$\Delta a_m/\Delta a_p$ Range	Average, $\Delta a_m/\Delta a_p$	Standard Deviation, $\Delta a_m/\Delta a_p$
Thermal gradient	5	1.017 to 1.135	1.052	0.047
427-649 IP TMF[b]	4	1.041 to 1.173	1.096	0.061
427-649 OP TMF[c]	3	1.067 to 1.174	1.131	0.056
538-649 IP TMF	5	1.022 to 1.301	1.129	0.124
538-649 OP TMF	6	0.934 to 1.169	1.067	0.079
All	23[d]	0.934 to 1.301	1.095	0.079

[a]Button Head SE(T) (width = 10.16 mm, thickness = 2.54 mm). Typical a_i = 300 μm; a_f = 7.6 mm.

[b]In phase thermal-mechanical fatigue.

[c]Out of phase thermal-mechanical fatigue.

[d]Total number of tests.

including selective corrosion pitting, hardness indentation, laser heating and identification of "fatal" inclusions, should be developed. It is likely that the obstacles confronting the next level of defect size and signal resolution can be overcome.

A particularly challenging application of the dcEPD method is the detection and monitoring of small naturally nucleated fatigue cracks, where the crack location is uncertain and multiple nucleation sites are possible. Halliday and coworkers concluded that the dcEPD method is not a practical means of monitoring the growth of such small and multiple cracks, for example, at the root of a notch [*67*]. The voltage increase with crack growth was small due to the large distance between probe location and crack initiation site. Additionally, multiple cracks within an active probe pair confounded the analytical calibration. This work indicates that line contact potential probes, nucleation specific specimen geometries, or improved small artificial defects may provide a means to detect the growth of microstructurally small fatigue cracks.

Three applications of the dcEPD method should be exploited. The technique has not been developed to yield information on crack closure. Better analysis of the origin of the load dependent potential for electrically conductive crack surfaces could yield improved insight on crack surface contact. Inferences of crack surface conductivity from measured electrical potentials could lead to improved mechanistic understanding relative to environmental cracking. Second, the dcEPD method with short surface and edge cracks is ideally suited for studies of low crack growth rates, at low frequencies, and as influenced by aggressive environments. To date, this aspect of corrosion fatigue has not been sufficiently studied because of the prolonged times required for standardized experiments with long cracks. Finally, fatigue crack initiation and early growth from blunt micronotches or similar defects, can be quantified by dcEPD measurement. A typical result, with an operational definition of initiation and early growth, is shown in Fig. 30. Crack initiation life for micronotches of the sort shown in Fig. 7 were successfully correlated with a fracture mechanics estimate of local strain range, by $\Delta K/\sqrt{\rho}$, where ρ is the notch tip radius [*14,21*]. The use of the dcEPD approach to study this "small notch" initiation problem should be exploited.

Conclusions

1. The dcEPD method is a proven means to quantitatively and continuously monitor the growth kinetics of short fatigue cracks sized above 75 μm, with 1- to 5-μm-average resolution. The crack initiation site must be predetermined by an artificial defect and the method is only demonstrated for single Mode I cracks.
2. A closed-form analytical model relates crack size to measured voltage for a variety of small/short surface elliptical, surface semicircular, corner and through-thickness edge cracks. The model is confirmed by over 500 experiments that demonstrate less than ±15% difference between model predicted and experimentally measured crack sizes in the range from 75 to 3000 μm.
3. The dcEPD method effectively monitors microstructurally small cracks, provided that the grain size exceeds 200 μm. The method h as not been successfully applied to monitor the growth of naturally or multiply nucleated small fatigue cracks.
4. While developed for isothermal and isocurrent conditions, the analytical dcEPD model reasonably predicts crack size for nonuniform current, thermal gradient, and thermal cycling conditions.
5. The dcEPD/short crack method is interfacable with computer controlled stress intensity experiments. Crack growth measurements at constant ΔK or K_{max} provide an effective means to study a variety of fatigue problems.
6. The dcEPD method provides in-situ monitoring of the growth of small/short cracks in

vacuum, gaseous, aqueous, and thermal environments. The method accurately measures low steady state growth rates at slow loading frequencies, or with prolonged hold periods, and transient crack propagation.

7. A large experience base demonstrates the effectiveness of the dcEPD method for quantitative studies of stress intensity, microstructure, alloy composition, loading frequency, stress ratio, loading spectra, temperature, and environment chemistry effects on the propagation kinetics of small and short fatigue cracks.
8. The dcEPD method to monitor small/short crack growth is an extension of the standardized procedure for long cracks. Operator and maintenance time are minimal, instrumentation is inexpensive, and operator judgement is of secondary importance.
9. The limitations of the dcEPD method include the requirement to predetermine and locally probe the crack nucleation site; errors due to thermal, electrical noise, and crack surface conduction effects; and the need to define crack shape by an independent means or multiple voltage probes.

Acknowledgments

The authors acknowledge the sustained contributions of their colleagues at the General Electric Corporate Research and Development Center (M. F. Henry, G. M. Roe, L. F. Coffin, M. G. Benz, D. C. Lord, R. Rosa, and W. R. Catlin), at the GE Aircraft Engine Group (Robert Volmer, D. D. Krueger, T. L. Richardson, and L. T. Duvelius), and at the Exxon Corporate Research-Science Laboratories (C. N. Marzinsky and F. H. Heubaum). The research reported here was sponsored by several Department of Defence agencies (RHV), the General Electric Company (RHV and RPG), the Exxon Research and Engineering Company (RPG), the NASA-Langley Research Center under Grant NAG-1-745 (RPG, RSP and DCS), and the Virginia Center for Innovative Technology (RPG and RSP) under a grant to the Center for Electrochemical Science and Engineering at the University of Virginia.

APPENDIX

Potential Solution for a Three-Dimensional Crack in an Infinite Body

This appendix describes the Roe-Coffin potential solution for a semi-elliptical notch having depth a, surface length $2c$, and height $2b$. For the case of a crack, b equals zero. The potential V can be described as

$$V = V_o L_p \frac{\dfrac{\sqrt{1 - k^2 \sin^2\Theta}}{\tan\Theta} + E(k, \Theta) - Q}{E(k, \pi/2) - Q} \tag{A1}$$

where

$$\begin{aligned} V_o &= \text{remote potential} \\ E(\delta_1, \delta_2) &= \int_0^{\delta_2} (1 - \delta_1^2 \sin^2\Phi)^{1/2}\, d\Phi \\ \Theta &= \tan^{-1}(\sqrt{\alpha}) \\ \Theta_0 &= \tan^{-1}(b/\beta) \\ Q &= E(k, \Theta_0) + \frac{b\beta^2}{ac\lambda} \end{aligned}$$

There are two solutions for α, β, and λ dependent on whether the crack aspect ratio is greater or less than unity. Within these two solutions the value of α varies dependent on the relative difference between crack dimensions and probe spacing. The probe location is given by $(x = L_p, y = 0, z)$, where z is the dimension by which the probe spacing is displaced from the centerline.

For $c \geq a \geq b$

$$\begin{aligned} \beta^2 &= a^2 - b^2 \\ \lambda^2 &= c^2 - b^2 \\ k^2 &= 1 - \beta^2/\lambda^2 \end{aligned} \tag{A2}$$

If $L_p^2 + z^2 > \lambda^2$

$$\alpha = \frac{1}{2}\left[\frac{L_p^2 + z^2 - \lambda^2}{\beta^2} + \sqrt{\left(\frac{L_p^2 + z^2 - \lambda^2}{\beta^2}\right)^2 + \frac{4\lambda^2 L_p^2}{\beta^4}}\right] \tag{A3}$$

If $L_p^2 + z^2 < \lambda^2$

$$\alpha = \frac{2\lambda^2 L_p^2/\beta^4}{\frac{\lambda^2 - L_p^2 - z^2}{\beta^2} + \sqrt{\left(\frac{\lambda^2 - L_p^2 - z^2}{\beta^2}\right)^2 + \frac{4\lambda^2 L_p^2}{\beta^4}}} \tag{A4}$$

For $a \geq c \geq b$

$$\begin{aligned} \beta^2 &= c^2 - b^2 \\ \lambda^2 &= a^2 - b^2 \\ k^2 &= 1 - \beta^2/\lambda^2 \end{aligned} \tag{A5}$$

If $L_p^2 + z^2 > \beta^2$

$$\alpha = \frac{1}{2}\left[\frac{L_p^2 + z^2}{\beta^2} - 1 + \sqrt{\left(\frac{L_p^2 + z^2}{\beta^2} - 1\right)^2 + \frac{4L_p^2}{\beta^2}}\right] \tag{A6}$$

If $L_p^2 + z^2 < \beta^2$

$$\alpha = \frac{2L_p^2/\beta^2}{1 - \frac{L_p^2 + z^2}{\beta^2} + \sqrt{\left(1 + \frac{L_p^2 + z^2}{\beta^2}\right)^2 + \frac{4L_p^2}{\beta^2}}} \tag{A7}$$

The only unmeasured parameter in this solution is V_o. The potentials can be normalized (V/V_n) to eliminate V_o.

The potential values measured during crack initiation and early growth are affected by the geometry of a crack initiation notch ($b > 0$). This complication can be treated using an algorithm, originally developed by Gangloff [*13*], with the Roe-Coffin potential solution. The total potential V is computed from a combination of the notch and crack solutions.

$$V = V_{ca} + Q_o(V_n - V_{cn}) \tag{A8}$$

where

V_n = potential for a notch with dimensions $a_n \times 2c_n \times 2b_n$,
V_{ca} = potential for a crack with dimensions $a \times 2c(a \geq a_n, c \geq c_n, b = 0)$,
V_{cn} = potential for a crack with the notch dimensions $a_n \times 2c_n$ $(b = 0)$, and
Q_o = an empirical function that guarantees that $V/V_n = 0$ for $a = a_n$ and that decays linearly to zero when the crack depth reaches twice the notch depth. That is

$$Q_o = (2 - a/a_n) \quad \text{for} \quad a_n \leq a \leq 2a_n$$

$$Q_o = 0 \quad \text{for} \quad a \geq 2a_n$$

References

[*1*] Ritchie, R. O. and Lankford, J., Eds., *Small Fatigue Cracks*, TMS-AIME, Warrendale, PA, 1986.
[*2*] Miller, K. J. and de los Rios, E. R., *The Behavior of Short Fatigue Cracks*, Mechanical Engineers Publishers, Ltd., London, United Kingdom, 1986.
[*3*] Hudak, S. J., Jr., *Journal of Engineering Materials Technology*, Vol. 103, 1981, pp. 289–310.
[*4*] Suresh, S. and Ritchie, R. O., *International Metals Reviews*, Vol. 29, 1984, pp. 445–476.
[*5*] McEvily, A. J., *Journal of the Society of Mechanical Engineers, International Journal*, Vol. 32, 1989, pp. 181–191.
[*6*] Ritchie, R. O. and Lankford, J., *Materials Science and Engineering*, Vol. 84, 1986, pp. 11–16.
[*7*] Gangloff, R. P. and Wei, R. P., *Small Fatigue Cracks*, Eds., R. O. Ritchie and J. Lankford, Eds., TMS-AIME, Warrendale, PA, 1986, pp. 239–264.
[*8*] Lankford, J. and Davidson, D. L., *Small Fatigue Cracks*, R. O. Ritchie and J. Lankford, Eds., TMS-AIME, Warrendale, PA, 1986, pp. 51–71.
[*9*] Wei, R. P. and Brazill, R. L., *Fatigue Crack Growth Measurement and Data Analysis, ASTM STP 738*, S. J. Hudak, Jr. and R. J. Bucci, Eds., American Society for Testing and Materials, Philadelphia, 1981, pp. 103–119.
[*10*] Beevers, C. J., Ed., *The Measurement of Crack Length and Shape During Fracture and Fatigue*, EMAS, West Midlands, United Kingdom, 1980.
[*11*] *Advances in Crack Length Measurement*, C. J. Beevers, Ed., EMAS, West Midlands, United Kingdom, 1982.
[*12*] Johnson, H. H., *Materials Research and Standards*, Vol. 5, No. 9, 1965, pp. 442–445.
[*13*] Gangloff, R. P., *Fatigue of Engineering Materials and Structures*, Vol. 4, 1981, pp. 15–33.
[*14*] Gangloff, R. P., *Advances in Crack Length Measurement*, C. J. Beevers, Ed., EMAS, West Midlands, United Kingdom, 1982, pp. 175–231.
[*15*] Van Stone, R. H., Krueger, D. D., and Duvelius, L. T., *Fracture Mechanics: Fourteenth Symposium-Volume II: Testing and Applications, ASTM STP 791*, J. C. Lewis and G. Sines, Eds., American Society for Testing and Materials, Philadelphia, 1983, pp. 553–578.
[*16*] Van Stone, R. H. and Richardson, T. L., *Automated Test Methods for Fracture and Fatigue Crack Growth, ASTM STP 877*, W. Cullen, R. Landgraf, L. Kaisand, and J. Underwood, Eds., American Society for Testing and Materials, Philadelphia, 1985, pp. 148–166.
[*17*] Li, Che-Yu and Wei, R. P., *Materials Research and Standards*, Vol. 6, No. 8, 1966, pp. 392–394.
[*18*] Roe, G. M. and Coffin, L. F., Jr., unpublished research, General Electric Corporate Research and Development Center, Schenectady, NY, 1978.
[*19*] Milne-Thompson, L. M., *Theoretical Hydrodynamics*, MacMillan, New York, 1960, pp. 506–511.
[*20*] Van Stone, R. H. and Krueger, D. D., *Investigation of Direct Aged Inconel 718 Fatigue Behavior*, final report, NAVAIR Contract N00019-82-C-0373, GE Aircraft Engines, Cincinnati, OH, 1984.

[21] Heubaum, F. H., *Propagation Kinetics of Short Fatigue Cracks in Low Alloy Steels: Crack Closure and Fracture Morphology*, Ph.D. Dissertation, Northwestern University, Evanston, IL, 1986.
[22] Piascik, R. S., *Mechanisms of Intrinsic Damage Localization During Corrosion Fatigue: The Al-Li-Cu System*, Ph.D. Dissertation, University of Virginia, Charlottesville, VA, 1990.
[23] Hicks, M. A. and Pickard, A. C., *International Journal of Fracture*, Vol. 20, 1982, pp. 91–101.
[24] Pickard, A. C. and Hicks, M. A., *Advances in Crack Length Measurement*, C. J. Beevers, Ed., EMAS, West Midlands, United Kingdom, 1982, pp. 97–113.
[25] Gangloff, R. P., *Metallurgical Transactions A*, Vol. 16A, 1985, pp. 953–969.
[26] Piascik, R. S. and Gangloff, R. P., "Environmental Fatigue of an Al-Li-Cu Alloy: Part I—Intrinsic Crack Propagation Kinetics in Hydrogenous Environments," *Metallurgical Transactions A*, in press, 1991.
[27] Piascik, R. S. and Gangloff, R. P., *Environment Induced Cracking of Metals*, R. P. Gangloff and M. B. Ives, Eds., NACE, Houston, TX, 1989, pp. 233–239.
[28] Van Stone, R. H. and Gangloff, R. P., *Rapid Solidification Processing, Principles and Technology II*, Claitors Press, Baton Rouge, LA, 1980, pp. 317–330.
[29] Henry, M. F., unpublished research, General Electric Corporate Research and Development Center, Schenectady, NY 1982.
[30] Gangloff, R. P., *Basic Questions in Fatigue, Vol. 2, ASTM STP 924*, R. P. Wei and R. P. Gangloff, Eds., American Society for Testing and Materials, Philadelphia, 1988, pp. 230–251.
[31] Gangloff, R. P., *Fatigue Crack Growth Measurement and Data Analysis, ASTM STP 738*, S. J. Hudak, Jr. and R. J. Bucci, Eds., American Society for Testing and Materials, Philadelphia, 1981, pp. 120–138.
[32] Coppin, P. and Gangloff, R. P., unpublished research, University of Virginia, Charlottesville, VA, 1989.
[33] Bardal, E., Berge, T., Grovlen, M., Haagensen, P. J., and Forre, B. M., *Advances in Crack Length Measurement*, C. J. Beevers, Ed., EMAS, West Midlands, United Kingdom, 1982, pp. 139–158.
[34] Coffin, L. F., *Fracture Mechanics: Nineteenth Symposium, ASTM STP 969*, T. A. Cruse, Ed., American Society for Testing and Materials, Philadelphia, 1988, pp. 235–259.
[35] Catlin, W. R., Lord, D. C., Prater, T. A., and Coffin, L. F., *Automated Test Methods for Fracture and Fatigue Crack Growth, ASTM STP 877*, W. H. Cullen, R. W. Landgraf, L. R. Kaisand, and J. H. Underwood, Eds., American Society for Testing and Materials, Philadelphia, 1985, pp. 67–85.
[36] Bachmann, V. and Munz, D., *Engineering Fracture Mechanics*, Vol. 11, 1979, pp. 61–71.
[37] LaFarie-Frenot, M. C., Petit, J., and Gasc, C., *Fatigue of Engineering Materials and Structures*, Vol. 1, 1979, pp. 431–438.
[38] Gangloff, R. P. and Wei, R. P., *Metallurgical Transactions A*, Vol. 8A, 1977, pp. 1043–1053.
[39] Heubaum, F. H., Marzinsky, C. N., and Gangloff, R. P., unpublished research, Exxon Research and Engineering Company, Clinton, NJ, 1985.
[40] Saxena, A., Hudak, S. J., Jr., Donald, J. K., and Schmidt, D. W., *Journal of Testing and Evaluation*, Vol. 6, 1978, pp. 167–174.
[41] Donald, J. K. and Schmidt, D. W., *Journal of Testing and Evaluation*, Vol. 8, No. 1, 1980, pp. 19–25.
[42] Kim, K. S., Van Stone, R. H., Malik, S. N., and Laflen, J. H., *Elevated Temperature Crack Growth*, NASA Contract Report CR 182247, 1988.
[43] Larsen, J. M., *The Effects of Slip Character and Crack Closure on the Growth of Small Fatigue Cracks in Titanium-Aluminum*, Ph.D. Dissertation, Carnegie-Mellon University, Pittsburgh, PA, 1989.
[44] Clark, W. G., Jr. and Hudak, S. J., Jr., *Journal of Testing and Evaluation*, Vol. 3, 1975, pp. 454–476.
[45] Van Stone, R. H., *Materials Science and Engineering*, Vol. A103, 1988, pp. 49–61.
[46] Newman, J. C., Jr. and Edwards, P. R., *Short-Crack Growth Behavior in an Aluminum Alloy—An AGARD Cooperative Test Programme*, AGARD Report 732, 1988.
[47] Johansson, S., *Corrosion Fatigue and Microstructure Studies of the Age-Hardening Al-Alloy AA-7075*, Ph.D. Dissertation, Linkoping University, Linkoping, Sweden, 1984.
[48] Venkateswara Rao, K. T., Yu, W., and Ritchie, R. O., *Metallurgical Transactions A*, Vol. 19A, 1988, pp. 563–569.
[49] Zurek, A. K., James, M. R., and Morris, W. L., *Metallurgical Transactions A*, Vol. 14A, 1983, pp. 1697–1703.
[50] Gangloff, R. P., *Environment Induced Cracking of Metals*, R. P. Gangloff and M. B. Ives, Eds., NACE, Houston, TX, 1990, pp. 55–109.

[51] Gangloff, R. P., Embrittlement by the Localized Crack Environment, R. P. Gangloff, Ed., TMS-AIME, Warrendale, PA, 1984, pp. 265–290.
[52] Turnbull, A. and Ferriss, D. H., *Corrosion Science*, Vol. 27, 1987, pp. 1323–1350.
[53] Piascik, R. S. and Gangloff, R. P., *Advances in Fracture Research*, K. Salama, K. Ravi-Chandar, D. M. R. Taplin, and P. Rama Rao, Eds., Pergamon Press, London, 1989, pp. 907–918.
[54] Van Stone, R. H., Gooden, O. C., and Krueger, D. D., *Advanced Cumulative Damage Modeling*, AFWAL-TR-88-4146, GE Aircraft Engines, Cincinnati, OH, 1988.
[55] Gangloff, R. P., *Critical Issues in Reducing the Corrosion of Steel*, H. Leidheiser, Jr. and S. Haruyama, Eds., NSF/JSPS, Tokyo, Japan, 1985, pp. 28–50.
[56] Lankford, J. and Hudak, S. J., Jr., *International Journal of Fatigue*, Vol. 9, No. 2, 1987, pp. 87–93.
[57] Howland, C., Hicks, M. A., and Jeal, R. H., *Small Fatigue Cracks*, R. O. Ritchie and J. Lankford, Eds., TMS-AIME, Warrendale, PA, 1986, pp. 607–622.
[58] Hudak, S. J., Jr., paper presented a the Symposium on Small-Crack Test Method, San Antonio, TX Nov. 1990.
[59] Van Stone, R. H., Gilbert, M. S., Gooden, O. C., and Laflen, J. H., *Fracture Mechanics: Nineteenth Symposium, ASTM STP 969*, American Society for Testing and Materials, Philadelphia, 1988, pp. 637–656.
[60] Walker, K., *Effects of Environment and Complex Load History on Fatigue Life, ASTM STP 462*, American Society for Testing and Materials, Philadelphia, 1970, pp. 1–23.
[61] Krueger, D. D., Antolovich, S. D., and Van Stone, R. H., *Metallurgical Transactions A*, Vol. 18A, 1987, pp. 1431–1449.
[62] Van Stone, R. H. and Krueger, D. D., *Fracture Mechanics: Nineteenth Symposium, ASTM STP 969*, American Society for Testing and Materials, Philadelphia, 1988, pp. 883–906.
[63] Nicholas, T., Laflen, J. H., and Van Stone, R. H., *Proceedings of the Conference on Life Prediction for High-Temperature Gas Turbine Materials*, V. Weiss, Ed., AP-4477, EPRI, Palo Alto, CA, 1985, pp. 4-1 to 4-61.
[64] Van Stone, R. H. and Kim, K. S., "Methods for Predicting Crack Growth in Advanced Structures," to be published in *Proceedings of the 1st Thermal Structures Conference*, University of Virginia, Charlottesville, VA, 1990.
[65] Johnson, R. E., Coles, A., and Popp, H. G., *Journal of Engineering Materials Technology*, Vol. 98, 1976, pp. 305–322.
[66] Kim, K. S., Van Stone, R. H., Malik, S. N., and Laflen, J. H., *Elevated Temperature Crack Growth*, NASA Contract Report CR182247, GE Aircraft Engines, Cincinnati, OH, 1988.
[67] Halliday, M. D., Blom, A. F., and Beevers, C. J., "Potential Difference Applied to the Measurement of Small Fatigue Crack Growth at Notches in Ti-6Al-4V," *Scandinavian Journal of Metallurgy*, in press, 1989.

Michael T. Resch[1] *and Drew V. Nelson*[2]

An Ultrasonic Method for Measurement of Size and Opening Behavior of Small Fatigue Cracks

REFERENCE: Resch, M. T. and Nelson, D. V., **"An Ultrasonic Method for Measurement of Size and Opening Behavior of Small Fatigue Cracks,"** *Small-Crack Test Methods, ASTM STP 1149*, J. M. Larsen and J. E. Allison, Eds., American Society for Testing and Materials, Philadelphia, 1992, pp. 169–196.

ABSTRACT: A surface acoustic wave (SAW) technique has been observed to be effective in the detection of initiation and measurement of growth behavior of surface microcracks during fatigue cycling. The experimental procedure involving excitation of Rayleigh waves on the surface of a specimen under investigation is described in detail in conjunction with automated data acquisition of the reflected echo from a small surface crack. The effectiveness of a split spectrum processing algorithm to separate specular reflections of isolated cracks from non-specular reflections of microstructural features is also described. A simplified model for predicting the relationship between crack size and the amplitude of the reflected echo from a crack is included along with a description of the technique for measuring opening behavior of individual cracks in-situ during fatigue cycling. Examples of effective utilization of the SAW technique in contemporary investigations of small fatigue crack growth behavior are presented. Finally, the advantages and limitations of the technique are discussed.

KEY WORDS: surface acoustic waves, crack initiation, small crack growth, crack opening stress, closure, crack opening displacement, fatigue, nondestructive evaluation, residual stress, laser interferometric technique, nonlinear signal processing, split spectrum processing

In studies of the initiation and growth behavior of fatigue microcracks it is of paramount importance to detect the existence of the cracks as early as possible during fatigue cycling. A number of experimental techniques have already proved useful to this end, such as direct observation with metallographic microscope, inspection of acetate replicas of the surface, gel electrode, AC and DC potential drop, low-frequency and high-frequency eddy current, and acoustic microscopy, to name but a few. However, these existing techniques are, for the most part, quite tedious and time consuming, and except for certain limited applications, not amenable to automated measurement techniques for detecting truly microscopic surface fatigue cracks during fatigue crack initiation and growth in the earliest stages.

The reason for developing new quantitative nondestructive evaluation techniques to detect and measure the size of surface microcracks is that, in the so called small-crack size regime, cracks have been observed to grow at rates that are orders of magnitude higher than large sized cracks when subjected to identical magnitudes of crack driving force. Quantitative measurements of crack depth below the surface for surface microcracks facilitate the eval-

[1]Assistant professor, Engineering Mechanics Department, University of Nebraska-Lincoln, Lincoln, NE 68588-0347.

[2]Associate professor, Mechanical Engineering Department, Stanford University, Stanford, CA 94305-4021.

uation of crack growth rate versus the number of cycles. Nondestructive measurements of crack-opening behavior are especially important here because many current theories that address the issue of why small cracks grow faster postulate that small cracks have less closure than large cracks, resulting in a higher driving force for growth of small cracks.

A number of researchers have demonstrated the usefulness of surface acoustic waves (SAW) as a means for evaluating crack size and investigating the crack-opening phenomenon during fatigue crack growth. These studies have tended to be either empirical correlations between crack size and the observed behavior of waves scattered by cracks [*1–3*] or theoretical analyses that address the scattering behavior in a rigorous manner [*4–5*].

The empirical approaches have provided useful insights into small crack behavior for the particular conditions of the experiments performed, but they have lacked sufficient generality for the results obtained to be widely applicable to other experimental conditions. On the other hand, the rigorous theoretical results are usually quite general, but computationally complex, and often contain parameters that are not readily determinable by existing experimental techniques. In contrast, the SAW method considered in this paper is designed to be simple enough to implement in fatigue microcrack initiation and growth experiments on a number of different specimen configurations during cyclic loading with the specimen gripped in a conventional servohydraulic load frame. Yet this SAW method design is sufficiently rigorous in its theoretical development to be in good quantitative agreement with acoustic predictions of crack size derived from the elastostatic approximations inherent in a long-wavelength scattering theory.

More recently, surface acoustic waves, SAW, or Rayleigh waves, have demonstrated the ability to measure changes in depth of cracks beneath the surface (occasionally during periods of crack growth caused by fatigue cycling in which no changes in crack dimension were evident at the surface) in 7075-T651 aluminum [*6*], quenched and tempered 4340 steel [*7*], quenched and tempered 4140 steel [*8*], and 300-M alloy steel [*9*]. The technique involves exciting Rayleigh waves on the specimen surface toward the initiation site using a contacting wedge transducer, and receiving the reflected echo along with reflections of microstructural origin with a separate contacting wedge transducer, in the classical pitch-catch configuration depicted schematically in Fig. 1.

Briefly stated, the SAW technique considered here uses a transducer in contact with a fatigue specimen to produce directed ultrasonic Rayleigh waves that travel along and just below the surface. An isolated small crack of interest is illuminated with a tone burst of

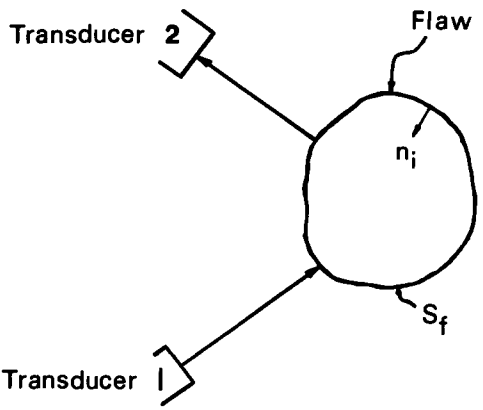

FIG. 1—*Schematic of generalized scattering of acoustic waves from a flaw.*

several wavelengths duration. After a wave packet interacts with a small surface crack, an echo is received at another transducer near the sending transducer. The ratio of the maximum amplitude of the reflected signal to the maximum amplitude of the input signal, called the reflection coefficient, is measured either periodically or continuously during the course of growth of a small surface crack. The reflection coefficient is then used to determine the maximum depth of the crack, assuming that it is approximately semi-elliptical in shape.

Additionally, in order to ensure that the reflection coefficient from the crack is representative of its true size, it is usually necessary to apply a tensile stress with orientation normal to the crack faces during the ultrasonic procedure so that the adjacent crack faces are traction free. Failure to achieve this experimental configuration for cracks exhibiting significant closure stress allows some of the ultrasonic energy in the incident wave to be transmitted instead of reflected, resulting in an erroneous prediction of crack size. Consequently, measurement of the reflection coefficient of a microcrack as a function of the applied tensile stress reveals the stress magnitude required to achieve this experimental condition.

The additional information that this companion experiment provides regarding the crack-opening behavior is discussed later in this paper. In the next section, the theoretical considerations relating the reflection coefficient to crack size will be summarized, along with a description of instrumentation needed to implement the SAW technique and experimental measurements required to furnish input parameters to the technique. Following that, experimental results of small-crack growth behavior as studied through combined use of optical and SAW techniques will be given.

Cracks as small as 50 μm radius (halfpenny shape) initiated because of fatigue have been detected using Rayleigh waves [*7–10*]. Although this is a reasonably small crack, which is approximately two orders of magnitude smaller than the crack size at which fast fracture would normally be expected to occur (for the materials and state of stress used in these experiments), it remains approximately an order of magnitude larger than necessary in order to characterize anomalous crack growth rate effects due to interactions between the advancing crack-tip and microstructural features such as grain boundaries.

The goal in the present work is to examine the practicality of measuring crack growth rates in the size regime between approximately 10 to 100 μm by continuously monitoring backscattered Rayleigh wave signals from cracks as they initiate and grow.

To date, the fatigue behavior of small cracks has been studied primarily by optical measurements of surface length and of crack-opening stress as inferred from crack-tip opening displacements. The paper will describe how ultrasonic surface acoustic waves can be used to detect the existence or formation of small cracks, to monitor their depth during growth, and to provide information about their opening behavior in depth. In addition, it will show that when optical and acoustic techniques are used in conjunction, the knowledge obtained about small-crack growth behavior is greatly enhanced relative to what might be gained from either technique by itself.

Surface Acoustic Wave Technique

Transducer Design

Rayleigh waves are produced on a substrate with a wedge transducer in the following manner. A pulsed *rf* signal excites a longitudinal wave transducer bonded to the wedge. The length of contact between the wedge and the substrate in the direction of wave propagation is defined as w. The longitudinal wave in the wedge is partially mode converted to a Rayleigh wave in the substrate at the wedge-substrate interface. For optimum conversion efficiency the angle θ between the incident longitudinal waves in the wedge and the normal

to the substrate surface should be

$$\theta = \sin^{-1}(V_L^w/V_R^s) \tag{1}$$

where V_L^w and V_R^s are the velocities of the longitudinal wave in the wedge and the Rayleigh wave in the substrate, respectively. In addition to this constraint the attenuation per unit length of contact between the wedge and substrate α caused by leakage of acoustic energy from the mode converted surface wave in the substrate back into the wedge is given by the relation [*11*]

$$\alpha = \frac{\omega f_z Z_L}{4V_S Z_S \cos\theta} \tag{2}$$

where ω is the angular frequency of the SAW, V_S and Z_S are the acoustic shear wave velocity and impedance of the substrate medium, respectively, Z_L is the longitudinal wave impedance of the wedge medium, and f_z is a dimensionless parameter for the substrate such that [*12*]

$$f_z = (V_S/V_R)^2 \frac{4F^2[1-(V_R/V_S)^2]^{3/2}}{3F - 2F(V_R/V_S)^2 - 1} \tag{3}$$

where F is defined by the expression

$$F^2 = \frac{(V_R/V_S)^2(V_S/V_L)^2}{1 - (V_R/V_S)^2} \tag{4}$$

Finally, if the attenuation per unit length of contact between the wedge and the substrate caused by loss in the wedge γ is considered, the net efficiency of mode conversion at the wedge-substrate interface η can be shown to be [*11*]

$$\eta = 2\exp(-2\gamma w)\{1 - \exp[-(\alpha - \gamma)w]\}^2/(\alpha - \gamma)w \tag{5}$$

where w is the length of contact between the wedge and substrate. Defining the normalized length of the transducer as the product of wave attenuation caused by leakage times the length of contact αw for $\gamma/\alpha = 0$ (ideal case with no loss in the wedge) the efficiency has a maximum value of 0.815 at $\alpha w = 1.26$, and a half power bandwidth of $0.27 < \alpha w < 4.8$. An additional factor important in optimization of the conversion efficiency involves the length of contact w as a function of wavelength of Rayleigh waves in the substrate. For maximum efficiency, the wedge length should be an integer multiple of the Rayleigh wavelength with the number of wavelengths of contact as large as possible to ensure plane wave excitation of the incident beam at the wedge/substrate interface.

It is evident then that the optimum length is determined by considering the maximum permissible value of the normalized length αw in conjunction with the value of the leakage rate α at the desired frequency and for the particular combination of materials used for the wedge and substrate. In other words, in order to optimize the performance of a wedge transducer, one must maximize the wedge length while minimizing the leakage rate. However, at a particular frequency the magnitude of the leakage rate is dominated by the ratio of acoustic impedance of longitudinal waves in the wedge to that of shear waves in the substrate. Consequently, only a few combinations of materials for wedge and substrate have an impedance ratio that is small enough to allow the length of the wedge/substrate interface to be more than a few wavelengths.

Specular Reflections from Cracks

The amplitude of the SAW reflected echo from a crack is a complicated function of crack size and shape, frequency of the ultrasonic waves, scattering geometry, material parameters, and electronic gain and loss from the detection equipment. In order to compare measurements from similar sized cracks in different materials as well as varying experimental conditions, it is customary to normalize the amplitude of the signal detected at the terminals of the receiving transducer with respect to the amplitude of the incident signal at the terminals of the transmitting transducer. This normalized quantity shall hereafter be referred to as the reflection coefficient S_{21} in which the subscripts refer to the transmitting transducer as "1" and the receiving transducer as "2."

Additionally, in order to compare the results of scattering experiments from similar sized cracks performed at varying frequencies, the crack depth a is normalized to the wavelength of the ultrasonic waves through the wave number κ where $\kappa = 2\pi/\lambda$. The normalized crack depth κa is the crack depth multiplied by the wave number. For surface acoustic waves produced at a frequency of 3 MHz on metals, such as aluminum and steel, the resulting wavelength is approximately 1 mm. As a point of reference, the crack depth that corresponds to a normalized crack depth of unity at this wavelength is $\lambda/2\pi$, or approximately 150 μm. This value of normalized crack depth is important, because it defines the maximum allowable crack size that may be inferred from an ultrasonic scattering experiment at a particular acoustic wavelength (defined by the frequency), as described in the next section.

In order to interpret the reflected echo from surface cracks in the classical pitch-catch configuration, two techniques have been demonstrated to be useful. In the most general case, cracks are assumed to be semi-elliptical in shape, with maximum depth beneath the surface a and length along the surface defined as $2c$. Under these conditions the length at the surface is measured independently (usually by optical microscopy), and a single valued relationship exists between the reflection coefficient of surface acoustic waves incident on an isolated crack and the normalized crack depth κa [*7,10*]. However, for crack growth in the "small-crack" size regime it has been observed experimentally that cracks quickly attain the halfpenny shaped configuration with $a = c$ [*9*]. For this simplified case it is not necessary to independently determine crack length at the surface, and a simplified scattering model is all that is necessary to evaluate the single valued relationship between the normalized crack depth and the reflection coefficient of the SAW.

Certain acoustic restrictions limit the size of maximum crack depth and minimum specimen thickness that can be utilized for a fixed value of the frequency of the ultrasonic waves. For example, the boundary conditions required for propagation of a surface acoustic wave on the surface of a substrate require that the thickness t of the substrate be at least 4λ of the acoustic wave. This limit is necessary so that the "tail" of the stress field of the SAW beneath the surface cannot interact with the free surface of the bottom of the finite thickness specimen. Additionally, the existing theory for predicting ultrasonic scattering from surface cracks requires that the normalized crack depth be within the range $0 < \kappa\alpha < 1$. This additional limitation is necessary for simplifying the calculation of the scattering of surface waves from a crack. In the next section the essential elements of this interaction will be discussed in some detail.

Scattering Theory and Its Implementation

A number of investigators have demonstrated the possibility of deducing information about crack size and shape from ultrasonic scattering experiments [*13–22*]. The approaches tend to fall into one of two categories: the short-wavelength scattering regime where crack

size a and acoustic wavelength λ are such that $\lambda \ll a$, or the long-wavelength regime where $\lambda \gg a$. For studies of small surface cracks, the long-wavelength regime is preferable because short wavelengths result in excessive attenuation of the acoustic waves for the materials tested. Another advantage of a long-wavelength approach is that the computation of the scattering theory is simplified, resulting in an easier implementation of the technique. For this work the problem has been constrained to the calculation of the reflection coefficient of Rayleigh waves from a flat, semi-elliptically shaped surface crack residing in the far field of SAW wedge transducers, at a frequency such that the scattering problem is in the long-wavelength regime. Details of the SAW transducer hardware and operation are given later in the section and in Refs *11*, *23*, and *24*.

A general scattering theory has been developed that describes the relative signal amplitude of an ultrasonic wave scattered from one transducer to another by a void of arbitrary shape [*25*,*26*]. As noted previously, the reflection coefficient S_{21} is defined as the amplitude ratio of the maximum reflected signal for the flaw A_2 received by transducer 2, to the maximum incident signal A_1 transmitted by transducer 1, measured at the terminals to the transducers, depicted schematically in Fig. 1. The general relationship that defines the reflection coefficient is given by

$$S_{21} = A_2/A_1 = j\omega/4P \int_{S_f} \sigma_{ij} u_j n_i \, dS \tag{6}$$

where P is the power input to the transmitting transducer, u_j is the acoustic displacement field at the flaw surface evaluated from the acoustic stress field that would exist if transducer 2 were the transmitter, σ_{ij} is the acoustic stress field evaluated in the vicinity of the flaw as if no flaw were present, n_i is the inward directed normal to the flaw surface S_f surrounding the scatterer, ω is the angular frequency of the acoustic wave, and $j = (-1)^{1/2}$.

Consider the case of a Rayleigh wave propagating in the z direction normally incident to the crack plane, where the crack depth at the semi-minor axis is a, and half the crack length at the surface is c, as shown in Fig. 2. There are three components of stress associated with the displacement field of a Rayleigh wave: a longitudinal component σ_{zz}, parallel to the direction of propagation, a shear component σ_{xz}, and a normal component σ_{xx} as seen in

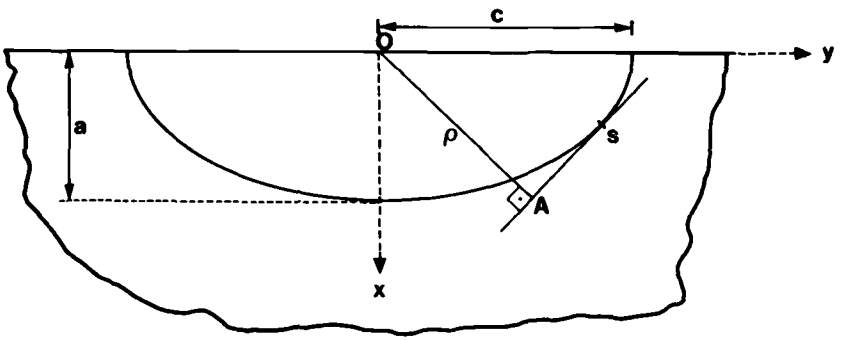

c = half crack length on surface,

a = maximum crack depth.

FIG. 2—*Schematic of semi-elliptical surface crack.*

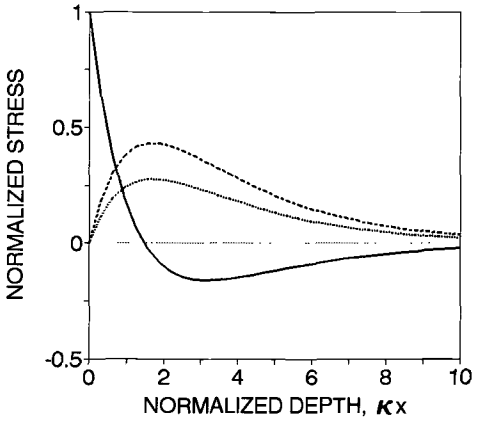

FIG. 3—*Components of stress in surface acoustic wave normalized by the value of longitudinal stress* σ^0_{zz} *evaluated at the surface, where* κ *is the wave number* ($\kappa = 2\pi/\lambda$). *Line Legend: solid* = $\sigma_{zz}/\sigma^0_{zz}$, *dashed* = $\sigma_{xz}/\sigma^0_{zz}$, *and dotted* = $\sigma_{xx}/\sigma^0_{xx}$.

Fig. 3. The components of σ_{xx} and σ_{xz} are close to zero near the surface, while the longitudinal component of stress σ_{zz} has its maximum value at the surface. The wave number κ is defined as $\kappa = 2\pi/\lambda$. Equation 6 can be evaluated for the case of a Rayleigh wave propagating along a surface normal to the crack plane by choosing the frequency of the acoustic wave such that the wavelength λ will be greater than the crack depth a. In the long wavelength limit with $a \ll \lambda$, the crack resides in a SAW stress field with σ_{zz} approximately uniform over the crack surface S_c, and with the other components of stress approximately equal to zero. For these conditions, Eq 6 reduces to

$$S_{21} = j\omega/4P \int_{S_c} \sigma_{zz} u_z \, dS \tag{7}$$

The integral of the displacement times stress evaluated over the surface of a crack can be expressed as a line integral of the stress intensity factor squared times a factor evaluated around the crack front C [*27*]. Utilizing this result, the reflection coefficient may be expressed as

$$S_{21} = \omega(1 - \nu^2)/6PE \int_C \rho K_I^2 \, ds \tag{8}$$

In Fig. 2, the factor ρ is the distance between the origin and the tangent line to the crack front at the point of inspection s. K_I is the Mode I stress intensity factor associated with the SAW acoustic stress field σ_{zz} stress component.

In order to evaluate Eq 8, the distribution of $K_I(s)$ around the crack tip must be known. For the case of a surface crack in a finite plate in pure bending for a material with Poisson's ratio ν the distribution in K_I has been evaluated numerically [*28,29*]. An approximation technique is utilized, which facilitates the adaptation of these numerical results to the problem of a small surface crack in a SAW stress field, with the limitation that the wavelength

normalized crack depth κa must be less than unity [*30*]. Consequently, the reflection coefficient S_{21} becomes [*6*]

$$S_{21} = \frac{2\pi f_z \eta c(\kappa a)^2}{3(1 - \nu)w\phi}[B_0 + B_1(\kappa a) + B_2(\kappa a)^2] \tag{9}$$

In Eq 9, the material associated variables are Poisson's ratio ν, the parameter f_z from Eqs 3 and 4 from Ref *12*, and the constants B_0, B_1, and B_2 where

$$B_0 = 2A_0/\pi \tag{10a}$$

$$B_1 = 2A_1(\beta/\kappa)/\pi \tag{10b}$$

$$B_2 = 2A_2(\beta/\kappa)^2/\pi \tag{10c}$$

The constants A_0, A_1, and A_2 have been evaluated numerically [*6,30*] using results [*29*] for a material with $\nu = 1/3$ giving $A_0 = 1.8137$, $A_1 = 0.83842$, and $A_2 = 0.44535$. The term β/κ relates to the wavelength normalized slope of the acoustic stress σ_{zz} versus depth below the surface evaluated at the surface so that

$$\beta/\kappa = \frac{[2(V_S/V_R)^2 - 1][1 - (V_R/V_S)^2]^{1/2}}{2[1 - (V_S/V_L)^2]} - \left[1 - \frac{[2(V_S/V_R)^2 - 1]}{2[1 - (V_S/V_L)^2]}\right][1 - (V_R/V_L)^2]^{1/2} \tag{11}$$

where V_S, V_R, and V_L are the shear, Rayleigh, and longitudinal phase velocities in the material, respectively. These velocities can be determined from the elastic constants and density of the desired substrate. Additional variables in Eq 9 are half the crack length at the surface c, the maximum crack depth below the surface a, the wave number κ, the beam width at the transducer w_b, and the elliptic integral of the second kind ϕ. Finally, η is a parameter to account for transducer insertion loss η_T, diffraction η_D, angular scattering η_ϕ, and the combined effects of attenuation and slight violation of far-field diffraction conditions η_a, that is [*31*]

$$\eta = \eta_T\eta_D\eta_\phi\eta_a \tag{12}$$

The components of the acoustic system that were used to determine these input parameters and subsequently to monitor the reflection coefficients of small fatigue cracks are depicted in Fig. 4. A function generator produced a gated sine wave at 3 MHz with three wavelengths duration at a repeat rate of approximately 100 Hz. The output from the function generator was amplified by the power amplifier from zero to peak voltage V_1 of 10 V. This is the input signal that goes to the sending transducer. Surface acoustic waves were produced on the specimen in a wave packet that traveled away from the sending transducer in a narrow beam, in this case, 4 mm wide. The beam reflected from the microcrack traveled back to the receiving transducer. The signal from this transducer was amplified by 60 dBV. The signal voltage V_2 was then monitored on an oscilloscope. The reflection voltage V_2 was measured in volts. The values of acoustic frequency, beam width, voltages, and so forth, just noted were those for the particular system used to generate the experimental results to be given shortly; systems utilizing different values can also be implemented.

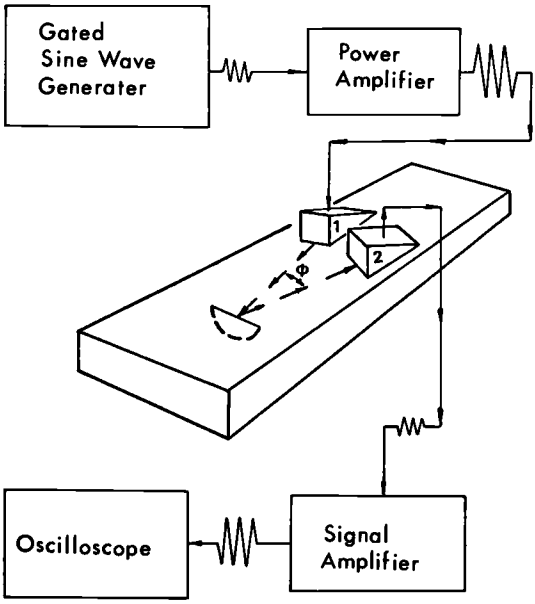

FIG. 4—*Schematic of the major components of the surface acoustic wave measurement system.*

Each sending and receiving transducer consisted of a small slice of piezoelectric PZT (lead-zirconate-titanate) crystal held at a specific angle by an RTV 615 silicone wedge as shown in Fig. 5. The wedge was cast into a hard polymer block that acted as the backing material. The incoming signal caused the PZT crystal to produce a longitudinal wave in the RTV silicone. The waves were converted to surface acoustic waves at the silicone/specimen interface. A low-viscosity ultrasonic fluid was used to couple the waves from the silicone to the sample. The transducers measured 14 mm in length, 12 mm in width, and 11 mm in height. Much smaller transducers may be fabricated using the general design philosophy described in Ref *11*.

For pitch-catch measurements of the reflection coefficient, η_T is defined as the amplitude ratio of the signal, V_2 received at transducer 2, to the signal input at transducer 1, V_1, when the two transducers are placed face-to-face (see Fig. 6*a*) on a specimen so that

$$\eta_T = V_2/V_1 \tag{13}$$

The diffraction loss in terms of amplitude in the far field of the transducer will be [*24*]

$$\eta_D = w_b/(\lambda z)^{1/2} \tag{14}$$

In order to calculate η_D, the beam width w_b of the wedge transducer must be found by direct measurement of the width at the bottom of the RTV silicon wedge of the transducer. The wavelength λ of the Rayleigh wave is calculated as a function of frequency and SAW phase velocity; additionally, the distance between the crack and the transducer z must be

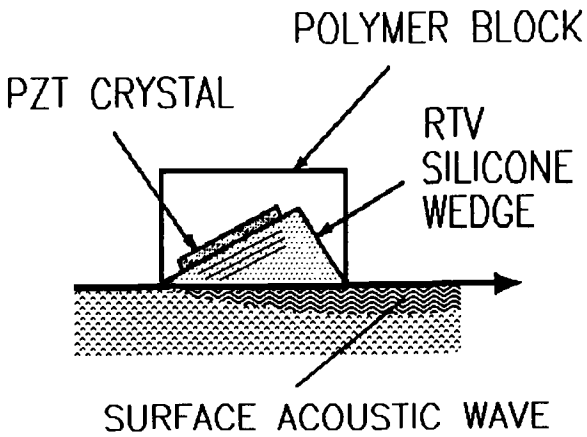

FIG. 5—*Schematic of surface acoustic wave (SAW) wedge transducer.*

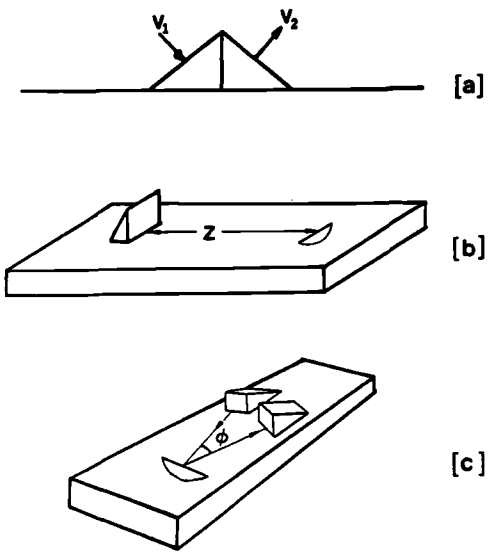

FIG. 6—*Variables used in determination of the parameter* η.

measured (Fig. 6*b*). The amplitude ratio of the reflected signal to the incident signal caused by angular scattering η_ϕ can be expressed as [*24*]

$$\eta_\phi = (1/4)[(1 - \nu) + (1 + \nu)\cos\phi]^2 - [(1 + \nu)^2/2(2 - \nu)]\sin^2\phi \qquad (15)$$

where the angle ϕ is twice the angle between the incident wave propagation direction and normal to the crack surface, as shown in Fig. 6*c*.

Finally, the combined effect of attenuation and slight violation of the far-field approximation of the diffraction loss term are combined into a single parameter η_a. This parameter is evaluated by measuring the reflection coefficient of a small crack of known size (obtained

from subsequent post fracture measurement) at a frequency of interest and several distances from the crack. Then the value of η_a is calculated for each measurement. Typical results of this calibration experiment at several frequencies for SAW wedge transducers with beam width, w_b = 4 mm, and a halfpenny shaped crack with crack depth, a = 140 μm, in a specimen of 7075-T651 aluminum are shown in Fig. 7. The results of this type of calibration can be used in either of two ways. If specimen size is not restricted, subsequent measurements of SAW reflection coefficient can be made at a distance from the crack such that $\eta_a = 1$. Alternatively, if size is restricted, then the value of η_a from the calibration experiment at the distance of interest may be used.

In Fig. 8, the reflection coefficient, S_{21} is plotted versus the normalized crack depth κa for halfpenny shaped cracks with $a = c$ for a material with $\nu = 0.3$ [*32*] using K_I from Ref *28*. In addition, the result for a material with $\nu = 1/3$ [*6*] using K_I from Ref *29* is included for comparison. Similar calculations may be performed using Eq 9 to determine the relationship between S_{21} and κa at different constant values of the crack aspect ratio a/c or alternatively at constant values of half the crack length at the surface c. Thus, measurements of reflection coefficient and surface crack length allows depth to be inferred for semi-elliptical cracks of unknown aspect ratio.

Verification of SAW Technique

Experiments have been performed in which crack depths were obtained from acoustic scattering measurements combined with optical measurements of crack length at the surface in ceramics and metals [*6,18,19,30,32,33*]. The data in Fig. 9 for 7075-T651 aluminum, Pyrex glass [*6*], 4340 quenched and tempered alloy steel [*32*] and 300 M steel [*9*] are representative of the size range in which measurements of small fatigue crack growth rate could be made with the acoustic components described previously. In these experiments, acoustic determinations of crack depth were compared to post-fracture measurements of depth for crack depth-to-surface length ratios between 0.4 and 1.0. For the 29 individual measurements

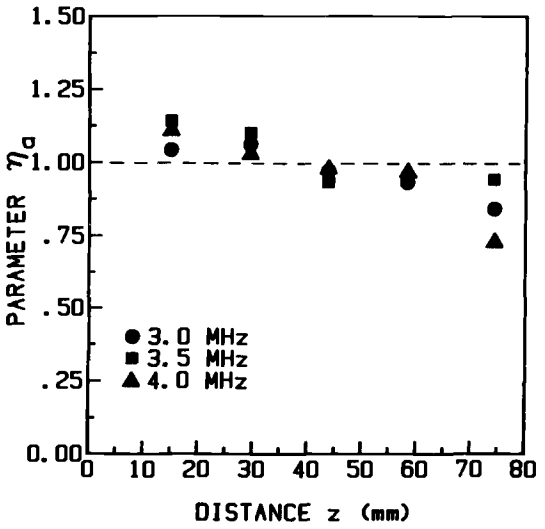

FIG. 7—*Change in η_a at different frequencies and distances from small crack.*

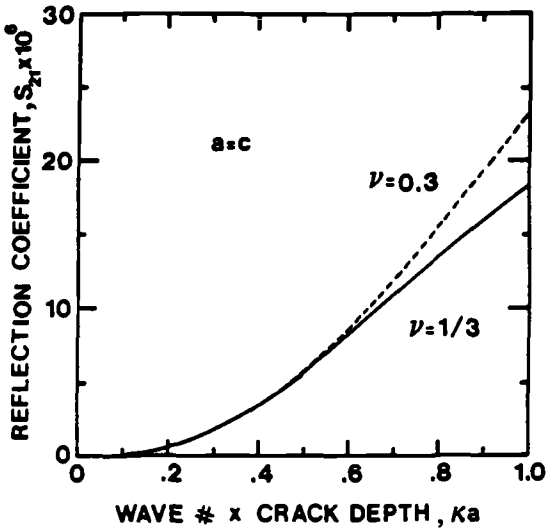

FIG. 8—*Reflection coefficient versus normalized crack depth.*

represented here, the average error between the measured and predicted depth was ±5.4%, with a standard deviation of 7.1%, and a maximum observed error of −17%. In principle, this technique could be used to measure the depth of much smaller surface cracks in the range of 0 to 50 μm depth; however, it has been observed experimentally that background noise in the reflected signal obscures the reflected signal from cracks this small.

Maximum Measurable Crack Size

SAW scattering measurements used for crack depth studies typically have been made at a single frequency, which minimizes the number of variables affecting the outcome of the experiment. Choosing a single frequency is valuable for comparing data from isolated cracks in different samples, but limits the maximum depth that can be inferred from the scattering measurement since the acoustic theory is valid only for the case when the normalized crack depth $\kappa a < 1$. The wave number, κ, is proportional to the frequency, so that lowering the frequency allows a deeper crack to be measured within the constraint that $\kappa a < 1$. The maximum measurable depth for cracks in aluminum and steel at a frequency of 3 MHz is approximately 150 μm. This useful depth can be increased 50% to 225 μm, by adjusting the frequency to 2 MHz. This depth corresponds to surface length of approximately 0.5 mm. In order to perform a scattering experiment in which the frequency of the acoustic wave varies during the experiment, the insertion loss of the transducers used to make the measurements must first be characterized as a function of frequency. Experiments have been performed [*9*] in which the transducer insertion loss parameter η_T has been measured over a range of frequencies from 2 to 4 MHz for 17 different materials, including aluminum, steel, and high temperature alloys. These experiments showed that, for all of the materials studied, a transducer designed to operate at a given center frequency could also be used as a variable frequency device, enabling crack growth data to be collected over an extended range of depths.

Nonspecular Reflections from Microstructure

Real engineering materials are not truly homogeneous, but contain microscopic regions that are locally anisotropic (grains) joined by planar areas that are atomically thin (grain boundaries). The orientations between adjacent grains are dissimilar enough to create a significant impedance mismatch for an ultrasonic wavefront attempting to travel across each boundary. This process results in an imperfect transfer of energy in the direction of propagation, and the ultrasonic energy reflected back toward the transmitter (or the receiver) will hereafter be referred to as the microstructural backscatter. A significant difference between reflections from the microstructure and cracks is that unlike the interaction of ultrasonic waves from cracks, which is frequency independent (specular), the microstructural backscatter is highly frequency dependent (nonspecular). For extremely small cracks with the amplitude of the reflected echo smaller than the amplitude of the microstructural backscatter, it has been observed experimentally that detection of crack initiation is relatively difficult, if not impossible, because of the complex interaction of the reflected echo with returning re-radiated signals from microstructural features in the vicinity of the crack.

Minimum Detectable Crack Size

The background acoustic noise level is of key importance since it places a lower bound on the size of microcracks that can be detected. How the noise varies with material and microstructure is important in the possible applicability of the SAW technique to a wide range of materials. The crack size that gives a predicted amplitude equal to the amplitude of the acoustic noise measured under identical scattering conditions is defined as the minimum detectable crack size. The minimum detectable crack depth for a particular alloy is a function of the crack aspect ratio a/c. It is convenient to compare the minimum detectable crack depth between different alloys utilizing the halfpenny shape, with $a = c$.

In Fig. 10, the minimum detectable crack depth is displayed for several alloys. Groups of metals (for example, aluminum, steel, and so forth), show similar values of background

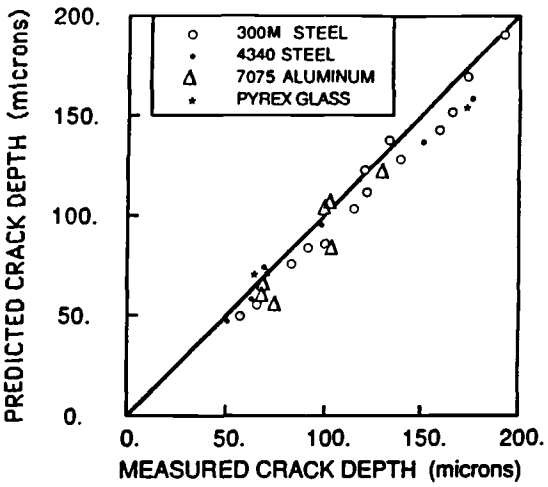

FIG. 9—*Acoustic prediction of crack depth versus post-fracture measurements of crack depth.*

noise and insertion loss, which result in similar values of crack size. The SAW transducers operated more efficiently on aluminum than on steel because of the increased insertion loss in steel for the transducers used. For most of the alloys shown, the interference pattern caused by microstructural features obscures the first 50 to 60 μm of crack growth, reducing the effective measuring range of the SAW scattering technique to the largest 2/3 of its potential range. Until recently, measurements of crack size between zero and approximately 50 μm have not been possible because of the masking effect of grain scattering. However, recently some progress has been made in the area of reducing the minimum detectable crack depth by applying a novel nonlinear digital filtering algorithm in an attempt to reduce the signal to noise ratio (SNR).

Split Spectrum Processing

A new signal processing technique has demonstrated that frequency diverse signals could be obtained in receive-mode by splitting the wideband spectrum of the received signal. This technique, called split spectrum processing (SSP) has been successfully implemented in a number of well documented experiments [*34–42*]. The primary benefit received by implementation of this signal processing technique to reflected echoes from cracks superimposed on nonspecular microstructural backscatter is that the SNR is dramatically improved [*43*]. This is possible because this nonlinear digital filtering technique differentiates between the coherent, frequency dependent interference noise caused by grain scatter and specular, frequency independent reflection caused by microcracks. Previous work in this area [*34–37*] showed that the technique could be effective in SNR enhancement applications (although in applications involving macroanomalies, that is, when the anomalous reflector is orders-of-magnitude larger than both the wavelength and grain size). In the next section, the split spectrum processing technique has recently been shown to be effective [*44*] for SNR enhancement of microcracks that are orders of magnitude smaller than the reflectors involved in the previous works [*34–37*].

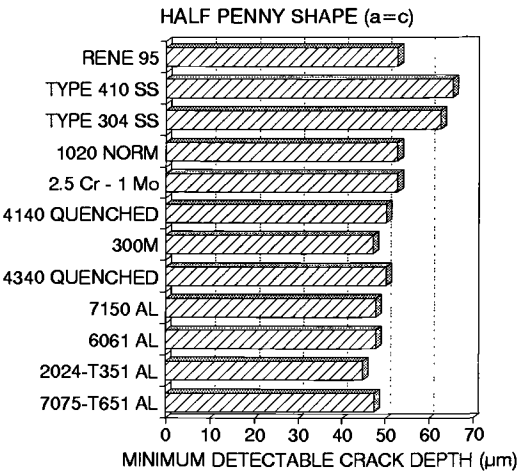

FIG. 10—*Minimum detectable crack depth for several aluminum and steel alloys.*

SAW Detection of Microcrack Initiation

Hourglass shaped specimens were metallographically prepared in the high stress region to minimize the effect of fabrication on surface roughness and residual stress. Before the fatigue cycling begins, the signal caused by backscattered Rayleigh waves from the high stress region was acquired and averaged over a sample size of 16 with a digitizing oscilloscope at a rate of 200 MS/s (200×10^6 samples/s). The resulting 1001 point data array that represents the time gated signal over the interval 10 μs before and after the echo were then transferred to the hard disk of a computer. At 2000 cycle intervals of applied fluctuating stress (maximum stress equal to 275 MPa with a stress ratio of 0.1), the digitizing, averaging, and storing process is repeated.

This procedure continues until the initiation and growth of at least one crack is obvious in the high stress region. The presence of the crack is determined not only because the reflection from the crack begins to emerge from the surrounding grain noise, but also because the reflection from the crack completely disappears when the tensile load on the specimen is released thereby closing the crack. At the termination of the fatigue cycling process (when the presence of the crack is obvious), all the acquired waveforms are processed for the evidence of earliest possible detection of reflections from surface microcracks using the SSP algorithm described previously.

Figure 11*a* shows the termination point of fatigue cycling for a typical specimen after 80 000 applied cycles. Figures 11*b* and 11*c* illustrate a few of the acquired signals during the fatigue cycling process (at 70 000 and 56 000 cycles, respectively). Figures 11*d* through 11*f* show the results of applying split spectrum processing to the signals shown in Figs. 11*a* through 11*c*. The processed signals show the presence of the microcrack without ambiguity because of the absence of the interfering grain clutter. Figure 12 shows the crack size inferred from the acoustic theory as a function of the number of fatigue cycles. The curve is monotonically increasing thereby indicating the growth rate of the microcrack. The earliest detection of the crack was at 58 000 cycles when the crack was only 20 μm deep. However, when the reflectors are of similar size as the surrounding grains, false indications also appear that usually disappear (and only the crack reflection amplitude grows) with increased number of fatigue cycles.

Crack Opening Behavior

SAW Measurement of Crack Opening

The use of acoustic NDE techniques for studying the opening behavior of "large" through-thickness fatigue cracks have also received considerable attention. Experimental studies [*31*] have been made of the transmission and reflection characteristics of bulk ultrasonic waves at an interface that simulates the acoustic response of a true fatigue crack. Detailed theoretical calculations have been performed [*45*] that demonstrate the nonlinear dependence on contact stress of transmission and reflection of bulk waves at an irregular interface. Transmission and reflection as a function of the geometry of the contacting surface area at an interface have also been analyzed [*46*]. In addition, a method has been developed [*47*] to calculate the scattering of surface acoustic, or Rayleigh, waves from partly closed surface breaking cracks. In principle, this method can be utilized to model cracks that are not simply connected (for example, have islands of closure). These studies provide a theoretical basis for the nonlinear behavior of crack acoustic signals versus applied stress observed experimentally by a number of investigators [*6,48,49*].

For the case of SAW scattering under conditions that normalized crack depth $\kappa a < 1$, it has been observed experimentally that measurement of the reflection coefficient S_{21} versus

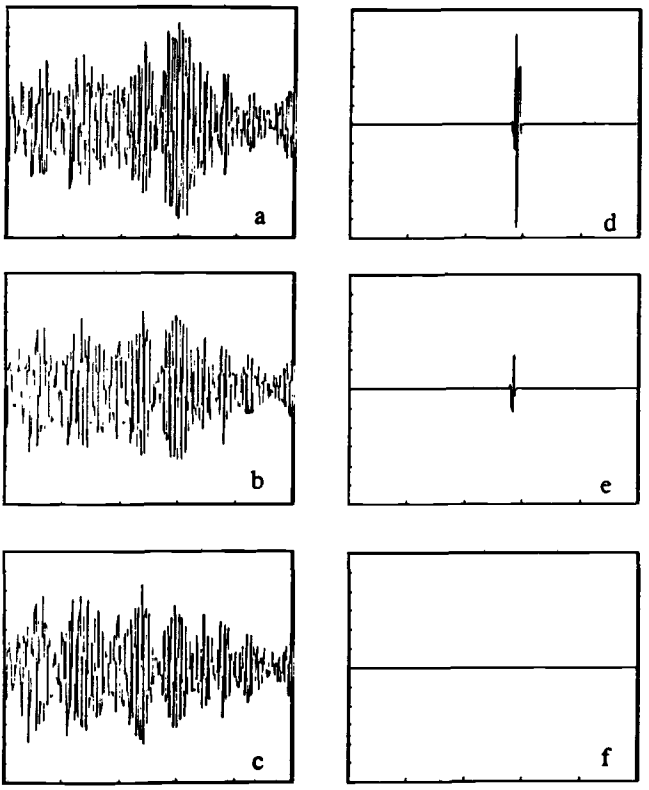

FIG. 11—(a) *Unprocessed signal at 80 000 cycles,* (b) *unprocessed signal at 70 000 cycles,* (c) *unprocessed signal at 56 000 cycles,* (d) *processed signal at 80 000 cycles,* (e) *processed signal at 70 000 cycles,* (f) *processed signal at 56 000 cycles.*

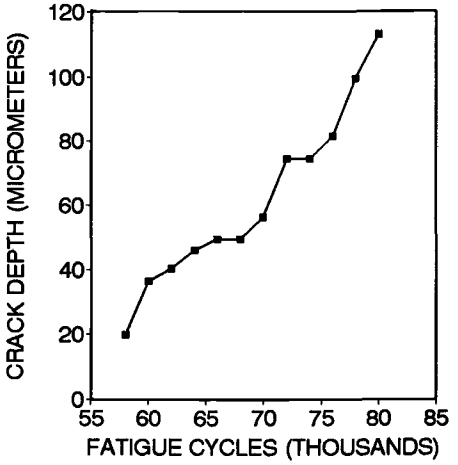

FIG. 12—*Crack depth* a *inferred from the processed amplitude of the crack as a function of the number of fatigue cycles.*

applied stress σ, facilitates the detection of two important physical events during crack opening. The first (see Fig. 13) is the approximate stress at which the crack faces just begin to separate. The presence of backscattered signals (noise) from microstructural features, such as grain boundaries and inclusions, partially obscures the acoustic reflection from the crack denoting the beginning of the opening of adjacent crack faces. The stress at which the reflection coefficient emerges from the noise actually denotes separation of a small portion of the previously closed adjacent crack faces. The second is the stress at which the crack faces completely separate, so that increasing the applied stress produces no subsequent increase in the reflection coefficient.

The stress at which the reflection coefficient "saturates" is denoted σ_{sat}. It has been observed experimentally [7] that σ_{sat} can change significantly during fatigue cycling as a consequence of changes in the applied stress range $\Delta\sigma$ and the stress ratio $R = \sigma_{min}/\sigma_{max}$, during tests. This type of measurement technique permits experimental investigations of the relation between crack growth rate and effective stress range of growth (difference between maximum applied stress and the stress required to fully open a crack). It is also of interest to understand the significance of these acoustic measurements with respect to optical methods for measuring the opening behavior of a crack at the surface. These topics will be considered in the next section.

Study of Small-Crack Growth by a SAW/SEM Technique

Experimental Approach

The SAW technique can be used in conjunction with various optical methods to obtain information about both surface crack length and depth as well as opening stress as determined from measurements of crack-tip opening displacement and of reflection coefficient as a function of applied tensile stress. For instance, the SAW technique can be combined with the use of a scanning electron microscope (SEM) as a method for investigating crack-tip opening displacement behavior and surface length. As an example of this, a study [9] has

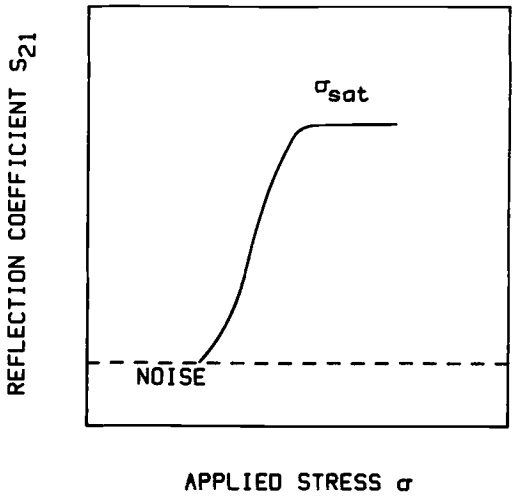

FIG. 13—*Typical response of the reflection coefficient versus applied tensile stress.*

been conducted of small-crack growth in 300M steel, a well-characterized [*50*], high-strength, silicon modified American Iron and Steel Institute (AISI) 4340 alloy. Crack growth tests were performed using the specimen design [*51*] depicted in Fig. 14. SAW transducers were placed at the larger end of each specimen, aimed towards the specimen throat. The transducers were held on the specimens by a flexible C-clamp device so that crack growth could be monitored continuously during fatigue tests. A small pit of approximately 25 μm in depth was produced on each specimen surface in the throat region by a spark discharge. The pit was small enough to allow a crack to form and grow as if it has initiated naturally from a microstructural defect. The cross section of the throat was tapered, creating a stress distribution that served the dual purposes of further localizing the crack initiation region and eliminating nucleation of cracks that had formed at the corners of rectangular cross-sectional specimens used in exploratory experiments.

Fatigue tests were conducted with constant amplitude, cantilevered bending at a stress ratio of $R = 0.5$ and frequencies between 3 and 5 Hz. The bending fixture illustrated in Fig. 15 was designed so that a single-axis electrohydraulic test machine could be utilized to produce bending with minimal axial or torsional loading on specimens. Fatigue tests were run at elastically calculated maximum stress levels of 75% and 90% of cyclic yield strength. Strain gages were installed on specimens, and applied deflection adjusted to produce desired bending strain levels and corresponding elastically calculated stress values.

Measurements of crack reflection coefficient versus applied stresses were made periodically during fatigue cycling while the reflection coefficient, and thus crack depth, was monitored continuously by the SAW transducers. After an interval of fatigue cycling and acoustic measurements were completed, a specimen would be removed from the bending fixture and mounted in the small flexure jig shown in Fig. 16, and placed in the chamber of an SEM. Crack surface length and crack-tip opening displacement versus applied strain (stress) were determined. The specimen was then returned for additional fatigue testing and further measurements that were repeated until the crack grew to the maximum measurable size.

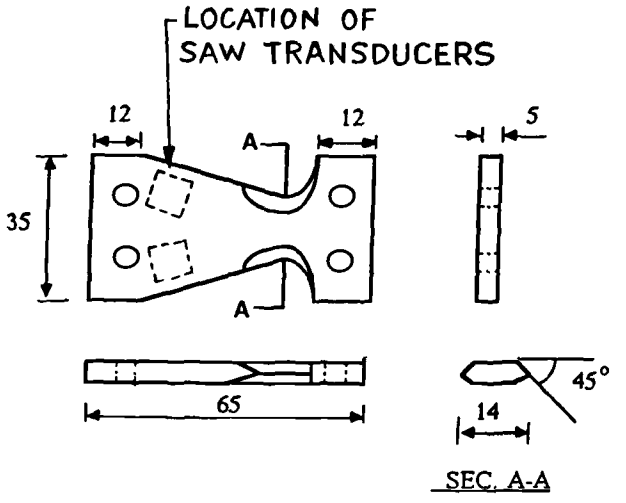

FIG. 14—*Schematic of cantilever bending specimen configuration.*

Effects of Residual Stress

It is well known that residual stresses can exert a strong influence on the growth behavior of large cracks. Surface residual stresses can also have a profound effect on small-crack growth [*52,53*]. Before starting fatigue tests of 300M steel specimens, longitudinal residual stresses caused by different surface preparations were determined. The residual stress distributions at and below the surface are shown in Fig. 17. Small-crack growth tests were performed with specimens that were either electropolished or ground, diamond paste polished, stress relieved, and then diamond paste polished (to 1 μm); the two procedures producing compressive surface residual stresses of approximately −35 and −340 MPa, respectively. Surface values of residual stress were also measured intermittently by X-ray diffraction during the course of fatigue tests. It was found that for both surface preparations used and both maximum stress levels applied, residual stresses remained close to their initial values.

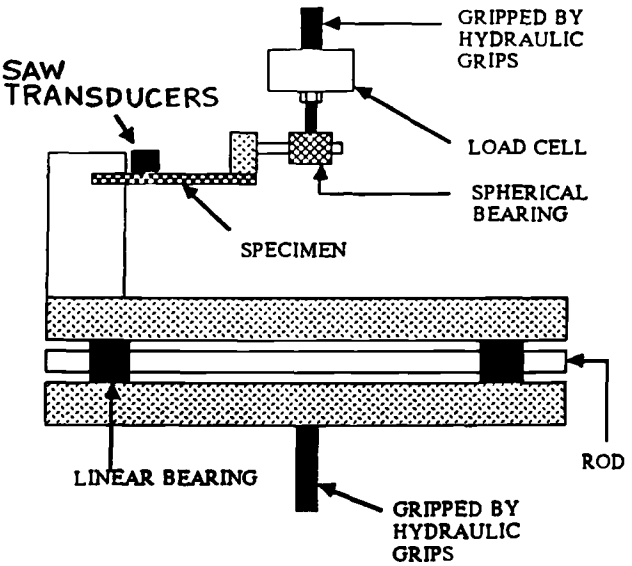

FIG. 15—*Schematic of cantilever bending specimen flexure jig.*

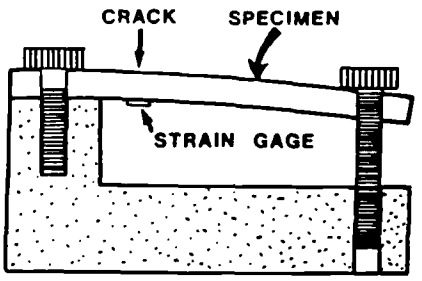

FIG. 16—*Schematic of a small specimen in an SEM flexure jig.*

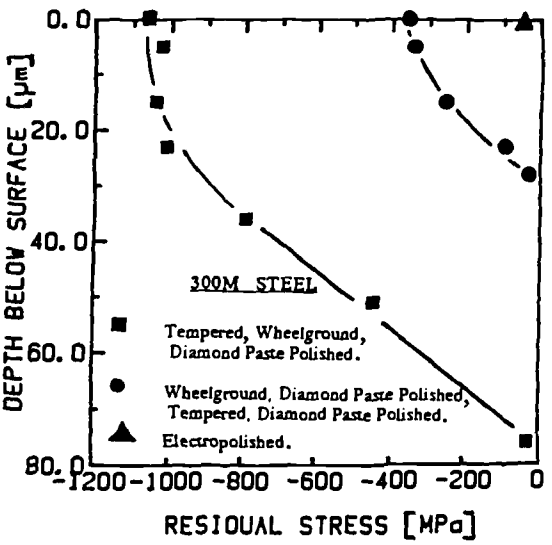

FIG. 17—*Variation in residual stress in depth with different surface preparations.*

Crack-mouth opening displacement (CMOD) and crack-tip opening displacement (CTOD) measurements have also been used in determining the opening behavior of small surface cracks [*54,55*]. The procedure is to make measurements of CMOD and CTOD for a specimen containing a microcrack while it is under static load in the vacuum chamber of a SEM. Opening stress is defined as the point where the slope of CMOD (or CTOD) versus stress changes markedly. Knowledge of opening stress can be important since the effective stress range driving crack growth is the difference between the maximum applied stress and the opening stress.

Experiments were conducted to investigate the relationship between the optically determined crack-tip opening stress σ_{CTOD}, crack-mouth opening stress σ_{CMOD}, and the ultrasonically determined crack opening stress described previously as the saturation stress σ_{sat}. Typical results used to determine these stresses are shown in Figs. 18 and 19. Combining the results from SEM and SAW measurements of an isolated microcrack during constant amplitude loading reveals subtle changes in crack-opening behavior as depicted in Fig. 20. In this figure σ_{CMOD} is the applied stress level when the crack mouth starts opening, σ_{CTOD} is the stress level when crack tips start opening, and finally σ_{sat} is the acoustically determined saturation stress level when the crack is thought to be fully open. This figure shows that the crack mouth starts opening first, then, at a certain stress level, the crack tips open. The important result is that even when the crack tips open, there is still a part of the crack front in depth that is not fully open. Figure 20 also shows changes in the saturation stress and the opening stress determined by COD during the course of a representative fatigue test.

Figure 21 shows the change in acoustically measured crack depth versus optically measured crack length at the surface for a typical test. The SAW technique is able to monitor how the crack aspect ratio varies with growth, knowledge of which can be very important for accurate calculations of stress intensity factors or other parameters used to characterize small crack growth rate. It was found, as might have been expected, that in the early stages of growth, small cracks started with a semi-elliptical shape, then became semi-circular.

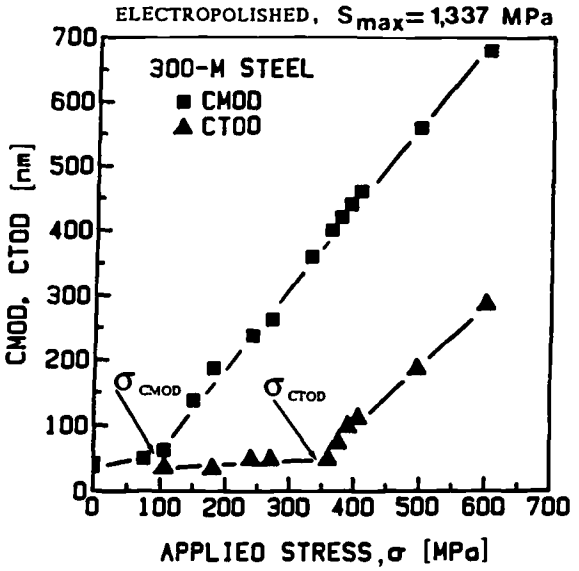

FIG. 18—*Typical change in crack-opening behavior with applied stress.*

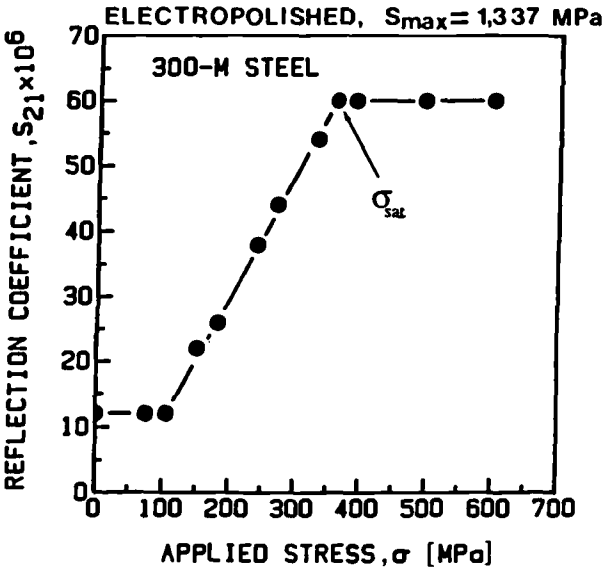

FIG. 19—*Typical change in reflection coefficient with applied stress.*

The variation of crack-tip opening stress and saturation stress with crack growth during several representative tests is shown in Fig. 22 for the two surface preparations described earlier. Electropolishing caused surface residual stresses of −35 MPa, a negligibly small level relative to the applied stress of 1115 MPa. Results of small-crack growth tests in electropolished specimens showed that cracks opened at the surface at stresses of approx-

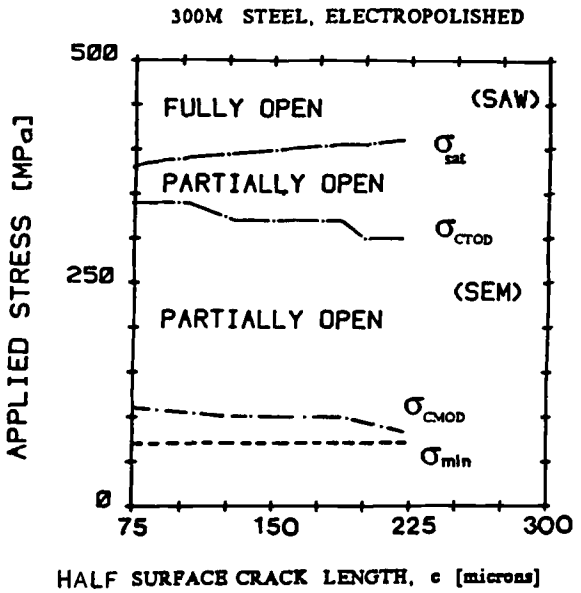

FIG. 20—*Representative crack-opening behavior during the course of a fatigue test.*

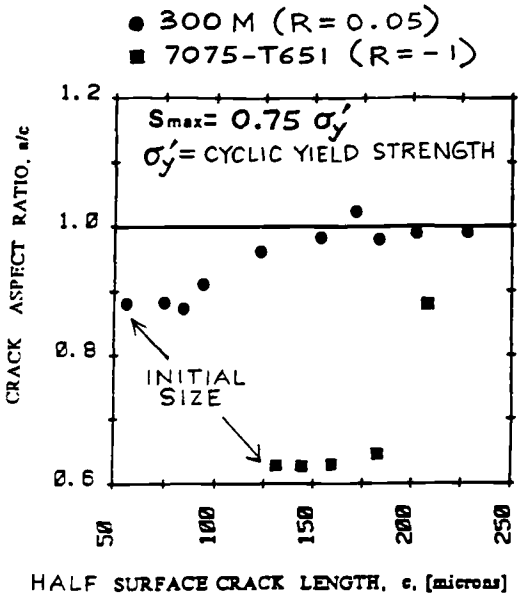

FIG. 21—*Typical growth behavior of small surface cracks during the course of a fatigue test.*

imately 30% of the maximum applied stress, but it took at least 10 to 15% higher stress to open cracks in depth. The other surface preparation, which ended with diamond paste polishing, caused surface residual stresses of −340 MPa, small relative to applied stresses, and acting over a depth comparable to that of initial sizes of small cracks. Even this shallow

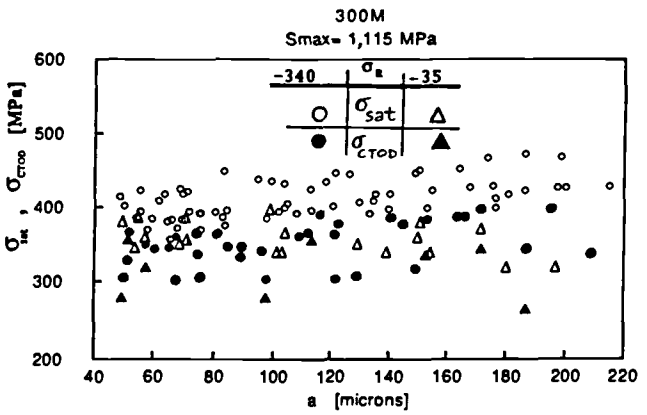

FIG. 22—*The change in saturation stress and crack-tip opening stress during the course of fatigue tests for two different surface residual stress conditions and an applied stress of 1115 MPa.*

layer of residual stresses exerted a significant influence on opening stresses, increasing both crack-tip opening and saturation stress levels by about 15% compared to values in electropolished specimens. The results in Fig. 22 also indicate that opening stress levels changed little with crack growth. Another study [*8*] that utilized the SAW technique showed that saturation stress decreased with small crack growth in tests of quenched and tempered 4140 steel.

Study of Crack Opening Behavior by a SAW/LID Technique

Experimental Approach

The amplitude of a time gated signal containing the reflection from a naturally initiated isolated surface microcrack was transferred from a digitizing oscilloscope to a computer at discrete values of force applied to the specimen with an orientation normal to the adjacent crack faces. The 1001 data points in each signal were acquired at 200 MS/s (200×10^6 sample/s) and were obtained by averaging 16 waveforms each of 20-μs duration. The analog signal from the load cell was acquired using a 12-bit analog to digital conversion board in a conventional microcomputer. Under manual control of the set point of the servohydraulic system in force control, applied force versus crack amplitude was acquired automatically point by point, while being simultaneously displayed on the computer screen.

Comparison of Acoustic-optical Opening Measurements

The results of a typical scan from an isolated surface microcrack are displayed in Fig. 23. The nonlinear portion of the curve from zero force up to the point at which the plot becomes vertical reveals the presence of surface tractions between adjacent crack faces. The vertical portion reveals the point at which surface tractions disappear (referred to as σ_{sat}), and the crack is fully open.

In order to compare ultrasonic measurements of microcrack opening behavior with another established technique, force versus CMOD for several naturally initiated surface microcracks was accomplished using the laser interference displacement gage (LIDG) available on Machine #1 in the High Temperature Metals and Ceramics Laboratory at the Wright Research

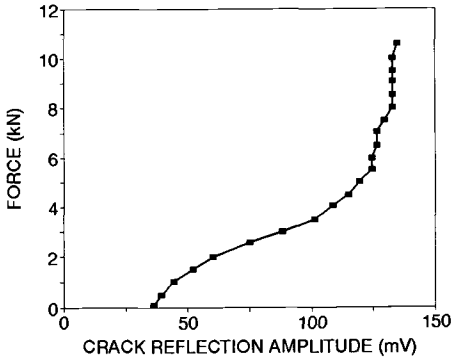

FIG. 23—*Crack reflection amplitude from SAW scattering versus force applied normal to the crack faces for a small naturally initiated fatigue microcrack in 2024 aluminum* (a = *150 μm*).

and Development Center (WRDC) at Wright Patterson Air Force Base. Details of this experimental system are available elsewhere in the literature [*56*]. A typical result of this type of measurement obtained for the crack that was also ultrasonically measured is shown in Fig. 24. An important feature is the stress range for which the observed linear relationship between CMOD and applied force is distinctly nonlinear in the ultrasonic measurement of opening behavior shown previously. It is a well accepted fact that the LIDG apparatus, while capable of exceedingly accurate measurements of crack-opening behavior and crack growth, still requires a "judicious" introduction of an apparent opening load into the measuring algorithm in order to achieve this accuracy. This preliminary result indicates that the SAW scattering technique is able to measure the force necessary for complete crack opening for cracks above the minimum detectable crack size.

In principle then, the ultrasonically determined crack-opening stress could be used to update the appropriate opening stress needed for the LIDG characterization of crack growth during a fatigue test, resulting in a fully automated testing technique for performing microcrack growth experiments.

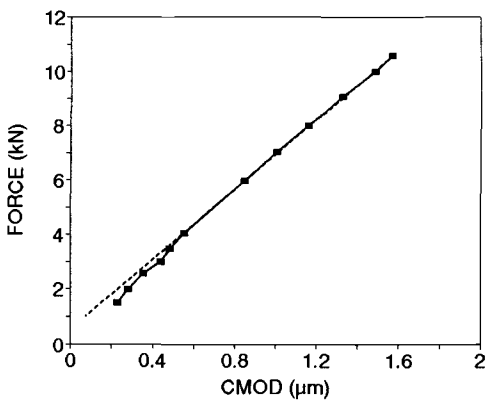

FIG. 24—*Crack-mouth opening displacement from LIDG versus force applied normal to crack faces for same crack depicted in Fig. 23.*

Discussion

The usefulness of any experimental technique is defined in part by its limitations. In this section, a number of assumptions necessary for acoustic evaluation of crack depth are discussed, and the principal limitations associated with these assumptions enumerated.

To measure the crack depth below the surface, the reflection coefficient first must be evaluated by calculating the integral of Eq 3 around the crack edge. In order to make this calculation, an assumption must be made concerning the shape of the crack below the surface. Use of an assumed semi-elliptical crack shape in the acoustic scattering model closely approximates the shape of small surface fatigue cracks occurring in nature.

Another assumption which is extremely important for accurate acoustic measurement of crack depth is that the crack should be growing in a direction approximately normal to the surface. In the long-wavelength scattering regime, the Rayleigh wave "sees" the projection of the crack in a plane normal to the propagation direction, to a first approximation. If a crack has a different orientation, then the simplifications used for evaluation of the elastic energy change for a crack in the field of a surface acoustic wave are no longer valid, and the effects of the shear stresses resolved along the crack plane could become important. To date, an analytical expression for the stress intensity factor distribution for a semi-elliptical surface crack with an arbitrary orientation with respect to applied stress has not been developed. Fortunately, however, fatigue cracks tend to grow normal to the surface, at least for the sizes considered here. In general, it is only in the earliest stages of growth that they may be at some different angle with respect to the surface.

Perhaps the most restrictive condition in the scattering technique is that the normalized crack depth κa be less than unity. In order to maintain the long-wavelength scattering conditions during continuous monitoring of the growth of a small crack, the frequency of the Rayleigh waves can be reduced as the crack grows deeper. For the case of relatively thick specimens, with depth h, such that $h >> 4\lambda$, the maximum measurable depth is limited only by the bandwidth of the particular transducers being used. However, for the case of a small crack growing in a relatively thin specimen, a lower limit on the usable frequency exists at which "pure" Rayleigh wave propagation is no longer possible and other modes of ultrasonic waves are produced. For example, it has been demonstrated [*57*] that scattering behavior of Lamb waves from small cracks can be computed, but quantitative evaluation of crack size is difficult owing to uncertainties in identification of the individual modes exising in the reflected wave.

Conclusions

1. Use of a surface acoustic wave technique in conjunction with conventional optical measurement of surface length allowed the depth and aspect ratio of artificially initiated small cracks to be monitored continuously as they grew. If cracks are either known or assumed to be semi-circular in shape, depth may be evaluated by the acoustic method alone.
2. Acoustic evaluations of crack depth in glass and several aluminum and steel alloys agreed well with post-fracture optical measurements of depth, with an average error of $\pm 5\%$ and a standard deviation of 7%.
3. With a surface acoustic wave transducer operating at frequencies between 2 and 3 MHz, it was possible to monitor crack growth from initial depths of approximately 50 μm (without processing) to depths of about 250 μm (or approximately 0.5-mm surface length) for cracks of known orientation with respect to the direction of ultrasonic wave propagation. This range of depth could be extended through use of transducers designed to operate at somewhat lower frequencies.

4. The surface acoustic wave technique is able to determine, during the course of a fatigue test, the tensile stress needed to cause a small crack to fully open in depth. This provides useful companion data to determinations of crack-opening stress based on measurement of crack-tip opening surface displacements.
5. The presence in fatigue specimens of a shallow layer of residual stresses resulting from diamond paste polishing of the surface had a significant influence on small-crack behavior, raising crack-opening stress levels, and reducing crack growth rates.
6. Split spectrum processing has been shown to be an effective tool for the enhancement of SNR when the reflector of interest is many times smaller than the wavelength of the interrogating ultrasound. Microcracks as small as 20 μm have been detected with this processing.
7. A new acousto-optical technique, termed the SAW/LID technique, has been developed to aid in the automation of fatigue microcrack initiation and growth experiments. Initial measurements of ultrasonically inferred crack-opening behavior appear to correlate well with optically inferred crack-opening behavior.

Acknowledgment

Split spectrum processing of ultrasonic signals and laser interference displacement gage measurement of crack opening was supported by and performed on-site at the Materials Laboratory, Wright Research and Development Center, Wright-Patterson Air Force Base, OH, Contracts F33615-89-C-5612 and F49620-88-C-0053. The first author is especially indebted to Dr. P. Karpur of WRDC for his outstanding work in improving the ultrasonically determined minimum detectable crack depth using the Split Spectrum Processing Technique. Special thanks are also due to Universal Energy Systems, Inc. for contributing to this effort through the AFOSR/SFRP program. Additionally, the guidance of Dr. T. Nicholas and Dr. T. Moran at WRDC was greatly appreciated.

References

[1] Klima, S. J., Lesco, D. J., and Freche, J. C., *Experimental Mechanics*, Vol. 6, March 1966, pp. 154–161.

[2] Buck, O., Ho, C. L., Marcus, H. L., and Thompson, R. B., *Stress Analysis and Growth of Cracks: Proceedings of the 1971 National Symposium on Fracture Mechanics, Part I, STP 513*, American Society for Testing and Materials, Philadelphia, 1972, p. 280.

[3] Teller, C. M., Barton, J. R., Matzkanin, G. A., Kusenberger, F. N., and Beissner, R. E., *Journal of Engineering Materials and Technology*, Vol. 102, January 1980, pp. 50–55.

[4] Achenbach, J. D., Viswanathan, K., and Norris, A., *Wave Motion*, Vol. 1, 1979, pp. 229–316.

[5] Visscher, W. M., *Review of Progress in Quantitative Nondestructive Evaluation*, Vol. 4A, D. O. Thompson and D. E. Chimenti, Eds., Plenum Press, New York, 1984, pp. 217–228.

[6] Resch, M. T., "Non-destructive Evaluation of Small Surface Cracks Using Surface Acoustic Waves," Ph.D. Dissertation, Stanford University, Stanford, CA, 1982.

[7] Resch, M. T., Nelson, D. V., Yuce, H. H., and London, B. D., *Basic Questions in Fatigue: Vol. I, STP 924*, American Society for Testing and Materials, Philadelphia, 1988, pp. 323–336.

[8] London, B., Nelson, D. V., and Shyne, J. C., *Metallurgical Transactions A*, Vol. 20A, July 1989, pp. 1257–1265.

[9] Yuce, H. H., "The Use of a Surface Acoustic Wave Technique to Study the Growth Behavior of Small Cracks in a High Strength Steel Alloy," Ph.D. dissertation, Stanford University, Stanford, CA, 1987.

[10] Resch, M. T., Nelson, D. V., Yuce, H. H., and Ramusat, G. F., *Journal of Nondestructive Evaluation*, Vol. 5, No. 1, 1985, pp. 1–7.

[11] Fraser, J. D., Khuri-Yakub, B. T., and Kino, G. S., *Applied Physics Letters*, No. 32, 1978, p. 698.

[12] Auld, B. A., *Acoustic Fields and Waves in Solids*, Vol. II, Wiley-Interscience, New York, 1973, p. 375.

[13] Schmerr, L. W., *Review of Progress in Quantitative Nondestructive Evaluation*, Vol. 1, D. O. Thompson and D. E. Chimenti, Eds., Plenum Press, New York, 1982, p. 511.
[14] Mal, A. K., *Review of Progress in Quantitative Nondestructive Evaluation*, Vol. 1, D. O. Thompson and D. E. Chimenti, Eds., Plenum Press, New York, 1982, p. 499.
[15] Achenbach, J. D., and Norris, A. N., *Review of Progress in Quantitative Nondestructive Evaluation*, Vol. 1, D. O. Thompson and D. E. Chimenti, Eds., Plenum Press, New York, 1982, p. 491.
[16] Fitting, D., Adler, L., de Billy, M., *Review of Progress in Quantitative Nondestructive Evaluation*, Vol. 1, D. O. Thompson and D. E. Chimenti, Eds., Plenum Press, New York, 1982, p. 525.
[17] Testa, A. J., and Burger, C. P., *Review of Progress in Quantitative Nondestructive Evaluation*, Vol. 1, D. O. Thompson and D. E. Chimenti, Eds., Plenum Press, New York, 1982, p. 557.
[18] Tien, J., Khuri-Yakub, B. T., Kino, G. S., Evans, A. G., and Marshall, D., *Review of Progress in Quantitative Nondestructive Evaluation*, Vol. 1, D. O. Thompson and D. E. Chimenti, Eds., Plenum Press, New York, 1982, p. 569.
[19] Resch, M. T., Shyne, J. C., Kino, G. S., and Nelson, D. V., *Review of Progress in Quantitative Nondestructive Evaluation*, Vol. 1, D. O. Thompson and D. E. Chimenti, Eds., Plenum Press, New York, 1982, p. 573.
[20] Angel, Y. C., Achenbach, J. D., and Norris, A. N., *Review of Progress in Quantitative Nondestructive Evaluation*, Vol. 3A, D. O. Thompson and D. E. Chimenti, Eds., Plenum Press, New York, 1985, p. 175.
[21] Rehbein, D. K., Thompson, R. B., and Buck, O., *Review of Progress in Quantitative Nondestructive Evaluation*, Vol. 4A, D. O. Thompson and D. E. Chimenti, Eds., Plenum Press, New York, 1985, p. 61.
[22] Achenbach, J. D., Hu, K. Y., Norris, A. N., Gray, T. A., and Thompson, R. B., *Review of Progress in Quantitative Nondestructive Evaluation*, Vol. 4A, D. O. Thompson and D. E. Chimenti, Eds., Plenum Press, New York, 1985, p. 91.
[23] Kino, G. S., *Science*, Vol. 206, 1979, p. 173.
[24] Auld, B. A., *Wave Motion*, Vol. 1, No. 1, 1979, pp. 3–10.
[25] Kino, G. S., *Journal of Applied Physics*, Vol. 49, No. 6, 1978, p. 3190.
[26] Auld, B. A., *Wave Motion*, Vol. 1, No.1, 1979, p. 3.
[27] Knowles, J. K. and Sternberg, E., *Archiv. Rat. Mech. Anal.*, Vol. 44, 1971–1972, p. 187.
[28] Newman, J. C. and Raju, I. S., "Analyses of Surface Cracks in Finite Plates Under Tension or Bending Loads," *NASA Technical Paper*, No. 1578, 1979.
[29] Smith, F. W., Emery, A. F., and Kobayashi, A. S., *Journal of Applied Mechanics*, Vol. 34, No. 4, 1967, p. 953.
[30] Tien, J., Khuri-Yakub, B. T., and Kino, G. S., "Proceedings of the DARPA/AFML Review of Progress in Quantitative Nondestructive Evaluation." Report AFWAL-TR-80-4078, 1980, p. 671.
[31] Buck, O., Fiedler, C. J., Reed, L. K., Lakin, K. M., and Thompson, R. B., *Nondestructive Testing, Proceedings of the 4th European Conference*, J. M. Farley and R. W. Nichols, Eds., Vol. 1, 1987, p. 199.
[32] Yuce, H. H., Nelson, D. V., and Resch, M. T., *Review Progress in Quantitative Nondestructive Evaluation*, Vol. 4A, D. O. Thompson and D. E. Chimenti, Eds., Plenum Press, New York, 1985, p. 103.
[33] Resch, M. T., London, B. D., Ramusat, G. F., Yuce, H. H., Nelson, D. V., and Shyne, J. C., *Review of Progress in Quantitative Nondestructive Evaluation*, Vol. 3A, D. O. Thompson and D. E. Chimenti, Eds., Plenum Press, New York, 1984, p. 217.
[34] Newhouse, V. L., Furgason, E. S., Bilgutay, N. M., and Saniie, J., *Proceedings of the Ultrasonic International Symposium*, Butterworth Scientific, Guildford, United Kingdom, 1979, pp. 152–156.
[35] Bilgutay, N. M., *Split-spectrum Processing for Flaw-to-Grain Echo Enhancement in Ultrasonic Detection*, Ph.D. Dissertation, Purdue University, Lafayette, IN, 1981.
[36] Brase, J., McKinney, R., Blaedel, K., Oppenheimer, J., Wang, S., and Simmons, J., *Materials Evaluation*, Vol. 42, 1984, pp. 1619–1625.
[37] Baligand, B., Grozellier, M., and Romy, D., *Materials Evaluation*, Vol. 44, 1986, pp. 577–581.
[38] Bencharit, "Spectral and Spatial Processing Techniques for Ultrasonic Imaging Techniques," Master's thesis, Drexel University, Philadelphia, 1987.
[39] Li, Y., "Two Signal Processing Techniques for the Enhancement of the Flaw-to-Grain Echo Ratio," Master's Thesis (in Chinese), Academia Sinica, China, 1985.
[40] Karpur, P., Shankar, P. M., Rose, J. L., and Newhouse, V. L., *Ultrasonics*, Vol. 25, 1987, pp. 204–208.
[41] Karpur, P., "Split Spectrum Processing: Process Modeling and the Evaluation of Polarity Thresholding Algorithm for Material Noise Reduction in Ultrasonic NDE," Ph.D. Dissertation, Drexel University, Philadelphia, 1987.

[42] Shankar, P. M., Karpur, P., Newhouse, V. L., and Rose, J. L., *IEEE Transactions on Ultrasonics, Ferroelectrics and Frequency Control*, Vol. 36, No. 1, 1988, pp. 114–122.
[43] Silk, M. G., *Non-destructive Testing, Proceedings of the 4th European Conference*, J. M. Farley and R. W. Nichols, Eds., Vol. 1, 1987, pp. 1647–1660.
[44] Karpur, P. and Resch, M. T., "Improved Detectability of Fatigue Microcracks by Split Spectrum Processing of Backscattered Rayleigh Waves," *Progress in QNDE*, Vol. 10, in press.
[45] Achenbach, J. D., and Norris, A. N., Nondestructive Testing, Proceedings of the 4th European Conference, J. M. Farley and R. W. Nichols, Eds., Vol. I, 1987, p. 163.
[46] Thompson, R. B., and Fiedler, C. J., Nondestructive Testing, Proceedings of the 4th European Conference, J. M. Farley and R. W. Nichols, Eds., Vol. I, 1987, p. 207.
[47] Visscher, W., Nondestructive Testing, Proceedings of the 4th European Conference, J. M. Farley and R. W. Nichols, Eds., Vol. I, 1987, p. 187.
[48] Teller, C. M., Barton, J. R., Matzkanin, G. A., Kusenberger, F. N., and Beissner R. E., *Journal of Engineering Materials and Technology*, Vol. 102, Jan. 1980, pp. 50–55.
[49] Thompson, R. B., Buck, O., and Thompson, D. O., *Journal of the Acoustics Society of America*, Vol. 59, No. 5, 1976, p. 1087.
[50] Ritchie, R. R., *Metal Science*, Aug./Sept. 1977, p. 368.
[51] London, B., *Review Science Instruments*, Vol. 56, No. 8, 1985, pp. 1632–1634.
[52] Leverant, G. R., Lander, B. S., Yuen, A., and Hopkins, S. W., *Metallurgical Transactions*, Vol. 10A, 1979, p. 251.
[53] Burck, L. H., Sullivan, C. P., and Wells, C. H., *Metallurgical Transactions*, Vol. 1, 1970, p. 1595.
[54] Morris, W. L., *Metallurgical Transactions*, Vol. 11A, 1980, p. 117.
[55] Morris, W. L., *Metallurgical Transactions*, Vol. 12A, 1981, p. 57.
[56] Larsen, J. M., Jira, J. R., and Weerasooriya, T., *Fracture Mechanics: Eighteenth Symposium, STP 945*, D. T. Read and R. P. Reed, Eds., American Society for Testing and Materials, Philadelphia, 1988, pp. 896–912.
[57] Harker, A. H., *Journal of Nondestructive Evaluation*, Vol. 4, No. 2, 1984, p. 9.

Richard Hertzberg,[1] *William A. Herman,*[2] *Thomas Clark,*[1] *and Robert Jaccard*[3]

Simulation of Short Crack and Other Low Closure Loading Conditions Utilizing Constant K_{max} ΔK-Decreasing Fatigue Crack Growth Procedures

REFERENCE: Hertzberg, R., Herman, W. A., Clark, T., and Jaccard, R., **"Simulation of Short Crack and Other Low Closure Loading Conditions Utilizing Constant K_{max} ΔK-Decreasing Fatigue Crack Growth Procedures,"** *Small-Crack Test Methods, ASTM STP 1149,* J. M. Larsen and J. E. Allison, Eds., American Society for Testing and Materials, 1992, pp. 197–220.

ABSTRACT: Small cracks can grow at ΔK levels previously thought safe (that is, $\Delta K < \Delta K_{th}$). It follows that ΔK_{th} values, measured according to ASTM Test Method for Measurements of Fatigue Crack Growth Rates (E 647) procedures and associated with long-crack test specimens, may lead to nonconservative lifetime estimates of a component that contains very small cracks. One major reason for this discrepancy may be traced to the fact that different closure levels are found at the same applied ΔK level for long and short cracks, respectively. Much effort has been given to the generation of conservative fatigue crack propagation (FCP) data through the development of large quantities of short-crack data. Unfortunately, the generation of these data are time-consuming, tedious, and subject to considerable amounts of scatter.

An alternative test method, based on the use of standard-sized samples and employing established automated data acquisition procedures, has been identified. This method is based on maintaining a constant maximum stress intensity level (K^c_{max}) during the ΔK-decreasing test procedure. By maintaining a constant K_{max} value, mean stress and associated R levels are found to increase markedly as ΔK decreases. The development of these high levels of mean stress and R ratios produces a long crack with negligible crack closure, which provides an upper bound estimate for the behavior of short cracks. K^c_{max} FCP data for several aluminum, iron, and nickel-based alloys have been generated and demonstrate the utility of the K^c_{max} test methodology as a simple and convenient means to obtain upper bound estimates of short-crack behavior in these structural alloy systems.

KEY WORDS: closure, fatigue crack propagation, life prediction, short cracks, threshold

Introduction

Most structural components experience some type of cyclic loading that often generates fatigue cracks. As these defects grow, the component's load-bearing capacity is diminished. If these cracks are not detected with appropriate nondestructive examination techniques, they can reach critical dimensions and result in catastrophic fracture. As a result, the ability

[1]New Jersey Zinc professor and research assistant, respectively, Department of Materials Science and Engineering, Lehigh University, Bethlehem, PA 18015.
[2]Lead engineer, General Dynamics Land Systems, Sterling Heights, MI.
[3]Senior scientist, Swiss Aluminum, Ltd., Zurich, Switzerland.

to accurately predict remaining fatigue lifetimes of damaged engineering components is of great importance. As such, damage tolerant design has become a widely used technique for predicting the service lifetime of engineering structures and components. Damage tolerance methodology utilizes fatigue crack propagation data in conjunction with the principles of linear elastic fracture mechanics (LEFM); furthermore, crack-tip similitude is assumed, which permits the use of laboratory-scale fatigue crack propagation (FCP) data to represent the fatigue behavior of full-scale structures. Similitude implies that different sized cracks will possess the same crack-tip plastic zone, stress, and strain distributions, and FCP rates, so long as the stress intensity factor is the same.

FCP data generated under conditions of decreasing stress intensity range at constant low R ratios (R^c) (Fig. 1*a*) can lead to overly optimistic estimates of component life [*1*,*2*]. This inability to accurately assess a component's service life can, to a large degree, be attributed to the generation of excessive amounts of crack closure in the threshold regime of laboratory tests [*3*]. Regardless of the operative closure mechanism, crack closure attenuates the stress intensity at the crack tip and results in a corresponding decrease in crack growth rates [*4–7*]. This difference between the applied and effective stress intensity factors is especially troublesome when laboratory FCP test data are utilized in damage tolerant designs because many frequently encountered service loading conditions involve crack growth under low, or greatly reduced, levels of crack closure. For example, cyclic loading in the presence of tensile residual stresses caused by welding [*8–12*], compressive load excursions caused by variable amplitude loadings [*13–16*], and the growth of physically short cracks [*17–25*] involve accelerated crack growth under conditions of greatly reduced crack closure. As a

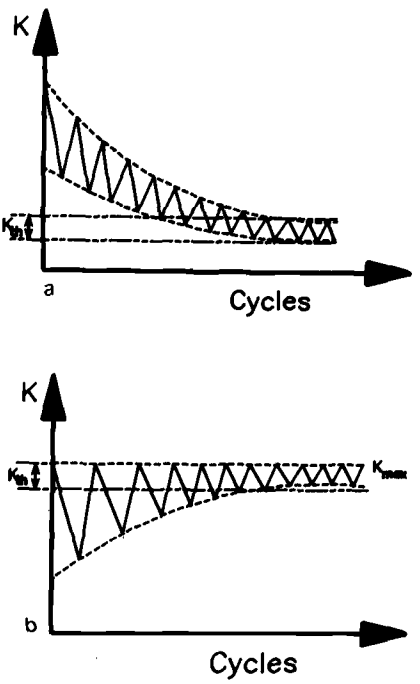

FIG. 1—*Schematic diagrams representing* ΔK*-decreasing threshold test methods:* (a) *constant* R*-ratio procedure* R^c *and* (b) *constant* K_{max} *test procedure* K^c_{max}.

result, conventional laboratory FCP data generated at low R ratios [*1*] must be corrected to account for low closure conditions typically seen in large structures [*6,26*].

While some attempts at correlating low closure FCP data to long crack ΔK_{eff} values have met with success [*27,28*], there is a large body of literature that indicates that precise and reproducible measurement of crack closure levels are difficult to achieve [*3,29–33*]. In fact, a recent ASTM round-robin study [*29*] reported that measured crack closure levels varied by a factor of five among different laboratory groups when both similar and different methods for measuring the opening stress intensity level K_{op} were utilized. Additionally, Donald [*32*] reported that even when a computerized "nulling" of the load-displacement signal is performed, closure measurements in the threshold regime are inherently subjective, therefore, unreliable. For example, Stofanak et al. [*3*] were unable to use ΔK_{eff} to rationalize FCP data at different R ratios near threshold, even though successful correlation was achieved at higher ΔK levels. More recently, Allison and You [*34*] studied the fatigue behavior of a silicon carbide (SiC) reinforced 2124 aluminum alloy, and determined that a unique ΔK_{eff} function could not be defined because of inconclusive measurements of crack closure levels.

Such uncertainties with closure measurements and associated ΔK_{eff} calculations make FCP data generated from conventional R^c test conditions inadequate for predicting crack growth when low closure loading conditions are experienced in structural components. Indeed, the recommended FCP ASTM Method for Measurements of Fatigue Crack Growth Rates (E 647) warns of the nonconservative nature of FCP data generated with low R ratio, ΔK-decreasing techniques.

Recent studies have shown that more conservative FCP data can be conveniently generated in the laboratory by conducting a long-crack ΔK-decreasing threshold test procedure in association with a constant maximum stress intensity level K^c_{max} (Fig. 1*b*) [*2,35–39*]. With this test method, ΔK decreases as the mean stress and R ratio continually increase; ultimately, closure-free long-crack FCP data are generated in the threshold regime (Fig. 2) [*2,36,39*]. As such, K^c_{max} FCP data in the ΔK_{th} regime provide a useful characterization of the crack propagation response of a material [*34,39,40*] in the absence of nominal levels of closure. These data then provide an upper bound measure of short crack response without dealing with the experimental scatter introduced by crack closure and short-crack measurements [*12,32,34,39*].

It is worth noting that during the course of the K^c_{max} ΔK-decreasing test procedure, crack closure levels gradually decrease as the crack lengthens and are observed to vanish as ΔK approaches the threshold regime. As such, these K^c_{max} data when viewed from the stand point of increasing ΔK conditions, describe crack closure conditions that parallel those associated with the normal growth of a "short" crack into a "long" crack. That is, the K^c_{max} data in the threshold regime typify the behavior of short cracks in that both involve crack growth under essentially closure-free conditions. As the crack lengthens, the associated crack wake generates micromechanisms thought responsible for the development of closure [*17–25*].

To be sure, the closure-free condition developed in the threshold regime of the K^c_{max} ΔK-decreasing test method can be matched by conducting an R^c test where R is equal to 0.8 or 0.9. Both the K^c_{max} ΔK-decreasing and high R ratio R^c test procedures generate a closure-free environment in the ΔK_{th} regime. The present authors maintain, however, that data obtained from the K^c_{max} ΔK-decreasing test methodology more realistically simulate the characteristics associated with the progression of a short crack to a long crack than that portrayed by a high-R R^c test procedure (see above). Furthermore, the K^c_{max} test procedure has the added advantage of reaching high R levels faster (up to four times) than possible by R^c test methods [*41*], which can be more difficult to conduct at extremely high R levels (R^c = 0.8 to 0.95).

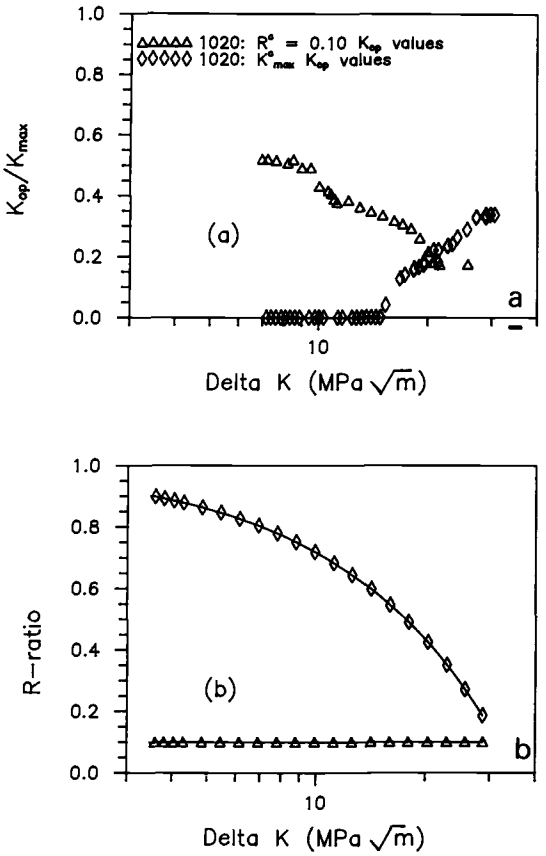

FIG. 2—*Variation of* (a) *crack closure levels and* (b) R-*ratio in 1020 steel during* K^c_{max} *and* R^c = *0.1* ΔK-*decreasing test procedures.*

When the FCP resistance for competitive materials are compared on the basis of low R^c versus K^c_{max} data, comparative rankings may change. To illustrate, consider the relative fatigue response of 2024-T3 and 2090-T8E41 aluminum alloys. The Al-Li-Cu-Zr 2090 alloy possesses attractively high low-R^c (R = 0.1) fatigue threshold behavior when compared with most other aluminum alloys [*25*,*42*]. This excellent long-crack fatigue response has been attributed to large closure levels associated with extensive amounts of crack tip shielding caused by crack deflection and crack wake asperity wedging [*42*]. As such, the R^c = 0.10 FCP data for 2090 show consistently superior resistance to FCP for all ΔK levels when compared to the more traditional 2024-T3 (Fig. 3*a*).

However, when the alloys are compared on the basis of K^c_{max} = 10 MPa·m$^{1/2}$ long-crack data, the FCP behavior of the two materials track together (Fig. 3*b*) over wide ranges of ΔK, especially in the near-threshold region. Figure 3*c* demonstrates the closure conditions present in each of the R^c = 0.1 tests. Note that the superior low R^c FCP results of 2090-T8E41 are due to an extrinsic crack closure effect; clearly, this apparent superiority is greatly reduced when the two materials are compared on the basis of K^c_{max} test results. The ramification of this finding is that 2024 and 2090 should behave similarly under low-closure service loading conditions, while low R^c laboratory tests would have anticipated much longer

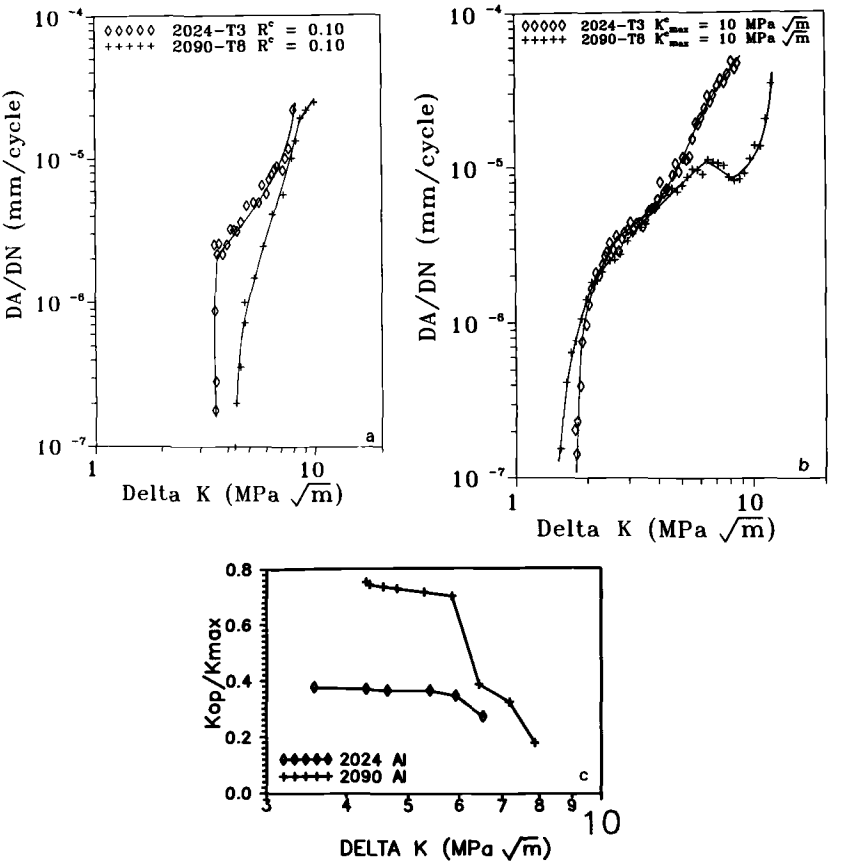

FIG. 3—*Comparison of FCP data for 2024-T3 and 2090-T8 aluminum:* (a) R^c = *0.1 data,* (b) K^c_{max} = *10.0 MPa* · $m^{1/2}$ [42], *and* (c) *closure information for* R^c = *0.1 tests* [39].

fatigue lifetimes for the aluminum-lithium (Al-Li) material. The reader must, therefore, identify the appropriate service conditions before utilizing certain laboratory data for predictive purposes.

Furthermore, Allison and You [*34*] have recently utilized K^c_{max} threshold test methods to define the intrinsic crack growth rates of SiC-reinforced aluminum alloys. Their study showed that the enhanced fatigue performance of these metal matrix composites, relative to unreinforced aluminum, was largely caused by the extrinsic effects of closure-related crack-tip shielding, rather than because of an intrinsic improvement in material properties. Additionally, Makhlouf and Jones [*40*] have recently shown that the increasing *R*-ratio, K^c_{max} FCP data obtained at 500°C provided an accurate indicator of the elevated temperature fatigue behavior for a 18%Cr-Nb ferritic stainless steel.

It follows that the use of K^c_{max} data in suitable lifetime calculations will result in conservative life predictions for engineering components that experience low-crack closure conditions [*2,3,16,39*]. Several examples of the application of K^c_{max} data for the prediction and simulation of component fatigue response under low-closure loading conditions are reviewed below.

Weldment Data

Tensile residual stresses generated during welding cause accelerated fatigue crack growth (especially in the threshold regime) because the high mean stress level at the crack tip effects a dramatic reduction of crack closure levels [*8–11*]. Consequently, fatigue life calculations, of welded components should be based on K^c_{max} rather than low R ratio data. Figure 4*a* [*12*] shows weld zone crack propagation data in JIS-42B steel from the work of Matsuoka [*9*], along with baseplate FCP data at $R^c = 0.1$ and $K^c_{max} = 35.2$ MPa · m$^{1/2}$ data for hot rolled 1020 steel [*41*]. It is clear that the $R^c = 0.1$ long crack data predicted none of the accelerated crack growth in the weld. In sharp contrast, the agreement between the closure-free weld zone crack growth data and the closure-free long crack K^c_{max} laboratory FCP data is excellent, with the two data sets tracking together at all stress intensity levels. It should be noted that while there are minor differences in composition and properties for the 1020 and JIS-SB42 steel alloys (Table 1), many steel alloys have been shown [*41*] to possess similar FCP behavior under K^c_{max} test conditions. Furthermore, the slight difference in low R ratio, long-crack threshold behavior (Fig. 4*a*) was expected since $R^c = 0.1$, ΔK-decreasing conditions were utilized for 1020 steel, while the baseplate FCP tests for JIS-SB42 steel were conducted at $R^c = 0.00$.

TABLE 1—*Comparison of 1020 steel and JIS-SB42 steel.*

	C	Mn	Si	Ni	Mo	V	Cr
1020 Hot Rolled Steel [**]	0.18-0.23	0.30-0.60	-	-	-	-	-
JIS-SB42 Steel [9]	0.17	0.81	0.19	0.01	0.001	0.001	0.02

	Yield Strength (MPa)	Ultimate Strength (MPa)	ΔK_{th} (MPa $\sqrt{m}$)
1020 Hot Rolled Steel [**]	210-240	390-410	8.25
JIS-SB42 Steel [9]	280	440	10.00

** *Metals Handbook, Desktop Edition (1986) ASM International, 1st edition.*

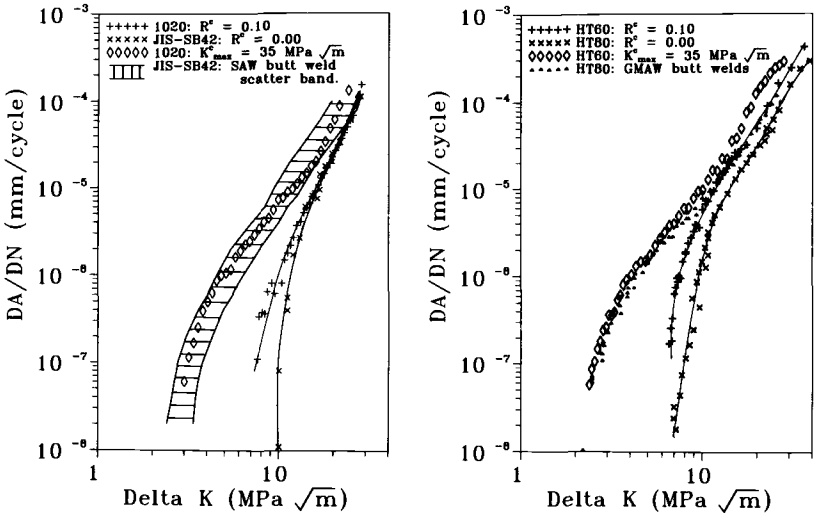

FIG. 4—*FCP data in weldments of similar steels with* $R^c = 0.1$ *data and* $K^c_{max} = 35$ *MPa* · *m*$^{1/2}$: (a) *SAW FCP results* [9] *and* (b) *GMAW FCP results* [8,12].

It should be noted that the uniformly high mean stress levels present in welded samples suggest that high-R R^c tests would provide a more realistic estimate of weld response than for the case of K^c_{max} data where R ratios are low at the beginning of the K^c_{max} test when ΔK levels are highest. At the same time, the reader should recognize that it is not possible to generate high R^c data in the intermediate and high ΔK regimes since K_{max} levels would exceed the material's fracture toughness. Since mean stress effects on FCP rates are not nearly as large at intermediate ΔK levels as in the threshold regime, the error in using an R increasing test method associated with K^c_{max}-decreasing test procedures is not considered to be of major consequence. Indeed, the correspondence of K^c_{max} test data with weld results (Fig. 4) is encouraging.

Further confirmation of the applicability of the K^c_{max} test procedures to account for the FCP response of weldments was found with data provided by Ohta [*8*] and Herman et al. [*41*]. Regardless of the welding process used (gas metal arc or submerged arc welding), inferior crack propagation behavior was seen in the weldments relative to the high-strength ferrite/pearlite HT80 baseplate. However, when Herman [*41*] compared the HT80 weld zone FCP data to baseplate K^c_{max} results for a slightly lower strength HT60 steel, the agreement was excellent (Fig. 4*b*).

Underloads and Negative R-*Ratio Tests*

Compressive load excursions of sufficient magnitude during service can crush oxide debris and asperities in the crack wake [*14,15*], thereby reducing the level of crack closure. It follows that low-closure K^c_{max} laboratory test data could provide an upper bound estimate of crack growth following damaging underloads. Indeed, Herman and Hertzberg [*12,16,41*] demonstrated that FCP data, generated under cyclic compression, were matched by K^c_{max} threshold test data. As seen in Fig. 5, K^c_{max} data for a 7075-T6 aluminum alloy lie at the upper limit of the 7475-T6 scatter band corresponding to a compressive precracking test procedure [*43,44*].

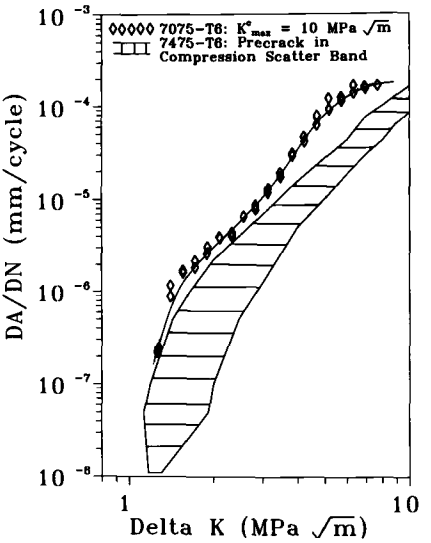

FIG. 5—*Comparison of* K^c_{max} ΔK-*decreasing FCP data for 7075-T6 with "precrack in compression" results for 7475-T6* [43,44].

Furthermore, K^c_{max} test data provide an upper bound for negative R ratio test results. Figure 6 demonstrates that as R becomes more negative, the curves shift to the left. This behavior is due to the crushing of the asperities by the high negative loads in the crack wake. The K^c_{max} = 10 curve provides an ultra conservative bound of FCP response in this material and reflects the likelihood that closure was not completely removed under R = −2 conditions. Note that at high ΔK levels, where closure has less of an influence on growth rates, the R^c = −2 and R^c = 0.1 curves come together as predicted by the present ASTM standard.

Short Crack

Since closure levels associated with short-crack growth are generally low, if not negligible [*27,28,45*], the data should be in agreement with any long-crack database associated with low-closure levels. While some success has been reported with the correlation of short-crack FCP data on the basis of long-crack ΔK_{eff} values [*25*], a more straightforward and reproducible simulation of short-crack behavior can be obtained by referring to low-closure long-crack fatigue data such as that provided by K^c_{max} test methods. Bolingbroke and King [*46*] as well as McCarver and Ritchie [*47*] demonstrated that long-crack samples tested at high R ratios displayed similar growth characteristics to physically short cracks. Their observations are not surprising, and are directly related to the absence of crack closure in both instances. This paper will demonstrate that data for short cracks and other low-closure loading conditions can be conservatively bound by long-crack test results when the latter are generated under constant K^c_{max} testing conditions.

Towards this end, K^c_{max} long crack data will be compared to short-crack growth rates for four different grades of aluminum, five different types of steel, and a hot isostatically pressed nickel based superalloy (Astroloy). Tables 2 and 3 detail the compositional and heat treatment information for these alloys. Attention will also be given to certain short crack test conditions for which K^c_{max} test methods do not adequately simulate short-crack behavior.

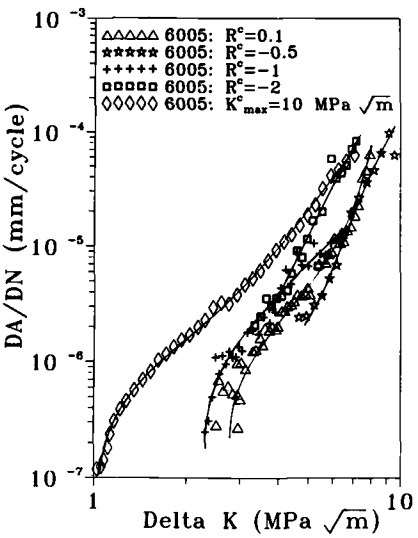

FIG. 6—*Comparison of* R^c = *0.1 data and* K^c_{max} = *10 MPa* · $m^{1/2}$ *test data to* R^c = −*0.1,* −*1, and* −*2 results. Note that* ΔK *values are based solely on the positive portion of the loading cycle.*

TABLE 2—*Chemical compositions and heat treatments for ferrous alloys.*

	C	Mn	P	S	Cr	Ni	Si	Mo	Fe
4130 [**]	0.25-0.33	0.40-0.60	-	-	0.80-1.10	-	-	0.15-0.25	bal
1020 [**]	0.18-0.23	0.30-0.60	-	-	-	-	-	-	bal
S10C [61]	0.11	0.38	0.019	0.013	-	-	0.20	-	bal
HT60 [61]	0.09	1.67	0.004	0.019	-	-	0.25	-	bal
304SS [63]	0.06	2.0	0.045	0.030	18.07	8.55	1.0	-	bal

4130 Steel (Q&T) - (1) Normalize 30 min. @ 870 C.
(2) Air cool.
(3) Austenize 30 min. @ 600 C.
(4) Oil quench.
(5) Temper 60 min. @ 600 C.
1020 Steel - As hot rolled.
S10C Steel (Fine grain) - (1) Normalize 60 min @ 900 C.
(2) Air cool.
S10C Steel (Coarse grain) - (1) Anneal 4 hrs. @ 1100 C.
(2) Air cool.
HT60 Steel - As received (normalized)

** - *Metals Handbook, Desktop Edition (1986) ASM International, 1st edition.*

TABLE 3—*Chemical compositions and heat treatments for nonferrous alloys.*

Alloy	Condition	Fe	Cu	Mn	Si	Mg	Zn	Cr	Li	Al
2014-T3	[**] ROLLED	-	0.40	0.60	-	1.50	-	-	-	bal
2090-T8E41	[41] ROLLED	0.02	2.86	0.005	0.01	0.01	-	-	2.05	bal
7075-T6	[**] ROLLED	-	1.60	-	-	2.50	5.60	0.23	-	bal
AA6005-T6	[+] EXTRUDED	0.21	0.17	0.03	0.63	0.54	0.08	0.11	-	bal

		Co	Cr	Mo	Al	Ti	Fe	W	Cu	Ni
Astroloy	[53]	16.98	14.80	5.07	3.99	3.58	0.21	0.01	0.01	bal

Heat Treatment for Astroloy:
(1) Hot isostatic pressing for 2 hrs. @ 1107 C.
(2) Solution treat for 2 hrs. @ 1121 C.
(3) Age for 24 hrs. @ 650 C.

** *Hatch, J.E., ed. (1980) Aluminum: Properties and Physical Metallurgy, ASM, Metals Park, OH.*

+ *Jaccard, R., Technical Data Sheets, Swiss Aluminum, Ltd.*

Experimental Procedures and Associated Discussion

All ΔK-decreasing threshold tests were conducted at ambient conditions under computer control using an Instron Corporation servo-hydraulic automated test system interfaced with either an Instron-supplied DEC PDP1123 or an IBM XT computer obtained by Fracture Technology Associates. In most cases, a minimum of two tests were conducted for each long-crack test condition in order to ensure reproducibility of results. Table 4 demonstrates that the amount of scatter (scatter factor = maximum growth rate at given ΔK/minimum growth rate at given ΔK) for these K^c_{max} tests is acceptable. The applied stress intensity range was controlled according to the following equation for both constant R (R^c) [*1*] and constant K_{max} (K^c_{max}) test conditions [*1,2,35,36*]

TABLE 4—*Degree of scatter (maximum observed growth rate/minimum observed growth rate for a given ΔK) in growth rates for K^c_{max} tests.*

Material	Factor of Scatter
2090 Al	1 to 1.5
2024 Al	1.1 to 1.9
6005 Al	1.2 to 1.6
1020 steel	1 to 1.1
4130 steel	1.1

$$\Delta K_i = \Delta K_o * (\exp(C(a_f - a_i)))$$

where

K_i = instantaneous stress intensity,
K_o = initial stress intensity,
a_i = initial crack length,
a_f = final crack length, and
C = stress intensity factor gradient, $(1/K) * (dK/da)$.

Fatigue threshold tests were performed for all of the following materials under $R^c = 0.10$ (Fig. 1*a*) and K^c_{max} (Fig. 1*b*) test conditions:

- coarse and fine grained S10C steel
- fine grained HT60 steel
- 1020 hot rolled steel
- 304 stainless steel
- 2024-T3 aluminum
- 7075-T6 aluminum
- 2090-T8 aluminum-lithium

All $R^c = 0.1$ tests were performed with a stress intensity factor gradient of -0.06 or -0.10 mm^{-1}, while a gradient of -0.20 mm^{-1} was utilized for the K^c_{max} tests. Higher gradients than that suggested by ASTM E 647 (-0.08 mm^{-1}) are allowable for K^c_{max} tests because load interaction effects are eliminated because of the fact that the monotonic plastic zone size remains constant throughout the ΔK-decreasing procedure. As such, K^c_{max} tests can be completed much more rapidly than that prescribed by the present ASTM E 647. K^c_{max} tests should then reduce the cost of FCP data acquisition, especially as it relates to the generation of data that represent an upper bound for short crack response. Figure 7*a* [*39*] illustrates the results of three experiments performed on the same specimen at load-shedding gradients that are all higher than the limit recommended by E 647 and, in one case, as much as five times greater than that recommended by E 647. The data are in excellent agreement and demonstrate for at least the steel alloy studied, the FCP rates under K^c_{max} test conditions are independent of K-gradient. Note that the -0.40 mm^{-1} data base extends only to 2×10^{-6} mm/cycle. This truncation in test results is attributed to the absence of available unbroken specimen ligament since the $C = -0.4$ mm^{-1} test was the third test performed on this specimen. Additional test results for 2024-T3 aluminum alloy are shown in Fig. 7*b* and demonstrate again the insensitivity of K-gradient on FCP data acquired with the K^c_{max} test procedure. In this instance, K-gradients extended from -0.06 to -0.2 mm^{-1}. Three

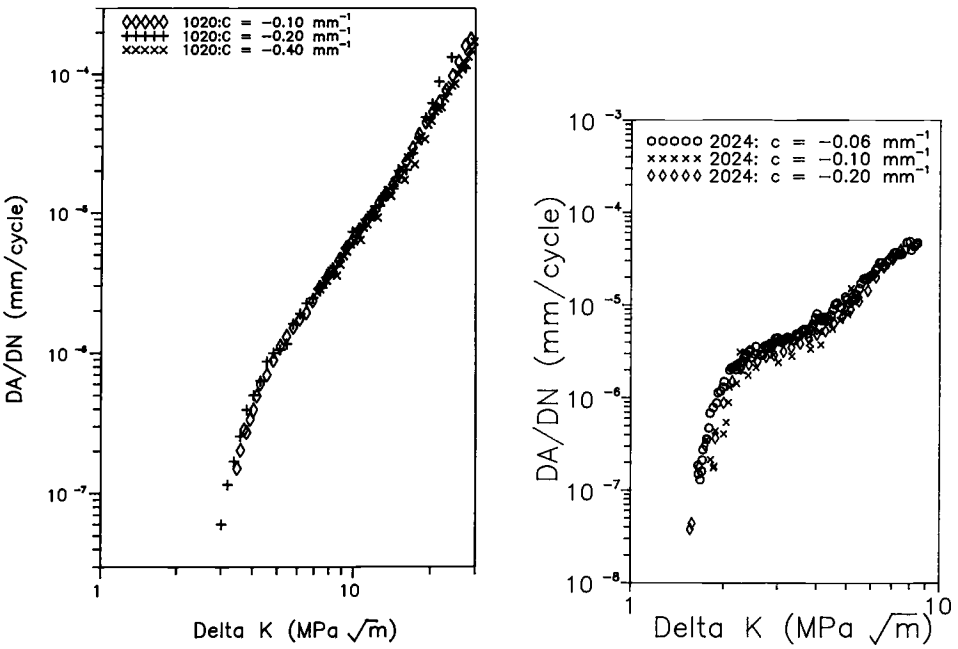

FIG. 7—*Constancy of crack growth data obtained from:* (a) *1020 steel* [39] *and* (b) *2024 aluminum using various* K*-gradients. Note absence of meaningful scatter in test results.*

separate test specimens were used with FCP rates observed in the 10^{-7} mm/cycle regime in each instance. The authors anticipate that similar agreement would be expected with other materials and at still higher K-gradients. Additional studies are needed to determine the limiting K-gradient wherein meaningful FCP data may be generated.

K^c_{max} tests were conducted at K_{max} values of 35.2, 55.0, and 10.0 MPa · $m^{1/2}$ for the steel, nickel, and aluminum samples, respectively. These particular K^c_{max} levels were chosen to ensure that measurable amounts of crack closure would be eliminated before the point where crack growth rates entered the threshold region. Depending on the K^c_{max} level chosen closure exhibited by the material as a result of differences in microstructure (such as grain size) may or may not account for ΔK_{eff} conditions that simulate what the short crack experiences.

Doker and Bachmann have shown that the ΔK_{th} value varies with the value of K^c_{max} used in the K^c_{max}-decreasing test procedure (for example, see Fig. 8*a*) [*48*]. Note that above a certain K_{max} level, there is little change in the ΔK_{th}, even up to very high K_{max} values [*49*,*50*]. Similar findings by the present authors for an aluminum alloy tested over a range of K_{max} values from 4 to 20 MPa · $m^{1/2}$ are shown in Fig. 8*b*. Depending on the level of closure exhibited by a given material, FCP data (especially in the ΔK_{th} regime) would differ by varying degrees when compared on the basis of $R^c = 0.1$ and different K^c_{max} test conditions. The "best" K^c_{max} test condition to use for the generation of FCP data needed for component life prediction remains a somewhat elusive target. The K^c_{max} values chosen for the iron, nickel, and aluminum based alloys examined in this study (35.2, 55, and 10 MPa · $m^{1/2}$, respectively), provide a database that serves as an upper bound for the majority of short-crack data in each instance. As such, these K^c_{max} values represent good educated guesses of the important K^c_{max} test variable. The reader should note that these values may not apply for all materials. For example, Jaccard reported a better simulation of S-N curves, based

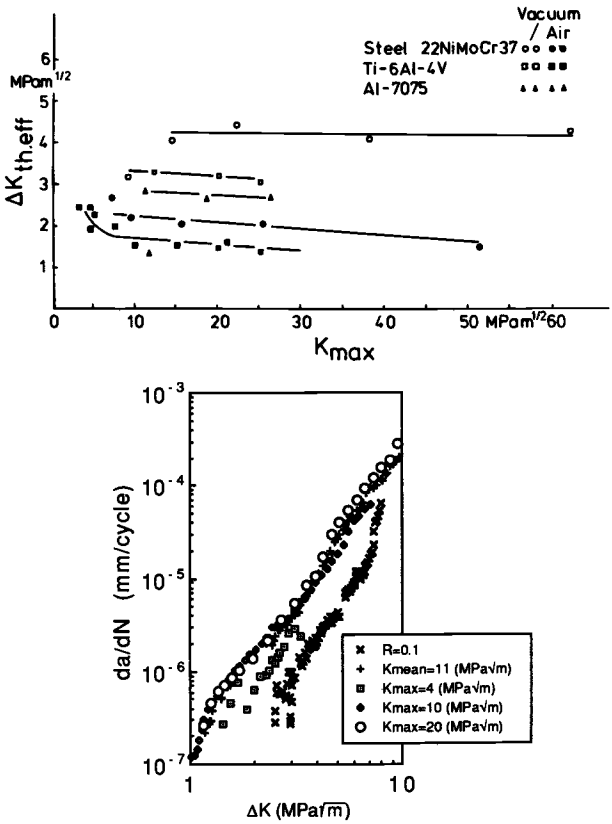

FIG. 8—*The effect of* K_{max} *level on fatigue behavior:* (a) ΔK_{th} *of different materials in air and in vacuum* [48] *and* (b) *FCP data at near threshold conditions for 6005 aluminum.*

on FCP-based life calculations with K^c_{max} values of 6.67 and 10 MPa · $m^{1/2}$ for two different aluminum alloys, respectively [*51*,*52*]. Based on our current understanding of the K^c_{max} test procedure, some additional information is needed for the selection of the "best" K^c_{max} value to use. Two such data bases include actual short-crack data and S-N information. Two applications of S-N data to determine the appropriate FCP data for use in life prediction is discussed below. Clearly, additional studies aimed at the establishment of suitable K^c_{max} levels for a given alloy is indicated.

The long-crack fatigue data generated in this study were obtained with the wedge opening load (WOL) or disk compact tension (DCT) sample configuration [*53*] with cracks propagating in the LT orientation [*54*]. The authors do not believe that specimen geometry will influence the data acquired since all tests under both R^c and K^c_{max} were generated under fixed K-gradients imposed by computer-controlled test conditions. Crack length was determined using compliance techniques in conjunction with a crack mouth COD gage along with periodic visual observations of the crack tip to verify the accuracy of the computer-calculated compliance values. Crack closure levels were monitored throughout the course of all ΔK-decreasing procedures, either through visual observation of a canceled load-displacement trace (generated by signal nulling) or with a computerized closure routine provided with the FTA automated test system [*32*]. Growth rate information (*da/dN*) was calculated using a modified secant technique [*1*].

Results and Discussion

A typical example of the nonconservative nature of low R-ratio FCP data, when compared to short-crack growth at the same ΔK levels, is portrayed in Fig. 9. Standard $R^c = 0.1$, ΔK-decreasing FCP data for commercial grade 7075-T6 aluminum are plotted together with short-crack FCP data taken from various sources in the literature [*19,55–57*]. Note that significant short-crack growth occurs at stress intensities below the long-crack threshold, and at considerably higher rates than the long crack, low R^c data. Clearly, utilization of low R ratio, ΔK_{app} data for lifetime calculations would not anticipate the accelerated crack growth associated with short crack behavior.

Previous studies by Herman and Hertzberg [*12,16,37,39*] addressed this problem and demonstrated that low-closure K^c_{max} threshold test procedures can, to a large extent, provide a conservative upper bound for the FCP behavior of physically short cracks in a wide variety of engineering materials. For all cases, the K^c_{max} curve tracked at or near the upper bound of the short-crack growth scatter band, whereas the $R^c = 0.1$ curve typically characterized the lower bound of the short-crack growth rate data.

In a separate analysis, the authors attempted to predict the S-N curve for 6082 aluminum alloy weldments, based on $R^c = 0.1$ and K^c_{max} databases. The starting assumption was made that the same semi-elliptical flow existed in test specimens corresponding to the shortest lifetime at each stress level. Starting with a calibration point of an applied stress range of 38 MPa, in association with a cyclic lifetime of 3 600 000 cycles (an actual data point), the "presumed" crack size was calculated from the integration procedure, based on K^c_{max} and R^c data, respectively.

For the case of the K^c_{max} computation, A and m values from the Paris relation were determined from the K^c_{max} – FCP database along with the appropriate R^c branch at higher ΔK levels [*39,51,52*]. The computed crack depth of 0.17 mm was judged to be reasonable for these specimens and corresponds to the observed incidence of grain boundary separation in association with grain boundary inclusions. The grain size of this alloy is on the order of 200 μm. The computer crack size was then used to calculate specimen fatigue life at all

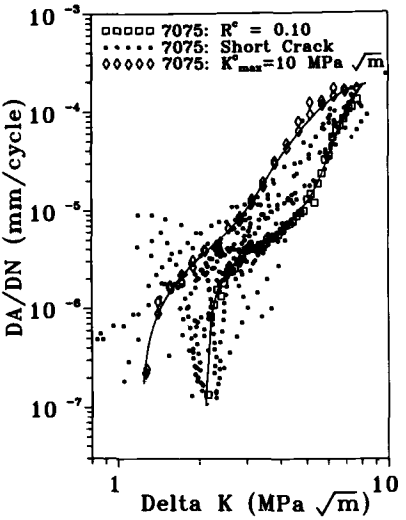

FIG. 9—*Comparison of short-crack data to* $R^c = 0.1$ *and* K^c_{max} *long-crack FCP data for 7075-T6 aluminum* [19,55–57].

additional stress levels from S-N database. The results of this analysis are shown in Fig. 10*a*. The computed S-N curve shows excellent prediction of the lower bound of the S-N database. If one uses the same computed crack size (that is, 0.17 mm) and repeats these life calculations with A and m values corresponding to the $R^c = 0.1$ database, the predicted S-N curve is shifted to much long lifetimes, which are nonconservative, relative to actual data points (Fig. 10*a*).

Alternatively, if the computation procedure is reversed and the calculated crack size based on the $R^c = 0.1$ database, a crack depth of 2.65 mm is determined. Based on practical experience, this calculated crack size is considered to be unrealistically large. When this crack dimension (2.65 mm) is used with the $R^c = 0.1$ database to compute the remaining portion of the S-N plot, the predicted S-N curve represents a conservative estimate for the actual lifetimes recorded (Fig. 10*b*). This finding is not surprising when one considers the large crack used in these calculations. Indeed, when K^c_{max} data are used along with the computed 2.65 mm crack, the calculated S-N curve falls further from the actual database and is more conservative than the plot based on R^c data.

A second S-N simulation was performed with data from aluminum alloy 6005, and the results are shown in Fig. 10*c* and *d*. Again, the K^c_{max}-based S-N simulation provided a better conservative bound of the actual S-N data than for the case of the $R^c = 0.1$ computations. Also, the calculated crack size (129 μm), based on the K^c_{max} calibration, was found to be physically reasonable, whereas the $R^c = 0.1$ based crack size (3.15 mm) was found to be unrealistically large.

To summarize, the K^c_{max}-based calculation leads to a more realistic estimate of presumed crack size, generates an S-N curve that corresponds to the lower bound of the actual S-N data base, and consistently predicts more conservative life estimates then for the case of R^c-based calculations.

Figure 11*a* compares the short-crack results of Vecchio [*58*], Brown et al. [*59*], Brown and Hicks [*60*], and Soniak and Remy [*24,61*] for fine grained Astroloy nickel alloy generated under conditions of $R^c = 0.1$ with two sets of long crack threshold data corresponding to $R^c = 0.1$ and K^c_{max} 55.0 MPa · $m^{1/2}$. Clearly, the K^c_{max} database tracks through most of the short crack data, whereas the R^c curve falls to the right of all short-crack data points. In view of the long-crack results, the nonconservative value of the low R ratio threshold (18.0 MPa · $m^{1/2}$) is contrasted with the value of 8.5 MPa · $m^{1/2}$, corresponding to the constant K_{max} results. As such, an unrealistically long fatigue lifetime would have been computed for an Astroloy component that contains a short crack, were one to have assigned a value of 18 MPa · $m^{1/2}$ for ΔK_{th}.

A similar comparison was made between long- and short-crack data for 2024-T3 [*22,23,62,63*] and 2090-T8E41 [*25,42*] aluminum alloys (Figs. 11*b* through *c*). As expected, at any ΔK level, crack growth rates associated with K^c_{max} tests represented an upper bound for 73–85% (as compared to 18–40% with $R^c = 0.1$ long crack data) of the existing short crack growth information, regardless of the test methods and specimens utilized for collection of the short-crack data.

It should be noted that the relatively larger degree of scatter associated with the 2024-T3 and 2090-T8E41 short-crack data sets can be rationalized in terms of the existence of microstructurally small cracks during short-crack testing; under these conditions, short-crack growth correlations to ΔK are likely to be invalid.

Similar comparisons of K^c_{max} and short-crack data obtained from the literature were made for a quenched and tempered (Q&T) 4130 steel [*21*], three types of ferritic/pearlitic steels [*20,64–67*], which were heat treated to different strength levels, and a 304 stainless steel alloy [*68*]. For the case of the hot rolled 1020, Q&T 4130, and 304 stainless steels, the long-crack K^c_{max} data once again provide a reasonable upper bound for most of the short-crack

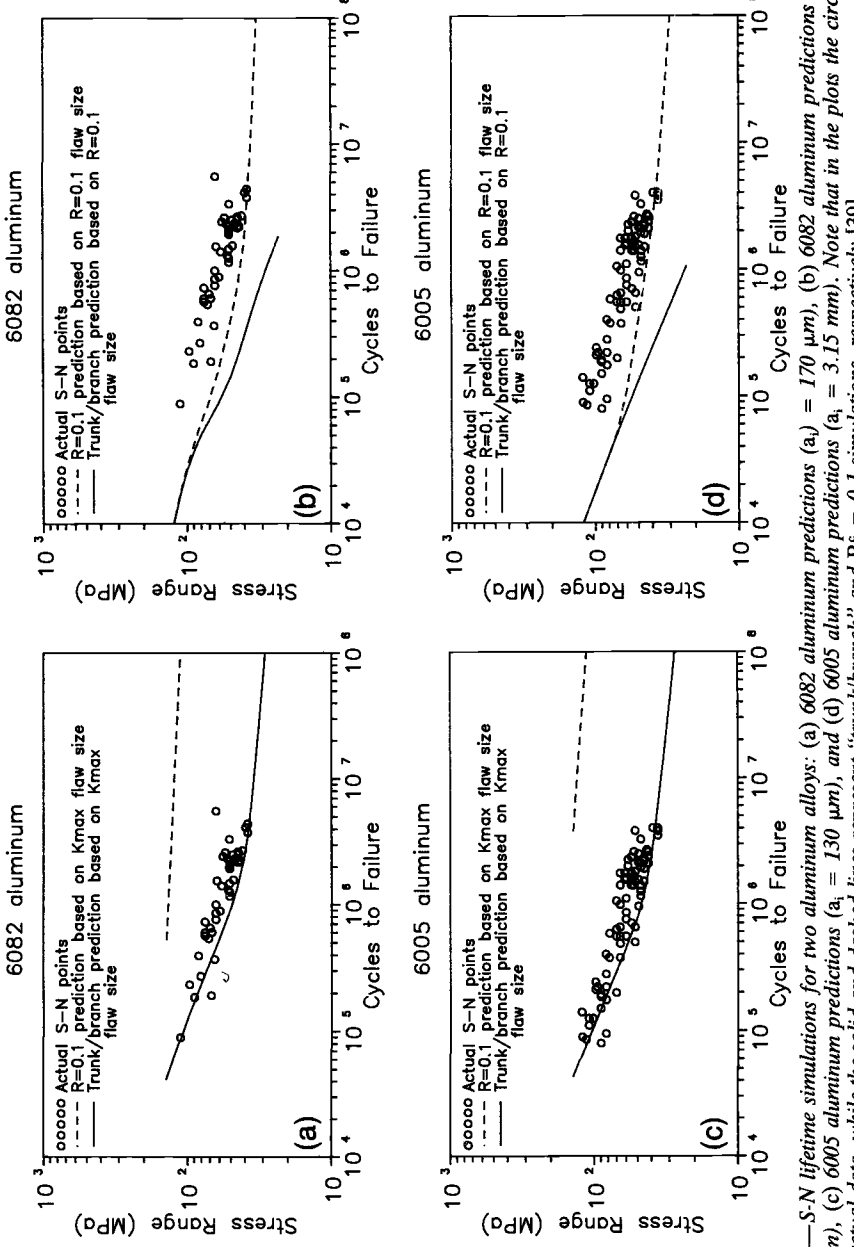

FIG. 10—*S-N lifetime simulations for two aluminum alloys:* (a) *6082 aluminum predictions* (a_i) = *170 μm*), (b) *6082 aluminum predictions* (a_i = *2.65 mm*), (c) *6005 aluminum predictions* (a_i = *130 μm*), *and* (d) *6005 aluminum predictions* (a_i = *3.15 mm*). *Note that in the plots the circles represent actual data, while the solid and dashed lines represent "trunk/branch" and* R^c = *0.1 simulations, respectively* [39].

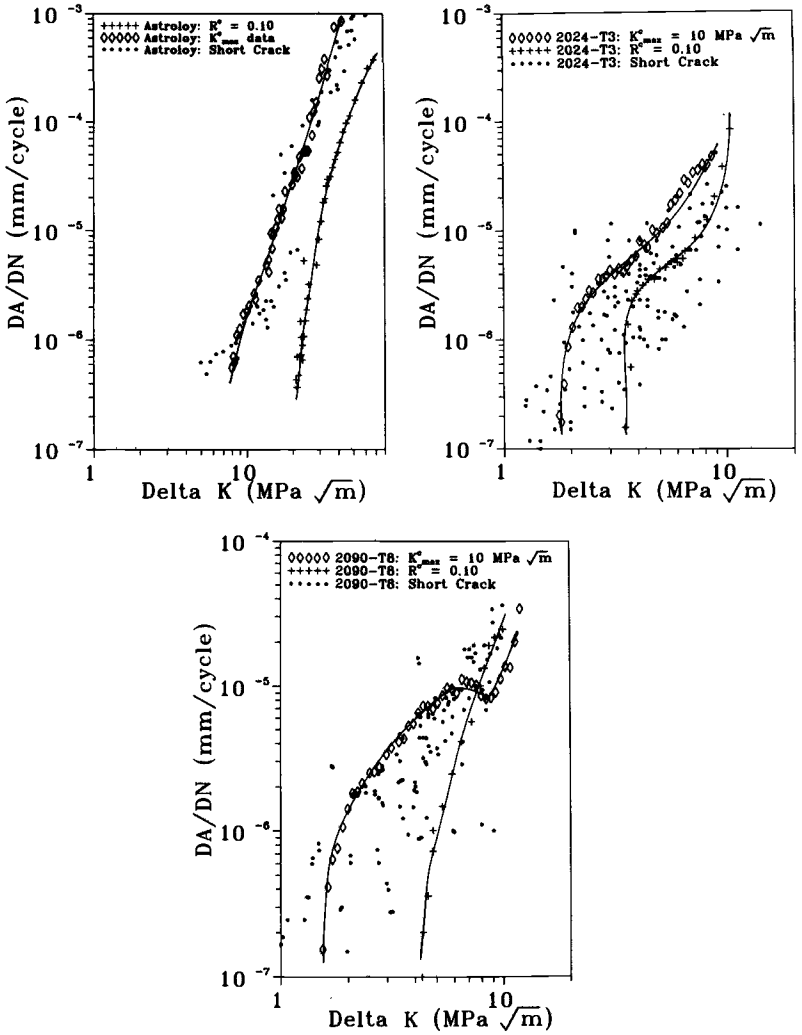

FIG. 11—*Comparison of short-crack data to* $R_c = 0.1$ *and* K^c_{max} *long-crack FCP results:* (a) *Astroloy nickel alloy* [24,58–61], (b) *2024-T3 aluminum* [22,23,62,63], *and* (c) *2090-T8 aluminum* [25,42].

database (Fig. 12*a* through *c*). As was the case with the aluminum alloys, the $R^c = 0.1$ curve provides only a nonconservative, lower bound for the short-crack data. Some of the near threshold points that fall outside of the K^c_{max} data set at low ΔK levels again may correspond to microstructurally small-crack growth, for which the use of ΔK in data analysis is suspicious because of obvious violations of continuum mechanics and similitude. The authors recognize the unsatisfactory circumstance wherein they possess no a priori knowledge as to whether a given short-crack datum is amenable to LEFM analysis. As such, we accept the weight of evidence as confirming that the K^c_{max} database represents an upper bound for most short crack results. At present, the authors are unaware of an alternative non-LEFM methodology that can conservatively account for the majority of short-crack data.

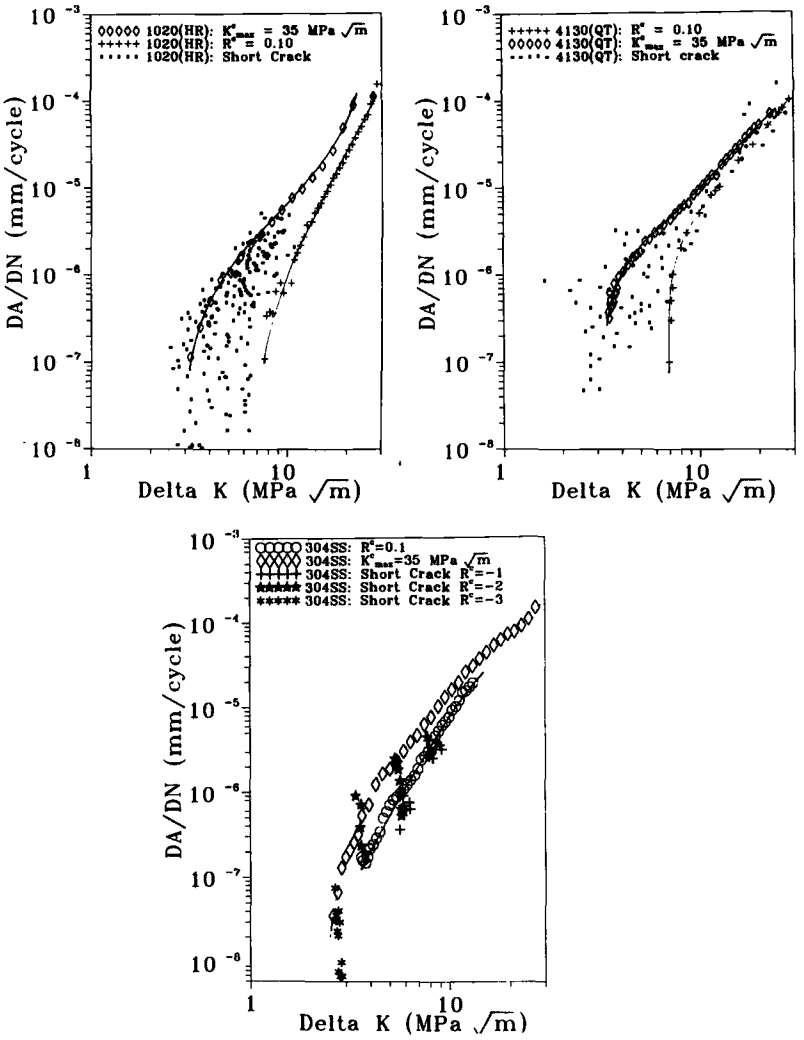

FIG. 12—*Short-crack data compared with* $R^c = 0.1$ *and* $K^c_{max} = 35.2\ MPa \cdot m^{1/2}$ *test results:* (a) *1020 hot rolled steel* [20], (b) *4130 quenched and tempered steel* [21], *and* (c) *304 stainless steel* [68].

Short-crack data for the coarse and fine grained S10C [*66*] steel, as well as the HT60 [*67*] materials appear to show a much poorer correlation with the corresponding long crack K^c_{max} data (Fig. 13*a* through *c*). However, when the bending stresses applied to the S10C steel during short-crack testing (310, 240, and 180 MPa) [*66*] are compared to the bulk yield strengths of the coarse grain, fine grain S10C steel samples (233 and 286 MPa, respectively), it is apparent that much of the short-crack data were generated at stress levels exceeding the material's bulk yield point. Consequently, the samples did not behave as an elastic continuum, and LEFM principles were clearly violated. As such, short-crack test data generated under these conditions cannot fairly be compared to the K^c_{max} FCP data. When the questionable short-crack data sets are removed, a much stronger correlation between the

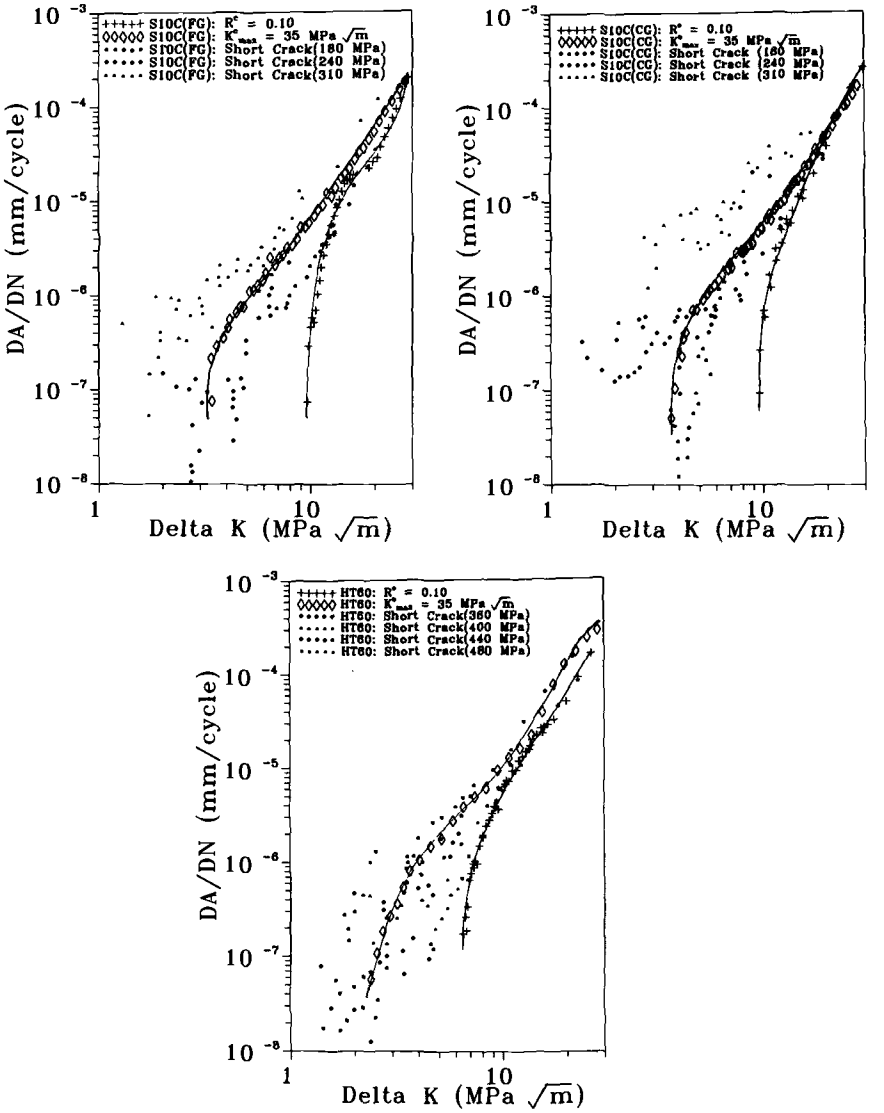

FIG. 13—*Comparison of short crack data to* $R^c = 0.1$ *and* $K^c_{max} = 35.2\ MPa \cdot m^{1/2}$: (a) *fine grained S10C steel* [66], (b) *coarse grained S10C steel* [66], *and* (c) *HT60 steel* [67]. *Note that numerous data points fall beyond* K^c_{max} *trend line.*

short crack, and K^c_{max} FCP data for both grain sizes of S10C steel is seen (Fig. 14*a* and *b*). Similarly, for the HT60 (YP = 510 MPa) [*67*], removal of the highest applied bending stress short-crack data result in a much better correlation between the short-crack FCP data and the K^c_{max} results for the material (Fig. 14*c*).

Note the extreme scatter that is generally associated with short-crack test results; up to a two-order of magnitude difference in growth rates is seen at any given ΔK level. This amount of experimental variability is consistent with the stochastic nature of short-crack growth, and with the inherent experimental difficulties in accurately measuring short-crack

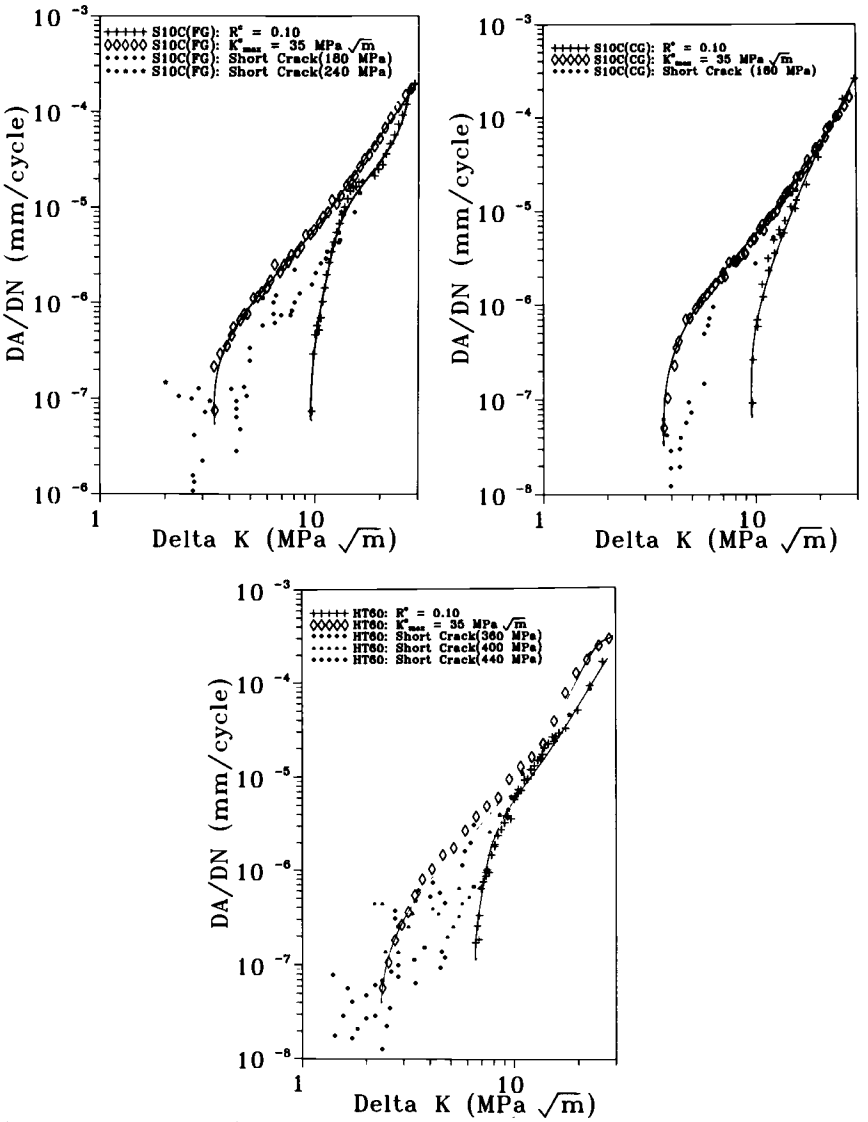

FIG. 14—*Same as Fig. 13, but without short crack data obtained at stresses above* σ_{ys}: (a) *fine grained S10C steel,* (b) *coarse grained S10C steel, and* (c) *HT60 steel. Note improved correlation.*

growth [*21,28,45,55,63*]. The inability to accurately and reproducibly characterize short-crack growth underscores the utility of the K^c_{max} threshold procedure as an effective tool for determining component life and for providing an upper bound of short-crack results [*39,51,52*].

In many of the previous examples, the low-closure K^c_{max} data were unable to account for short-crack growth that involved microstructurally short cracks and cracks propagating under applied stresses close to or exceeding the bulk yield point. This should not be viewed as a shortcoming of the K^c_{max} test procedure. Rather, it relates to the limitations of linear elastic fracture mechanics to adequately describe the crack driving force for microstructurally short

cracks, and in samples that experience applied stresses near or above yield. For these cases, the stress intensity factor cannot properly define the crack-tip stress state [*69*]. Rather, it may be advantageous to utilize other parameters, such as the J integral or strain energy density, to describe conditions at the crack tip. Vecchio [*58*] and Vecchio and Hertzberg [*70*], for example, found good agreement between short- and long-crack FCP data for Astroloy nickel alloy when both long- and short-crack growth rate data were plotted versus the strain energy density ΔS.

Advantages of K^c_{max} Test Procedure

1. It provides for rapid determination of FCP data since larger K-gradients can be used than that recommended by ASTM E 647. This leads to a reduction in testing time and test material.
2. It provides an efficient method of generating closure-free FCP data especially in the ΔK_{th} regime. As such, it provides a convenient method by which ΔK_{eff} may be estimated.
3. It provides an easier method for the generation of FCP data at high R ratios than for the case of high R R^c tests.
4. It provides an upper (conservative) bound estimate of FCP behavior in situations involving low levels of crack closure. These include short cracks, components possessing tensile residual stresses, and components that experience compressive underloads.
5. With the appropriate K^c_{max} database, conservative component lifetime estimations can be obtained.

Disadvantages

1. One cannot, at present, choose a priori the appropriate K^c_{max} value to generate an upper (conservative) bound for short-crack data or predict component lifetimes. In some instances, the chosen K^c_{max} values may prove to be too conservative relative to the body of short-crack data. Further studies are needed to identify necessary calibration procedures. These may include the use of existing S-N data, selective use of short-crack and closure information, or other, as yet, undefined methods. The authors recommend that methods to determine the target K^c_{max} value be developed in order to minimize the generation of short-crack data since the latter are very time consuming, labor intensive, and expensive to generate.
2. The methods cannot fully account for short-crack growth under conditions that violate the principles of LEFM. In this situation, J integral or strain energy density analyses may apply. Alternatively, total life may need to be addressed from the standpoint of quantifying an initiation period involving the development of a crack of some size, using ASTM Recommended Practice for Constant-Amplitude Low-Cycle Fatigue Testing (E 606), and adding that life estimate to the life estimate of the propagation stage, based on LEFM integration methods. For this integration, K^c_{max} data are suggested since the latter reflect changing crack closure conditions as the initiated crack grows to be a long crack.

Conclusions

1. The long-crack K^c_{max} test procedure is capable of adequately predicting accelerated FCP rates in low-closure loading situations associated with tensile residual stresses due to welding, compressive underloads, and growth of short cracks. As such, FCP data

derived from constant K_{max}, ΔK-decreasing test methods K^c_{max} can provide a conservative assessment of the fatigue life of engineering components.

2. Since the K^c_{max} procedure involves the development of high R-ratios and the elimination of globally measured crack closure in the threshold regime, a realistic assessment of the intrinsic FCP resistance of a given material can be obtained with enhanced accuracy and speed. As such, the resulting K^c_{max} database can be interpreted as a nominally "closure-free" measure of the *effective* stress intensity.
3. The K^c_{max} test methodology may reduce the need to generate actual "short-crack" data, thereby resulting in a substantial reduction in testing time and associated costs. It should be recognized, however, that while K^c_{max} data can provide a conservative upper bound for most short-crack growth data, the method may not fully account for short-crack growth that occurs under conditions that violate the principles of LEFM; these include, cracks that are short relative to microstructural features, and short cracks that experience applied stresses close to or exceeding the material's yield point. For both of these cases, crack growth similitude breaks down and LEFM correlation parameters are suspect. Further studies are necessary to define an adequate parameter, which can describe short-crack growth when ΔK no longer can be utilized.
4. The decision to use a specific R^c or K^c_{max} value in life prediction should be made on a case by case basis, and determined from the prevailing service conditions. In some instances life predictions based solely on K^c_{max} data may indeed provide an overly conservative lifetime. Correspondingly, life predictions based on $R^c = 0.1$ data may prove to be nonconservative.
5. While identical threshold conditions (that is, comparable ΔK and R ratios) can be obtained with either K^c_{max} or high R^c test methods, the K^c_{max} test procedure has a definite advantage over the R^c procedure in terms of relative testing ease and speed.

Acknowledgments

The authors would like to acknowledge the financial support of the Swiss Aluminum Company. Mr. Eugene Kozma is also acknowledged for his assistance in maintaining the operational readiness of the Instron servo-hydraulic machines. Finally, Regina Kline's aid in preparing this manuscript is greatly appreciated.

References

[1] ASTM Specification E647-86a, "Test Method for Measurement of Fatigue Crack Growth Rates," *1986 Annual Book of ASTM Standards*, American Society for Testing and Materials, Philadelphia, 1986.

[2] Herman, W. A., et al., "A Re-evaluation of Fatigue Threshold Test Methods," *Fatigue 87*, EMAS Ltd., Vol. 2, 1987, p. 819.

[3] Stofanak, R. J. et al, "On the Cyclic Behavior of Cast & Extruded Aluminum Alloys: Part A—Fatigue Crack Propagation," *Engineering Fracture Mechanics*, Vol. 17, No. 6, 1983, p. 527.

[4] Elber, W., "The Significance of Crack Closure," *Damage Tolerance in Aircraft Structures*, STP 486, American Society for Testing and Materials, Philadelphia, 1971, p. 230.

[5] Ritchie, R. O. and Suresh, S., "Some Considerations on Fatigue Crack Closure at Near-threshold Stress Intensities Due to Fracture Surface Morphology," *Metals Transactions A Communications*, Vol. 13A, 1982, p. 937.

[6] Suresh, S., Zamiski, G. F., and Ritchie, R. O., "Oxide Induced Crack Closure: An Explanation for Near-Threshold Corrosion Fatigue Crack Growth Behavior," *Metals Transactions A*, Vol. 12A, p. 1435.

[7] Gray, G. T., Williams, J. C., and Thompson, A. W., "Roughness Induced Crack Closure: An Explanation for Microstructurally Sensitive Fatigue Crack Growth," *Metals Transactions A*, Vol. 14A, 1983, p. 421.

[8] Ohta, A. et al, "Fatigue Crack Propagation Rates and Threshold Stress Intensity Factors for Welded Joints of HT80 Steel and Several Stress Ratios," *International Journal of Fatigue*, Vol. 4, No. 14, 1982, p. 233.

[9] Matsuoka, S. et al, "A Method for Determining Conservative Fatigue Thresholds While Avoiding Crack Closure," *Journal of Testing and Evaluation*, Vol. 14, No. 6, 1986, p. 312.

[10] James, M. N., "Some Observations of the Effect of Microstructure, Wake Plasticity, and Fast Cooling on Fatigue Crack Closure," *International Journal of Fatigue*, Vol. 9, No. 7, 1987, p. 179.

[11] Geary, W. and King, J. E., "Residual Stress Effects During Near Threshold Fatigue Crack Growth," *International Journal of Fatigue*, Vol. 9, No. 1, 1987, p. 11.

[12] Herman, W. A., Hertzberg, R. W., and Jaccard, R., "Prediction and Simulation of Fatigue Crack Growth Under Conditions of Low Crack Closure," *Advances in Fracture Research, 7th International Conference on Fracture*, Vol. 2, 1989, p. 1417.

[13] Newman, J. C., "A Non-linear Approach to the Growth of Small Cracks," *Behavior of Short Cracks in Airframe Components*, AGARD Conference Proceedings 328, Paper 6, 1983.

[14] Newton, C. H., "The Influence of Tensile Overloads and Compressive Underloads on Fatigue Crack Propagation in the Near Threshold Region," PhD Dissertation, Lehigh University, Bethlehem, PA, 1984.

[15] Zaiken, E. and Ritchie, R. O., "On the Role of Compressive Underloads in Influencing Crack Closure and the Threshold Condition for Fatigue Crack Growth in 7150 Aluminum Alloy," *Engineering Fracture Mechanics*, Vol. 22, No. 1, 1985, p. 35.

[16] Herman, W. A., Hertzberg, R. W., and Jaccard, R., "On the Influence of Compressive Load Excursions Under the Influence of Low Crack Closure," *Scripta Metallurgica*, Vol. 23, p. 1285.

[17] De Los Rios, E. R., Tang, Z., and Miller, K. J., "Short Crack Fatigue Behavior in a Medium Carbon Steel," *Fatigue Fracture Engineering Materials Structure*, Vol. 5, No. 2, 1984, p. 97.

[18] Zurek, A. K., James, M. R., and Morris, W. L., "The Effect of Grain Size on Fatigue Crack Growth of Short Cracks," *Metals Transactions A*, Vol. 14A, No. 8, 1983, p. 1697.

[19] Lankford, J., "The Growth of Small Fatigue Cracks in 7075-T6 Aluminum," *Fracture of Engineering Material Structures*, Vol. 5, No. 3, 1982, p. 233.

[20] Lee, H. W. and Stephens, R. I., "Comparison of Short and Long Fatigue Crack Threshold Behavior of Wrought and Cast Mild Steels," *Fatigue 84*, EMAS Ltd., Vol. 1, 1984, p. 255.

[21] Tokaji, K., et al., "Limitations of LEFM in Respect to Small Fatigue Cracks and Microstructure," *Fatigue Fracture Engineering Materials Structure*, Vol. 9, No. 1, 1986, p. 1.

[22] Leis, B. N. and Forte, T. P., "Fatigue Growth of Initially Physically Short Cracks in Notched Aluminum and Steel Plates," *Fracture Mechanics: Proceedings of the 13th National Symposium on Fracture Mechanics, STP 743*, American Society for Testing and Materials, Philadelphia, p. 100.

[23] Tanaka, K., Akiniwa, Y., and Matsui, E., "Propagation of Small Fatigue Cracks in 2024-T3 Aluminum Alloy," *Fatigue 87*, Vol. 1, EMAS Ltd., p. 361.

[24] Soniak, F., and Remy, L., "Behavior of Long and Short Fatigue Cracks in a Powder Metallurgy Superalloy at Room and High Temperature," *Fatigue 87*, EMAS Ltd., Vol. 2, 1987, p. 351.

[25] Venkateswaro Rao, K. T., Yu, W., and Ritchie, R. O., "On the Growth of Small Fatigue Cracks in Aluminum-Lithium Alloy 2090," *Scripta Metallurgica*, Vol. 20, No. 10, 1986, p. 1549.

[26] Yoder, G. R., Cooley, L. A., and Crooker, T. W., "On Microstructural Control of Near-Threshold Fatigue Crack Growth in 7000-Series Aluminum Alloys," *Scripta Metallurgica*, Vol. 16, 1982, p. 1021.

[27] Ritchie, R. O. and Yu, W., "Short Crack Effects in Fatigue, A Consequence of Crack Tip Shielding," *Small Fatigue Cracks*, R. O. Ritchie and J. Lankford, Eds., The Metallurgical Society, 1986, p. 167.

[28] Liaw, P. K. and Logsdon, W. A., "Crack Closure: An Explanation for Small Fatigue Crack Growth Behavior," *Engineering Fracture Mechanics*, Vol. 22, No. 1, 1984, p. 115.

[29] ASTM Round Robin Test Program on Crack Closure, reported at the 1987 Fall Meeting, Bal Harbor, FL, Nov. 87.

[30] Vecchio, R. S., Crompton, J., and Hertzberg, R. W., "Anomalous Aspects of Crack Closure," *International Journal of Fatigue*, Vol. 31, No. 2, 1986, p. R29.

[31] Hertzberg, R. W., Newton, C. H., and Jaccard, R., "Crack Closure: Correlations and Confusion," *Fatigue Crack Closure, STP 982*, American Society for Testing and Materials, Philadelphia, 1988, pp. 139–148.

[32] Donald, J. K., "A Procedure for Standardizing Crack Closure Levels," *Fatigue Crack Closure, STP 982*, American Society for Testing and Materials, Philadelphia, 1988, pp. 222–229.

[33] Broek, D. and Leis, B. N., "Similitude and Anomalies in Crack Growth Rates," *Fatigue 81*, Westbury House, Surrey, United Kingdom, 1981, p. 129.

[34] Allison, J. E. and You, C. P., "Problems Associated with Quantification of Fatigue Crack Closure," *Fatigue 90*, Vol. X, EMAS Ltd., 1990, p. 1249.
[35] Doker, H., Bachman, V., and Marci, G., "A Comparison of Different Methods of Determination of the Threshold for Fatigue Crack Propagation," *Fatigue Thresholds*, J. Backlund, A. Blom, and C. J. Beevers, Eds., EMAS Ltd., 1982, p. 45.
[36] Doker, H. and Peters, M., "Fatigue Threshold Dependence on Material, Environment, and Microstructure," *Fatigue 84*, Vol. 1, EMAS Ltd., p. 275.
[37] Hertzberg, R. W., Herman, W. A., and Ritchie, R. O., "Prediction of Small Crack Growth in 2090-T8E41 Aluminum-Lithium Alloy," *Scripta Metallurgica*, Vol. 21, No. 11, 1987, p. 1541.
[38] Doker, H. and Marci, G., "Threshold Range and Opening Stress Intensity Factor in Fatigue," *International Journal of Fatigue*, Vol. 5, No. 4, 1983, p. 187.
[39] Herman, W. A., Hertzberg, R. W., and Jaccard, R., "A Simplified Laboratory Approach for the Prediction of Short Crack Behavior," *Fatigue Fracture Engineering Materials Structure*, Vol. 11, No. 4, 1988, p. 303.
[40] Makhlouf, K. and Jones, J. W., "Near Threshold Fatigue Crack Growth Behavior in Ferritic Stainless Steel; Applicability of K^c_{max} Testing at Elevated Temperatures," *Fatigue 90*, Vol. X, EMAS Ltd., 1990, p. 1547.
[41] Herman, W. A., "Re-Evaluation of Fatigue Threshold Test Procedures and the Simulation and Prediction of Fatigue Crack Growth Under Conditions of Low Crack Closure," PhD dissertation, Lehigh University, Bethlehem, PA, 1989.
[42] Venkatesware Rao, K. T., Yu, W., and Ritchie, R. O., "Fatigue Crack Propagation in Aluminum-Lithium Alloy 2090. Part I—Long Crack Behavior," submitted to *Metallurgica Transactions A*, 1986.
[43] Nowack, H. and Marrisen, R., "Fatigue Crack Propagation of Short and Long Cracks: Physical Basis, Prediction, and Engineering Significance," *Fatigue 87*, Vol. 1, EMAS Ltd., 1987, p. 207.
[44] Suresh, S., et al., "Crack Initiation & Growth Under Far-Field Cyclic Compression, *Small Fatigue Cracks*, TMS, 1986, p. 513.
[45] Suresh, S. and Ritchie, R. O., "Propagation of Short Fatigue Cracks," *International Metals Review*, Vol. 20, No. 10, 1984, p. 1549.
[46] Bolingbroke, R. K. and King, J. E., "A Comparison of Long and Short Fatigue Crack Growth in a High Strength Aluminum Alloy," *The Behavior of Short Fatigue Cracks*, K. J. Miller and E. R. De Los Rios, Eds., Mechanical Engineering Publications, London, 1986, p. 101.
[47] McCarver, J. F. and Ritchie, R. O., "Fatigue Crack Propagation Thresholds for Long and Short Cracks in Rene 95 Nickel Base Superalloy," *Materials Science and Engineering*, Vol. 55, No. 1, 1982, p. 63.
[48] Doker, H. and Bachmann, V., "Determination of Crack Opening Load by Use of Threshold Behavior, Mechanics of Fatigue Crack Closure," *Mechanics of Fatigue Crack Closure, STP 982*, J. C. Newman, Jr. and M. Elber, Eds., American Society for Testing and Materials, Philadelphia, 1988, p. 247–259.
[49] Marci, G., Castro, D. E., and Bachmann, V., "Fatigue Crack Propagation Threshold, *Journal of Testing and Evaluation*, JTEVA, Vol. 17, No. 1, 1989, p. 28.
[50] Castro, D. E., Marci, G., Munz, D., "A Generalized Concept of a Fatigue Threshold," *Fatigue Fracture Engineering Materials Structure*, Vol. 9, No. 4, 1987, p. 305.
[51] Jaccard, R., "Fatigue Life Prediction of Aluminum Components Based on Local Stress Fields," 3rd International Conference on Aluminum Weldments, Munich, Germany, April, 1985.
[52] Jaccard, R., "Fatigue Life Prediction of Aluminum Structures Based on SN Curve Simulation," *2nd International Conference on Aluminum Weldments*, Aluminum-Verlag, Dusseldorf, Germany, 1982.
[53] Saxena, A. and Hudak, S. J., "Review and Extension of Compliance Information for Common Crack Growth Specimens," *International Journal of Fracture*, Vol. 14, No. 5, 1978, p. 453.
[54] ASTM Specification E 399, "Test Method for Plane Strain Fracture Toughness of Metallic Materials," *1983 Annual Book of ASTM Standards*, American Society for Testing and Materials, Philadelphia, 1983, p. 482.
[55] Bu, R. and Stephens, R. I., "Comparison of Short and Long Fatigue Crack Growth in 7075-T6 Aluminum," *Fatigue Fracture Engineering Materials Structures*, Vol. 9, No. 1, 1986, p. 35.
[56] Wagner, L. and Lutering, R., "A Comparison of Short Crack Propagation in an Aluminum Alloy with Different Age Hardening Conditions and Grain Sizes," *Fatigue 87*, Vol. 3, EMAS Ltd., 1987.
[57] Zurek, A. K., James, M. N., and Morris, W. L., "The Effect of Grain Size on Fatigue Growth of Small Cracks," *Metallurgica Transactions A*, Vol. 14A, No. 8, 1983, p. 1697.
[58] Vecchio, R. S., "Application of Fracture Mechanics Principles to Fatigue Crack Growth in a Powder Metallurgy Nickel-Base Alloy," Ph.D. dissertation, Lehigh University, Bethlehem, PA, 1985.

[59] Brown, C. W., King, J. E., and Hicks, M. A., "Effects of Microstructure on Long and Short Crack Growth in Nickel-base Superalloys," *Materials Science,* Vol. 18, 1984, p. 374.

[60] Brown, C. W. and Hicks, M. A., "A Comparison of Short Crack Growth Behavior in Engineering Alloys," *Fatigue 84,* EMAS Ltd., Vol. 2, 1984, p. 1337.

[61] Soniak, R. and Remy, L., "Fatigue Growth of Long and Short Cracks in a Powder Metallurgy Nickel Base Superalloy," *The Behavior of Short Fatigue Cracks,* K. J. Miller and E. R. De Los Rios, Eds., Mechanical Engineering Publications, London, 1986, p. 133.

[62] Newman, J. C., Swain, M. H., and Phillips, E. P., "An Assessment of the Small Crack Effect for 2024-T3 Aluminum Alloy," *Small Fatigue Cracks,* R. O. Ritchie and J. Lankford, Eds., The Metallurgical Society, 1986, p. 240.

[63] Lee, J. J. and Sharpe, W. N., "Short Fatigue Cracks in Notched Aluminum Specimens," *Small Fatigue Cracks,* R. O. Ritchie and J. Lankford, Eds., American Institute of Mechanical Engineers, 1980, p. 323.

[64] Taira, S., et al., "Grain Size on Crack Nucleation and Growth in Long Life Fatigue of Low Carbon Steel," *Fatigue Mechanisms, STP 675,* J. T. Fong, Ed., 1987, p. 135.

[65] Tanaka, K. and Nakai, Y., "Propagation and Non-Propagation of Short Fatigue Cracks at a Sharp Notch," *Fatigue Fracture Engineering Materials Structures,* Vol. 6, No. 4, 1983, p. 315.

[66] Tokaji, K., Ogawa, T., and Harada, Y., "The Growth of Small Fatigue Cracks in a Low Carbon Steel: The Effect of Microstructure and Limitations of Linear Elastic Fracture Mechanics," *Fatigue Fracture Engineering Materials Structures,* Vol. 9, No. 3, 1986, p. 205.

[67] Tokaji, K., Ogawa, T., and Harada, Y. "Evaluation of Limitations of Linear Elastic Fracture Mechanics for Small Fatigue Crack Growth," *Fatigue Fracture Engineering Materials Structures,* Vol. 10, No. 4, 1987, p. 281.

[68] Ogawa, T., Miyoshi, Y., and Nishikawa, I., "Fatigue Crack Growth and Closure of Small Cracks at the Notch Root," *Current Research on Fatigue Cracks,* T. Tanaka, M. Jono, and K. Komai, Eds., 1986, p. 67.

[69] Ritchie, R. O. and Suresh, S., "The Fracture Mechanics Similitude Concept: Questions Concerning Its Application to the Behavior of Short Fatigue Cracks," *Materials Science and Engineering,* Vol. 57, No. 2, 1987, p. 27.

[70] Vecchio, R. S. and Hertzberg, R. W., "A Rationale for the Apparent Anomalous Growth Behavior of Short Fatigue Cracks," *Engineering Fracture Mechanics,* Vol. 22, No. 6, 1985, p. 1049.

Summary

There are now several well-established techniques available for characterizing various aspects of small-crack propagation. Some are more amenable than others for routine use; some require significant expertise. Some require almost no financial investment, while others require more significant expenditures. All are useful for measuring the growth of fatigue cracks on the order of 50 to 75 μm or greater, and some are applicable to even smaller cracks. There is little evidence the techniques yield *da/dN* versus ΔK data, which is technique dependent; however, extensive comparisons on a common set of material have not been conducted. Some techniques have relative limitations for use in characterizing three-dimensional shape changes (for example, replication), although all must make some assumptions about crack shape changes that require pre- or post-test verification. Shape changes may be deduced from the combination of some of the measurements.

Fatigue crack closure has been shown to be an important factor affecting small (and large) crack propagation. Some of the techniques reviewed here are very useful for characterizing crack compliance and closure (for example, ISDG and SEM) while others yield little or no quantitative closure information (for example, replication and photomicroscopy). Some techniques provide information that is clearly related to crack-closure behavior, however, the degree with which it can be used to quantify crack closure is open to interpretation (for example, ultrasonic and electric potential methods). Finally, novel techniques have been developed for conducting large-crack experiments (for example, constant-K_{max}), which may be closure free and thus may be useful for bounding those small-crack effects that are attributable to crack closure.

There is little disagreement that the small-crack effect exists and is important. However, in addition to the major and natural controversies regarding mechanistic interpretation, controversy exists in testing practice as well. These include the following:

1. Use of $\Delta\sigma = \sigma_{max} - \sigma_{min}$ where $\sigma_{min} < 0$ in calculating ΔK.
2. Use of established increments for data collection, fixed Δa versus fixed ΔN increments.
3. Methods for dealing with multiple cracks/rejection of data for crack interaction effects.
4. Use of large-crack procedures for bounding small-crack *da/dN* versus ΔK data.
5. Use of ultrasonic and electric potential, and perhaps even SEM, techniques for quantifying crack closure.

Future activity by ASTM Committees' E-9/E-24 Joint Task Group on Small Fatigue Cracks should concentrate on resolving these controversial measurement issues, which will pave the way to a recommended practice for small-crack test methods that is technique independent. In addition there is a need for more extensive comparison of *da/dN* versus ΔK data and closure data for a variety of techniques (for example, round-robin activity). Finally, research challenges exist in extending small-crack test methods to characterization of fatigue cracks less than 50 to 75 μm in size. Of obvious and general importance is research directed at understanding small-crack growth mechanisms, including environmental interactions, and characterizing/correlating small-crack behavior. This information is needed for development of more fatigue resistant and damage tolerant materials. In addition, as methods of non-destructive evaluation continue to improve, and the minimum detectable crack size de-

creases, a more thorough understanding of small-crack behavior will be needed for life prediction of high-performance structural applications.

Given the importance of small fatigue crack information for use in alloy development and the critical requirement for its use in component design, we are hopeful that this publication will be useful to students, researchers, and practicing engineers and will provide a means to make the experimental and analytical methods used to characterize small fatigue cracks more accessible.

John E. Allison
Ford Scientific Laboratory,
P.O. Box 2053, Dearborn, MI 48121;
symposium cochairman and coeditor.

James M. Larsen
Wright Laboratory, Materials Directorate,
Wright-Patterson Air Force Base, OH 45433;
symposium cochairman and coeditor.

ISBN 0-8031-1469-9